

出藍 第33号

2020年6月

目次

【原著論文(査読有)】

- 1 Control of short-pulsed laser induced periodic surface structures with machining -picosecond laser nanotexturing with magnetic abrasive finishing- 1
Shuhei Kodama, Hitomi Yamaguchi, Keita Shimada, Masayoshi Mizutani, Tsunemoto Kuriyagawa, Precision Engineering, Vol. 60 (2019) pp. 428–436.
- 2 単結晶窒化ガリウム (GaN) 基板の高速高精度加工法の開発 —紫外線援用テープ研削法の提案— 10
鷹巣良史, 嶋田慶太, 水谷正義, 厨川常元, 砥粒加工学会誌, Vol. 63, No. 11 (2019) pp. 569–574.
- 3 微細ラティスコーティング技術の開発 —重力落下式粉末供給手法による壁構造の評価— 16
前花英一, 白沢太一, 石橋信治, 嶋田慶太, 水谷正義, 厨川常元, 砥粒加工学会誌, Vol. 64, No. 1 (2020) pp. 39–46.
- 4 Processing capabilities of micro ultrasonic machining for hard and brittle materials: SPH analysis and experimental verification 24
Jingsi Wang, Jingguo Fu, Jinlong Wang, Fengming Du, Pay Jun Liew, Keita Shimada, Precision Engineering, Vol. 63 (2020) pp. 159–169.
- 5 Ultrasonic-Assisted Face Milling for Fabricating Hierarchical Microstructures 35
Keita Shimada, Ziqi Chen, Masayoshi Mizutani, Tsunemoto Kuriyagawa, International Journal of Automation Technology, Vol. 14, No. 2 (2020) pp. 238–244.

【国際会議プロシーディング(査読有)】

- 1 Micrometer-scaled hierarchical structures fabricated by ultrasonic-assisted cutting 42
Keita Shimada, Ziqi Chen, Masayoshi Mizutani, Tsunemoto Kuriyagawa, International Advancement in Ultraprecision Machining Process (The Proceedings of the 15th CJUMP), Vol. 6 (2019) pp. 21–24.
- 2 Design of Pore Morphology in Porous Metal Manufactured via Selective Laser Melting 46
Shinji Ishibashi, Masataka Chuzenji, Masaki Tsukuda, Hidekazu Maehana, Keita Shimada, Masayoshi Mizutani, Tsunemoto Kuriyagawa, The 8th international Conference of Asian Society for Precision Engineering and Nanotechnology (ASPEN 2019) (2019)

3 Ultrasonic assistance on the generation of hydroxyl radicals in ultrafine bubble suspended water	48
Keita Shimada, Kazuki Suzuki, Masayoshi Mizutani, Tsunemoto Kuriyagawa, The 8th international Conference of Asian Society for Precision Engineering and Nanotechnology (ASPEN 2019) (2019)	
4 Bactericidal effect of ultrafine bubble against <i>Pseudomonas aeruginosa</i> in grinding fluid	50
Hiroko Yamada, Kensuke Konishi, Keita Shimada, Masayoshi Mizutani, Tsunemoto Kuriyagawa, The 22nd International Symposium on Advances in Abrasive Technology (2019)	
5 Formation of Hydroxyapatite and Zirconia Composite Films with Powder Jet Deposition and Their Color Measurement	56
Keita Shimada, Takaaki Sunouchi, Hiroki Yamamoto, Kuniyuki Izumita, Keiichi Sasaki, Masayoshi Mizutani, Tsunemoto Kuriyagawa, The 22nd International Symposium on Advances in Abrasive Technology (2019)	
6 Wettability and osteoblast-like cell behavior on zirconia surface irradiated with nanosecond pulsed laser	62
Tomohiro Harai, Keita Shimada, Masayoshi Mizutani, Satomi Oizumi, Keisuke Nakamura, Masatsugu Hirota, Tohru Hayakawa, Hitoshi, Ohmori, Tsunemoto Kuriyagawa, The 22nd International Symposium on Advances in Abrasive Technology (2019)	
【総説】	
1 Manufacturing technologies toward extreme precision	69
Zhiyu Zhang, Jiwang Yan, Tsunemoto Kuriyagawa, International Journal of Extreme Manufacturing, Vol. 1 (2019) pp. 1–22.	
2 究極の形状創成と機能創成が拓く高付加価値製造技術	91
厨川常元, 精密工学会誌, Vol. 85, No. 4 (2019) pp. 299–303.	
【解説記事・紹介記事】	
1 機能性発現のための超音波援用切削による微細テクスチャリング	96
嶋田慶太, 水谷正義, 厨川常元, 超音波テクノ, Vol. 31, No. 6 (2019) pp. 25–28.	
2 機能性インターフェース創成を可能とする超音波振動援用プラズマ放電研削加工システムの開発	100
小林敏, 立花享, 嶋田慶太, 水谷正義, 厨川常元, 超音波テクノ, Vol. 31, No. 6 (2019) pp. 19–24.	
3 機能創成加工から「未来の医療」へ	106
厨川常元, 医薬経済, Vol. 1597 (2019) pp. 62–64.	
4 地域貢献を目指して	109
久慈千栄子, まてりあ, Vol. 59, No. 3 (2020) p. 161.	

【国内発表】

- 1 選択的レーザー溶融法による根状多孔質構造体の創成 110
中善寺優昂, 石橋信治, 溝井琢巳, 前花英一, 嶋田慶太, 水谷正義, 厨川常元, 2019年度精密工学会学術講演会講演論文集 (2019) pp. 359–360.
- 2 パウダージェットでポジションの審美歯科への応用 112
本郷那美, 山本浩己, 富江瑛彦, 泉田一賢, 佐々木啓一, 嶋田慶太, 水谷正義, 厨川常元, 2019年度砥粒加工学会学術講演会 (2019) pp. 525–526.
- 3 プラズマ援用パウダージェットデポジションに関する研究 114
森田隆輝, 本郷那美, 山本浩己, 嶋田慶太, 水谷正義, 厨川常元, 2020年砥粒加工学会卒業研究発表会発表論文集 (2020) pp. 45–46.

【修士論文】

- 1 Study of Tape CMP Grinding of Gallium Nitride Wafer 116
Kota Orino, 令和元年度機械機能創成専攻修士学位論文要旨
- 2 Study on high functionality of cutting tool by Plasma-Shot Treatment 118
Yorihito Shibata, 令和元年度機械機能創成専攻修士学位論文要旨
- 3 Study on creation of fine periodic structure on V-shaped groove with short-pulsed laser 120
Ryohei Takase, 令和元年度機械機能創成専攻修士学位論文要旨
- 4 Study on creating functional biointerfaces by laser irradiation 122
Chiaki Takita, 令和元年度医工学研究科修士学位論文要旨
- 5 Development of Dental Handpiece of Powder Jet Deposition 123
Hiroki Yamamoto, 令和元年度機械機能創成専攻修士学位論文要旨



Control of short-pulsed laser induced periodic surface structures with machining -picosecond laser nanotexturing with magnetic abrasive finishing-

S. Kodama^{a,*}, H. Yamaguchi^b, K. Shimada^c, M. Mizutani^c, T. Kuriyagawa^c

^a Tokyo University of Agriculture and Technology, 2-24-16 Naka-cho, Koganei, Tokyo, 184-0012, Japan

^b University of Florida, 226 MAE-B, P.O. Box 116300, Gainesville, FL, 32611-6300, USA

^c Tohoku University, 6-6-01 Aramaki-Aza-Aoba, Aoba-ku, Sendai, 980-8579, Japan

ARTICLE INFO

Keywords:

Short-pulsed laser
Magnetic abrasive finishing
Straight sub-micrometer groove
Surface roughness

ABSTRACT

An active area of research is the altering of surface functions (e.g., wettability and cell adhesion) by controlling fine surface structures such as laser-induced periodic surface structures (LIPSS). It has been found that micrometer-scale grooving (produced, for example, using ultraprecision cutting) followed by short-pulsed laser irradiation can result in efficient LIPSS coverage of a large area. However, micrometer-scale grooves can remain on the surface after short-pulsed laser irradiation. In this paper, to clarify the phenomenon and processing principle of groove-assisted short-pulsed laser irradiation, a finite-difference time-domain simulation is developed and experiments are conducted using 304 stainless steel and nickel-phosphorus (Ni–P) plating layer substrates. The use of magnetic abrasive finishing (MAF) is proposed for fabricating sub-micrometer-deep straight grooves with various peak-to-peak distances (pitch length) prior to the short-pulsed-laser irradiation. The subsequent short-pulsed-laser irradiation produces sub-micrometer-deep straight structures superimposed on the MAF-produced surface. While the pattern and depth of LIPSS are influenced by the groove depth made by MAF prior to the short-pulsed laser irradiation, the pitch length of LIPSS is dependent on the laser wavelength. This demonstrates the ability of MAF to produce grooves that guide the LIPSS and the efficacy of the developed method for fabricating fine LIPSS. The geometry of the sub-micrometer deep grooves—made prior to the short-pulsed laser irradiation—is the dominant factor in determining the pattern and geometry of the LIPSS.

1. Introduction

Many research projects have been carried out to study the creation of fine structures on a surface to impart various functionalities such as a reduction of friction [1–3], control of wettability [4,5] and enhancement of cell adhesion [6,7]. Laser-induced periodic surface structures (LIPSS) enable those surface functions, and it has been shown that short-pulsed laser irradiation is a promising method for fabricating LIPSS in a self-organizing manner [8]. However, it has been difficult to finely control the LIPSS made by short-pulsed laser irradiation due to a lack of understanding of the processing principle and the phenomenon itself [9–12]. While it has been reported that the pitch length and the direction of LIPSS are controlled by using two lasers [13,14], there are a few reports to control LIPSS by changing the original surface shape before laser irradiation.

Our previous study revealed that LIPSS are influenced by the crystal structures, as shown in Fig. 1 [15]. Another study revealed that LIPSS follow debris or depressions on the substrate surface that easily induce plasma waves [16]. We proposed groove-assisted short-pulsed-laser irradiation, a method based on this phenomenon to fabricate LIPSS patterns guided by micrometer-deep grooves made using ultraprecision cutting followed by short-pulsed laser irradiation [17]. As shown in Fig. 2 [17], straight, high-aspect-ratio LIPSS were fabricated on top of the microgrooves; however, the cutting grooves remained on the surface. To eliminate the remaining deep groove and control the structures made using groove-assisted short-pulsed-laser irradiation, the effects of the groove geometry (roughness) on the laser-irradiation phenomena needs to be further studied.

Magnetic abrasive finishing (MAF) is a process by which material is removed by magnetic abrasives sliding against a target surface in a

* Corresponding author.

E-mail addresses: shuhei-kodama@go.tuat.ac.jp (S. Kodama), hitomiy@ufl.edu (H. Yamaguchi), shimada@m.tohoku.ac.jp (K. Shimada).

<https://doi.org/10.1016/j.precisioneng.2019.06.015>

Received 2 November 2018; Received in revised form 10 May 2019; Accepted 31 May 2019

Available online 11 September 2019

0141-6359/© 2019 Elsevier Inc. All rights reserved.

magnetic field, capable of polishing a complicated three-dimensional curved surface with high accuracy and efficiency [18–20]. The MAF-processed surface is the accumulation of generated scratches, which are between nanometers and micrometers deep, depending on the abrasive size and the magnetic force acting on the magnetic abrasive [21].

The objectives of this study are to apply MAF to fabricate grooves with various geometries (e.g., depth and pitch length) and to investigate the effects of the groove geometry on short-pulsed laser irradiation. A finite-difference time-domain (FDTD) simulation was developed to investigate the effects of straight micro/nanogrooves on the electric field intensity distribution by laser irradiation, causing fabrication of LIPSS, and experiments were conducted using 304 stainless steel and Ni–P substrates in which sub-micrometer- and micrometer-deep straight grooves, fabricated using MAF, was irradiated using short-pulsed laser energy. This paper describes the efficacy of MAF to produce grooves assisting the short-pulsed-laser irradiation and identifies the effects of the geometry, especially roughness, of the grooves made using MAF on the structures made using short-pulsed laser irradiation.

2. Principles

Fig. 3 shows the MAF processing principle for the inner surface of a nonferrous magnetic tube. A magnetic field magnetizes and attracts a mixture of iron particles and magnetic abrasives, pressing them against the inner tube surface. The magnetic force F acting on a magnetic particle in a non-uniform magnetic field is expressed as follows:

$$F = V\chi H \cdot \text{grad}(H) \quad (1)$$

where V is the volume of the magnetic particle, χ is the susceptibility, and H and $\text{grad}(H)$ are the intensity and the gradient of the magnetic field, respectively.

When the tube is rotated at high speed, the mixture of iron particles and magnetic abrasives move relative to the inner surface of the tube, finishing it. The motion of the mixture of iron particles and magnetic abrasives (shown in Fig. 3(b)) leads to self-generating action.

Fig. 4 shows the processing principle of short-pulsed laser irradiation [17]. Surface unevenness provides the starting points for the plasma waves created by the parametric decay when the surface is irradiated [22,23], as shown in Fig. 4(a). Surface plasmon occurs due to interference between the plasma wave and the incident light, causing periodic Coulomb explosions on the surface. After the collisional relaxation time (CRT), heat is distributed on the surface, inducing ablation or inhibition of structures, eventually producing LIPSS [24,25]. The wavelength of the plasma wave is 0.5–0.85 times as long as the wavelength of the irradiating laser and is approximately equal to the pitch length between LIPSS [22,23]. LIPSS are fabricated when the pulse duration, a major factor in the fabrication of LIPSS, is shorter than the CRT [26,27], and a short-pulsed laser with a 20 ps pulse duration has been used in our research since the 20 ps pulse duration is similar to the CRT and the increase of the pulse duration reduces machining cost and stabilizes

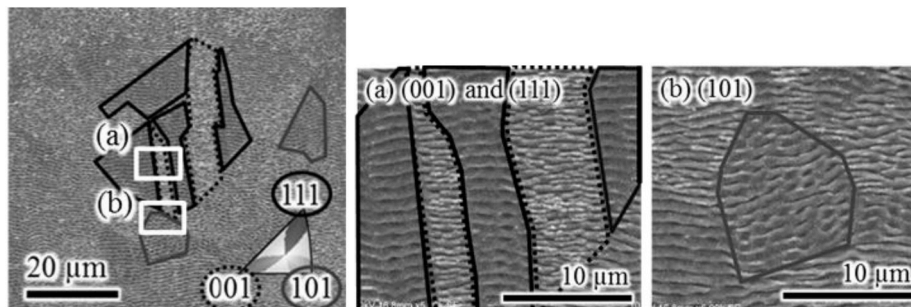


Fig. 1. LIPSS on a 304 stainless steel surface [15].

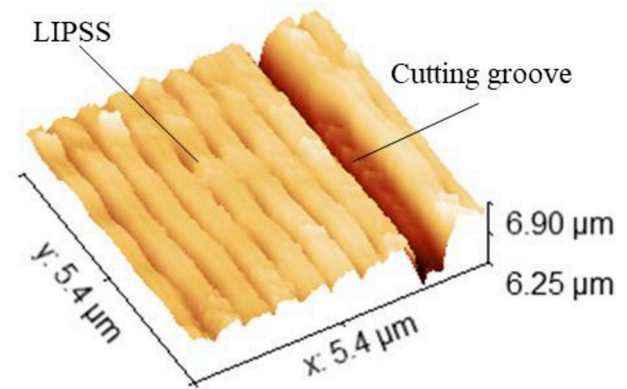


Fig. 2. LIPSS on a flat surface and a Ni–P surface with cutting groove [17]

(a) Schematic of internal MAF

(b) Behavior of magnetic particles and abrasives at finishing area.

laser irradiation.

3. Electromagnetic field analysis

3.1. Methodology

A finite-difference time-domain (FDTD) simulation was conducted for investigation of the effect of the groove depth on the electric-field intensity when fabricating LIPSS using a short-pulsed laser. This method involves the calculation of the electromagnetic field intensity by solving the time-dependent Maxwell’s equations in differential form, introduced by Yee in 1966 [28–32]. The time arrangement is determined by Eqs. (2) and (3) by solving Maxwell’s equations. Each electric field is located in the middle between a pair of magnetic fields.

$$E^n = \frac{1 - \frac{\sigma \Delta t}{2\epsilon}}{1 + \frac{\sigma \Delta t}{2\epsilon}} E^{n-1} + \frac{\Delta t}{1 + \frac{\sigma \Delta t}{2\epsilon}} \nabla \times H^{n-\frac{1}{2}} \quad (2)$$

$$H^{n+\frac{1}{2}} = H^{n-\frac{1}{2}} - \frac{\Delta t}{\mu} \nabla \times E^n \quad (3)$$

where E is the electric field, B is the magnetic flux density, D is the electric flux density, H is the magnetic field, ρ is the electric charge density, J is the current density, μ is the permeability, ϵ is the permittivity and σ is the conductivity, superscript n is the time steps, Δt is the time increment.

3.2. Analytical setup and conditions

Electromagnetic field analysis was conducted by using an FDTD simulation (using nanophotonic FDTD simulation software from Lumerical Inc.) to investigate the effects of the optical constants (the refractive index, the extinction coefficient) for each material. Fig. 5

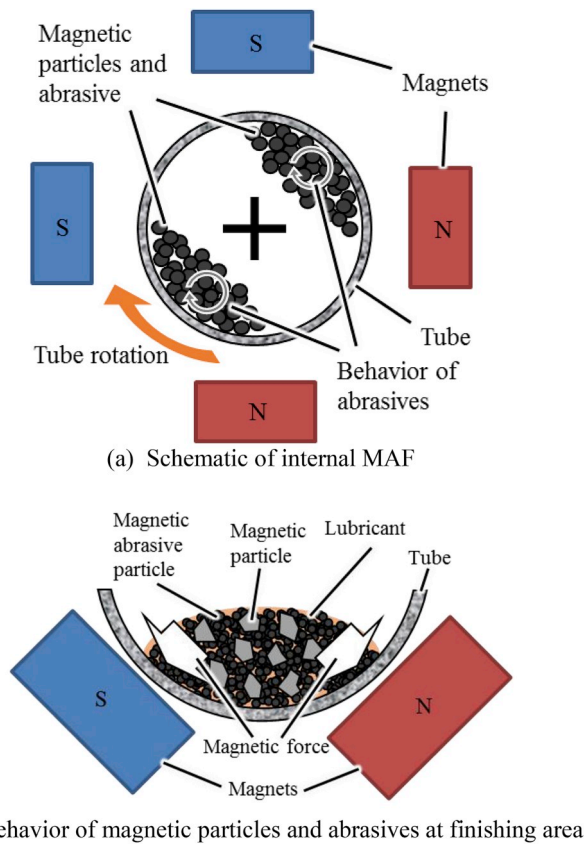


Fig. 3. Processing principle of internal magnetic abrasive finishing process
 (a) Mechanism of surface plasmon due to parametric decay
 (b) Processing model.

shows the analytical model of the initial process of LIPSS: the insides of the orange-bordered rectangle and the yellow-bordered square are the analysis area and the monitor area, respectively, and the purple arrow and the blue double-headed arrow indicates the direction of the incident light and the direction of the laser polarization, respectively. Nickel-phosphorus (Ni-P) and 304 stainless steel were used for analysis objects, and the analytical conditions are listed in Table 1, including the refractive index and the extinction coefficient measured by an ellipsometer. The pitch length of grooves (P_l) was set to 800, 850 and 900 nm to investigate the difference of the electric field distribution for each material and to predict the geometry of LIPSS. The two-dimensional analysis was conducted, and the boundary conditions of x-axis and y-axis were set to the periodic boundary conditions and the perfectly matched layer (PML) conditions absorbing and attenuating lights incident on the boundary surface with little reflection, respectively, modeling the laser irradiated on the surface with periodic structures.

Next, the same analysis was performed to investigate the effects of and the initial surface with a groove on the height of LIPSS. Fig. 6 and Table 2 show the analytical model of a surface with a groove irradiated by a laser and the analytical conditions. The two-dimensional analysis was conducted, and the boundary conditions of x-axis and y-axis were set to the PML conditions, modeling the laser irradiated on the surface with a groove. The groove depth was set to 500, 1000 nm to investigate the effects of groove depth smaller than 1000 nm on the fabrication of LIPSS since the previous study investigated the effect of the groove with 1000 nm depth [17].

3.3. Results and remarks

Fig. 7 shows the analytical results for each material, suggesting that ablation might occur at the area with large electric field intensity (EFI) due to the multiple ionization and the Coulomb explosion. The upper and the lower parts in the analytical results show the atmosphere and the workpiece, respectively. If the penetration depths of the EF at the bottoms of the grooves is larger than that at the tops of grooves, the bottoms of the grooves might be removed. Fig. 7 shows that the electric field at the bottom of the grooves reached deeper into the material than

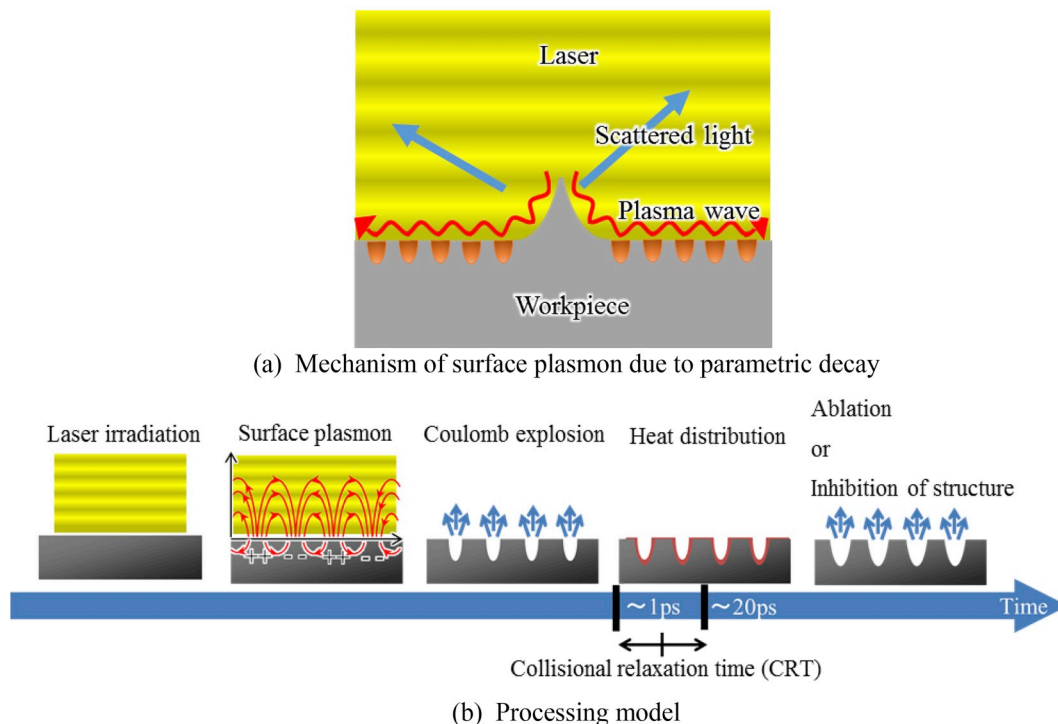


Fig. 4. Processing mechanism of short-pulsed laser [17].

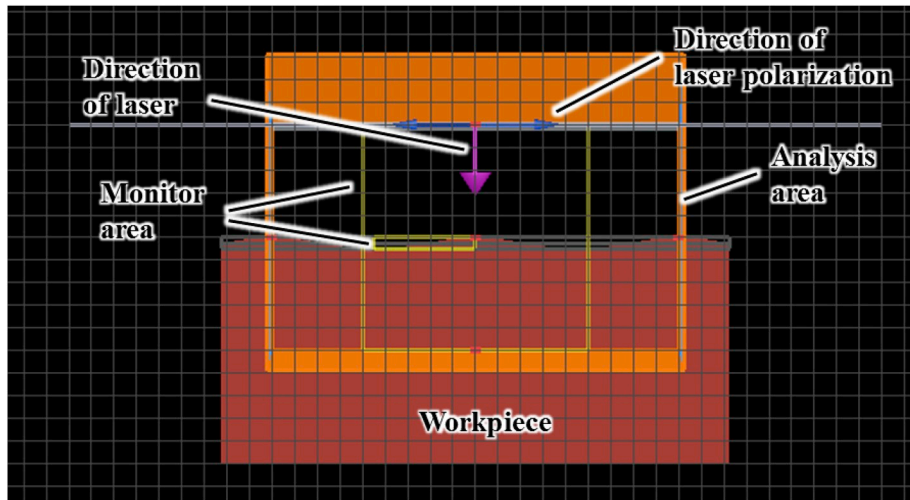


Fig. 5. Analytical model of periodic structures.

Table 1
FDTD analytical conditions.

Laser wavelength	900 nm	
Pulse duration	20 ps	
Material	Ni-P	304 stainless steel
Refractive index	2.73	3.11
Extinction coefficient	3.68	4.89
Pitch length P_l	800, 850, 900 nm	
Height	50 nm	
Boundary condition (x-axis)	Periodic	
Boundary condition (y-axis)	PML	

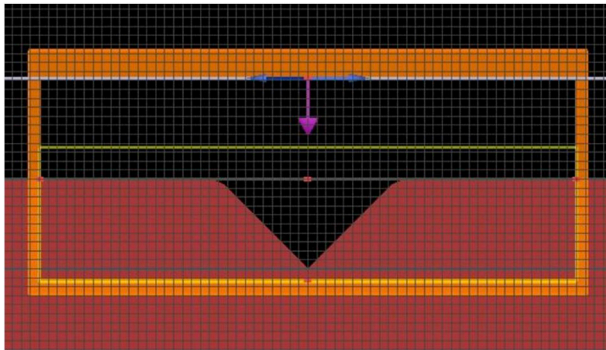


Fig. 6. Analytical model of surface with a groove.

Table 2
FDTD analytical conditions.

Laser wavelength	900 nm	
Pulse duration	20 ps	
Material	Ni-P	
Groove depth G_d	100, 500, 1000 nm	
Groove angle	90°	
Boundary condition (x-axis)	PML	
Boundary condition (y-axis)	PML	

that at the top of them on all surfaces except for $P_l = 900$ nm on 304 stainless steel surface. Fig. 8 shows the relationship between P_l and the EFI of the bottom and the top of grooves for each material. The gap of EFI between the bottom and the top of grooves were the largest when $P_l = 850$ and 900 nm on 304 stainless steel and Ni-P surface,

respectively, suggesting that the pitch length of LIPSS on a 304 stainless steel surface might be shorter than that on a Ni-P surface because it has the high refractive index, shortening the wavelength of incident lights. The EFI of Ni-P was smaller than that of 304 stainless steel due to a less extinction coefficient inducing small absorption.

Fig. 9 shows the analytical results of the surface with a groove irradiated. The EF is distributed periodically on all surfaces with grooves inducing surface plasma waves, and the EF reached deeper into the surface with increasing the groove depth. Fig. 10 shows the maximum and minimum electric field intensity on the substrate surface for each analytical condition. The maximum and minimum EFI slightly increased and decreased with the increase of the groove depth, causing much ablation of material and resulting in LIPSS with a high aspect ratio (depth divided by pitch length), since a deeper groove had larger inclined planes which induce the multiple reflections and strong surface plasma waves.

These results show that a material with a higher extinction coefficient and surfaces with deeper grooves are key factors to effectively fabricate LIPSS with high aspect ratio.

As shown in Fig. 2, the previous research showed that the micrometer-scale deep grooves, which were helpful in LIPSS fabrication, remained on the Ni-P surface after the laser irradiation. The groove depth before the laser irradiation was about 1 μm , which was longer than the height of LIPSS. This result and the FDTD simulation combine to suggest that the groove should be deep enough to facilitate LIPSS fabrication but should not exceed the depth of ablation.

4. Experiments

Experiments were conducted to fabricate straight high-aspect-ratio LIPSS and to investigate the effects of the groove depth on the fabricated LIPSS. Grooves with various depths were fabricated using MAF, and these grooves were irradiated by a short-pulsed laser. The resultant structures were observed with a scanning electron microscope (SEM) and measured using an atomic force microscope (AFM).

4.1. Groove fabrication

4.1.1. Experimental setup and conditions

Ni-P-plated 304 stainless steel tubes (19 mm OD \times 17.2 mm ID \times 100 mm long) with the film thickness of 200 μm and 304 stainless steel tubes (20 mm OD \times 18 mm ID \times 100 mm long) were prepared as workpieces for this study to fabricate LIPSS on the free curved surface. Fig. 11 shows the MAF equipment, which includes four Nd-Fe-B permanent magnets (9.53 \times 9.53 \times 19.05 mm) to generate the magnetic

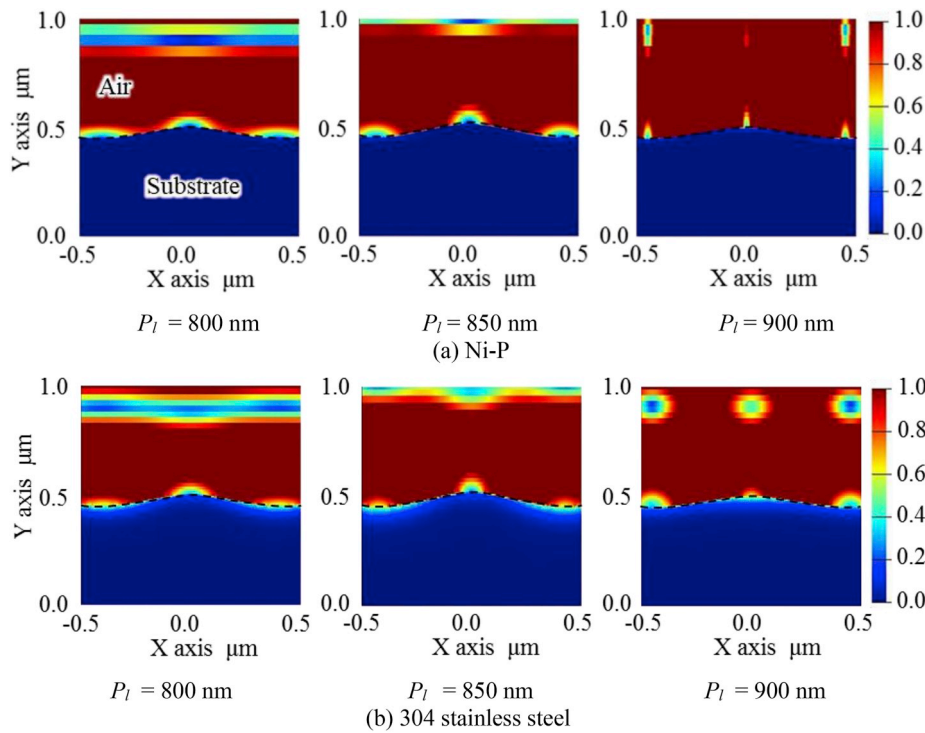


Fig. 7. Electric field distribution for each material with different pitch.

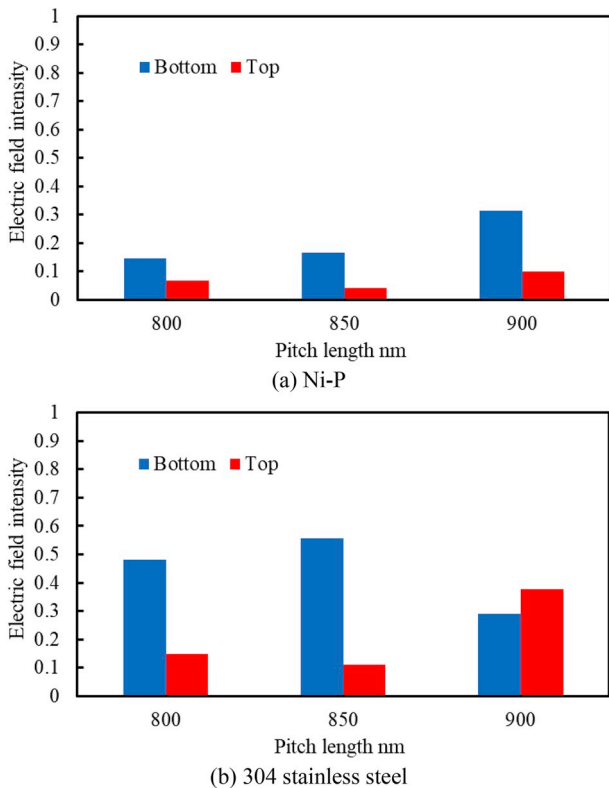


Fig. 8. Changes in electric field intensity for each material with different pitch.

field inside the tube, a chuck to hold the tube, and motors for tube rotation and magnet vibration (in the tube axial direction).

The finishing conditions are provided in Table 3. The abrasive depth of cut mainly determines the groove depth in the tube surface. In this study, the abrasive depth of cut was altered by changing the magnetic

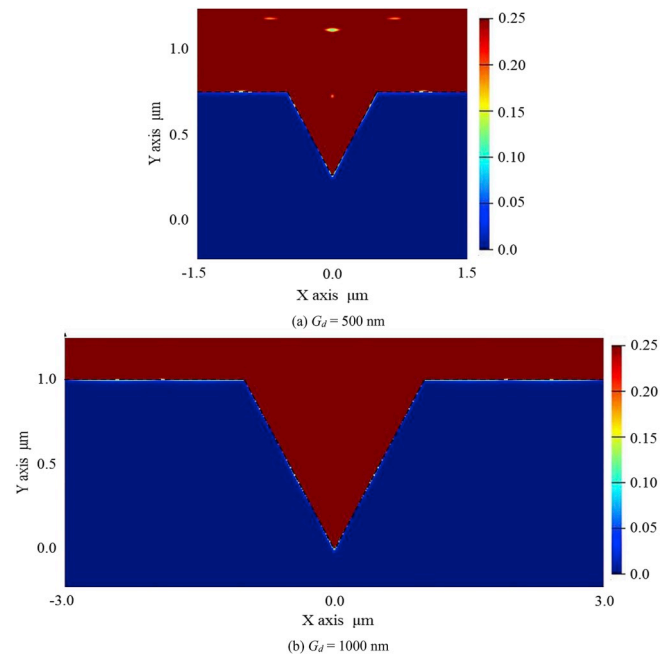


Fig. 9. Electric field distribution for each groove with different depth.

particle size and the magnetic force acting on the magnetic particles pressing the magnetic abrasive against the tube surface. As shown in Eq. (1), the magnetic force acting on the particle is proportional to the volume of the particle. Four different sizes of ferromagnetic particles were used in the case of Ni-P-plated tubes. The initial surface roughness of the plated tubes was about 1.6 μm Rz (average maximum height). They were initially finished with the largest magnetic particles for 5 min and they were then rinsed using an ultrasonic cleaner, and the surface roughness was measured with a diamond-stylus profilometer. The finishing experiments were continued with smaller magnetic particles for

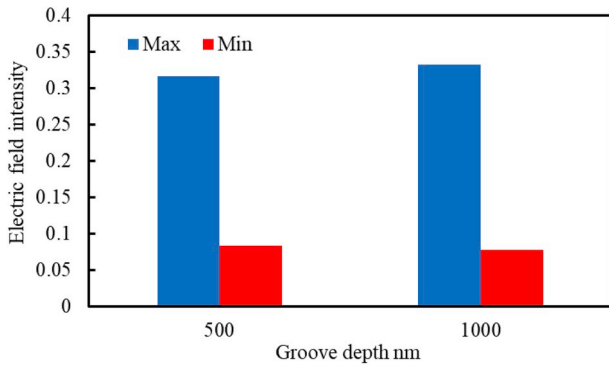


Fig. 10. Changes in electric field intensity for each groove with different depth.

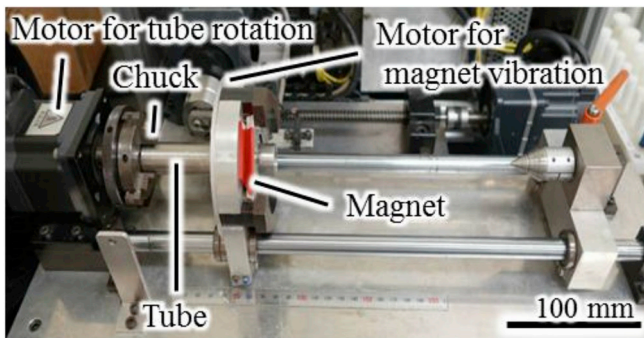


Fig. 11. MAF equipment.

Table 3

Finishing conditions.

Workpiece	Ni-P plated 304 stainless steel tube ($\varnothing 19 \times \varnothing 17.2 \times 100$ mm), 304 stainless steel tube ($\varnothing 20 \times \varnothing 18 \times 100$ mm)
Workpiece revolution	2000 min ⁻¹
Magnetic particle	MP1) 1.6 g Iron particles (grain diameter 44–149 μ m) MP2) 1.6 g Iron particles (grain diameter 149–297 μ m) MP3) 1.6 g Iron particles (grain diameter 177–595 μ m) MP4) 1.6 g Steel grit 50 (mean diameter 297 μ m)
Abrasive	0.4 g Magnetic abrasive (mean diameter 80 μ m, Alumina particles < 10 μ m)
Lubricant	Soluble-type barreling Compound: 0.8 mL
Permanent magnet	Neodymium (Nd-Fe-B) permanent magnet: 9.5 \times 9.5 \times 19.05 mm
Amplitude	2.5 mm
Frequency	0.8 Hz
Finishing time	5 min

another 5 min, followed by another roughness measurement. This sequence was repeated four times to meet the polishing limit. In the case of the unplated 304 stainless steel tubes, the initial surface roughnesses were not consistent. Therefore, both the magnetic particle size and finishing time were adjusted to obtain the roughnesses similar to the Ni-P-plated surfaces by using the largest magnetic particle and gradually reducing the magnetic particle size. After completing the surface finishing, the tubes were sectioned and the surface geometries were further analyzed using an AFM.

4.1.2. Results

Figs. 12 and 13 show the AFM images and the peak-to-valley R_z of the Ni-P surface after finishing in each condition, respectively. Figs. 14 and 15 show the AFM images and the peak-to-valley R_z of 304 stainless steel surfaces after finishing in each condition, respectively. The peak-to-valley R_z was obtained from the sectional profile of the AFM image.

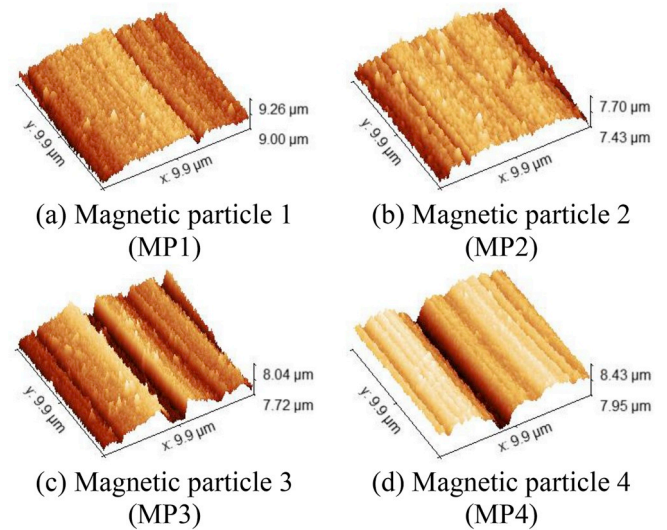


Fig. 12. AFM images of the Ni-P surfaces finished by MAF.

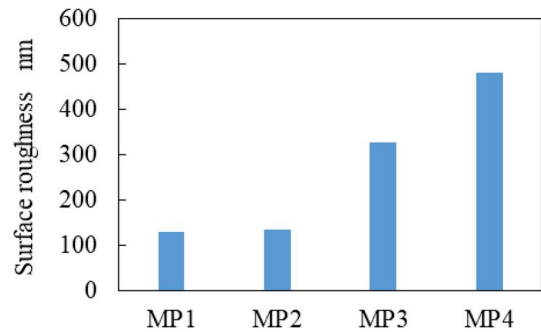


Fig. 13. Relationship between Ni-P surface roughness and finishing conditions.

In both cases, the finished surfaces had roughnesses between 0.1 and 1.0 μ m R_z . It was observed that the larger the iron particle, the stronger the magnetic force acting on the iron particle. The G50 steel grit is harder than the iron particle and has a sharp edge, which occasionally caused deep scratches on the surface. This resulted in the roughest surface among the four conditions in both cases.

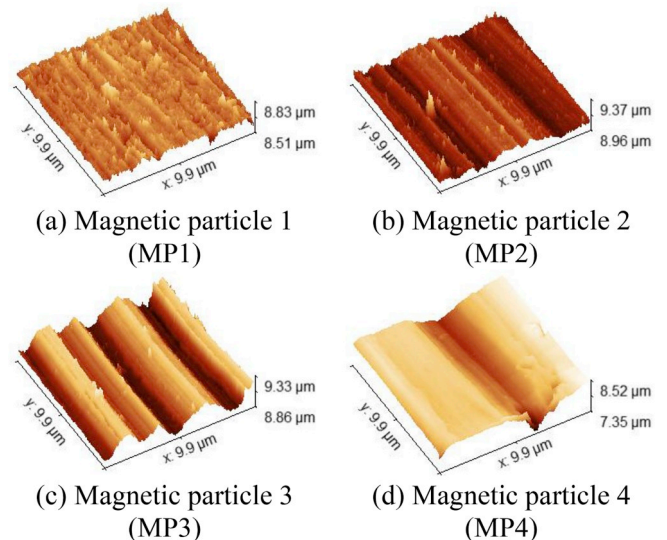


Fig. 14. AFM images of the 304 stainless steel surface finished by MAF.

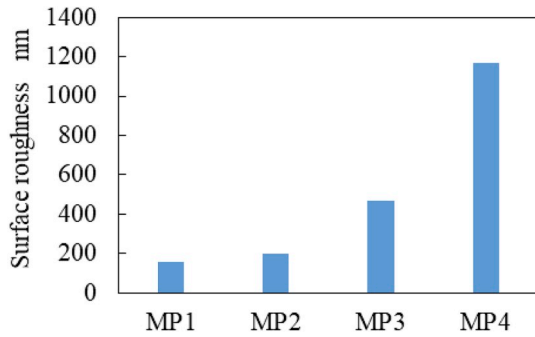


Fig. 15. Relationship between 304 stainless steel surface roughness and finishing conditions.

4.2. Fabrication of LIPSS using short-pulsed laser irradiation

4.2.1. Experimental setup and conditions

Short-pulsed laser irradiation experiments on the MAF-finished surfaces were conducted with a picosecond-pulse laser oscillator (EKXPLA, PL 2250–50P20) with 20 ps pulse duration due to lower cost and more stable laser irradiation with longer pulse duration and because the maximum of the collisional relaxation time of metals is about 20 ps. Fig. 16 shows the experimental setup including a polarizer to isolate the specific polarization of a light, a beam splitter to separate a laser beam into a necessary beam and a redundant beam, and a collecting lens with a focusing range of 150 mm.

The laser irradiation conditions are provided in Table 4. The laser was a Gaussian beam and was irradiated on the fixed point of a workpiece surface without scanning, inducing ablation at the central part of an irradiated area where was analyzed with an AFM. The energy density E_d was set to relatively small values, 0.14 and 0.10 J/cm², in the case of Ni–P-plated tubes and 304 stainless steel tubes, respectively, since the laser with low E_d is favorable to fabricate LIPSS. Additionally, compared the thermal conductivity, 5 W/m/K of Ni–P is less than 16 W/m/K of 304 stainless steel, causing ablation of the whole irradiated surface with an increase of the number of shots n , thus n was set to 10 and 150 shots in the case of Ni–P-plated tubes and 304 stainless steel tubes, respectively.

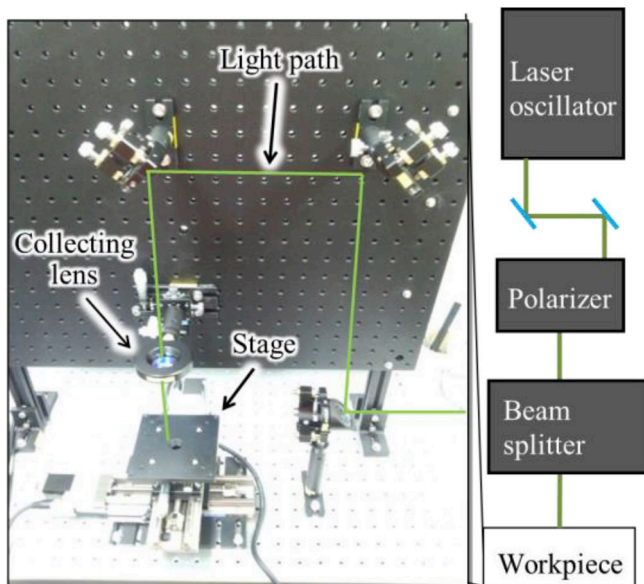


Fig. 16. Setup of short-pulsed laser processing.

Table 4
Laser irradiation conditions.

Workpiece	Ni–P plated 304 stainless steel	304 stainless steel
Wavelength	1064 nm	
Pulse duration	20 ps	
Frequency	50 Hz	
Beam diameter (Gaussian profile)	≥2500 μm	
Irradiation number n	10 shots	150 shots
Entire laser power	6.70 mW	4.69 mW
Energy density E_d (1 pulse)	0.14 J/cm ²	0.10 J/cm ²

4.2.2. Results

Fig. 17 shows AFM images of short-pulsed-laser-irradiated zones of Ni–P surfaces. This demonstrates that straight LIPSS were fabricated on all surfaces superimposed on the surfaces finished using MAF. The direction of the straight LIPSS was perpendicular to the laser polarization. Fig. 18 shows the changes in groove depth in the Ni–P surfaces for each surface condition. The average LIPSS height on the MAF-polished surfaces was about 200 nm which was higher than the LIPSS height of about 100 nm on the mirror surface [17]. The average LIPSS height increased slightly with increasing surface roughness of the MAF-finished surface. The average height of LIPSS was similar to the MAF-finished surface roughness R_z of MP1 and MP2 but less than the roughness of MP3 and MP4. This can be attributed to the multiple scattering of the electromagnetic waves at the surface, increasing the energy absorptivity at both peaks and valleys [33–35].

AFM images of LIPSS on the surface of processed 304 stainless steel are shown in Fig. 19. Although the condition MP4 had a surface roughness similar to the laser wavelength, straight LIPSS were produced. While the straight LIPSS were fabricated on the central part of the laser-irradiated spot, the LIPSS at the edge of irradiated spots were distorted as shown in Fig. 20. The reason is because the laser had a Gaussian beam profile, and the laser fluence at the edge of irradiated surface was smaller than that at the central part, decreasing surface plasma waves and ablation. Fig. 21 shows the heights of LIPSS on each 304 stainless steel surface. Like the Ni–P case, the rougher the MAF-finished surface, the higher the fabricated LIPSS since the electric field reached deeper into the workpiece and the maximum electric field intensity on the surface increased with the increase of the groove depth as shown in the analytical results. The LIPSS fabricated on the 304 stainless steel surfaces were taller than the ones fabricated on the Ni–P surfaces. This was because the extinction coefficient and the maximum electric

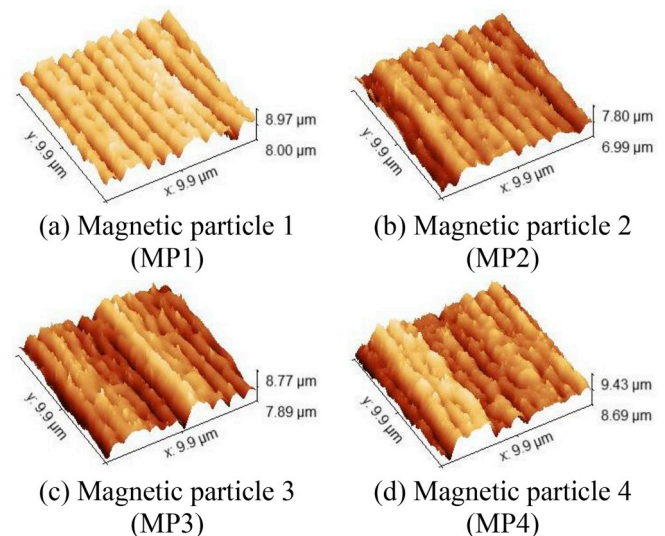


Fig. 17. AFM images of LIPSS on Ni–P surfaces.

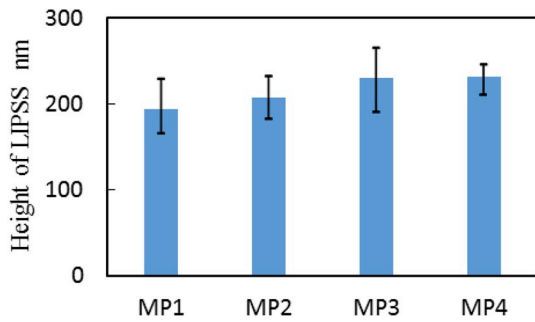


Fig. 18. Relationship between height of LIPSS on Ni-P surface and surface conditions.

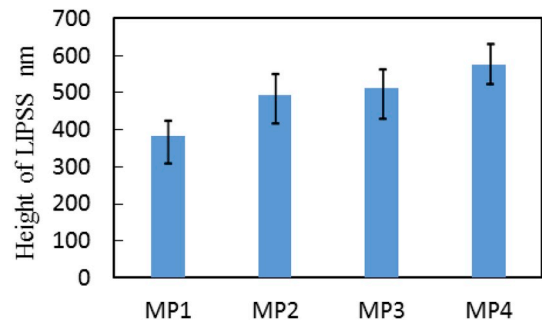


Fig. 21. Relationship between height of LIPSS on 304 stainless steel surface and laser irradiation conditions.

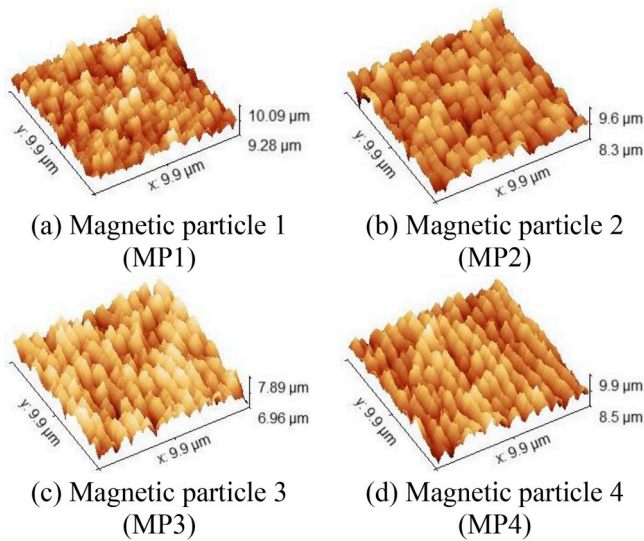


Fig. 19. AFM images of LIPSS on the 304 stainless steel surface.

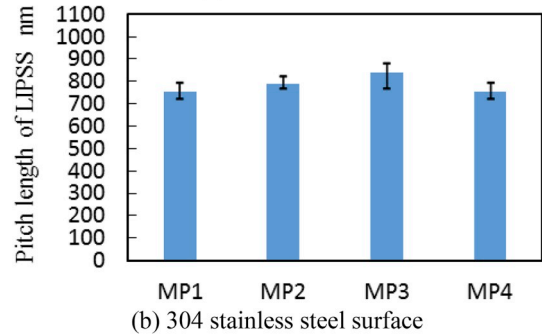
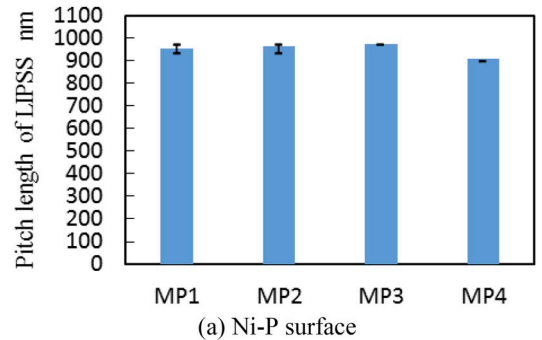


Fig. 22. Relationship between pitch length of LIPSS and laser irradiation conditions.

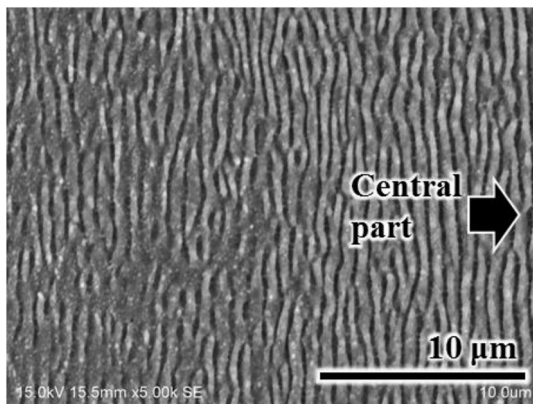


Fig. 20. An SEM image of LIPSS at the edge of the irradiated spots (304 stainless steel, MP1, $E_d = 0.09 \text{ J/cm}^2$, $n = 50$).

field intensity on the surface of 304 stainless steel are higher than those of Ni-P as shown in the analytical results, resulting in large ablation.

Fig. 22 shows changes in the pitch length of LIPSS fabricated on (a) Ni-P and (b) 304 stainless steel surfaces for each irradiation condition. The pitch length was independent of the surface roughness conditions after MAF in both cases. The pitch lengths of LIPSS on the Ni-P and 304 stainless steel surfaces were about 900 nm and 780 nm, respectively. While the pitch length in the case of Ni-P was calculated to be about 0.85 times the irradiation laser wavelength of 1064 nm, the pitch length

in the case of 304 stainless steel was about 0.74 times the laser wavelength. These phenomena were attributed to the surface plasmons whose wavelength is extended with the decrease of the refractive index of the irradiated material [36], which corresponded with the analytical results that the pitch length of grooves with the largest gap of EFI between the bottom and the top of grooves was longer on the Ni-P surface with the low refractive index than that on the 304 stainless steel surface with the high refractive index. In both cases, the pitch increased slightly as the roughness of MAF-finished surface increased since the EFI increased with the increase of the groove depth, increasing the electron density and extending the pitch length of surface plasma waves explained by the parametric decay [13], but slightly decreased in condition MP4. To determine the cause, this trend needs further study.

Overall, these results demonstrated the efficacy of groove-assisted short-pulsed laser irradiation to fabricate straight LIPSS on Ni-P and 304 stainless steel surfaces and the efficacy of an FDTD simulation to investigate the effects of original surface roughness on fabrication of LIPSS and to predict the LIPSS geometry. The aspect ratio (depth divided by pitch length) of the structures fabricated on the Ni-P and 304 stainless steel are approximately 0.21–0.25 and 0.42–0.71, respectively.

5. Conclusions

This paper studied the effects of surface roughness before the short-pulsed laser irradiation on the resultant LIPSS. The results of experiments are summarized as follows:

1. MAF enables the fabrication of straight, sub-micrometer-deep grooves, which facilitate the induction and propagation of surface plasma waves periodically and linearly on Ni-P and 304 stainless steel surfaces.
2. As long as the groove depths are shorter than the wavelength of laser irradiation, the short-pulsed laser irradiation enables the fabrication of LIPSS superimposed on the grooved substrate structures.
3. The structures guided by grooves were higher than the structures made on mirror surfaces. The height of the structure increased with increasing surface roughness (generated using MAF). FDTD simulation also showed that deeper grooves facilitate the creation of electric fields at the bottoms of grooves.
4. The pitch lengths of LIPSS on the Ni-P and 304 stainless steel surfaces were about 0.85 and 0.74, respectively, times the laser wavelength due to the parametric decay of the laser light to the plasma waves.

Acknowledgement

The authors would like to express their gratitude to the Nontraditional Manufacturing Laboratory at the University of Florida for supporting this research with an internship for one of the Japanese researchers. The authors also would like to express their appreciation to the Interdepartmental Doctoral Degree Program for Multi-dimensional Materials Science Leaders for their support of this research. This work was supported by JSPS KAKENHI Grant Numbers JP17K06074 and JP17KK0126.

References

- [1] Sawada H, Kawahara K, Ninomiya T, Mori A, Kurosawa K. Effect of precise periodic structures with femtosecond-laser on tribological characteristics under sliding tests. *J Jpn Soc Precis Eng* 2004;70(1):133–7.
- [2] Mizuno A, Honda T, Kiuchi J, Iwai Y, Yasumaru N, Miyazaki K. Friction properties of the DLC film with periodic structures in nano-scale. *Tribol Online* 2006;1(2):44–8.
- [3] Yasumaru N, Miyazaki K, Kiuchi J. Control of tribological properties of diamond-like carbon films with femtosecond-laser-induced nanostructuring. *Appl Surf Sci* 2008;254:2364–8.
- [4] Groenendijk M. Fabrication of super hydrophobic surfaces by fs laser pulses. *Laser Technik J* 2008;5(3):44–7.
- [5] Orazi L, Gnillitskiy I, Serro AP. Laser nanopatterning for wettability applications. *J Micro Nano-Manuf* 2017;5(2):1–8. 021008.
- [6] Lu J, Rao MP, MacDonald NC, Khang D, Webster T. Improved endothelial cell adhesion and proliferation on patterned titanium surfaces with rationally designed, micrometer to nanometer features. *Acta Biomater* 2008;4:192–201.
- [7] Shinanaga T, Tsukamoto M, Kawa T, Chen P, Nagai A, Hanawa T. Formation of periodic nanostructures using a femtosecond laser to control cell spreading on titanium. *Appl Phys B* 2015;119:493–6.
- [8] Sawada S, Kawahara K, Ninomiya T, Kurosawa K, Yokotani A. Precise periodic structuring with femtosecond-laser. *J Jpn Soc Precis Eng* 2003;69(4):554–8.
- [9] Minami Y, Toyoda K. Incident-angle dependency of laser-induced surface ripples on metals and semiconductors. *Laser Original* 2000;28(12):824–8.
- [10] Miyazaki K, Miyaji G. Nanograting formation through surface plasmon fields induced by femtosecond laser pulses. *J Appl Phys* 2013;114:1–6. 153108.
- [11] Miyaji G, Miyazaki K, Zhang K, Yoshifuji T, Fujita J. Mechanism of femtosecond-laser-induced periodic nanostructure formation on crystalline silicon surface immersed in water. *Opt Express* 2012;20(14):14848–56.
- [12] Tomita T. Laser ablation: from the viewpoint of solid state physics. *J Plasma Fusion Res* 2013;89(7):493–9.
- [13] Hashida M, Gemini L, Nishi T, Miyasaka Y, Sakagami H, Shimizu M, Inoue S, Limpouch J, Mocek T, Sakabe S. Periodic grating structures on metal self-organized by double-pulse irradiation. *J Laser Micro/Nanoeng* 2014;9(3):234–7.
- [14] Hashida M, Nishi T, Miyasaka Y, Sakagami H, Shimizu M, Inoue S, Sakabe S. Orientation of periodic grating structures controlled by double pulse irradiation. *Appl Phys A* 2016;122:1–5. 484.
- [15] Kodama S, Suzuki S, Shibata A, Shimada K, Mizutani M, Kuriyagawa T. Effect of crystal structure on fabrication of fine periodic surface structures with short pulsed laser. *Int J Autom Technol* 2018;12(6):868–75.
- [16] Ninomiya T, Sawada H, Kawahara K, Kurosawa K. Formation of periodic surface structure by double-pulsed femtosecond laser irradiation. *J Jpn Soc Precis Eng* 2005;71(7):921–5.
- [17] Kodama S, Suzuki S, Hayashibe K, Shimada K, Mizutani M, Kuriyagawa T. Control of short-pulsed laser induced periodic surface structures with machining-Picosecond laser micro/nanotexturing with ultraprecision cutting-. *Precis Eng* 2019;55:433–8.
- [18] Yamaguchi H, Shinmura T. Study of an internal magnetic abrasive finishing using a pole rotation system Discussion of the characteristic abrasive behavior. *Precis Eng* 2000;24(3):237–44.
- [19] Sato T, Yamaguchi H, Shinmura T, Okazaki T. Study of mirror finishing process using magneto-rheological fluid. *J Jpn Soc Abras Technol* 2007;51(4):238–43.
- [20] Yamaguchi H, Shinmura T, Ikeda R. Study of internal finishing of austenitic stainless steel capillary tubes by magnetic abrasive finishing. *J Manuf Sci Eng* 2006;129(5):885–92.
- [21] Yamaguchi H, Shinmura T. Study of the surface modification resulting from an internal magnetic abrasive finishing process. *Wear* 1999;225–229:246–55.
- [22] Sakabe S, Hashida M, Tokita S, Namba S, Okamoto K. Mechanism for self-formation of periodic grating structures on a metal surface by a femtosecond laser pulse. *Phys Rev B* 2009;79:1–4. 033409.
- [23] Okamoto K, Hashida M, Miyasaka Y, Ikuta Y, Tokita S, Sakabe S. Laser fluence dependence of periodic grating structures formed on metal surfaces under femtosecond laser pulse irradiation. *Phys Rev B* 2010;82:1–5. 165417.
- [24] Hashida M. Basic research about improvement of processing rate of femto second laser process. *Amada Found res brief rep* 2013;26:160–4.
- [25] Costache F, Henyk M, Reif J. Surface patterning on insulators upon femtosecond laser ablation. *Appl Surf Sci* 2003;208–209:486–91.
- [26] Fujita M, Hashida M. Femtosecond-laser processing. *J Plasma Fusion Res* 2005;81 (Suppl):195–201.
- [27] Hashida M, Shimizu M, Sakabe S. Nano-abrasion with short pulse laser. *Rev Laser Eng* 2005;33:514–8.
- [28] Yee KS. Numerical solution of initial boundary value problems involving maxwell's equations in isotropic media. *IEEE Trans Antennas Propag* 1966;(3):302–7. AP-14.
- [29] Hashimoto O. Practice FDTD (finite difference time domain) method. *Morikita Publishing*.
- [30] Skolski JZP, Romer GRBE, Obona JV, Ocelik V, Huis in't Veld AJ, JThMDe Hosson. Inhomogeneous absorption of laser radiation Trigger of LIPSS formation. In: Proceedings of LPM2012 – the 13th international symposium on laser precision microfabrication, Washington, USA. 2012. Japan-Laser-Processing-Society; 2012. p. 1–5.
- [31] Skolski JZP, Romer GRBE, Obona JV, Ocelik V, Huis in't Veld AJ, JThMDe Hosson. Laser-induced periodic surface structures Fingerprints of light localization. *Phys Rev B* 2012;85:1–9. 075320.
- [32] Skolski JZP, Romer GRBE, Obona JV, Huis in't Veld AJ. Modeling laser-induced periodic surface structures Finite-difference time-domain feedback simulations. *J Appl Phys* 2014;115:1–12. 103102.
- [33] Peters M, Forberich K, Battaglia C, Aberle AG, Bläsi B. Comparison of periodic and random structures for scattering in thin film microcrystalline silicon solar cells. *Proc SPIE* 2012;8438:1–9. 84380F.
- [34] King WE, Anderson AT, Ferencz RM, Hodge NE, Kamath C, Khairallah SA, Rubenchik AM. Laser powder bed fusion additive manufacturing of metals; physics, computational, and materials challenges. *Appl Phys Rev* 2015;2:1–26. 041304.
- [35] Liu MQ, Zhao CY, Wang BX, Fang X. Role of short-range order in manipulating light absorption in disordered media. *J Opt Soc Am B* 2018;1–10.
- [36] Nagashima K. Basics and applications of surface plasmon. *J Plasma Fusion Res* 2008;84(1):10–8.

単結晶窒化ガリウム(GaN)基板の高速高精度加工法の開発 —紫外線援用テープ研削法の提案—

鷹巣良史^{*1}, 嶋田慶太^{*2}, 水谷正義^{*2}, 厨川常元^{*3}

Development of high-speed and high-accurate manufacturing of gallium nitride
Suggestion of UV assist tape grinding method

Yoshifumi TAKASU, Keita SHIMADA, Masayoshi MIZUTANI and Tsunemoto KURIYAGAWA

ワイドギャップ半導体材料である単結晶窒化ガリウム(GaN)は電力損失の低いパワーデバイスへの活用が期待され、基板の高品質化や大口径化などの取り組みが進められている。しかし同材は、高硬度、高化学安定性、および脆性という特性を有するため、従来のシリコン基板に対する手法では加工が困難である。そこで本研究では、GaN(0001)基板 Ga 面において、過酸化水素水(HP)への紫外線(UV)照射によってヒドロキシル(OH)ラジカルを発生させて、GaN 材料表層を改質し、加工の高効率化を試みた。さらに改質と除去を連続的に行うことのできる UV 援用テープ研削加工法を考案した。その結果、同加工法を利用することにより、通常の加工法に比べて表面平坦化に及ぼす時間が 1/6 となり、6 倍以上の加工速度向上の可能性が見いだされた。

Key words: gallium nitride, grinding with abrasive tape, ultraviolet, hydroxyl radical

1. 緒言

現在世界の電力消費量は年間約3%ずつ拡大しており、電力制御で大きな省エネルギーを狙える次世代半導体デバイスのニーズが高まっている¹⁾。次世代半導体デバイスを構成する基板材料はバンドギャップが大きく、ワイドギャップ半導体とも呼ばれる。そのなかでも単結晶窒化ガリウム(以下、単に GaN と称す)は、バンドギャップが 3.4eV と現行材料のシリコン(Si)の 1.2eV と比して大きい²⁾。また材料特性として、(i)高温での動作が可能、(ii)電子の飽和速度が速い、さらには(iii)絶縁破壊電圧が高いといった特長を有している³⁾。そのため、電力損失の低いパワーデバイスへの活用が期待されており、基板の高品質化や大口径化などの取り組みが進められている。

一方加工の観点からは、ピッカース硬度が 1800Hv~2000Hv と Si の 1050Hv と比較して硬く、かつ脆い難加工材として知られている。また、気相成長面として活用される Ga 面は化学的に安定なため、酸やアルカリとの反応がほと

んど起こらないことも加工を難しくする一因となっている⁴⁾。

同材を基板形状に加工するためには、素材を円柱状に加工する外形加工、また表面の凹凸を除去し平坦な面を加工する平面加工、そして最後に原子レベルでの平坦面を加工する CMP 加工の工程が必要である。これらの加工工程のなかで、外形加工、平面加工ではダイヤモンド砥粒研削加工が用いられるが、GaN 材料は硬脆材料であるため、条件によっては、加工面あるいはその内部に脆性破壊を起因とするクラック層(加工変質層)が生じる。CMP 工程では加工変質層を完全に除去する必要があるため、最大加工変質層厚み $\delta_{SSD,max}$ が CMP 工程の律速条件となる。このため、研削加工において、加工変質層の発生を抑制し、かつ高速に加工することが重要となる。この課題に対して前報⁵⁾では砥粒の切込み量、すなわち切り取り厚みを小さく制御することで GaN(0001) 基板 Ga 面においても延性領域での加工が可能であることを明らかにした。一方、切り取り厚みを小さくすると除去量が小さくなることから、加工能率の維持・向上のためには工具・工作物の相対運動を高速化し、切削作用の回数を増加させることが必要である。

硬脆材料への加工能率向上の取組として、バンドギャップから求められる分子の結合エネルギーよりも短い波長である紫外線(Ultraviolet, 以下 UV)を照射し、大気中の水分子と反応させラジカルを生成し GaN や SiC 表面に酸化膜を形成する方法⁶⁾や、鉄触媒と過酸化水素水(Hydrogen peroxide, 以下 HP)の反応によるヒドロキシル(OH)ラジカルを用いた平滑化の取組⁷⁾、またプラズマによる表面改質層の高速除去⁸⁾

*1 パナソニック(株)(東北大・学): 〒571-8502 大阪府門真市松葉町2番7号
Panasonic Corporation
*2 東北大学 大学院工学研究科: 〒980-8579 宮城県仙台市青葉区荒巻字6-6-01
Tohoku University
*3 東北大学 大学院工学研究科: 〒980-8579 宮城県仙台市青葉区荒巻字6-6-01
Tohoku University

(学会受付日:2019年 5月22日)
(採録決定日:2019年 6月24日)

等, ラジカルを用いた化学反応と表面酸化による高速化の可能性が提唱されている。

本稿では, 延性領域での加工状態を維持しながら, 更なる高速化を実現できる加工機構の提案を目的とし, 高速化の可能性として GaN (0001) 基板 Ga 面への OH ラジカル作用効果の検証と, 改質と除去を連続的に行うことのできる UV 援用テープ研削加工法を考案したので報告する。

2. GaN (0001) 基板 Ga 面表面の酸化検証

GaN (0001) 基板 Ga 面への化学反応として, 酸やアルカリでは反応がほとんど起こらないが, OH ラジカルを反応させることで, Ga 面において Ga-N 結合内に酸素が入り込み, 表面酸化を促進できる可能性があることが, 量子分子動力学によるシミュレーション結果⁹⁾にて報告されている。そこで本稿では, GaN (0001) 基板 Ga 面を試料として用い, 表面酸化を促進させる方法として, HP に対して UV を照射した際に生じる反応を利用した OH ラジカル発生機構に注目し利用した。HP に UV を照射した際の化学反応式は理論的には式(1)で示される。



OH ラジカルは活性化エネルギーが高く, 反応性も高いため, 生成されたラジカルの寿命は平均約 75 μs と非常に短い¹⁰⁾。また HP への UV 照射では, 波長が短いほど OH ラジカルの発生量が多いことが知られている¹¹⁾。本稿では波長 300nm 以下の波長も有し, 400nm 以下の短波長領域に総出力エネルギーの半分以上のエネルギー領域を有する低圧水銀ランプを用いた。

2.1 実験方法

表面酸化検証実験の構成を図 1 に示す。試料表面が UV 光源側に向く状態で HP 中に浸し, UV 光を Ga 面に対して直接照射する。また温度の影響を検証するために, ヒータの上にビーカーを配置し加熱できる構成とした。この構成により試料表面との OH ラジカルの反応による表面酸化状態の有無と最表面からの酸化状態の深さ依存性を検証した。HP の水位は UV 照射によって試料表面から気泡が発生する位置を目安に, 表面から 3mm の位置とした。酸化状態の検証として, X 線光電子分光分析 (XPS) による元素分析を行った。具体的には, 最表面から Ar イオンによるイオンミリングにより微量加工 (加工レート: SiO_2 換算で約 5nm/min) し, その加工面に対して随時 XPS による評価を繰り返し実施することで深さ方向での酸化状態を評価した。なお酸素濃度への変換は分析装置内の相対感度係数を用いて算出した元素量を酸素濃度へ換算し実施した。実験条件を表 1 に示す。

2.2 実験結果

試料最表面での酸素割合の結果を図 2 に示す。なお酸素割合は各試料の 4 カ所を測定した平均値であり, 分析対象元

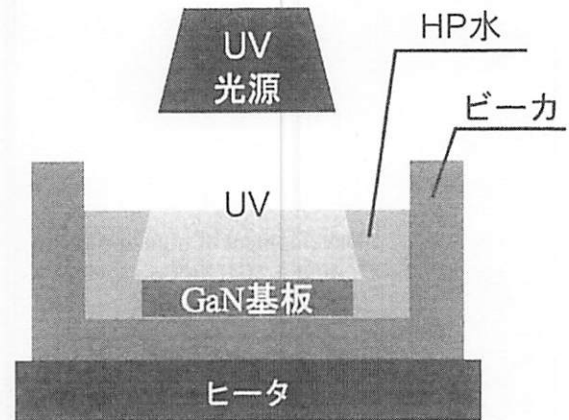


図 1 表面酸化検証実験構成

表 1 表面酸化検証実験条件

試料	GaN (0001) 基板 Ga 面
試料サイズ	□10 mm
紫外線光源	低圧水銀ランプ
UV 照射強度	100 W
HP 濃度	30 w%
照射時間	10 min
試験条件	(1) CMP 後 (UV 照射無) (2) HP 含侵のみ, 室温 (22°C) (3) UV+HP, 室温 (22°C) (4) UV+HP, ヒータ加熱 50°C (5) UV+HP, ヒータ加熱 100°C
X 線光電子分光分析	
装置	PHI ESCA-5600 (アルバック・ファイ社製)
使用 X 線	Mg-K α 線
分析領域	400 μm ϕ

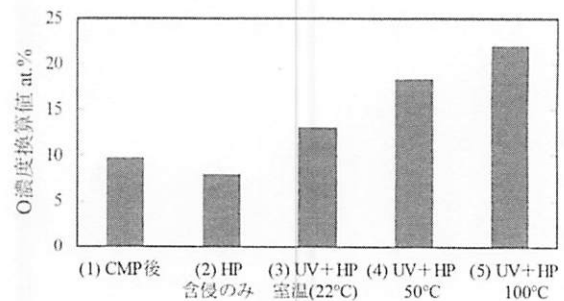


図 2 試料最表層での酸素割合

素として炭素, 窒素, 酸素, カリウムの 4 元素として, それらの中の酸素量を割合として算出した。図 2 より UV 照射により酸素元素の割合が増加しており, さらに加熱により割合が上昇したことが確認できる。本結果より試料表面に対して HP+UV という構成によって表面の酸素割合が増加することが判明した。また CMP 後よりも HP 含侵のみで表面の酸素濃度が

低くなっている。CMP 後の XPS 分析では C 濃度換算値が 34.2at%であり、HP 含侵の他の条件は 10~20at%であったことより、CMP 後の洗浄工程において有機系酸化物の薄膜が生成され、過酸化水素水に含侵することで除去されたと推測される。

次に、温度 50°C、100°C の環境下でそれぞれ UV 照射を行った試料の照射面から内部方向への酸素濃度測定結果を図 3 に示す。同図より CMP 後の試料を基準として、CMP 後の酸素濃度と同じ濃度になる深さは、50°C 条件の試料で、0.3nm、100°C 条件の試料でも 0.45nm となった。XPS では X 線照射による光電子の平均自由行程距離の情報しか取得できず、最大 2~3nm の厚み情報の平均値となるが、イオンミリングでの除去により表層除去で酸素濃度が大きく低減していることから、酸化反応は 0~0.45nm 程度の極表面でのみ起きていると推測される。このことより、HP+UV 照射で生成される酸化膜厚みは非常に薄く、またラジカルの寿命が約 75μs ということを考えて、短時間で反応が終了し、その後反応が深さ方向に進展しないと予測される。本結果より OH ラジカル活性種の反応を利用した加工速度向上を実施するためには、表面を酸化させる工程と、酸化した GaN 材料を除去する工程を高速に繰り返す機構が効果的と推測される。

3. テープ研削機構の特徴と基本実験

基板加工の重要な要素として基板全面での平面度を維持させる必要があり、本機構では、前加工において平面加工を実施した状態を想定して機構を検討した。加工点近傍にて OH ラジカルを発生させるため、加工点近傍に UV が届き、かつ繰り返し被加工面との相対運動が可能な円柱形状を採用した。また基板全面への加工性を担保させかつ延性加工状態での加工できる機構として弾性体を用いたテープ研削機構を考案した。

3.1 弾性体を用いたテープ研削機構

テープ研削機構の構成要素を図 4 に示す。樹脂素材上に砥粒を分散させたテープ(研削テープ)を弾性ホイールに巻きつけ、基板に押し付けた状態で回転および摺動の相対運動により加工を行う。同図に示すように弾性ホイールは接触点で大きく変形することにより、加工域での有効砥粒数を増加させる。また有効切れ刃数の増加は砥粒 1 個当たりの切込み深さを減少させ、均一な加工が可能となることから低ダメージで平滑な仕上げが期待される。さらに加工域は線接触であることから面接触となる一般的な研磨加工と比較して UV や HP の援用が容易である。

3.2 切込み量に関する理論的検証

続いて、テープ研削における砥粒の最大切込み深さについて検証する。弾性ホイールと基板の接触を円筒体対平面のヘルツ接触と仮定すると、 x の位置における接触圧 $p(x)$ 、接触幅 b は弾性ホイールのヤング率 E 、接触長さ L 、ホイール直径 D および負荷荷重 W より次式で表される¹²⁾。

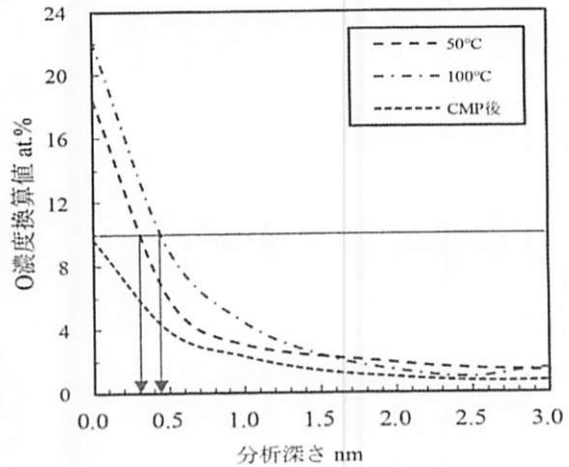


図 3 試料照射面から内部方向への酸素濃度測定結果

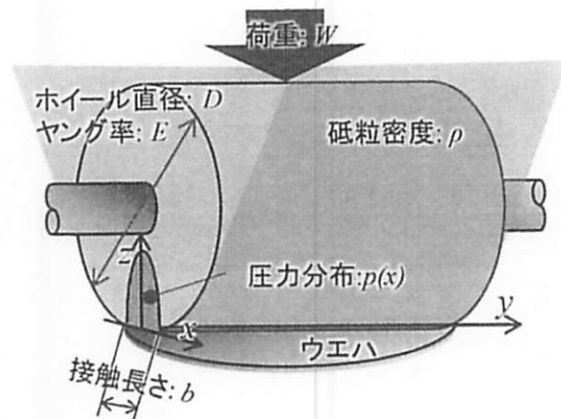


図 4 テープ研削機構モデル

表 2 計算条件

臨界切削力 f_c (N)	0.5
ホイール直径 D	25 mm
接触長さ L	100 mm
ヤング率 E	45 MPa
負荷荷重 W	250 N
砥粒径 d_g	0.001 mm

$$p(x) = \frac{2W}{\pi b L} \sqrt{1 - \left(\frac{x}{b}\right)^2} \tag{2}$$

$$b = 2 \sqrt{\frac{DW}{\pi E L}} \tag{3}$$

砥粒が受ける力が砥粒の投影断面積に比例すると仮定すると、基板に作用する最大切削力 f_{max} は使用する砥粒の最大粒径 d_{max} と最大接触圧 $p_{max} (=p(0))$ を用いて次式のように表せる。

$$f_{\max} = \frac{\pi c_{\max}^2}{4} P_{\max} \quad (4)$$

前報⁵⁾で求めた延性-脆性加工の臨界切込み深さ $\delta_c = 180$ nmであったことから砥粒サイズは小さい方が延性加工状態を再現できると仮定し、#10000での砥粒サイズを想定し切込み深さを考察した。なお、UV+HPでの表面改質は0.5nm以下と極表面で行われるため、臨界切込み深さの2.7%であるため、表面改質の影響は除いて計算を実施した。表2の条件と式(4)よりこの弾性体の接触状態で考えられる最大切削力 f_{\max} を計算すると、

$$f_{\max} = 1.03 \mu\text{N} \quad (5)$$

となる。次に切削深さ δ と加工力 f の関係について、切削断面積に比例する、すなわち係数 k を用いて

$$f = k\delta^2 \quad (6)$$

と表せることを仮定する。前報の臨界切込み深さ $\delta_c = 180$ nm および臨界切削力 $f_c = 0.5$ N を用いて式(6)の k を求め、 f_{\max} の際の切込み深さを計算すると、

$$\delta = 0.26 \text{ nm} \quad (7)$$

となる。この深さは改質層の深さ 0.45nm よりも小さいため、#10000での砥粒を用いた加工での除去量にて問題無いと判断し、最大砥粒径が 0.001mm サイズであるダイヤモンド#10000を用いた。

3.3 テープ研削試験

テープ研削機構の実験装置を図5に示す。平面研削盤(ナガセインテグレックス製 SHSD80 α)に弾性体(ウレタンゴム材)と研削テープを治具にて固定している。また試料として GaN(0001) 基板 Ga 面が被加工面になるように熱溶融性ワックスにて、X軸方向に往復運動する揺動テーブル上に固定した。本機構による除去量と、加工変質層の発生について検証するため表面仕上げの異なる2種の試料を準備した。材料除去量の検証用には平面研削盤にて粗加工した試料(表面粗さ Ra 10.3nm)を用いた。また、加工による加工変質層評価には Ga 面をコロイダルシリカ砥粒での CMP 加工にて加工変質層を完全に除去し、表面粗さを Ra 0.3nm の面粗さに仕上げた試料を用いた。加工時にはテープ研削加工条件を表3にまとめる。

3.4 テープ研削試験結果

粗加工を実施した試料への加工前、加工後の表面粗さを白色干渉型表面測定器(ZYGO社 NewView)により測定した結果を図6に示す。加工前後で表面粗さは Ra 10.3nm から Ra 4.2nm へと表面粗さが低減しており、本機構にて試料の除去加工ができていないことが判明した。次に表面粗さが Ra 0.3nm の光学鏡面を持つ試料に対しての加工性評価を実施した。加工結果を図7に示す。加工前表面粗さ Ra 0.3nm に対して加工後の表面粗さは Ra 0.314nm とほぼ変化はないが、

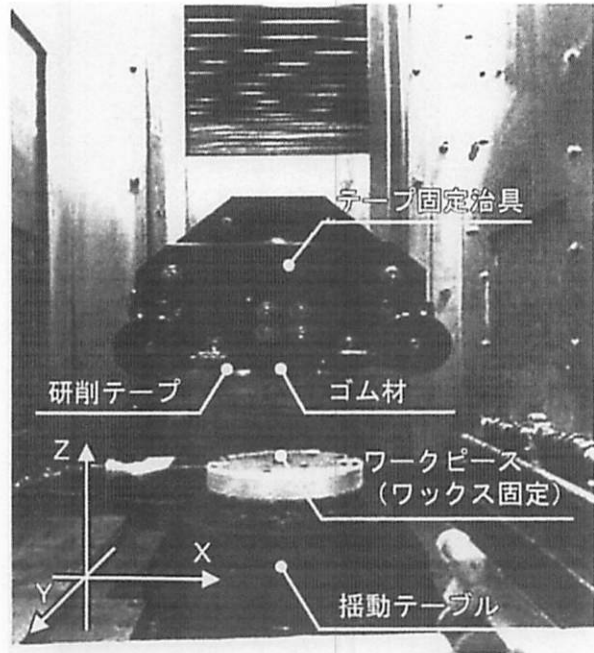
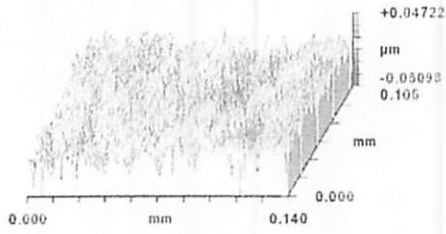


図5 テープ研削機構実験装置

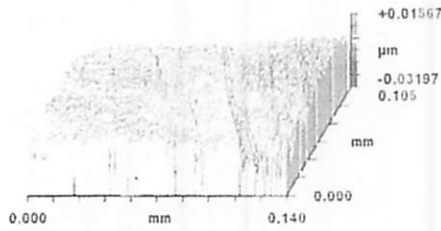
表3 テープ研削条件

試料	GaN (0001) 基板 Ga 面
加工前の表面	平面研削(除去量検証用) Ra 10.3nm, CMP 仕上げ(加工変質層評価用) Ra 0.3nm
試料サイズ	□10 mm
加工装置	ナガセインテグレックス製 SHSD80 α
弾性体	ウレタンゴム ショア硬さ 95
砥粒サイズ	ダイヤモンド#10000
加工条件	
揺動幅	± 2.5 mm
揺動回数	1000 回/min
加工時間	5 min
切込み量	5 μm

研削による加工痕が確認でき、研削による除去加工ができていると考えられる。この加工面についてより詳細な分析を行うため、加工変質層の観察を行った。具体的には、集束イオンビーム(FIB)による断面加工を実施し、透過電子顕微鏡(TEM)により断面の原子配列の観察を実施した。図8に示す結果より、加工面極表面において原子配列の乱れが原因の加工変質層が存在することがわかる。これはテープ研削を施したことによるダメージに起因するものであると考えられるが、同変質層にはクラックのような脆性破壊状態は観察されないことから、当初の狙いであった延性状態における除去加工が実施できたといえる。また最大加工変質層厚み $\delta_{SSD,max}$ も 146 nm と非常に小さく、加工での原子配列の乱れが少ない低ダメ



(a)テープ研削前(粗仕上げ後) Ra 10.3nm



(b)テープ研削後 Ra 4.2nm

図6 粗仕上げ面に対するテープ研削前後の表面性状

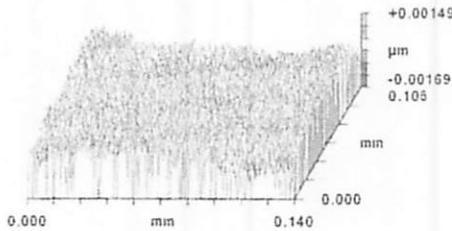


図7 鏡面に対するテープ研削後の表面

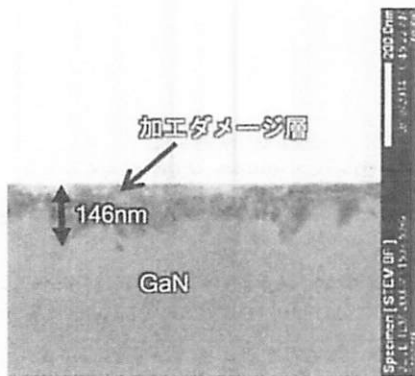


図8 テープ研削後の断面 TEM 画像

加工が実現されている。本実験により弾性体を用いたテープ研削機構によって、延性状態にて試料を加工できることが判明した。

4. 複合機構での検証

HP での装置汚染を防ぐために、ステンレス製の廃液トレイを設け、長時間の加工検証を実施できる検証モデル機を構

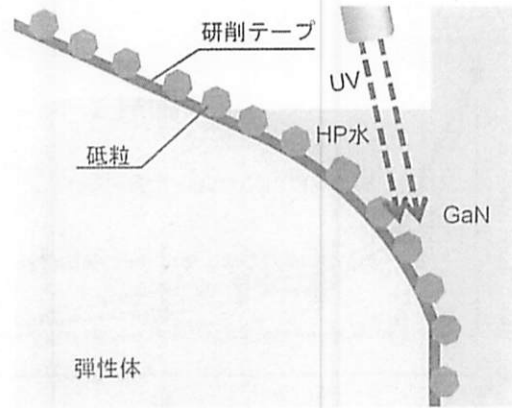


図9 UV 援用テープ研削モデル

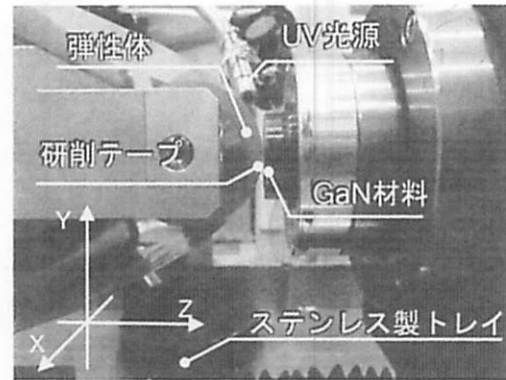


図10 UV 援用テープ研削実験装置

表4 複合機構条件

試料	GaN (0001) 基板 Ga 面
試料サイズ	□10 mm
弾性体	ウレタンゴム ショア硬さ 95
砥粒サイズ	ダイヤモンド#10000
加工条件	
揺動幅	±1.5 mm
揺動回数	500 回/min
切込み量	5 μm
UV 照射強度	1.0 W
UV 波長	365 nm
HP 濃度	30 w%

築した。本機構での加工点近傍での加工モデルを図9に、検証装置概観を図10に示す。円柱状の弾性体に砥粒を保持した研削テープを巻き付け、試料と研削テープが接触部に HP が滞留するように、スポイトにて HP の滴下と、スポット型 UV 装置により研削テープと試料の接触点への照射を実施する。駆動軸として研削テープを X 方向に揺動する揺動機構と、Z 軸方向の移動を行うためのスライドレールを有し、試料は熱溶解性ワックスにて固定した。また弾性体、テープ材、砥粒サイズはテープ研削機構で検証した条件を採用した。

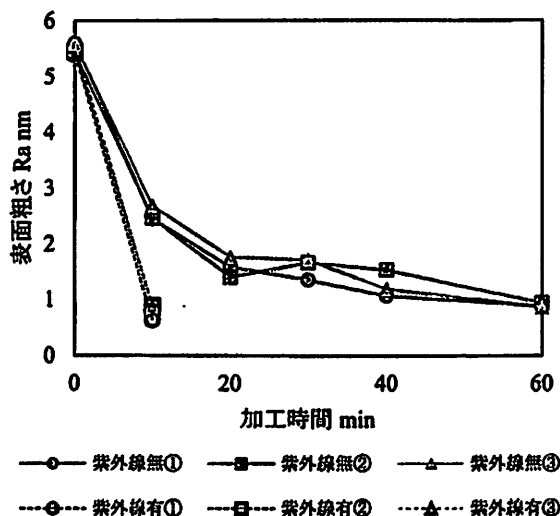


図 11 検証機構での加工結果

本実験ではテープ研削による前加工での面粗さ除去速度を検証目的として、試料表面を平面研削加工し、Ra 5.3nm の表面粗さとした。また加工時間 10min 毎に表面粗さを先述の白色光干渉計にて測定し、Ra が 1nm 以下となるまで加工を実施した。また加工バラツキの影響を鑑み、UV+HP 有、無でそれぞれ 3 サンプルを準備し、計 6 サンプルにて加工を実施した。実験条件を表 4 に示す。また、本検証機構での加工結果を図 11 に示す。

測定結果より、UV+HP 援用が無い場合において、表面粗さの低減は初期の 10min までが最も大きく、最初の 10min 間で約半分の Ra 値になっていることがわかった。10min 以降は Ra 値の低減率は下がるものの徐々に低減し、目標である Ra 1nm 以下には 60min 後の測定時に到達した。本挙動は表面粗さが粗い状態では、凹凸の高い部分を優先的に除去するため、初期が表面粗さの低減率が最も高く、凹凸の差が少なくなると平面部の面積が増加し、表面粗さの低減率が低下していると予測される。一方 UV+HP 援用での試料は最初の 10min 後の測定時にすでに表面粗さが 1nm 以下になっていた。本結果より、提案したテープ研削機構によって試料表面の平坦化が出来ることと、UV+HP 援用を用いることで、平坦化までの時間が低減することが判明した。UV+HP 援用による表面改質が極表面ということも鑑み、平坦化には加工による除去が支配的と考え、UV+HP 援用により援用がない場合と比較して 6 倍以上の除去速度向上の効果があると推測される。

5. 結言

HPへのUV照射におけるOHラジカルのGaN (0001) 基板Ga面表面改質状態評価と、改質と除去を連続的に行うことのできるUV援用テープ研削加工法での検証により、下記の結果を得た。

- (1) GaN (0001) 基板 Ga 面に対して UV+HP の構成により表面の酸素割合が増加し、酸化反応は 0~0.45nm 程度の極表面で起きていることがわかった。本結果より OH ラジカルの反応を利用した加工速度向上を実施するためには、表面を酸化させる工程と酸化した Ga 材料を除去する工程を高速に繰り返す機構が効果的と推測される。
- (2) 弾性ホイールに樹脂素材上に砥粒を分散させたテープ (研削テープ) を巻きつけ、基板に押し付けた状態で回転および摺動の相対運動により加工を行うテープ研削機構を提案した。テープ研削機構での加工検証の結果、クラックのような脆性破壊状態は観察されず、また最大加工変質層厚み $\delta_{SSD,max}$ も 146nm と非常に小さいことが判明した。
- (3) UV+HP の援用効果とテープ研削機構を複合することにより、初期表面の Ra 5.3nm が 10min 加工後の測定時に表面粗さが 1nm 以下になった。UV と HP を用いない場合では表面粗さが 1nm 以下になるまで平均 60min の時間を要したことから、UV+HP 援用により、援用効果を使用しない場合と比較して 6 倍以上の加工速度向上の効果の可能性があると判明した。

謝辞

本研究は JSPS 科研費 16H02305, 19H00734 の助成を受けたものである。

6. 参考文献

- 1) T. Ueda, S. Takahashi and H. Hiroyuki: Next-generation Power Switching Devices for Automotive Applications: GaN and SiC, Panasonic Technical Journal 61, 1 (2015) 67 (in Japanese).
- 2) A. A. Burk Jr. et al.: SiC and GaN wide bandgap semiconductor materials and devices, Solid-State Electron. 43, 8 (1999) 1459.
- 3) M. Hikita, M. Yanagihara, Y. Uemoto, T. Ueda, T. Tanaka and D. Ueda: GaN-Based Power Devices, Panasonic Technical Journal 55, 2 (2009) 91 (in Japanese).
- 4) Zhuang, D. and J. H. Edgar: Wet etching of GaN, AlN, and SiC: a review, Materials Science and Engineering, R: Reports 48, 1 (2005) 1.
- 5) Y. Takasu, K. Shimada, M. Mizutani and T. Kuriyagawa: Study of crack generation process in scratching of gallium nitride, J. Jpn. Soc. Abras. Technol., 61, 7(2017) 392 (in Japanese).
- 6) T. Sakamoto, A. Kubota and M. Touge: Ultraviolet-assisted polishing of 2inch SiC substrate, J. Jpn. Soc. Avras. Technol., 57, 8 (2013) 524 (in Japanese)
- 7) J. Murita, A. Kubota, K. Yagi, Y. Sano, H. Hara, K. Arima, T. Okamoto and K. Yamauchi: Chemical planarization of GaN using hydroxyl radicals generated on a catalyst plate in H_2O_2 , Journal of Crystal Growth, 310, 7(2008)1637.
- 8) TK. Doi, Y. Sano, S. Kurokawa, H. Aida, O. Ohnishi, M. Uneda and K. Ohyama: Novel Chemical Mechanical Polishing / Plasma-Chemical Vaporization Machining (CMP/P-CVM) Combined Processing of Hard-to-Process Crystals Based on Innovative Concepts, Sensors and Materials., 26, 6,(2004)403.
- 9) K. Kawaguchi, T. Aizawa, Y. Higuchi, N. Ozawa and M. Kubo: Chemical mechanical polishing mechanisms for gallium nitride, Proc. Int. Conf. on Planarization/CMP Technol. (2014) 39.
- 10) 佐野 浩亮, 内海 英雄: 活性酸素・フリーラジカルの分析, 化学と生物, 37, 5 (1999) 328.
- 11) T. Toki et al: Synergistic interaction between wavelength of light and concentration of H_2O_2 in bactericidal activity of photolysis of H_2O_2 , J. BIOSCI. BIOENG., 119, 3 (2015) 358 (in Japanese).
- 12) 村木 正芳: 固解トライボロジー 摩滅の科学と潤滑技術, 日刊工業新聞 (2007).

微細ラティスコーティング技術の開発 —重力落下式粉末供給手法による壁構造の評価—

前花英一^{*1}, 白沢太一^{*1}, 石橋信治^{*2}, 嶋田慶太^{*2}, 水谷正義^{*2}, 厨川常元^{*3}

Development of a fine lattice coating system:
Evaluation of printed wall structures by powder supply method with gravity fall

Hidekazu MAEHANA, Taichi USUZAWA, Shinji ISHIBASHI, Keita SHIMADA,
Masayoshi MIZUTANI and Tsunemoto KURIYAGAWA

本研究は、レーザを用いた金属 3D プリント技術を基盤とした、機能を有する多孔質構造をバルク材表面に付与する、微細ラティスコーティング技術の開発を目的とする。本報では新たな粉末供給手法である重力落下式供給法を提案し、これを用いて微細ラティスコーティングの土台となる壁構造の造形を行うことで、その積層過程における最上層の表面プロファイルについて考察した。その結果、積層過程の堆積状態によって堆積層が一定値を超えるとレーザ走査による造形体表面が平滑となることを明らかにした。また本供給手法で造形した壁構造は、直立状態で 0.4 mm の高さまで造形することが可能となり、重力落下式供給手法を用いたレーザ走査による造形の有効性を示した。

Key words: powder gravity fall, fine lattice coating, pure titanium powder, pulse laser, high speed camera

1. 緒言

金属材料表面に微細なテクスチャを形成することによって、濡れ性や潤滑性、生体親和性などの機能が、その表面に発現することが知られている¹⁾²⁾。ただし、これまでの機能創生加工技術は、除去加工による平面的な表面テクスチャによるものがほとんどであったが、機能を生み出す構造を 3 次元構造に置き換えることができれば、より効果的な機能を発現できるのではないかと筆者らは考えている。機能をもつ 3 次元構造としては、多孔質(ポーラス)構造が有名であり、ポーラス金属は吸音性、熱交換機能、衝撃吸収性などの機能性材料³⁾として活用されている。このような金属多孔質構造の製造法には、発泡溶融法や粉末冶金法などがあるが、これらによって得られる多孔質構造の気孔や支柱の配列は不規則であり、それらの大きさの制御は困難である。

一方、近年注目されている金属 3D プリントであれば、その積層造形手法により、規則性のある多孔質構造を自由なデザインで作り出すことができる⁴⁾。その一例が図 1 に示すラティスコーティングであり、このような多孔質な部分と、緻密な部分の両方を併せもった部品を作り出すことも可能である。例えば、生体内に埋入される歯科インプラント、人工関節などは、多孔質内

部の骨成長による生物学的固定性が求められるため、このような金属 3D プリントによる製造に注目が集まっている⁶⁾⁷⁾。

ただし、金属 3D プリント技術で造形した製品内部には、意図しない気孔であるポロシティの残留といった大きな課題⁸⁾があり、厳密に言えば、緻密性が要求される部位がある製品を作り出すことはできない。この課題を解消するための手法は、いくつか提案されているが、大掛かりな後工程を用いずに、これを完全に無くすことは難しく、市販のバルク材ほどの緻密な金属組織を作り出すことができない。そのため、金属 3D プリントで製造された部品については、ポロシティを起因とする疲労破壊と、表面に現れる気孔について考慮しておく必要がある。

以上の課題をふまえ、筆者らは表面の高機能化と、製品としての強度の問題を同時に解決する手法として、緻密材料(バルク材)をベース材として用い、例えば歯科インプラントのねじ山高さ(約 0.5 mm)程度のごく薄い多孔質構造(機能を担う)を、その表面に積層造形するという革新的な手法を提案す

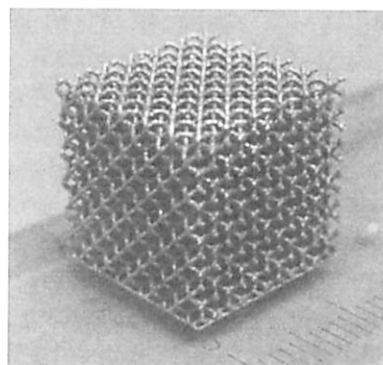


図 1 PBF 法で得られた 12 mm 角の立方ラティスコーティング⁵⁾

*1 コマツNTC株式会社: 〒939-1595 富山県南砺市野尻641
Komatsu NTC Ltd.

*2 東北大学大学院工学研究科: 〒980-8579 宮城県仙台市青葉区荒巻字青葉6-6-01
Graduate School of Engineering, Tohoku University

*3 東北大学大学院医工学研究科: 〒980-8579 宮城県仙台市青葉区荒巻字青葉6-6-01

Graduate School of Biomedical Engineering, Tohoku University
(学会受付日: 2019年 5月 22日)
(採録決定日: 2019年 8月 8日)

る。この概念の造形手法を筆者らは微細ラティスコーティングと呼称している。

本報では、既存の金属3Dプリンタ技術を参考にして、微細ラティスコーティング実現のための新たな粉末供給方法について説明し、これを提案している。さらに、この供給方法によってラティスコアの土台となる、壁構造の造形に取り組み、その積層過程における最上層のプロファイルの変化についてまとめている。

2. ラティスコーティング技術の開発

現在、代表的なレーザ金属3Dプリンタ手法として、粉末床溶融結合法(Powder Bed Fusion : PBF法)および、指向エネルギー堆積法(Direct Energy Deposition : DED法)がある⁸⁾。これらは共に、制御可能なレーザによって目的の位置に溶融プールを形成し、そこに金属粉末が接近することで、溶融プールに取り込まれ一体化する。その後、レーザが離れることで自然冷却し、凝固によって任意の形状を得る。

これらの造形手法の差異は、粉末の供給手法による。例えばレーザによる溶融プールに対して、粉末の供給量が多すぎた場合、ポーリング欠陥と呼ばれる大きな球状の塊が発生し、造形品質を著しく悪化させる⁹⁾。このことから、溶融プールへの粉末供給は、目的の位置に粉末を輸送し、配置させると同時に、その供給量を厳密に制御する必要がある。このためPBF法では、ローラやブレードを用いたスキージング(Squeezing)工程によって、所定の堆積厚に制御しながら、金属粉末は平坦な粉末床として充填する。DED法では、ロボット先端に装着されたトーチから不活性キャリアガスとともに金属粉末は噴射され、溶融プールに投入しており、キャリアガスの設定などで、その供給量の安定に努めている。

この供給方法の違いにより、形成できる構造体にも差異が生じる。PBF法では造形に使われなかった粒子も、造形が完了するまで、基本的にはその場を保持する。このため、これらの粒子が足場となって、上の層で形成した溶融プールの重量や金属蒸気などの反発力も支持することがある程度可能である。これによって、オーバーハング構造や梁構造のように真下に空洞がある構造も造形可能であり、内部に複雑な空洞をもつラティスコアを作り出すことができる。それに対してDED法では、トーチから噴射するキャリアガスおよび、酸化防止のためのシールドガスは0.1 m/s以上の流速を有して¹⁰⁾おり、前述した足場となる粒子を留まらせることができない。このため形成できるオーバーハング構造は限定的である¹¹⁾。

その一方、PBF法では、平坦な基準プレート上に造形を行うことが前提であり、最終的にはこのプレートを切り離す必要がある。その点においてDED法は曲面をもつようなバルク材上にも造形が可能であり、バルク材自体も製品の一部とすることができるという利点がある。

以上のことから、バルク材上に多孔質構造を造形するという、筆者らが掲げる微細ラティスコーティング技術については、これらの手法では実現できず、新たな手法が必要となる。前述したとおり、オーバーハング構造を形成するには、溶融プールを支える足場が必須である¹²⁾。3Dプリンタでは、この支持

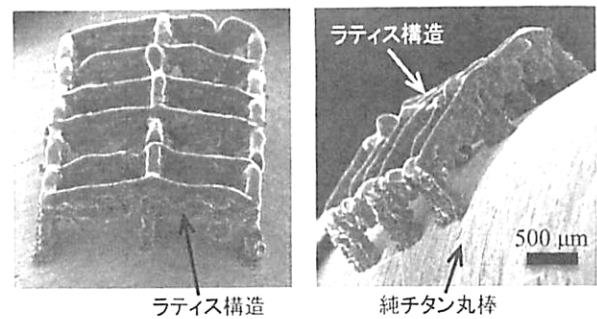


図2 重力落下式粉末供給による造形例

表1 供試材の化学成分

	化学成分(ppm max.)				
	Fe	O	C	H	Ti
Ti粉末	50	1300	200	1300	残部
Ti基材	2000	1500	800	1500	残部

のためサポート体を造形することも行われているが、造形後にこの多孔質内部から大きいサイズのサポート体取り除くことは現実的でなく、微小な粉末粒子が支持体となるべきである。

そこで、微量な粉末を脈動なく搬送できる高精度粉末供給器を用いることを考えた。本装置から真下に排出される粉末は、重力および、それによる空気抵抗以外の外力を可能な限り抑えた形で落下し、バルク材上に堆積する。さらにバルク材を等速運動すれば、その表面に均一な堆積層を作ることができる。堆積した粉末はその摩擦力や分子間力によって比較的緩やかな曲面においても、その場を維持することが可能である。この重力落下式粉末供給法とレーザ照射によって、造形した事例が図2である。同図は、バルク材として純チタン製の直径6 mmの丸棒を用いており、その表面に高さ約0.6 mmの簡単なラティスコアを形成している。なおPBF法で形成される構造よりも歪ではあるが、多孔質構造として必要な横穴が形成できることを確認できている。このような薄い多孔質構造を自由曲面にコーティングできる技術が、筆者らが掲げる微細ラティスコーティング技術である。

3. 実験方法

3.1 供試材

本研究では、歯科インプラントを具体的なニーズと定め、生体親和性の高い純チタンを素材として採用した。ラティスコアとなる純チタン粉末に関しては、ガスアトマイズ法によって得られた高品質の粉末粒子であるが、さらにこれをふるい分けによって粒度分布を25 ~ 38 μm とすることで、供給時の流動性を向上させている。基材は板厚2 mmの純チタン2種熱間圧延材で、本報ではフライス仕上げされた平坦な表面の試験片で評価を行った。粉末および基材の化学成分については表1に示す。

3.2 レーザ発振器とレーザ条件

レーザ発振器およびレーザの集光特性を表2に示す。微細ラティスコーティングの適応先としては薄い板金材も想定し

表2 レーザ発振器および集光特性

波長	1064 nm
最大発振出力	500 W CW ファイバーレーザー
ビーム強度	ガウシアン分布
スポット径	φ16.5 μm
焦点位置	粉末堆積層上面
レンズ焦点距離	100 mm

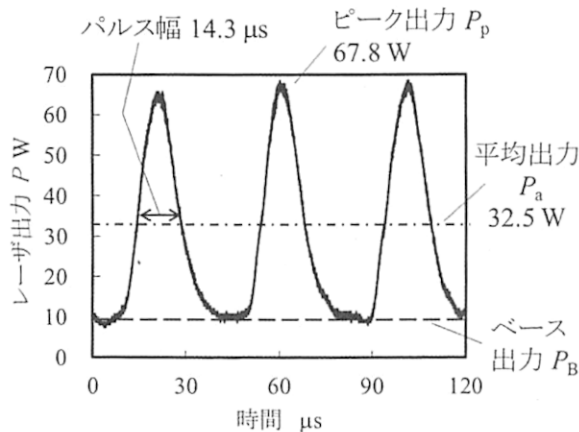


図3 パルス波形⁵⁾

ている。このため、レーザーによる熱影響による被コーティング板材の寸法精度変化を可能な限り抑制したい。そこで、筆者らの前報⁵⁾を参考にした 14.3 μs パルス幅で平均出力 32.5 W のパルスレーザー(図 3)を採用することとした。さらに走査速度は 100 mm/s とすることで、造形幅が細く、熱影響範囲が極めて狭い造形が可能になる。

3.3 高精度粉末供給器

図4に供給装置の概要を示す。モータに連結した縦型のスクリーウの先端は4枚刃のフラットエンドミルを模した構造となっており、これの回転によって粉末が運搬される。さらにスクリーウの先端には、それとほぼ密接した形で薄平板が配置しており、薄平板に設けられた幅0.2 mmのスリットを通過した粉末だけが、シュートを通じて真下に落下し基材上に堆積する。スクリーウは、そのらせん溝に入り込んだ粉末を、持ち上げる方向に回転しているため、スリットを通過できなかった粉末はスリットに押し込まれることがなく、上方へ排出される。これによってスリットとスクリーウ間での粉末の圧縮が抑制され、粉末づまりによる供給量の脈動を低減させた。

図5は本供給器による0.1秒間あたりの供給量の変化を、再現性0.1 mgの音叉式分析てんびんを用いて0.1 s毎に測定した結果であり、スクリーウの回転速度によってまとめている。同図より、供給開始直後の1秒間を取り除けば、スクリーウ回転速度 24 min⁻¹の設定において、0.1秒間あたり約1.0 mgの脈動の小さい粉末供給が可能となる。

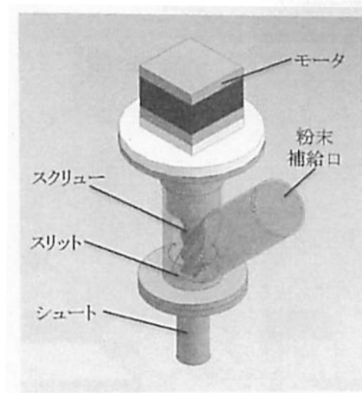


図4 高精度粉末供給器

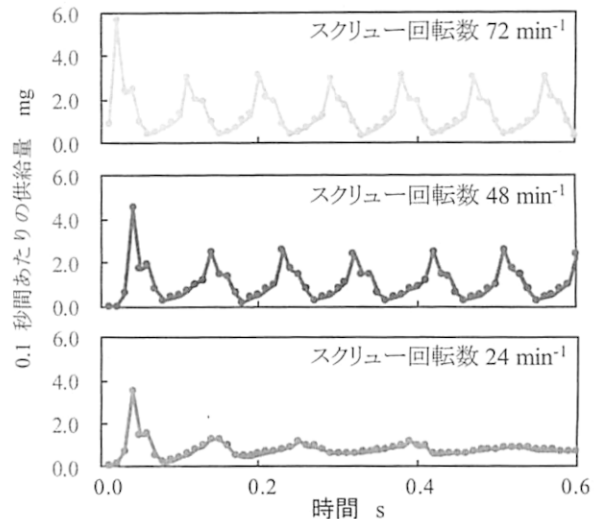


図5 粉末供給器の0.1秒間あたりの供給量の変化

3.4 実験装置および加工プロセス

実験装置は図6に示すように、4つのステーションによって成り立っている。造形を施す基材は、造形ステージに固定されており、これが繰り返し精度±1 μmのリニアサーボモータによって各ステーション間を移動する。造形の流れとしては、まず高精度粉末供給ステーションにて、真上に設置された粉末供給器から適量粉末を落下させ、同時に造形ステージを等速運動させることで、基材上に均一な堆積層を作る。次に、3次元プロファイル測定ステーションに移動し、形成した堆積層を、高さ方向の繰返し精度0.2 μmの能力を持つレーザー2次元プロファイル検出器によって測定する。この際も、造形ステージは16.0 mm/sの等速運動しているため、堆積層の3次元プロファイルの取得および、その評価が可能である。

その後、レーザー造形ステージに移動するが、レーザー溶融時のチタンの酸化反応を抑制するために、基材を覆う形で造形ステージにチャンバを手動で設置し、その内部をアルゴンガスに置換させる必要がある。チャンバにはガスの流入口と排出口があり、堆積させた粉末を動かさないように、1.0 L/min以下の流速でガスを流入し続け、この状態を30秒以上維持することで、低酸素環境を作っている。チャンバの上面には、ガルバノスキャナの走査範囲をカバーするファイバーレーザー用の透過窓が付属している。なお、チャンバ側方には加工状態を高速度カメラにて撮影できる観察窓と、カメラ用の照明窓が相対する位置に設置されている。

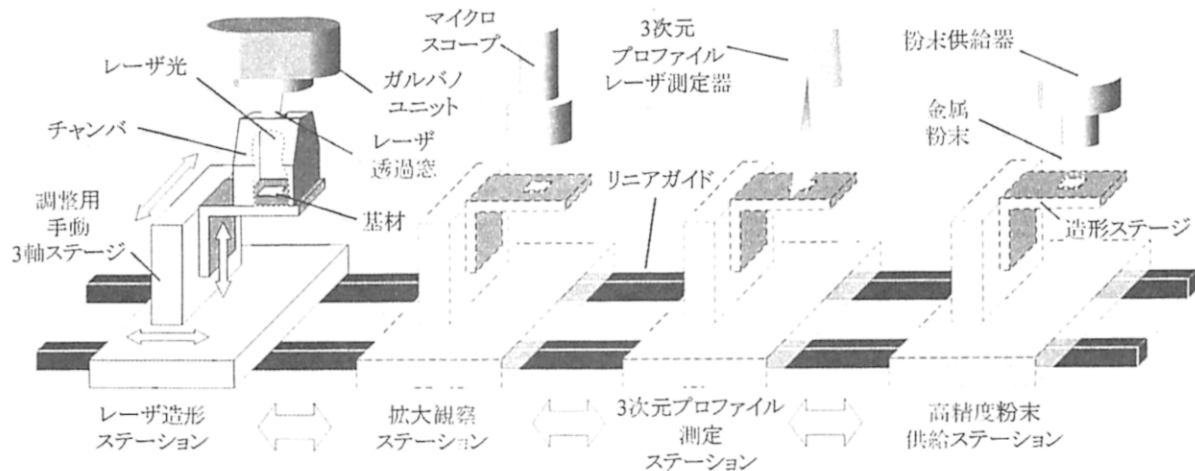


図6 実験装置の構成

レーザー造形完了後、拡大観察ステーションにてマイクロSCOPEによる造形状態を判定し、1層分の造形が完了する。なお、次層の造形を行うためにチャンバを取り外す必要がある。以上の動作を繰り返すことで、3次元造形を行う。

4. 実験結果および考察

4.1 重力落下式粉末供給による壁構造の造形

PBF法において、1層あたりの粉末の堆積厚は造形品質に大きく影響を与える要素であると言われている。そこでまず、本報で採用した、造形の微細性に優れたレーザー条件を用いて、堆積厚の影響を調査した。1層あたりの粉末堆積厚が50 μm 、75 μm 、100 μm となるように、先端がフラットなブレードを用いて、スキージングを施して粉末床を形成した。この粉末床に直線造形を行い、これを5層分積層することで、壁構造を造形した。この造形断面を図7に示す。同図より堆積厚が厚い条件ほど、1層あたりの造形高さが高くなる傾向があり、造形効率については有利ではあるが、1層ごとに丸みを帯びた輪郭となりやすく、層間部分はいくびれとなってしまう。また、堆積厚が厚い条件ほど大きなポロシティが発生しやすくなることも確認された。

本結果と造形効率を考慮して、重力落下式粉末供給による堆積層においても、その堆積厚が50 μm 程度になるような供給条件の調整が必要であると考えた。そこで図5の粉末供給量の脈動が小さい24 min^{-1} の条件のもとで、堆積層中央付近の厚さ平均が50 μm になる造形ステージ移動速度を調べた。その結果、30 mm/s の移動速度を得ることができ、これらの条件を基準として、基材上に幅が約6 mm で、長さが約20 mm の粉末堆積層を形成した。さらに、この堆積層の断面中央を狙って堆積方向と平行に、10 mm の長さのレーザーを走査させ、1層分の造形体を形成した。図8の3Dプロファイルは、この粉末堆積層において表面性状が比較的均一な5 mm の区間を選択したものであり、それと同位置に形成された造形体も併せて示している。なお、造形体の3Dプロファイルは周囲の粉末粒子を刷毛によって取り除いた状態のものである。さらに、選択した領域の造形体稜線部の2Dプロファイルと、

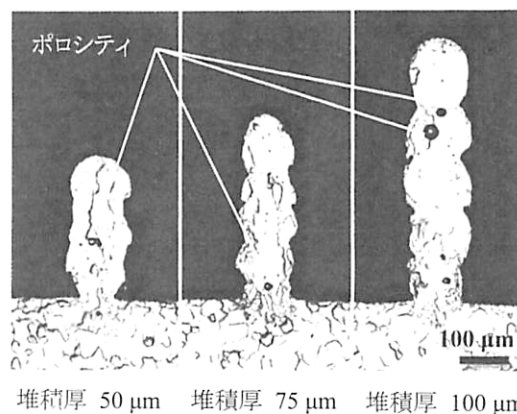


図7 スキージング手法を用いて造形した各堆積厚設定の壁構造断面

それと同位置の造形前の粉末堆積層の2Dプロファイルも併せて示す。

厚さ50 μm を狙い値とし、スキージング操作によっても堆積層を形成し、同様にレーザー走査によって形成された造形体についても調査した。このスキージングの結果を図9に示す。これらの画像により、重力落下式においても、レーザー走査によって造形体を形成することが可能なことが確認できたが、スキージングによって形成された造形体の方が、プロファイルの高低差が少ない。また、短時間に多量の粒子が溶融プールに合流することで発生する、ポーリング欠陥の頻度についても、スキージングを施したもののほうが少ないことが確認できた。このような1層目の造形体の凹凸は、造形前の堆積層の表面性状に起因すると考えられるが、本報においてはその関連性の十分な解明に至っていないため、引き続き検討する予定である。

次に、重力落下式供給による積層について調査した。ここで、加工直後の造形体に目を向けると、レーザー照射によって飛散した粒子や、蒸気流によって引き寄せた粒子が、造形体の上に接合せずに付着している場合があり、造形体の正確なプロファイル測定ができない。また、これがスキージング手法であれば、次層においてこの粒子はブレードによって最適な位置に移動させられるが、本手法では、付着粒子の上さら

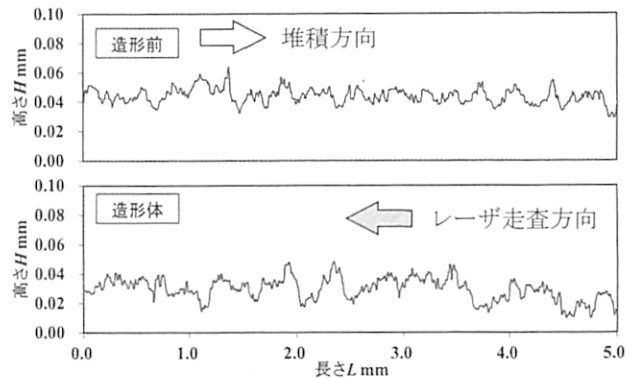
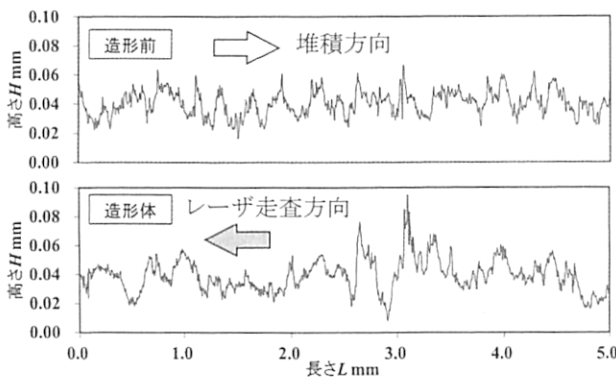
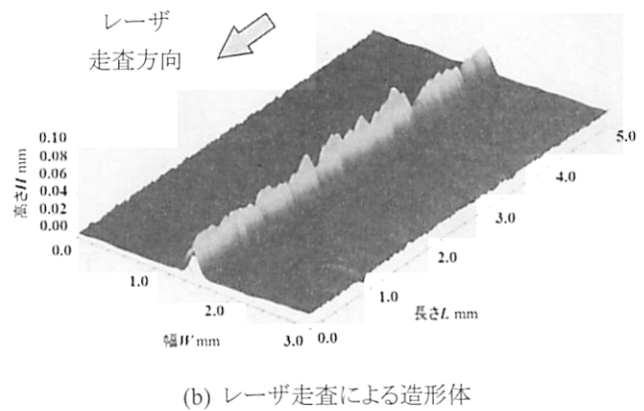
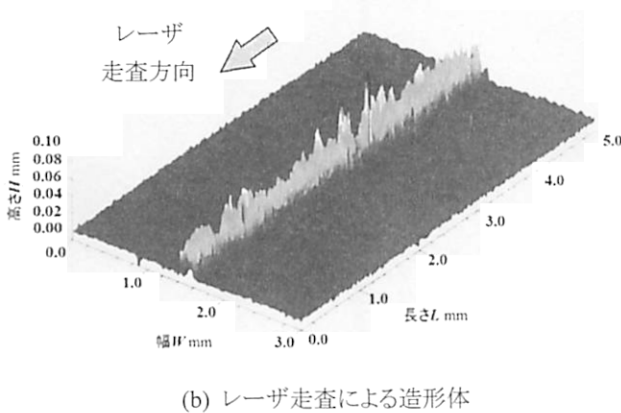
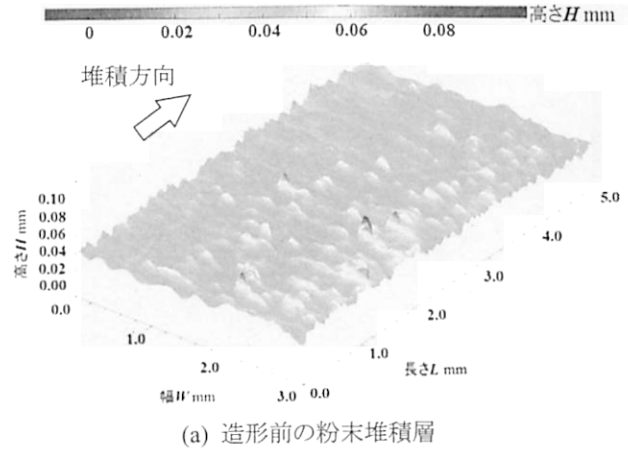
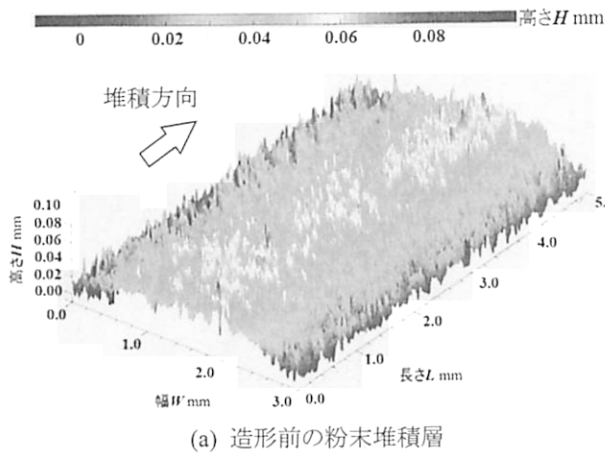


図8 重力落下式供給による造形

図9 スキージング手法による造形

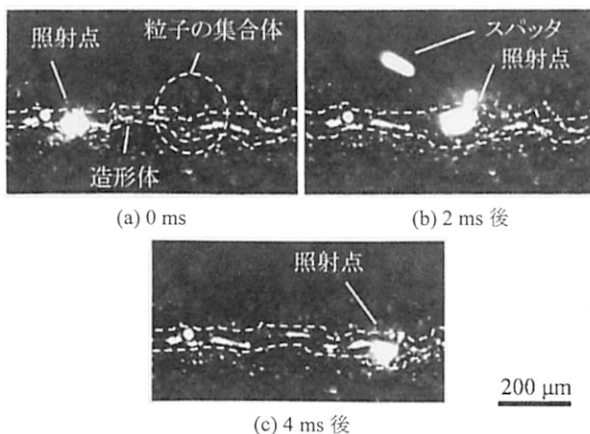


図10 2次加工による粒子の除去

に粉末を供給するため、付着粒子分が堆積厚のばらつきの原因となってしまふ。そこで、付着粒子の除去を目的として、造形と同一条件のレーザーで、再度造形体表面を走査することとした。この2次加工による造形体の時間変化を、高速度カメラで撮影したものを図10に示す。同図より造形体上に付着している粒子の集合体が、ねらいどおりレーザー射線と干渉することで、スパッタとして発光しつつ弾き飛ばされるのが確認された。

この2次加工をプロセスに含めて、重力落下式供給による7層分の積層造形を行い、図11に示す約0.4 mmの高さをもつ垂直な壁構造を造形した。また、重力落下式供給による壁構造断面を示したのが図12である。本図において造形幅約120 μ mの垂直な壁構造が形成されており、その内部には図

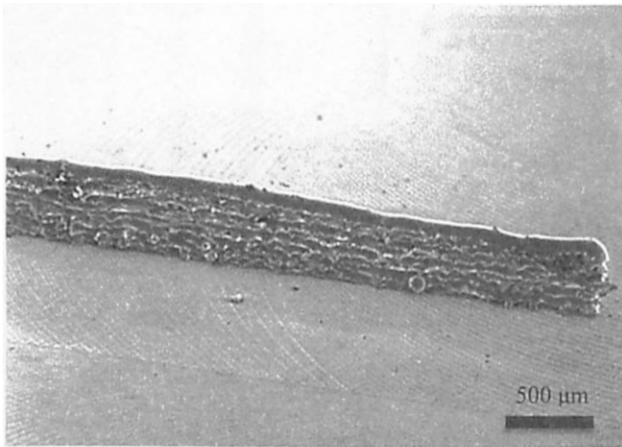


図 11 重力落下式粉末供給による壁構造の造形

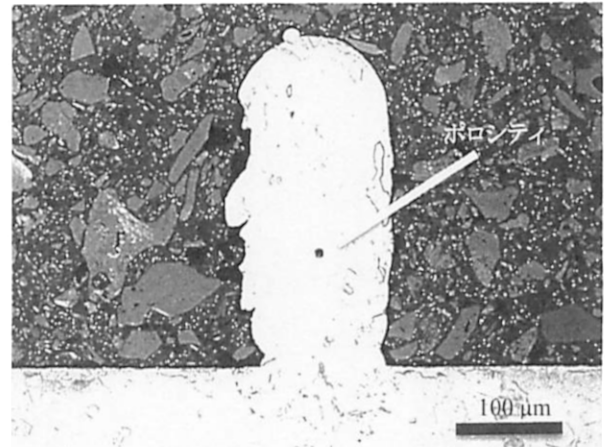


図 12 重力落下式供給法を用いて造形した壁構造断面

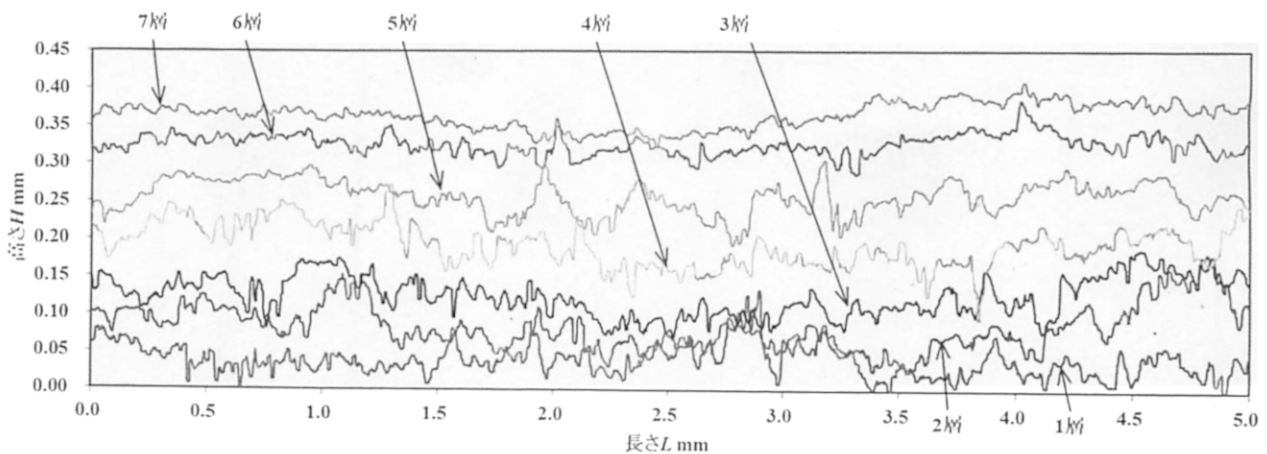


図 13 重力落下式積層造形による各層の 2D プロファイル(長手方向)

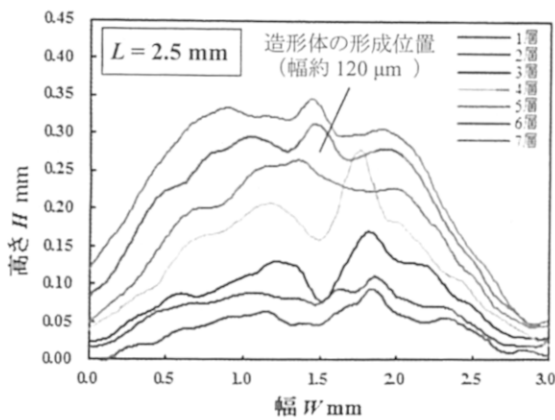


図 14 積層造形後の 2D プロファイル(断面)

7 のスキージング手法を用いた壁構造よりも比較的小さいポロシティがいくつか確認された。図 13 は、図 11 における、1 層ごとの造形体表層の稜線長手方向の同一領域を、2D プロファイルで 7 層分まとめたものであり、粉末供給条件は図 8 で採用したものと同一である。図 13 の各層のプロファイルから、下層においては供給粉末の堆積厚より大きな段差が不規則に発生することはあるが、それがその上層で拡大することはほとんどなく順次積層されていき、第 7 層の基材からの高低差のばらつきは約 50 μm となった。また、表面性状に注目すると、第 6 層、7 層はその下の層に比べ、大きな突起は低減される傾向があることが確認できた。

4.2 上位層における段差の緩和

重力落下式では、場所によらず均一に粉末が堆積することを想定しているため、下層に段差があれば、それを引き継いだ形で造形されていくはずである。しかしながら、図 13 をみれば、この影響はそれほど大きくない。この原因を調査するために、図 13 の $L = 2.5 \text{ mm}$ における断面を 2D プロファイルとして抜き出したものを図 14 に示す。図 14 の $W = 1.5 \text{ mm}$ 部分がレーザの狙い位置であり、紙面に対して垂直にレーザを走査している。これにより、この位置を中心に全幅約 $120 \mu\text{m}$ の造形体が形成される。なお図 14 は、各層の積層造形中のプロファイルであるため、造形体およびその周囲の粉末堆積状態も明示されており、この堆積の傾向を明確にするために各プロファイルにはスムージング処理を施している。このプロファイルより層が増加するごとに、第 4 層の $W = 1.7 \text{ mm}$ 付近を除き、ほぼ全域で増加している。しかし、第 3、4 層をみると、造形体の位置 ($W = 1.5 \text{ mm}$) には窪みが生じているのに対して、第 6、7 層については逆に突起となっており、これらの造形現象の違いがあることが考えられる。

第 3、4 層において段差が拡大しない原因について考察する。図 15 は第 4 層および第 6 層のレーザ照射前後の断面 2D プロファイルをもとめたものである。第 4 層の照射前後のプロファイルに注目すると、レーザ照射前は中央にピークのある山なり形状である。この中央位置にレーザを照射したあとのプ

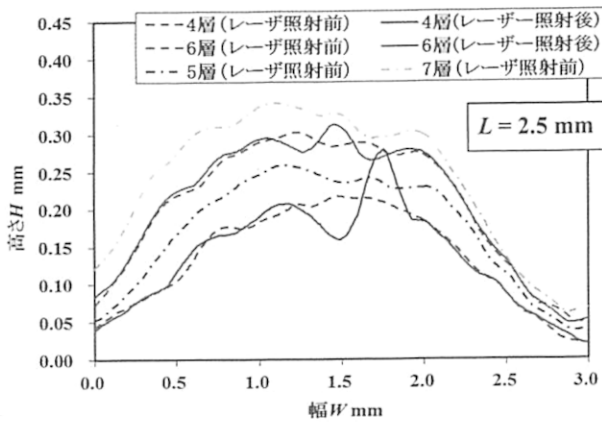


図 15 レーザ照射前後のプロファイルの比較(断面)

ロファイルでは、照射前のプロファイルに対して中央位置に約 50 μm の深さの窪みが生じており、その位置に造形体が形成されている。この窪みは PBF 法でも指摘されている¹³⁾粉末のかさ密度に起因するものや、造形中の粒子の飛散などが原因と考えられる。また、粉末が堆積しているのみの位置である $W = 1.7 \text{ mm}$ には大きなピークができています。これは、いくつかの粒子が溶融、一体化したことによる大きな塊(ポーリング)が粉末層上に残留したものであると考えており、その発生原因については後述する。

その後の、第 5 層の粉末供給(図 15 の第 5 層レーザー照射前のプロファイル)によって、窪みは埋められ、ポーリングによるピークはその滑り落ちなどにより解消され、再びなだらかな堆積層となる。この第 5 層の堆積層と、第 4 層の造形体について長手稜線の 2D プロファイルを示したものが図 16 である。同図をみても、粉末供給による堆積によって細かな凹凸が解消されていることが分かる。これらのことから、重力落下式供給によって、粉末粒子はそのまま真下に落下するだけでなく、造形体の表面性状や既にある粉末層の堆積状態に影響を受けて、堆積することが推察され、これが、下層部で生じた段差が拡大しない原因の 1 つだと考えられる。なお、本報では粉末供給の時間あたりの量については注目したが、粉末粒子の落下による運動量および、それによる堆積層などへの衝突についても、重要であることが示唆されている。

4.3 高速度カメラ像による各層の造形挙動

次に図 13 の下層部において、頻繁に発生する突起の原因と、これが第 6, 7 層で抑制される原因について考察する。図 15 のレーザー照射位置 ($W = 1.5 \text{ mm}$) において、第 6 層の造形体と、第 7 層の粉末堆積層のプロファイルの差は、粒子 1 粒程しかなく、ほぼ堆積粒子が存在していない。これは、採用した粉末は流動性が高く、安息角は小さいが、堆積層の高さが増えるにつれて、堆積層の斜面を滑り落ちる粒子が増えるためだと考えられる。しかし、図 13 や図 14 の結果より、第 7 層のレーザー走査によって、造形体が成長していることが確認できる。これについて、第 7 層における造形中の高速度カメラ像である図 17 によって説明する。同図 (a) より、レーザー走査前でありながら、第 6 層で作られた造形体が見えており、この上に供給したはずの粉末粒子は、造形体上にほとんど乗っていないことが確認できる。造形体上をレーザーが走査すると、造形体表

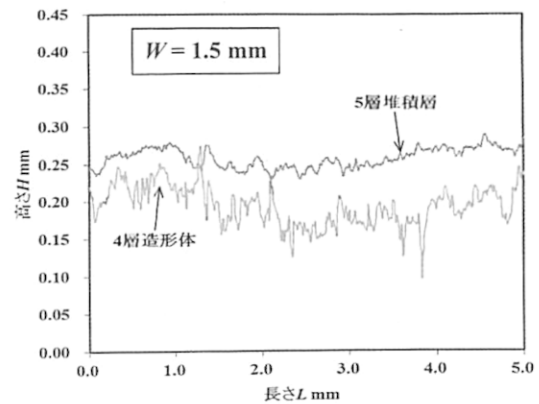


図 16 第 4 層造形体と第 5 層堆積層のプロファイル(長手)

層に溶融プールが形成される。この溶融プールから発生した金属蒸気は、周囲の粉末粒子を引き寄せる効果があることが知られている^{14) 15)}。図 17 においても、溶融プール進行方向の粒子よりも、その側方の粒子が多く引き寄せられ、溶融プールに合流し、造形体の成長に繋がっている。

一方、第 4 層における造形中の高速度カメラ像である図 18 をみると、第 3 層の造形体上に粒子が堆積しているのが確認できる。図 18 と同様に、走査ライン側方から引き寄せられた粒子についても第 4 層の造形に利用されるが、第 4 層の造形の主体は、第 3 層の造形体上の粒子、つまり進行方向に堆積した粒子である。この堆積粒子に溶融プールが近づくと、そのまま溶融プールに取り込まれる場合と、前方に傾斜した金属蒸気によって、弾き飛ばされる場合がある。この金属蒸気の傾斜は、第 3 層の造形体が下り勾配の場合、より起こりやすい。この前方に傾斜した金属蒸気の高いエネルギーによって、曝された粒子は弾かれると同時に、加熱され、発光し、液滴のように振る舞う。このような粒子どうしが接触することで一体化し、50 ~ 200 μm ほどの大きな塊(ポーリング)となる。このポーリングはその質量により、遠くに飛ばされず、進行方向のレーザー走査ライン上に付着する。あるいはライン沿いに堆積する。図 14 および図 15 における第 4 層の $W = 1.7 \text{ mm}$ 付近で高いピークとなっているのは、この塊によるものと考えている。また、金属蒸気によって弾かれた粒子は、周囲の粒子も巻き込んで飛散していくこともあるため、図 18 は図 17 に比べスパッタ量は圧倒的に多く、進行方向の粒子が喪失してしまうことも多くある。これらが複合的に働くため、下層部の造形体の表面は大きな凹凸が形成されやすい。

以上のことから、第 4 層と第 7 層の表面性状の違いは、その下層で形成された造形体の表面性状と、その周囲の粉末堆積層の状態によるものと推察される。これによって、意図的に第 7 層のような堆積状態を作り出し、平滑な表面性状を作り出せることも期待できる。

5. 結言

機能を有する多孔質構造を、バルク材表面に付与する技術として、微細ラティスコーティング技術を提案し、その実現のために、重力落下式粉末供給を利用したプロセスを開発した。また、同プロセスにより多孔質構造(ラティス構造)のペー

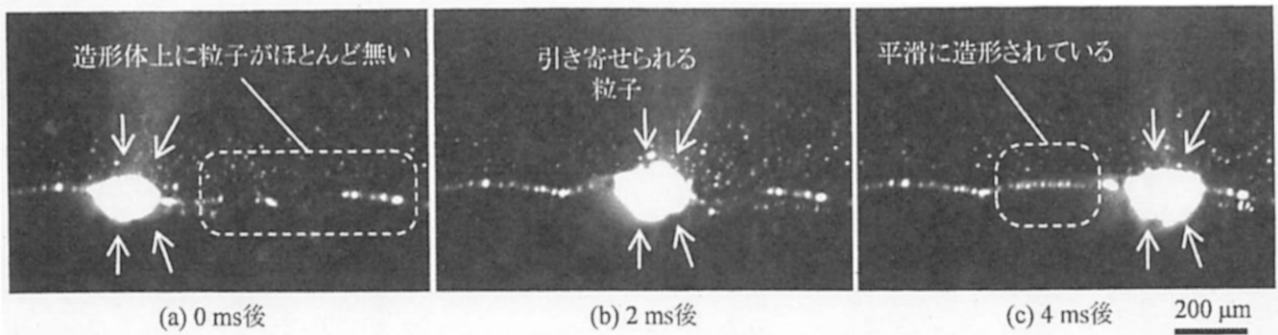


図 17 第 7 層における造形中の溶融プールおよび周囲の粉末の挙動

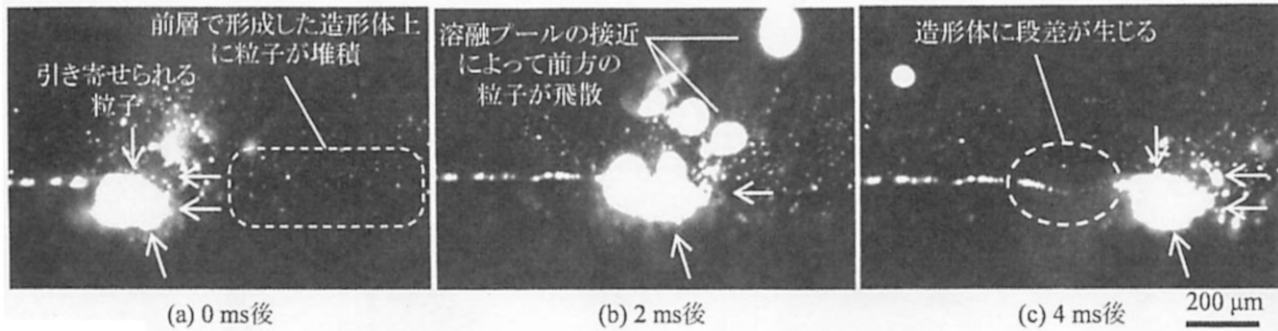


図 18 第 4 層における造形中の溶融プールおよび周囲の粉末の挙動

スとなる壁構造を造形した際の、各層表面におけるプロファイル(表面性状)に注目して詳細な評価を行った。

その結果、下層部では凹凸が大きいプロファイルを形成するが、層が増加するにつれて、これが緩和され、6 層を超えた辺りから平滑な表面性状が得られることが明らかとなった。これは、下層部と上層部で、造形体の表面性状と、供給された粉末の堆積状態が異なり、それによって、造形中の溶融プールと、造形の素となる周囲の粉末粒子の挙動に差異が生じるためだと考えられる。

さらに、本手法によって作られた壁構造は、直立した形で 0.4mm の高さまで造形することが確認でき、重力落下式供給法における造形の有効性が確認できた。

6. 参考文献

- 1) N. Moronuki: Surface Functions Brought by Surface Micro Structures, Morikita Publishing Co., Ltd., (2011) 32 (in Japanese).
- 2) K. Shimada, T. Hirai, M. Mizutani and T. Kuriyagawa: Fabrication of Functional Surface by Ultrasonic-assisted Cutting, Journal of Japan Society for Abrasive Technology, 62, 1, (2018) 39 (in Japanese).
- 3) 中嶋 英雄: ポーラス材料学 多孔質が創る新機能性材料, 内田老鶴圃, (2016) 235.

- 4) 京極 秀樹, 池庄司 敏孝: 図解 金属 3D 積層造形のきそ, 日刊工業新聞社, (2017) 161.
- 5) H. Maehana et al: The Creation of Fine Structure by Laser Additive Manufacturing of Metal, Journal of the Japan Society for Abrasive Technology, 62, 10, (2018) 527 (in Japanese).
- 6) K. Yamamoto: Biomaterials for Artificial Hip Joints, Medical View Co., Ltd., (2017) 126 (in Japanese).
- 7) M. Yoshinari: Materials of Dental Implant Q&A Volume1, Material, Ishiyaku Publishers, inc., (2017) 59 (in Japanese).
- 8) M. Zhang et al: Competing Influence of Porosity and Microstructure on the Fatigue Property of Laser Powder Bed Fusion Stainless Steel 316L, Proceedings of the 28th Annual International Solid Freeform Fabrication Symposium – An Additive Manufacturing Conference, (2017) 365.
- 9) I. Yadroitsev et al: Single Track Formation in Selective Laser Melting of Metal Powders, Journal of Materials Processing Technology, 210, (2010) 1624.
- 10) GTV Verschleißschutz GmbH: Technical Description GTV Multi-jet Nozzle PN 6625, (2018).
- 11) 岡田 直忠: レーザメタルデポジション法の実際, 金属, 88, 10, (2018) 827.
- 12) H. Chen et al: Improving Additive Manufacturing Processability of Hard-to-process Overhanging Structure by Selective Laser Melting, Journal of Materials Processing Technology, 250, (2017) 99.
- 13) 千葉 晶彦: 電子ビーム積層造形(パウダーヘッド法)の実際, 金属, 88, 10, (2018) 818.
- 14) M. Manyalibo et al: Denudation of Metal Powder Layers in Laser Powder Bed Fusion Processes, Acta Materialia, 114, (2016) 33.
- 15) S. Ly, A. M. Rubenchik et al: Metal Vapor Micro-jet Controls Material Redistribution in Laser Powder Bed Fusion Additive Manufacturing, Scientific Reports, 7, 4085 (2017).



Processing capabilities of micro ultrasonic machining for hard and brittle materials: SPH analysis and experimental verification

Jingsi Wang^{a,*}, Jinguo Fu^a, Jinlong Wang^a, Fengming Du^a, Pay Jun Liew^b, Keita Shimada^c

^a Marine Engineering College, Dalian Maritime University, 1 Linghai Road, Ganjingzi District, Dalian, 116026, China

^b Fakulti Kejuruteraan Pembuatan, Universiti Teknikal Malaysia Melaka, Hang Tuah Jaya, 76100, Durian Tunggal, Melaka, Malaysia

^c Department of Mechanical Systems Engineering, Graduate School of Engineering, Tohoku University, Aramaki, Aoba 6-6-01, Aoba-ku, Sendai, 980-8579, Japan

ARTICLE INFO

Keywords:

Ultrasonic machining (USM)
Smoothed particle hydrodynamics (SPH)
Hard and brittle materials
Micromachining
Processing capability

ABSTRACT

Micro ultrasonic machining (micro-USM) is an unconventional micromachining technology that has capability to fabricate high aspect ratio micro-holes, intricate shapes and features on various hard and brittle materials. The material removal in USM is based on brittle fracture of work materials. The mechanical properties and fracture behaviour are different for varied hard and brittle materials, which would make a big difference in the processing capability of micro-USM. To study the processing capability of USM and exploit its potential, the material removal of work materials, wear of abrasive particles and wear of machining tools in USM of three typical hard and brittle materials including float glass, alumina, and silicon carbide were investigated in this work. Both smoothed particle hydrodynamics (SPH) simulations and verification experiments were conducted. The material removal rate is found to decrease in the order of glass, alumina, and silicon carbide, which can be well explained by the simulation results that cracking of glass is faster and larger compared to the other materials. Correspondingly, the tool wear rate also dropped significantly thanks to the faster material removal, and a formation of concavity on the tool tip center due to intensive wear was prevented. The SPH model is proved useful for studying USM of different hard and brittle materials, and capable of predicting the machining performance.

1. Introduction

Nowadays, although manufacture technologies are well developed, considerable problems such as long machining cycle and high production cost still exist in the machining of hard and brittle materials including ceramics, crystals, and glass. Particular difficulties are the production of complex micro/nano structures with stringent requirements such as high machining efficiency, good shape control, high aspect ratios, and superior surface quality. Hence, there is a crucial need for exploring efficient and precision micromachining techniques for these difficult-to-machine materials. Unconventional machining technologies including electric discharge machining (EDM) [1], laser beam machining (LBM) [2], electrochemical machining (ECM) [3] have been developed to solve the problems in micromachining of hard and brittle materials. However, LBM is less effective for drilling thick workpiece materials because the limited working range of the beam, and always subjected to heat-induced damages which also happens to EDM technique. In addition, ECM and EDM cannot machine electrically non-conductive materials, this greatly limits the use of the two

techniques for fabricating glass and ceramic materials which are always have high electrical resistivity. Ultrasonic machining (USM) using loose abrasive particles suspended in a liquid slurry for material removal is another alternative technique for fabricating various hard and brittle materials. During USM, the tool ultrasonically vibrates to impact the workpiece surface through the abrasive particles and make a large number of tiny fractures, therefore a considerable amount of workpiece materials would be removed away. The material removal process only relies on small mechanical forces and does not suffer from heat or chemical effects, so that no thermal damages, significant levels of residual stress or chemical alterations occur [4,5]. This ensures stable micromachining on hard and brittle materials.

Generally, the material removal is induced by brittle fracture of the work materials in USM. The mechanical properties and fracture behaviour are different for varied materials, which would make a big difference in the processing capability of micro-USM. Markov [6] classified workpiece materials into three categories in consideration of the USM suitability as shown in Table 1. The most suitable materials for USM process are quite brittle materials, such as glass, mica, and quartz,

* Corresponding author.

E-mail address: wjs@dlnu.edu.cn (J. Wang).

<https://doi.org/10.1016/j.precisioneng.2020.02.008>

Received 2 October 2019; Received in revised form 29 January 2020; Accepted 14 February 2020

Available online 27 February 2020

0141-6359/© 2020 Elsevier Inc. All rights reserved.

Table 1
Classification of materials and fields of application for USM [6,9].

Group of material	Criterion of brittleness	Predominant type of deformation	Type of failure	Field of application of ultrasonic machining
I glass, mica, quartz, ceramic, diamond, germanium, silicon, ferrite, alsiifer	Over 2	Elastic	Brittle	Manufacturing parts of semiconducting materials. Making industrial diamonds. Fabricating special ceramics.
II alloys tempered to high hardness carburized and nitrided steels, titanium alloys	1–2	Elastic-plastic	Brittle after work hardening by plastic deformation	Manufacturing parts of glass quartz or minerals in the optical and jewelry industries. Machining ferrite, alsiifer and other materials. Making and repairing hard alloy dies, press tools, and purchases. Shaping or sharpening hard alloy tools.
III lead, copper, soft-steel	Less than 1	Plastic	No failure (or ductile failure)	Unsuitable for ultrasonic machining.

which are cut by the initiation and propagation of tiny cracks of the workpiece. The materials that exhibit some plastic deformation before fracture like titanium alloys, carburized and nitride steels can be machined by USM with some difficulty. However, the ductile materials, such as soft steel and copper, are not suitable in principle for USM. The ductile substrate materials are not really removed but are displaced, which also have been observed for some fine polishing operations [7]. Tough materials are considered to cause a low material removal rate, high tool wear and reasonable surface roughness [8]. Komaraiah and Reddy [9] stated that the fracture toughness and hardness of the workpiece material play an important role with respect to material removal rate. As the fracture toughness and hardness increase, there is a reduction in the material removal rate.

Even though the basic principle and characteristics of USM are well reported, not much research has been conducted to clarify the mechanism of micro-USM up to date. In micro-USM, the tool diameter, abrasive particle size, and the tool vibration amplitude are reduced to microscale, which brings about several problems. The top two problems are low machining rate and the surface/subsurface micro-cracks. The volume of material removal per stroke is very little due to the use of micrometer-sized abrasive particles. And microcracks generated during this process may remain on machined surfaces. Especially, for micro products, such a crack strongly influences the service life and several functional properties [10–12]. The easiest method to reduce cracks is by using smaller abrasive particles, however this will further reduce the material removal rate. It is therefore important to find ways to remove the cracks with no sacrifice of the machining rate. However, the current knowledge of the technology is not sufficient to provide a comprehensive understanding of the material removal mechanism and instructive rules for improving the machining performance. Therefore, the development of micro-USM has been quite slow in recent years. The processing capability of micro-USM for different hard and brittle materials should be separately discussed and further illustrated by studying the material removal mechanisms involved. In this work, the material removal of work materials, wear of abrasive particles and wear of machining tools in USM of three typical hard and brittle materials including float glass, alumina, and silicon carbide were investigated by both smoothed particle hydrodynamics (SPH) simulations and verification experiments. The processing capability of micro-USM for the three kinds of materials were compared, and the nature of the material removal mechanism was discussed based on these results.

2. SPH simulation on different hard and brittle materials

As the abrasive slurry in USM blurs the machining zone, where cracks initiate and propagate beneath the work surface within an extremely short time due to the ultrasonic tool vibration, it is nearly impossible to investigate the material removal process during USM directly. Therefore, the current authors proposed a SPH model for studying the USM process. SPH does not require a numerical grid, instead, a set of particles endowed with material properties are distributing in the domain and interacting with each other according to the governing conservation equations. Therefore, it has some potential advantages including solving problems involved in large deformations and fractures which cause error due to mesh distortion and tangling in the FEM [13,14]. The SPH offers substantial potential in a variety of problems such as explosion [15], underwater explosion [16], high velocity impact [17–19], metal forming process [20], and the erosive wear in solids by particle impact [21]. Encouraging results have been acquired, for example, in the simulations of penetrator impact on concrete targets [22,23], SPH well demonstrated the fracture process in a brittle concrete plate caused by high velocity impact. In particular, fracture distribution agreed well with the experimental results. Consequently, SPH method is suitable to study the material removal due to fracture failure of hard and brittle materials in USM, and the former studies proved its effectiveness [24,25]. This section will present the SPH

Table 2
Material models and relevant parameters.

	Float glass	SiC	Al ₂ O ₃	B ₄ C	SS304
Equation of state	Polynomial	Polynomial	Polynomial	Polynomial	Shock
Density g/cm ³	2.53	3.215	3.89	2.51	7.9
Bulk modulus A ₁ GPa	45.4	220	231	233	None
Grüneisen coefficient Γ	None	None	None	None	1.93
Strength	Johnson-Holmquist	Johnson-Holmquist	Johnson-Holmquist	Johnson-Holmquist	Steinberg-Guinan
Shear modulus GPa	30.4	193.5	152	199	77 (G ₀)
Hugoniot elastic limit GPa	5.95	11.7	6.57	12.5	None
Yield stress MPa	None	None	None	None	340
Failure	Johnson-Holmquist	Johnson-Holmquist	Johnson-Holmquist	Johnson-Holmquist	None
Hydro tensile limit MPa	150	750	262	7300	None

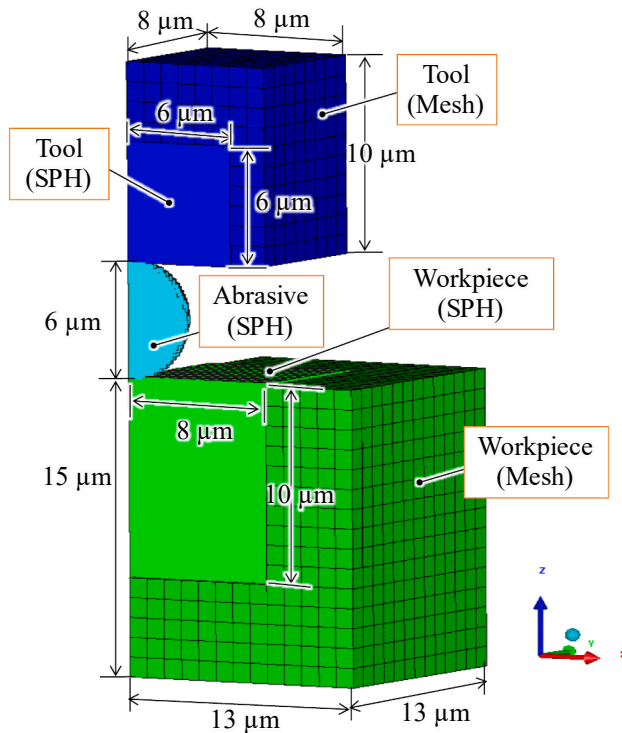


Fig. 1. A snapshot of the simulation model.

simulation approach and results for different work materials.

2.1. Material modelling

In this work, for the hard and brittle workpiece and abrasive materials, the Mie-Grüneisen polynomial equation of state [26] was employed to describe the initial elastic response of the materials. The strength and damage behavior of these hard and brittle materials were modeled with Johnson-Holmquist material model, which was first developed for facilitating simulations of ballistic problems. The Johnson-Holmquist material model is suitable to simulate the phenomena where brittle materials are subjected to load and damage, similar to the situation in USM of hard and brittle materials. The model defines that material damage begins to accumulate when the stress exceeds a critical value under compressive loading [27]. This damage accumulation for fracture is tracked via a damage parameter (ranging from 0 to 1.0). For undamaged material, $D = 0$, while for entirely fractured material, $D = 1.0$. When $0 < D < 1.0$, it indicates that irrecoverable plastic strain occurs, and the material is considered to be partially damaged. The detailed definition of Johnson-Holmquist material model is introduced in the references [28,29].

The tool material used in this work is 304 stainless steel, here

referred to as SS304. For this material, the Shock equation of state [26] was used to model the relation between the hydrostatic pressure, the specific volume, and the specific energy, by considering that accurate description of shock transition states is very important for impact calculations. In this model, the reference function for the Mie-Grüneisen equation of state is chosen as the Hugoniot relations [30]. The strength of SS304 material is formed by Steinberg-Guinan model [31].

Because materials used as abrasive particles should be harder than those of workpieces in USM for material removal, the abrasive for silicon carbide workpiece was modeled by boron carbide. For the other two workpiece materials, silicon carbide was used in abrasive modelling. The constants related to the equations of the material models and material properties, for glass [32,33], silicon carbide (SiC, also used as abrasive material) [34], and alumina (Al₂O₃) [35] used for workpiece modeling; boron carbide (B₄C) [33,36] employed for abrasive modeling; SS304 [37] utilized for tool modeling, are obtained from existing test data and summarized as shown in Table 2.

2.2. Modelling description

A snapshot of the simulation model for studying USM on different workpiece materials was built as shown in Fig. 1. A one-quarter model with symmetric boundary conditions was used to reduce the calculation amount. And as the SPH generally takes more computation time, the simulation was conducted with a combination of SPH solver and grid-based Lagrange solver by constructing the part in large and small deformation with the SPH particles and Lagrange grids, respectively. The dimensions for each part are as defined in the figure, and the finite element mesh size is 1 μm for workpiece and tool modeling. The smoothing length of SPH particles used in the model was 200 nm. The top surface of the tool was endowed with the velocity condition which is simplified from ideal ultrasonic vibration in the experiments introduced later. The calculation method of the velocity was introduced in our former work [24,38]. An initial velocity of 0.6 m/s was applied in this study. A transmit boundary condition was used on the bottom and side surfaces of the workpiece, so the pressure transmitted without reflection. This allows the calculation of a large target in reality.

2.3. Simulation results

2.3.1. Fracture of workpiece and abrasive particle

The time-dependent cracking of the workpiece and abrasive particle along x-z symmetric plane are shown in Fig. 2, the left half was the mirror images of the original model. Green, blue and red elements indicate the materials are in elastic, plastic and failure states. After a calculation of 0.15 μs, a plastic region (in blue color) appears in both float glass and Al₂O₃ workpiece, even though the area is very small for Al₂O₃ workpiece. With further penetration driven by the tool, a median/radial crack can be confirmed to be generated and propagate into the two materials, with those growing faster in the glass workpiece. While for the SiC workpiece, no fractures can be confirmed during the downward stroke of the tool (0–2 μs). Then, when the tool is unloaded, the

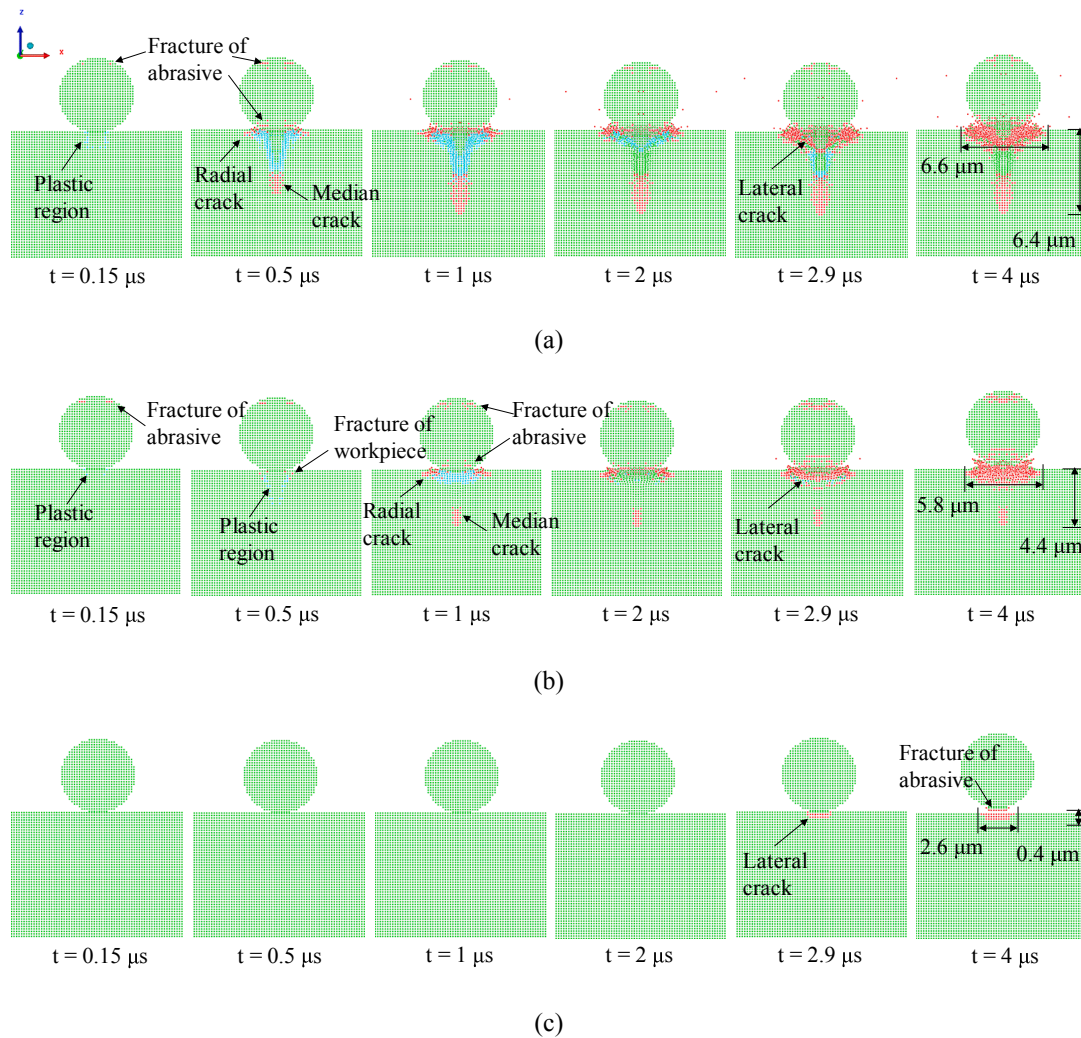


Fig. 2. Simulation results of material status: (a) float glass, (b) alumina, and (c) silicon carbide.

plastic region under the impact site in the glass and Al_2O_3 workpiece is transformed to material failure in the form of a lateral crack as pointed out in the figure. For the SiC workpiece, crack is also found near the work surface during the unloading process, which is similar to a lateral crack pattern. The final crack depth for glass, Al_2O_3 , and SiC, is 6.4, 4.4, and 0.4 μm , respectively. The crack is larger for glass with a lower hardness and fracture toughness than the other two materials. Also, same tendency can be found for the crack width on the workpiece surface, which is 6.6, 5.8, and 2.6 μm , for glass, Al_2O_3 and SiC, respectively.

It is exciting to know that the crack formation process is similar to the median crack system [39,40] for glass and Al_2O_3 , the median/radial crack generated during tool downward stroke and the lateral crack initiated in the upward stroke. While in the SiC workpiece, crack grew after unloading and its extension is tiny. The different crack pattern indicates that the distribution of the stress field for the three materials is different even though the impact conditions are the same. In this simulation, the maximum tensile hydrostatic pressure for SiC is 750 MPa, which is much higher than 150 MPa for glass and 262 MPa for Al_2O_3 . This means more difficult for SiC to fracture and explains the different cracking behavior.

Fractures of abrasive particles working on different substrates were also confirmed as shown in Fig. 2. Both glass and Al_2O_3 workpiece used SiC abrasive particle, and SiC workpiece used boron carbide abrasive particle. As harder Al_2O_3 workpiece resist fracture better than float glass, higher pressure would be applied on the abrasive particle working

on the Al_2O_3 workpiece and induce large fracture in the particle. On the other hand, boron carbide is too hard to be broken, so only small fractures can be found on boron carbide abrasive particle as shown in Fig. 2(c).

The growth of crack during micro-USM is demonstrated by using the SPH model. According to the various crack patterns resulted from the calculations, the machining conditions such as the workpiece material would have a large effect on the crack initiation and propagation. If the model is reliable, it may be extremely useful to clarify the material removal mechanism of micro-USM and to study the processing capability.

2.3.2. Deformation of tools

Plastic strains on SS304 tools during calculation are shown in Fig. 3. The strain value is highest for SiC workpiece, followed by Al_2O_3 workpiece, and it is lowest for float glass. This means pressure applied on the tool for float glass workpiece is lower, and less wear is expected to occur. The results also show that the abrasive particle not only indented into the workpiece, but also penetrated into the tool. As the SiC workpiece is hard and not easily broken, the penetration of boron carbide particle into the tool is large, inducing large plastic deformation, which is considered to induce large wear of the tool. In respect to SiC abrasive particles, the material is not that hard as boron carbide to penetrate into the tool deep and the area in contact with the tool were fractured during the hammering as illustrated in Fig. 2(a) and (b).

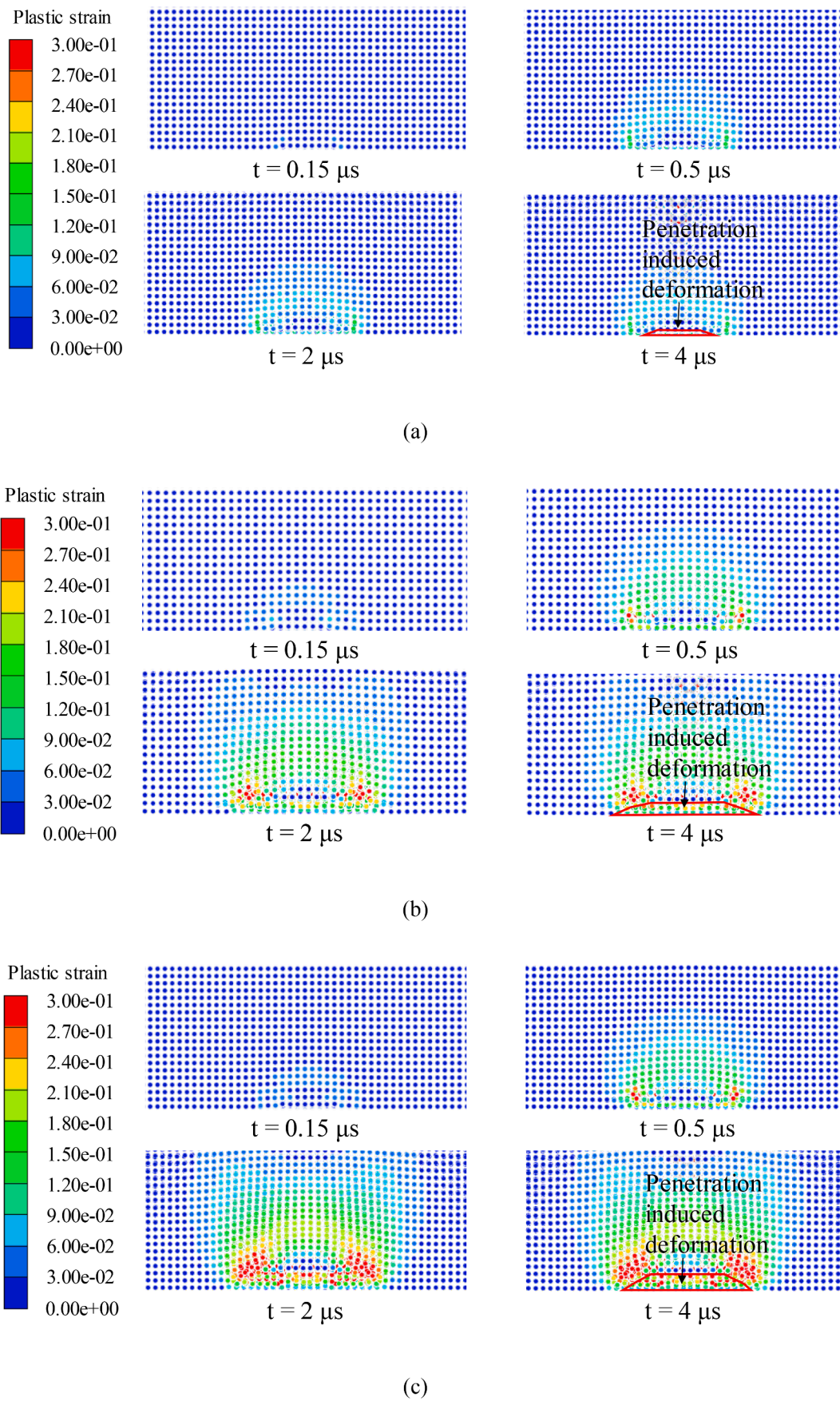


Fig. 3. Plastic strain on the tools: (a) float glass, (b) alumina, and (c) silicon carbide.

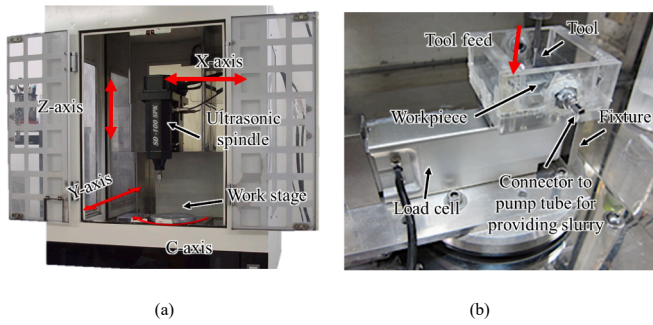


Fig. 4. Experimental setup: (a) the main machine body, (b) installation of the load cell.

Table 3
Physical and mechanical properties of the workpiece materials.

	Silicon carbide	Alumina	Glass
Density g/cm ³	3.1	3.7	2.5
Poisson ratio	0.14	0.21	0.23
Knoop hardness kg/mm ²	2800	1100	465
Young's modulus GPa	407	280	70
Fracture toughness MPa m ^{1/2}	4.1	3.5	0.8

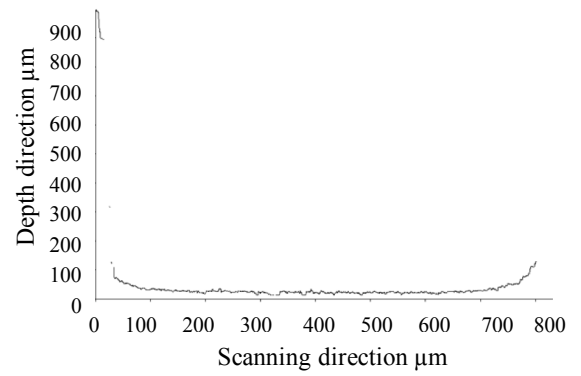
Table 4
Experimental conditions for deep blind hole drilling on different work materials.

Process parameters	Value
Vibration frequency	About 61 kHz
Vibration amplitude	About 4 μm (peak-to-peak)
Maximum tool feed depth	1 mm
Machining force	Lower than 3 N
Tool feed rate	0.5–10 μm/s
Tool material	304 stainless steel (∅ 1 mm)
Flow rate of slurry	50 mL/min
Abrasive material	Silicon carbide (mean size: 8 μm) Diamond (mean size: 6 μm)
Workpiece material	Glass, alumina Silicon carbide

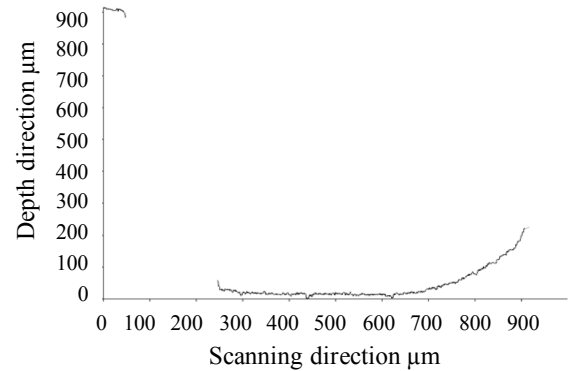
3. USM experiments on different hard and brittle materials

3.1. Machining conditions

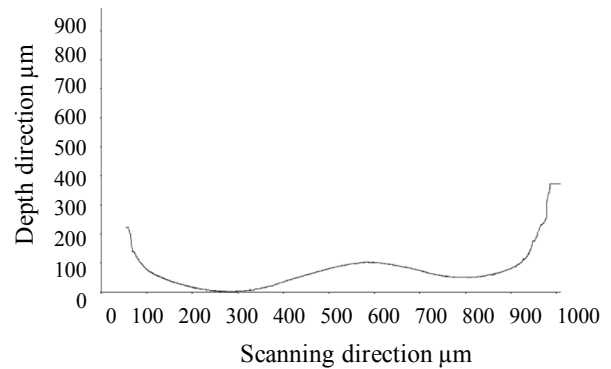
Fig. 4 shows the photograph of the experimental setup. A precision 4-axis desktop type CNC machine tool with three linear axes and one rotary axis was used. An ultrasonic vibration spindle is mounted on this CNC tool for micro ultrasonic machining experiments. The vibration frequency and the amplitude at the tool tip were about 61 kHz and 4 μm (peak to peak), respectively. The tool top surfaces were all finished by a micro-EDM machine with the same finishing conditions before USM experiments. Deep blind hole drilling tests were conducted on glass, alumina (Al₂O₃), and silicon carbide (SiC). The original surfaces of the three materials were polished to confirm no defects existed and comparable with the simulation. In each experiment, a constant feed rate was applied to the tool and the feed depth was monitored by following a CNC program. A load cell with a resolution of 10 mN was employed to trace the machining force during the hole drilling process. Stop machining conditions when either the feed depth is bigger than 1 mm and the maximum machining force is larger than 3 N were used. The machining process ends while either of the two conditions achieved. Table 3 lists the physical and mechanical properties of the three materials. Detailed experimental conditions are listed in Table 4.



(a)



(b)



(c)

Fig. 5. Cross-section profiles of the holes for the measurement of machined depth: (a) glass, (b) Al₂O₃, (c) SiC.

3.2. Experimental results

3.2.1. Material removal rate

The material removal rate was calculated as the depth of the machined holes over the machining time. The machined area was scanned to measure the hole depth using a laser probe profilometer with 1 nm resolution on Z direction and 0.1 μm resolution on XY direction (NH-3T) produced by Mitaka Kohki Corporation. The test results are as shown in Fig. 5. Even though an entire profile of deep holes (side surface is along the light path) cannot be achieved by the laser profilometer, the

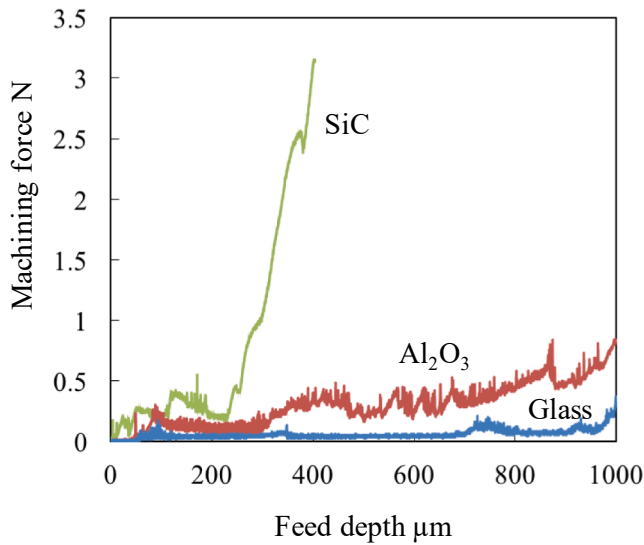


Fig. 6. Machining force.

hole depth can still be calculated from the distance between the original workpiece surface and the bottom surface. In this way, the measured machined hole depth was 996 µm, 914 µm, and 373 µm for glass, Al₂O₃, and SiC workpiece, respectively. The machining time was calculated by dividing the feed depth by the feed rate. A feed depth of 1 mm was finished when fabricating glass and Al₂O₃, while only 415 µm feed was completed for SiC. The feed rate was set as 1 µm/s for glass, 0.5 µm/s for both SiC and Al₂O₃ samples. Therefore, the average material removal rate was calculated and equal to 0.996 µm/s, 0.457 µm/s, and 0.449 µm/s decreasing in the order of glass, Al₂O₃, and SiC. With the increase of fracture toughness and hardness of workpiece materials, there is a reduction in the material removal rate. Note that the value for Al₂O₃ is far lower than its feed rate of 0.5 µm/s and only a little higher than the one for SiC, which results from the difficulty in machining deeper holes. Generally, the material removal rate decreases with the increase of hole depth due to the restriction of slurry movement [41,42].

3.2.2. Machining force and maximum feed rate

The machining force for drilling the above holes on the three materials is shown in Fig. 6. The force rapidly increases and reaches 3 N when fabricating SiC due to a lower real-time material removal rate than the tool feed rate. On the other hand, the forces of machining glass and Al₂O₃ plates were stable and lower than 3 N, which indicates that the material removal went on smoothly. Commonly, in order to obtain optimum machining performance, the feed rate should be set appropriately since too low chosen will not yield a maximum machining rate while too high one will cause a jamming between the tool and the abrasives. The jamming leads a decrease of material removal efficiency and finally increases the machining force.

Different tool feed rates were applied to fabricate the three materials and each experiment was repeated three times. The maximum feed depth under different feed rates for the three materials were listed in Table 5. The circle symbol means that the feed depth reaches the stop

machining condition of 1 mm before the machining force achieves 3 N. And the value listed in the table is the maximum feed depth when the machining force reaches 3 N. Blank in the table means no experiments were conducted. The results show that the tool feed rate can increase up to 6 µm/s within completing a 1 mm deep hole for glass, while up to 0.5 µm/s for Al₂O₃. In the case of SiC, the maximum feed depth can be 415 µm when the feed rate is 0.5 µm/s. The machining efficiency can be evaluated with the maximum feed rate, which decreases in the order of glass, Al₂O₃, and SiC.

3.2.3. Machining accuracy and surface quality

The cross-sections of machined holes were observed with a scanning electron microscope (model SU1510) developed by Hitachi Corporation. A hole with high form accuracy was observed on the glass plate, whose bottom is quite flat as same as the contour scanned by the laser profilometer in Fig. 5(a). The hole shape on an Al₂O₃ substrate is not as symmetrical as that of glass, which may result from local uneven abrasion of the tool. However, in the case of SiC, an obvious protrusion was formed in the middle of the bottom surface as same as the contour in Fig. 5(c). The material removal is commonly greater at the periphery of the work zone [4,43], whereas it is lower in the center because the abrasive renewal and debris removal are more difficult at the center zone [44–46]. The difference of the material removal rate then results in the initiation of the protrusion in the center area. In addition, abrasive particles in the gap may abrade the sloping machined surface due to oblique impact direction and consequently facilitate the formation of a large protrusion. The surface roughness of the machined surfaces was measured using the laser probe profilometer. The arithmetic average of absolute values (Ra) of the smoothest part on the bottom surface of the machined holes for SiC, Al₂O₃ and glass plate was 0.334 µm, 0.603 µm and 0.657 µm, respectively. Even though the form accuracy is lowest for SiC, fine surface was still obtained. The micro-USM presents a good surface finish for hard and brittle materials. From the magnification views of the bottom and the side surfaces as shown in Fig. 7, cracks remaining on the Al₂O₃ and glass plates were identified; however, no obvious cracks were found on the SiC substrate. These results are consistent with the simulation results that more and large cracks formed on glass workpiece due to continuous impact of abrasive particles and this will make sufficient material removal. The sufficient material removal ensures high material removal rate and machining accuracy. Conversely, if cracks propagated seriously in the depth direction, they may be not removed totally during machining process and may remain on the machined surfaces.

According to the simulation and experimental results, the cracks initiated close to the work surface and propagated into the surrounding material almost parallel to the surface such as the lateral crack finally induce large chipping of materials, which causes main material removal in micro-USM. On the other hand, cracks generated beneath the work surface and extended deep into the material such as the median crack may remain inside the material and ultimately lead to subsurface defects.

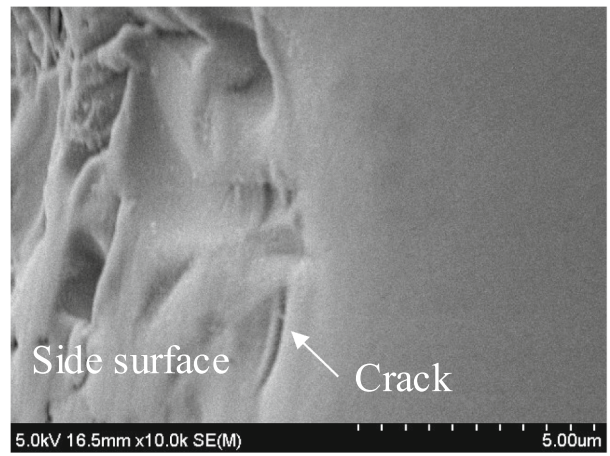
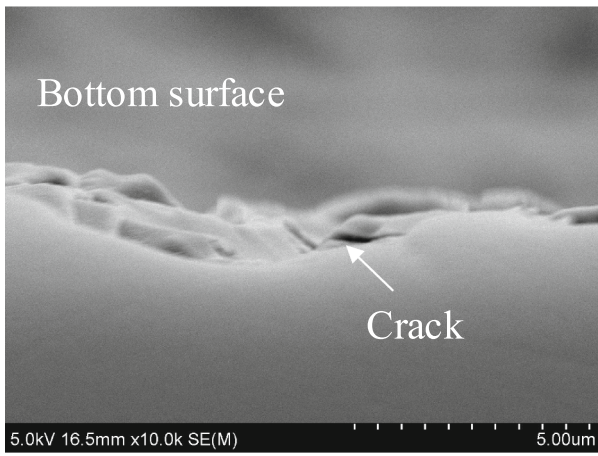
3.2.4. Tool wear rate

The tool wear rate was calculated as the ratio of reduction of the tool length along the longitudinal direction to the machined hole depth. To measure the change of tool length, a 60 µm square was firstly marked on

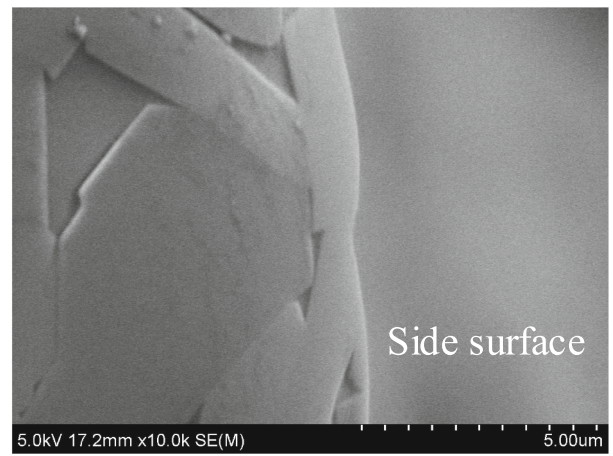
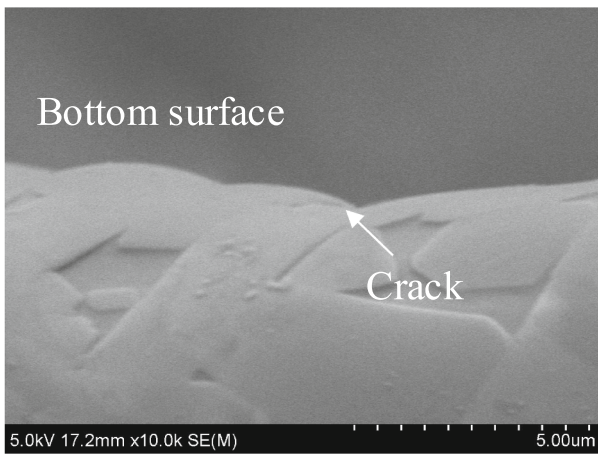
Table 5
Maximum feed depth under different feed rates for the three hard and brittle materials.

Work material	Feed rate (µm/s)										
	0.5	1	2	3	4	5	6	7	8	9	10
Glass	○	○	○	○	○	○	○	350	146	151	146
Al ₂ O ₃	○	516	106	111							
SiC	415	100	103								

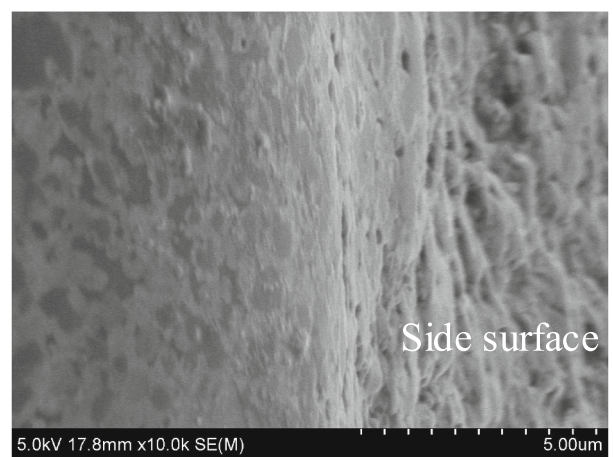
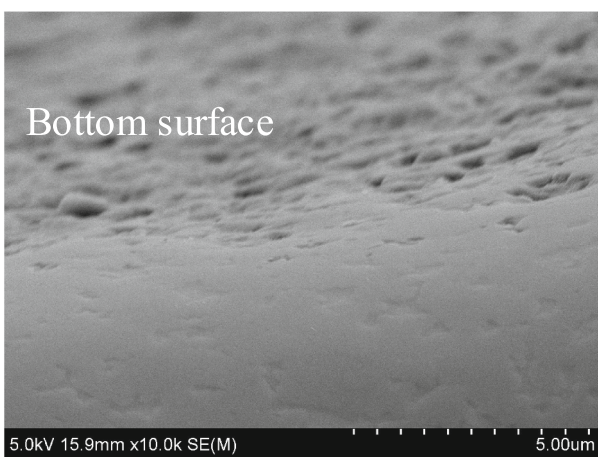
Unit: µm.



(a)



(b)



(c)

Fig. 7. Cross-sections of machined holes: (a) glass plate, (b) Al₂O₃ plate, (c) SiC plate.

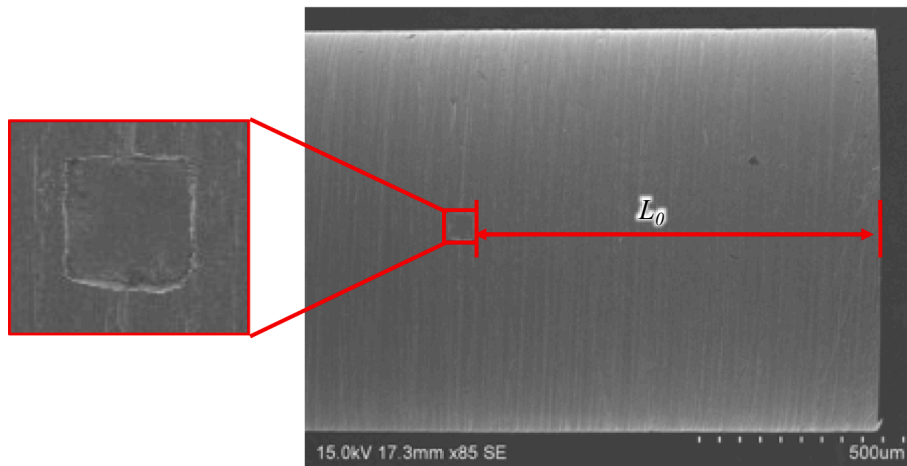


Fig. 8. Laser mark for tool length measurement.

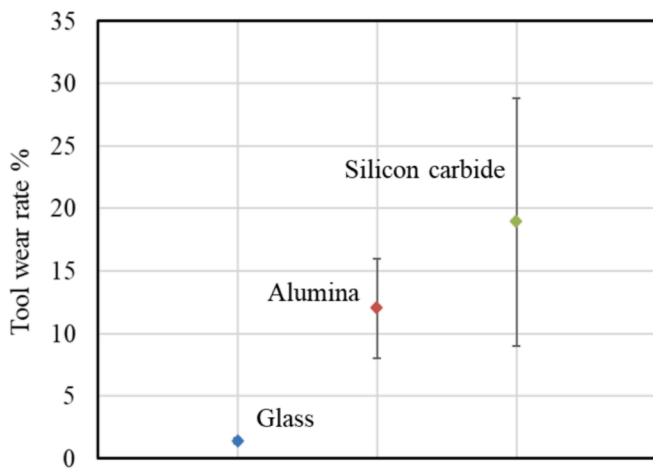


Fig. 9. Tool wear rate for different workpieces.

the tool as shown in Fig. 8 by an Nd:YAG laser (532 nm wavelength), and the length (L_0) from the mark to the tool tip was then measured with 0.1 μm resolution using the laser probe profilometer. Accordingly, the reduction of the tool length can be obtained by comparing L_0 before and after USM. The hole drilling experiments were carried out three times for each work material, and the feed rate was kept to 1 $\mu\text{m}/\text{s}$ for glass, and 0.5 $\mu\text{m}/\text{s}$ for both Al_2O_3 and SiC. The tool wear rate for different materials is summarized in Fig. 9. The test results demonstrated that the wear of tool increased in the order of glass, Al_2O_3 , and SiC. The deviation is also small when fabricating glass, which means the hole drilling process is stable.

Next, the tool geometry after USM was investigated. Fig. 10 presents the cross-sectional profile of the tool tip measured with the laser profilometer. Besides the length wear and corner wear, hole wear also occurred in the center of the tool tip when fabricating SiC plate. A concave shape was formed as shown in Fig. 10(c), which is opposite to the workpiece. A slight concavity was also found on the tool after machining Al_2O_3 plate in Fig. 10(b). In the narrow machining gap, the stagnation of debris occurs during micro-USM [44]. As the slurry flushing in the center zone of the hole is more difficult, debris accumulates intensively in the center zone, where the debris interacts with the tool causing the concavity in the center of the tool tip. The machining gap between the vibrated tool and the workpiece decreases due to the low material removal rate while fabricating SiC, where the piled debris density becomes higher inducing bigger concavity on the tool tip. However, the concavity formation was prevented when

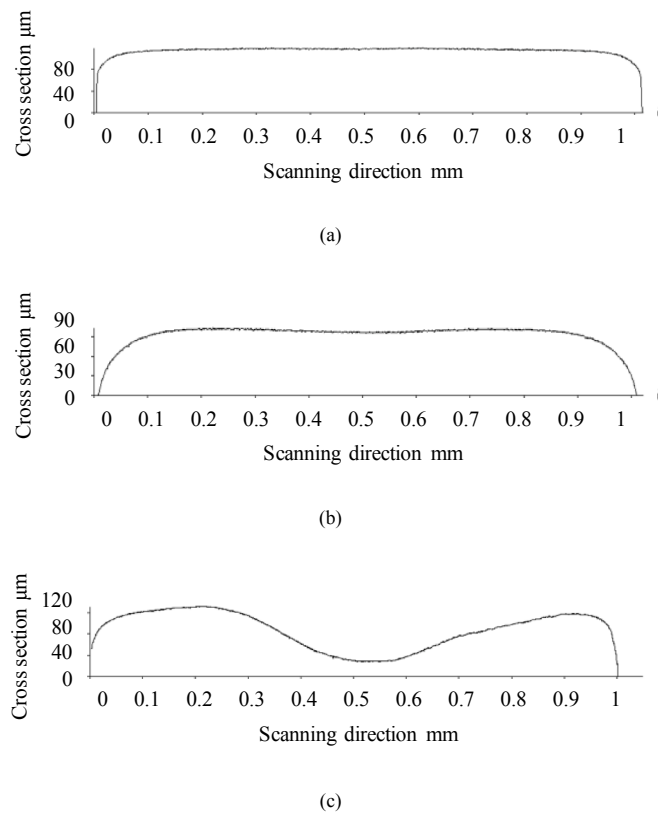


Fig. 10. Cross-sectional profiles of tool tip after micro-USM: (a) for fabrication of glass plate, (b) for fabrication of Al_2O_3 plate, (c) for fabrication of SiC plate.

fabricating glass plate in which effective debris flushing takes place thanks to the high material removal rate. In turn, better form accuracy can also be obtained on the work side as mentioned above.

4. Discussions

Above results and discussions indicate that the material removal in micro-USM is mainly determined by the crack generation of workpieces, fast and large cracking of the workpiece facilitate the material removal, and reduce the wear of abrasive particles and tools. Numerous cracks can lead to chip removal of materials and directly affects the material removal efficiency. On the other hand, cracks extended deep into the material may remain inside the material and ultimately lead to

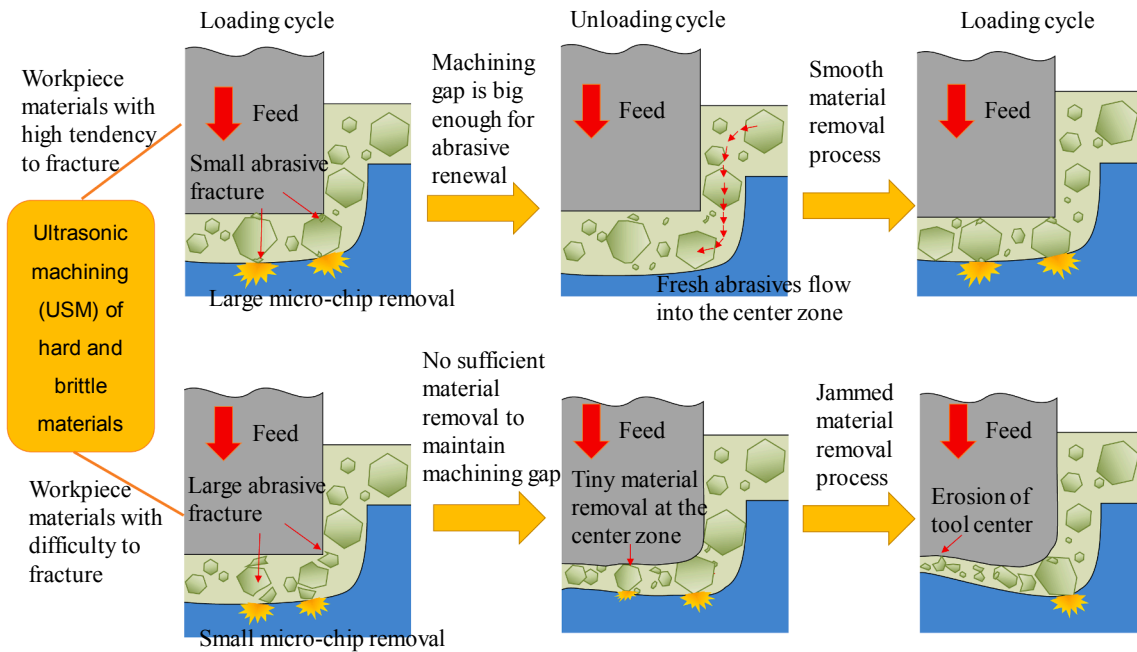


Fig. 11. Material removal process in micro-USM.

subsurface defects. Therefore, it is important to control the crack generation and propagation that ensures effective material removal and high surface quality.

In addition, in practical machining process, sufficient material removal is necessary to maintain a large machining gap for abrasive renewal and debris flushing, and ensures smooth material removal in entire machining zone. While fabricating materials with higher hardness and fracture toughness, cracking of workpiece is not enough to generate large chip removal and the abrasive particles in the machining zone fracture seriously. Therefore, the machining gap between the tool and work surface would be decreased with the on-going downward feed of machining. The narrower the machining gap becomes, the harder new abrasive particles flow into the center zone. The fractured particles in the narrow gap will gradually lose their cutting ability but abrade the tool material. The material removal process in micro-USM is schematically shown in Fig. 11. Larger crack generation in substrates and smaller wear of abrasive particles are helpful to maintain the machining gap and improve the machining efficiency. In this study, extremely hard abrasive was used to machine silicon carbide workpiece, even though the particle did not fracture seriously in the SPH calculation, we should know that the abrasive particle will be finally worn under constant impact action and the material removal process will become jammed due to slow and tiny cracking of silicon carbide.

5. Conclusions

The machining capabilities of micro-USM for hard and brittle materials were investigated in this study with both SPH simulations and blind hole fabrication experiments. The cracking process of workpiece, the wear of abrasive, and deformation of tool were visually demonstrated by the simulation models. The material removal rate, machining force, form accuracy, surface roughness, surface damage, tool wear rate and tool geometry when fabricating glass, alumina, and silicon carbide were compared. The following conclusions can be drawn:

Cracks remaining on the machined surfaces after micro-USM were identified. The cracks are formed during the machining process, and have a close relation to the material removal mechanism in USM.

The material removal rate decreased in the order of glass, Al_2O_3 and SiC. With the increase of fracture toughness and hardness, crack

generation becomes difficult and there is a reduction in the material removal rate. It can be well demonstrated by the simulation results that cracking of glass is faster and larger compared to the other materials.

The tool wear rate drops significantly when fabricating glass. Formation of concavities on the tool tip was prevented because fast and large cracking process of glass and effective abrasive renewal under a big machining gap. In turn, better form accuracy was also obtained on the glass workpiece.

In order to improve the processing capability of micro-USM for hard and brittle materials, we need find ways increasing the speed and degree of cracking process for effective material removal while reducing the tendency of cracks to extend deep into the work materials. Methods including heat treatment and chemical immersion can be tried in the future study.

Funding

This work is supported by the National Natural Science Foundation of China, China [Grant no. 51805067], China Postdoctoral Science Foundation, China [Grant no. 2019M651093], Fundamental Research Funds for the Central Universities of China, China [Grant no. 3132019193] and [Grant no. 3132019330].

Declaration of competing interests

The author(s) declared no potential conflicts of interest with respect to the research, authorship, and/or publication of this article.

Acknowledgements

The authors gratefully acknowledge the support from Professor Tsunemoto Kuriyagawa, Associate Professor Masayoshi Mizutani at Tohoku University for their kind suggestions of our research work. The authors would also like to thank Taga Electric Corporation in Japan with respect to the manufacture of USM tool used in the experiments.

References

- [1] Abbas NM, Solomon DG, Bahari MF. A review on current research trends in electrical discharge machining (EDM). *Int J Mach Tool Manufact* 2007;47(7–8): 1214–28.
- [2] Dubey AK, Yadava V. Laser beam machining—a review. *Int J Mach Tool Manufact* 2008;48(6):609–28.
- [3] Saxena KK, Qian J, Reynaerts D. A review on process capabilities of electrochemical micromachining and its hybrid variants. *Int J Mach Tool Manufact* 2018;127:28–56.
- [4] Thoe TB, Aspinwall DK, Wise MLH. Review on ultrasonic machining. *Int J Mach Tool Manufact* 1998;38(4):239–55.
- [5] Zhang C, Rentsch R, Brinksmeier E. Advances in micro ultrasonic assisted lapping of microstructures in hard–brittle materials: a brief review and outlook. *Int J Mach Tool Manufact* 2005;45(7–8):881–90.
- [6] Markov IA. In machining of intractable materials with ultrasonic and sonic vibrations. Iliffe Books; 1966.
- [7] Klocke F, Dambon O, Capudi Filho GG. Influence of the polishing process on the near-surface zone of hardened and unhardened steel. *Wear* 2005;258:1794–803.
- [8] Dam H, Quist P, Schreiber MP. Productivity, surface quality and tolerances in ultrasonic machining of ceramics. *J Mater Process Technol* 1995;51:358–68.
- [9] Komaraiah M, Reddy PN. A study on the influence of workpiece properties in ultrasonic machining. *Int J Mach Tool Manufact* 1993;495–505.
- [10] Tanaka M, Shiina T. Micro crack analysis of optical fiber by specialized TD-OCT. *Optic Laser Technol* 2019;116:22–5.
- [11] Deng J, Lee T. Ultrasonic machining of alumina-based ceramic composites. *J Eur Ceram Soc* 2002;22:1235–41.
- [12] Langan SM, Deepak R, Mann AB. Mitigation of damage during surface finishing of sapphire using laser-assisted machining. *Precis Eng* 2019;56:1–7.
- [13] Liu GR, Liu MB. In smoothed particle hydrodynamics: a meshfree particle method. World Scientific Publishing; 2003.
- [14] Liu MB, Liu GR. Smoothed particle hydrodynamics (SPH): an overview and recent developments. *Arch Comput Methods Eng* 2010;17:25–76.
- [15] Liu MB, Liu GR, Lam KY, Zong Z. Meshfree particle simulation of the detonation process for high explosives in shaped charge unlined cavity configurations. *Shock Waves* 2003;12:509–20.
- [16] Swegle JW, Attaway SW, Heinstein MW, Mello FJ, Hicks DL. In an analysis of smoothed particle hydrodynamics. Albuquerque, NM (United States): Sandia National Labs.; 1994.
- [17] Hayhurst CJ, Clegg RA. Cylindrically symmetric SPH simulations of hypervelocity impacts on thin plates. *Int J Impact Eng* 1997;20(1–5):337–48.
- [18] Hayhurst CJ, Livingstone IH, Clegg RA, Fairlie GE. Numerical simulation of hypervelocity impacts on aluminum and Nextel/Kevlar Whipple shields. In: *Hypervelocity Shielding Workshop*; 1998.
- [19] Hiermaier S, Schäfer F. Hypervelocity impact fragment clouds in high pressure gas numerical and experimental investigations. *Int J Impact Eng* 1999;23:391–400.
- [20] Bonet J, Kulasegaram S. Correction and stabilization of smooth particle hydrodynamics methods with applications in metal forming simulations. *Int J Numer Methods Eng* 2000;47:1189–214.
- [21] Wang FY, Yang ZG. A coupled finite element and meshfree analysis of erosive wear. *Tribol Int* 2009;42:373–7.
- [22] Miwa K, Beppu M, Itoh M, Katayama M, Ohno T. A numerical simulation of the local damage on concrete plate subjected to impacted by different nose shape projectile. *Proceedings of the Symposium on Impact Problems in Civil Engineering* 2008;9(43):235–40 (in Japanese).
- [23] Clegg RA, Sheridan J, Hayhurst CJ, Francis NJ. The application of SPH techniques in AUTODYN-2D to kinetic energy penetrator impacts on multi-layered soil and concrete targets. In: *8th International symposium on interaction of the effects of munitions with structures*; 1997.
- [24] Wang J, Shimada K, Mizutani M, Kuriyagawa T. Material removal during ultrasonic machining using smoothed particle hydrodynamics. *Int J Autom Technol* 2013;7(6):614–20.
- [25] Wang J, Shimada K, Mizutani M, Kuriyagawa T. Tool wear mechanism and its relation to material removal in ultrasonic machining. *Wear* 2018;394:96–108.
- [26] In AUTODYN: theory manual. Century Dynamics; 2005.
- [27] Cronin DS, Bui K, Kaufmann C, McIntosh G, Berstad T. Implementation and validation of the Johnson-Holmquist ceramic material model in LS-Dyna. In: *The 4th European LS-DYNA users conference*; 2003.
- [28] Johnson GR, Holmquist J. A computational constitutive model for brittle materials subjected to large strains, high strain rates and high pressures. In: *Shock-wave and high-strain-rate phenomena in materials*. Marcel Dekker; 1992. p. 1075–81.
- [29] Johnson GR, Holmquist TJ. An improved computational constitutive model for brittle materials. *High-Pressure Science and Technology*. 1994. p. 981–4.
- [30] Segletes SB. In an analysis on the stability of the Mie-Grüneisen equation of state for describing the behavior of shock-loaded materials. U.S. Army Laboratory Command; 1991.
- [31] Steinberg DJ, Cochran SG, Guinan MW. A constitutive model for metals applicable at high-strain rate. *J Appl Phys* 1980;51(3).
- [32] Holmquist TJ, Johnson GR, Grady DE, Lopatin CM, Hertel Jr ES. High strain rate properties and constitutive modeling of glass. In: *Proceeding of the 15th International Symposium on Ballistics*. 237; 1995.
- [33] In AUTODYN: material model libraries. 2005.
- [34] Holmquist TJ, Johnson GR. Response of silicon carbide to high velocity impact. *J Appl Phys* 2002;91(9).
- [35] Anderson CE, Johnson GR, Holmquist TJ. Ballistic experiment and computations of confined 99.5% Al₂O₃ ceramic tiles. In: *Proceeding of the 15th International Symposium on Ballistics*. 65; 1995.
- [36] Westerling L, Lundberg P, Lundberg B. Tungsten long-rod penetration into confined cylinders of boron carbide at and above ordnance velocities. *Int J Impact Eng* 2001;25:703–14.
- [37] Steinberg DJ. In equation of state and strength properties of selected materials. Lawrence Livermore National Laboratories; 1996.
- [38] Wang J, Shimada K, Mizutani M, Kuriyagawa T. Effects of abrasive material and particle shape on machining performance in micro ultrasonic machining. *Precis Eng* 2018;51:373–87.
- [39] Lawn BR, Fuller ER. Equilibrium penny-like cracks in indentation fracture. *J Mater Sci* 1975;10:2016–24.
- [40] Cook RF, Pharr GM. Direct observation and analysis of indentation cracking in glasses and ceramics. *J Am Ceram Soc* 1990;73:787–817.
- [41] Singal RK, Singal R, Singal M. Nonconventional machining processes. In: *Fundamental of machining and machine tools*. I. K. International Publishing House; 2008. p. 151–7.
- [42] Guzzo PL, Shinohara AH, Raslan AA. A comparative study on ultrasonic machining of hard and brittle materials. *J Braz Soc Mech Sci Eng* 2004;26(1):56–61.
- [43] Singh R, Khamba JS. Ultrasonic machining of titanium and its alloys: a review. *J Mater Process Technol* 2006;173(2):125–35.
- [44] Yu Z, Hu X, Rajurkar KP. Influence of debris accumulation on material removal and surface roughness in micro ultrasonic machining of silicon. *CIRP Ann - Manuf Technol* 2006;55(1):201–4.
- [45] Saito O, Kuriyagawa T, Syoji K. Protrusion appearance and abrasive motion between tool-workpiece interface in ultrasonic die sinking-studies on the mechanism of ultrasonic machining (2nd report). *J Jpn Soc Abras Technol (JSAT)* 2000;44(4):25–30 (in Japanese).
- [46] Saito O, Syoji K, Kuriyagawa T. Stagnancy of machining process in ultrasonic die sinking-studies on ultrasonic machining (1st report). *J Jpn Soc Abras Technol (JSAT)* 1998;42(12):34–9 (in Japanese).

Paper:

Ultrasonic-Assisted Face Milling for Fabricating Hierarchical Microstructures

Keita Shimada^{*,†}, Ziqi Chen^{*}, Masayoshi Mizutani^{*}, and Tsunemoto Kuriyagawa^{**}

^{*}Graduate School of Engineering, Tohoku University
6-6-01 Aoba, Aramaki, Aoba-ku, Sendai, Miyagi 980-8579, Japan

[†]Corresponding author, E-mail: keita.shimada.c6@tohoku.ac.jp

^{**}Graduate School of Biomedical Engineering, Tohoku University, Sendai, Japan

[Received August 19, 2019; accepted December 12, 2019]

Surface microstructures can provide various functionalities, and wettability is a typical surface property that can be controlled by the surface textures. This study attempted to fabricate hierarchical microstructures through ultrasonic-assisted face milling (UAFM) to change the surface functionality by specifically focusing on the wettability. The fabrication involved the use of an ultrasonic generating spindle and a self-designed diamond tool. The locus of the tip of the diamond tool was computed based on the equation of motion, and the micro- and macrostructures are illustrated in this paper. The structures were confirmed through observations using a white-light interferometer. The wettability on six zones of the processed area was measured, and the results indicated that the central zone of the UAFM surface became hydrophobic, whereas the edge zone became hydrophilic.

Keywords: ultrasonic cutting, functional surfaces, wetting, surface finishing

1. Introduction

Surface microstructures can provide various functionalities, such as friction reduction, antireflection, and structural colors, to materials [1–3]. Wetting is also a typical and important surface phenomenon, which is affected by the surface microstructures as well as surface chemical properties [4, 5]. Some organisms naturally possess microstructures to gain such functionalities, and the research to artificially imitate their structures to obtain their excellent functions is termed “biomimetics” [6–15]. Lotus leaves exhibit ultrahydrophobicity due to both their hierarchical double (micro/nanometer-scaled) structure and the covering waxes. The ultrahydrophobicity confers self-cleaning properties [8, 9]; therefore, the properties are referred to as the lotus effect, and much research has been conducted to artificially fabricate the structures [8–10]. The wings of a butterfly (*Morpho aega*) have lamellar-stacked nanometer-sized tips that allow not only waterproof surfaces but unidirectional sliding, therefore allowing their bodies to avoid wetting [14]. Zheng et al. [14]

explained this unidirectional sliding phenomenon through the pinning and rolling states of the droplets caused by the micro- and nanostructures; they pointed out that the unidirectional wetting properties have the potential to be applied on various smart fluid-controllable interfaces. Chu et al. [15] and Malvadkar et al. [16] artificially fabricated microstructures via selective chemical patterning and bottom-up vapor-phase technique, respectively, and confirmed unidirectional wetting properties. Additionally, Extrand [17, 18] stated that the unidirectional wetting in the capillary tube with asymmetric surface structures was generated by the difference of retention forces between both directions. These biomimetically inspired structures are mainly fabricated using process based on micro-electromechanical systems (MEMS), such as photolithography patterning [11], nanoimprint [12], and electron beam lithography; however, it is not impossible to create them mechanically. The mechanical material-removal processes, such as cutting, grinding, and polishing, have advantages such as a variety of workpiece materials, low processing cost, and high productivity. Asakura and Yan [19] reported that the surface with V-shaped microgrooves, cut by a diamond tool, could increase the contact angle twice as much as a flat surface.

Ultrasonic-assisted cutting (UAC) is a well-known method to reduce the cutting force and improve the quality of surface finish [20, 21]. This method leaves characteristic cutting marks due to the machining conditions including the vibration frequency, amplitude, and feed rate. Such micrometer-scaled cutting marks are usually regarded as undesirable roughness; however, in the current study, they have been utilized proactively to shape the above-mentioned microstructures [22–25]. Previous studies have reported on the UAC of side milling, while in this study, we tried to fabricate hierarchical microstructures through ultrasonic-assisted face milling (UAFM) and clarify the effect of the structures on the wettability. A single-pass UAFM was performed to obtain hierarchical microstructures by adjusting the combination of the relative motions including those of the feed, rotation, and ultrasonic vibration. The differences between the central and side areas within the single-pass were then verified through a contact-angle meter.

Nomenclature

Symbol	Description [Dimension]
a	Amplitude of the ultrasonic vibration [L]
f_r	Rotational frequency [T^{-1}]
f_u	Ultrasonic vibration frequency [T^{-1}]
l_{fr}	Spatial interval of the structure caused by feed and rotation [L]
l_{ru}	Spatial interval of the structure caused by rotation and ultrasonic vibration [L]
r	Rotational radius [L]
t	Time [T]
v_f	Feed rate [$L T^{-1}$]
α	Rake angle
β	Clearance angle
θ	Front tool angle of V-shaped tool

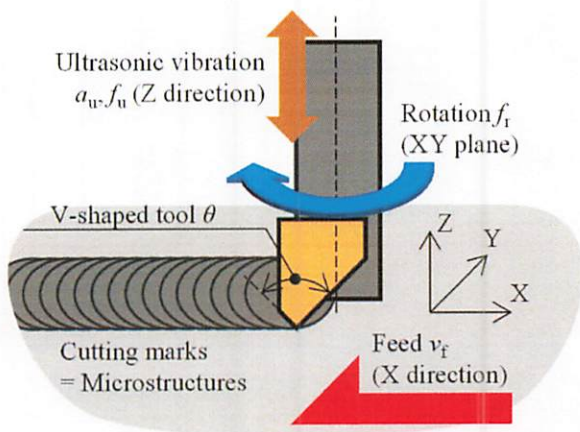


Fig. 1. Schematic of ultrasonic-assisted face milling (symbols refer to Nomenclature).

2. Ultrasonic-Assisted Face Milling

2.1. Expected Cutting Locus and Structures

Figure 1 shows a schematic of the UAFM used in this study. The workpiece feed was along the X direction and the diamond tool rotated around the Z direction; thus, the tip of the tool would ideally run within the X–Y plane when an ultrasonic vibration was not applied. The ultrasonic vibration was applied to the diamond tool along the Z direction. The locus of the tip of the tool (here, let the position be (x, y, z)) can be expressed using the machining parameters as

$$\begin{Bmatrix} x \\ y \\ z \end{Bmatrix} = \begin{Bmatrix} r \cos(2\pi f_r t) + v_f t \\ r \sin(2\pi f_r t) \\ a \sin(2\pi f_u t) \end{Bmatrix} \dots \dots \dots (1)$$

It is notable that the initial phases of the rotation and vibration are omitted and the initial position is $(r, 0, 0)$. Fig. 2 illustrates the locus of the tip point of a tool and shows the estimation of the microstructures by us-

ing Eq. (1). The microstructure in Fig. 2(a) was computed using Microsoft Excel 2013, those in Figs. 2(b) and (c) were obtained using GNU Octave version 4.4.1. Fig. 2(c) was drawn as a remaining shape after removing the part at which the rake face passes. Each small element of the trochoid curve shown in Fig. 2(a) is composed of a three-dimensional sinusoidal curve, as shown in Fig. 2(b). Therefore, the microripples are expected to remain on the macroscopic structure (hereinafter, the structure is referred to as “macrostructure”), as shown in Fig. 2(c). Spatial intervals of these macro- and microstructures (l_{fr} and l_{ru}) were determined by the combinations of (i) the feed and rotation, and (ii) the rotation and ultrasonic vibration, respectively, and are expressed as

$$l_{fr} = \frac{v_f}{f_r}, \dots \dots \dots (2)$$

$$l_{ru} = \frac{2\pi r f_r}{f_u} \dots \dots \dots (3)$$

They are indicated in Fig. 2(c). Additionally, the macrostructures of the side and central zones are pyramid- and groove-like, respectively, and thus the wettability was expected to be different in each zone.

2.2. Experimental Setup

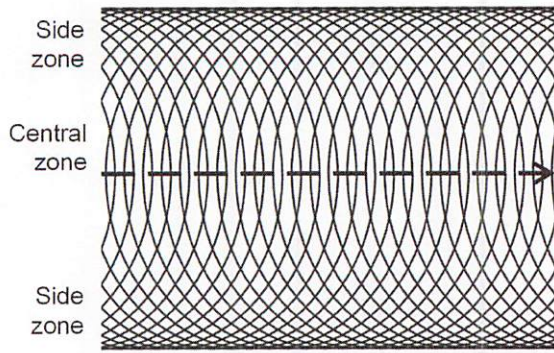
The UAFM was performed using a three-directional ultrasonic generating spindle (SC-45 SP-H24, Taga Electric Co., Ltd.) that was mounted on the X- and Z-axes slider on a four-axis desktop CNC machining table (Trider-X, Nexsys Corp.). The contact of the tool to workpiece was detected using a dynamometer (Type 9256A, Kistler Instrument Corp.) placed beneath the workpiece jig. The workpiece material was electroless nickel-phosphorous (Ni-P) plating that is employed as a molding die material. The thickness of the plating was 100–150 μm and the base material was stainless steel (JIS SUS430). Fig. 3 depicts the experimental setup and motion directions.

Figure 4 illustrates the design dimension of the diamond tool and shows the tool tip. The whole shape was designed to resonate with the supplied ultrasonic vibration. The front angle of the V-shaped tool was 90° , and the tip was rounded with a 20.0- μm radius to prevent breakage caused by the impact of ultrasonic vibration.

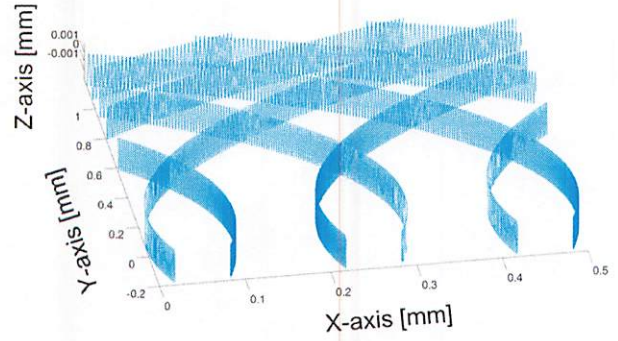
3. Experiment and Results

3.1. Observation of the Fabricated Structures

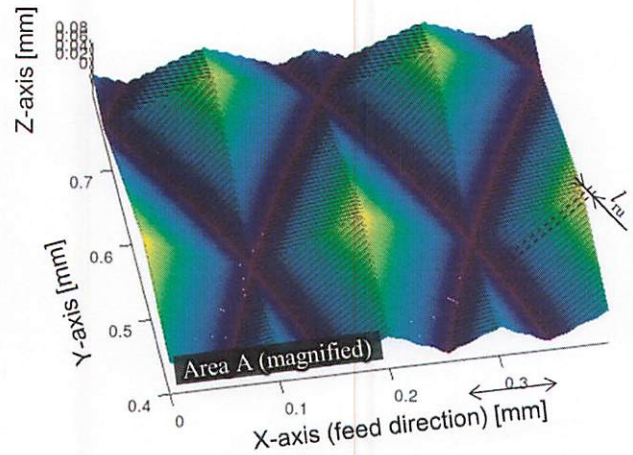
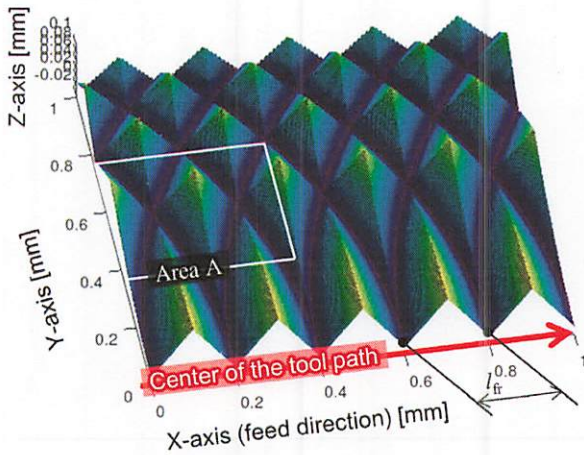
Table 1 lists the details of the UAFM experiment. The Ni-P workpiece was preliminarily flattened with a 3-mm-radius diamond tool under the conditions of 10- μm -deep, 20- μm -pitch, and 10000-mm/min planer cutting. Its theoretical roughness was 25 nm. The combination of the feed speed and rotational frequency was set at (a) 40 mm/min and 1000 min^{-1} , and (b) 20 mm/min and 500 min^{-1} . Therefore, the expected structural intervals were $l_{fr} = 40 \mu\text{m}$ in both conditions, and $l_{ru} =$ (a) 6.3 μm and (b) 3.1 μm , which can be obtained through



(a) Overview on the X-Y plane



(b) Three-dimensional locus of the tip of the tool



(c) Expected microstructures on the macroscopic structures (left: overview, right: magnified)

Fig. 2. Calculated cutting locus and microstructure (calculation conditions: $a = 1.8 \mu\text{m}$, $f_r = 1000 \text{ min}^{-1}$, $f_u = 25 \text{ kHz}$, $r = 1.5 \text{ mm}$, $v_f = 200 \text{ mm/min}$, $\alpha = 90^\circ$, and $\theta = 90^\circ$).

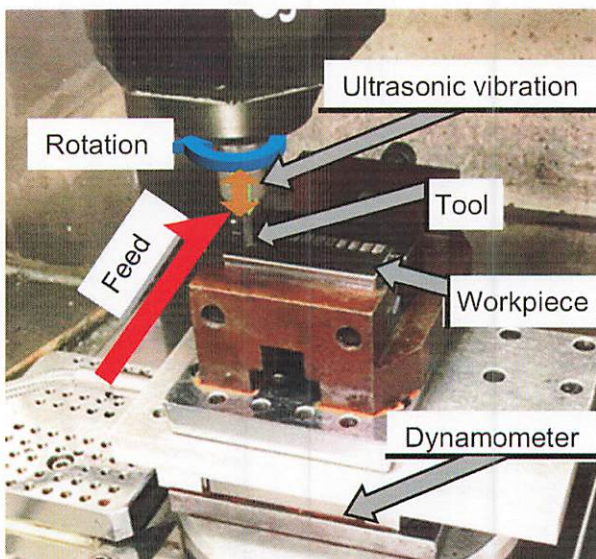


Fig. 3. Experimental setup.

Eqs. (2) and (3). Note that the face milling without ultrasonic vibration could not fabricate even the structure illustrated in **Fig. 1** because the cut marks of the forward cutting were destroyed by those of the backward cutting.

Figure 5 shows the microphotographs of the surfaces machined through UAFM on the central and side zones, which were observed through a white-light interferometer (Talysurf®CCI, Taylor Hobson, Ametek, Inc.). As expected, the macrostructures were groove- and pyramid-like in the central and side zones, respectively, with intervals of around $40 \mu\text{m}$ in both (a) and (b). The microstructures were also formed similar to the expectation; the lower rotational frequency could achieve finer microstructures.

3.2. Change of Wettability

A contact-angle meter (DM-501, Kyowa Interface Science Co. Ltd.) was employed to evaluate the wettability. In the measurement trial, a purified water droplet of $0.7 \mu\text{L}$ was placed on the UAFM surface and the tangent method was used to calculate the contact angle. The machined surface was separated into six sections, numbered from the center to the edge, as shown in **Fig. 6**,

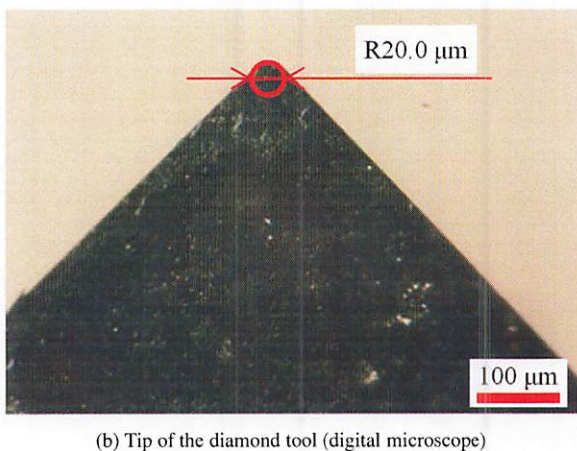
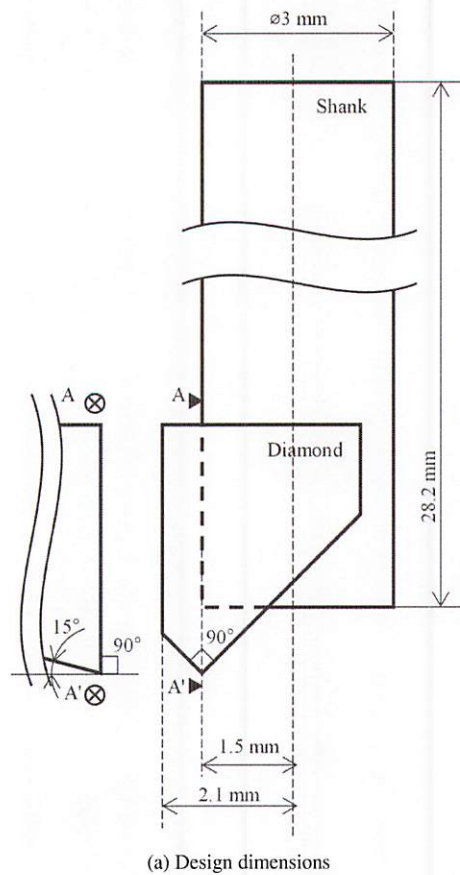


Fig. 4. Design and picture of the diamond tool.

and the contact angle of each section was measured three times and the results are shown in **Fig. 7**.

The contact angle of the flat surface was 48.5° . The zones of positions 1–5 indicate a certain degree of hydrophobicity, and this was maximized in positions 3 and 4. It seems that both the groove- and pyramid-like macrostructures may influence the wettability change. By focusing on the microstructures, no significant difference was observed in the wettability at positions 1–4; in contrast, the structures have certain effects at positions 5 and 6. The density of the macroscopic structure maxi-

Table 1. Conditions of UAFM.

Workpiece material	Ni-P
Feed speed	20 and 40 mm/min
Rotational frequency	500 and 1000 min^{-1}
Cutting depth	8 μm
Vibration mode	Longitudinal vibration
Vibration frequency	25 ± 3 kHz
Vibration amplitude	1.8 μm
Cutting lubricant	Kurecut (soluble type)

mized around positions 5 and 6. Additionally, in condition (a), denser microstructures were fabricated than that in condition (b); however, condition (b) brought more difference on wettability from the result of the flat surface. These results may indicate that a certain macrostructural density is required for the microstructures to affect the surface, and there may be an optimized value of the microstructures. It is notable that the wettability turned to hydrophilicity at position 6, which may cause no pyramid microtexture to be formed because the excessive cut density may destroy the macrostructures. However, the ultrasonic vibration can generate a small and protruding microtexture on those zones, which may bring certain hydrophilicity to the surface, and the interval may affect the wettability.

4. Conclusions

This study tried to fabricate hierarchical microstructures by using UAFM with single-pass processing. The fabricated structures were then observed and their wettability was evaluated. The following conclusions can be drawn from the results.

1. The UAFM can fabricate hierarchical microstructures by using a diamond tool.
2. The structure to be fabricated can be expected with the calculation of the tool tip motion.
3. The structural features can be partly controlled by modulating the cutting parameters including the spatial intervals of the macro- and microstructures.
4. The hierarchical structures can increase the contact angles in the middle zones, and the edge zone indicated hydrophilicity.

Acknowledgements

This work was supported by JSPS KAKENHI Grant Number JP18K13666.

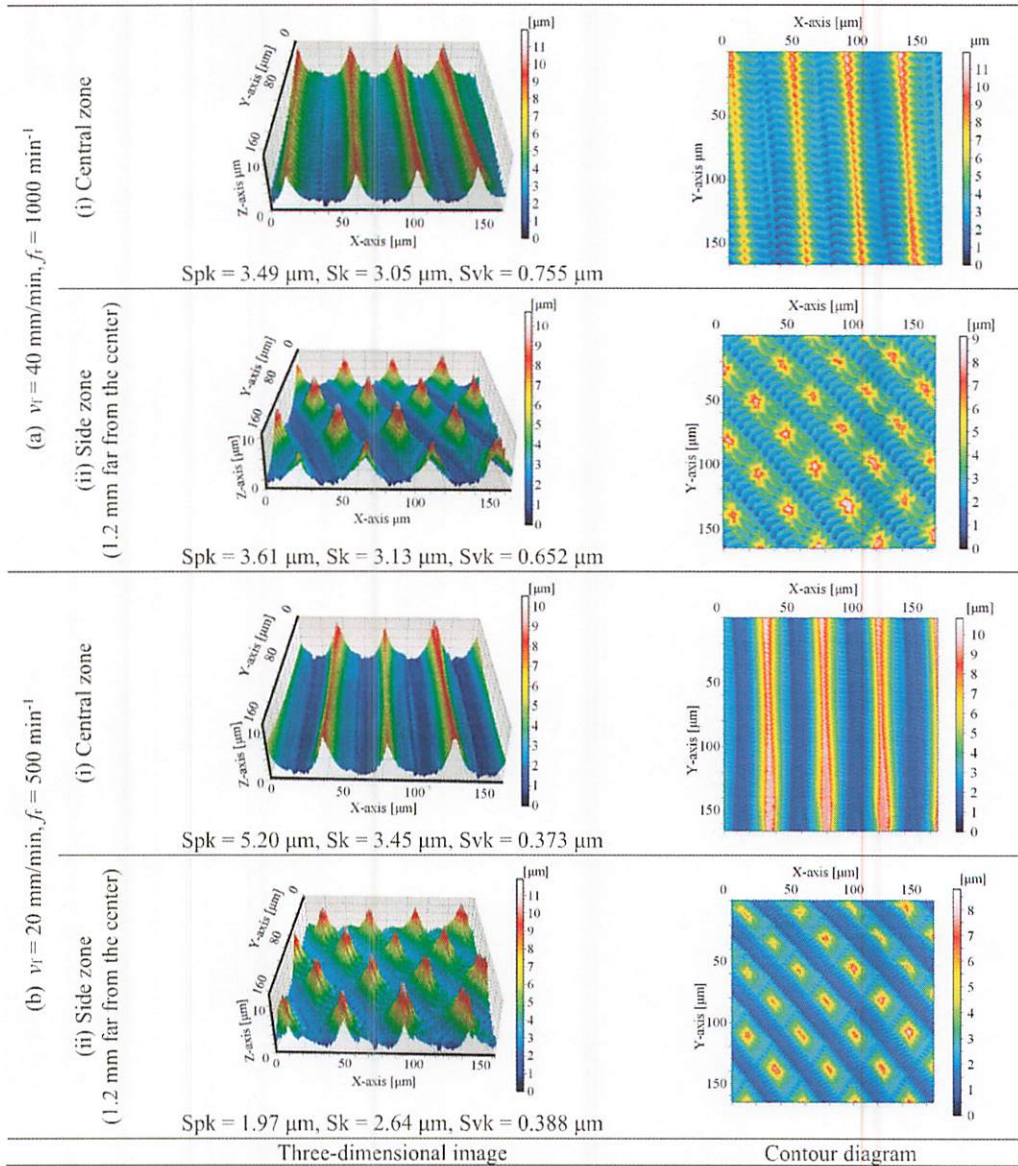


Fig. 5. Topographies of the surfaces machined by UAFM.

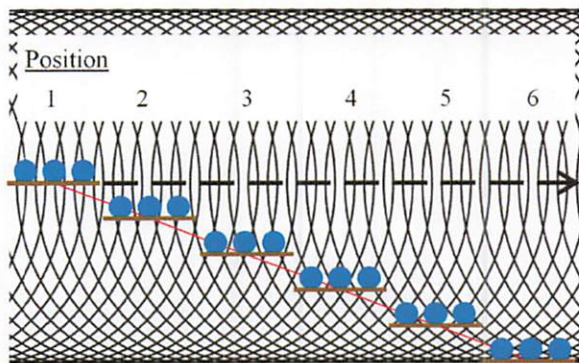


Fig. 6. Positions where the contact angles were measured.

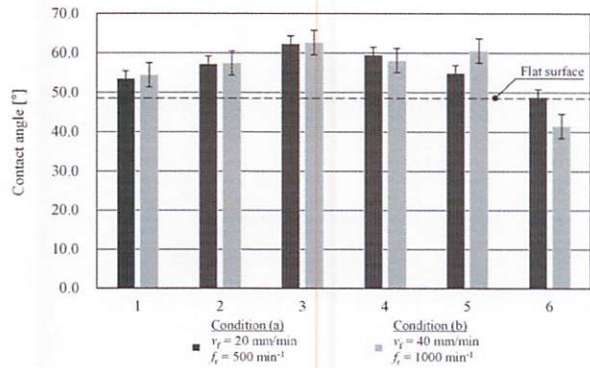


Fig. 7. Contact angles of the UAFM surfaces.

References:

- [1] C. J. Evans and J. B. Bryan, "'Structured,' 'Textured' or 'Engineered' Surfaces," *CIRP Annals – Manuf. Tech.*, Vol.48, Issue 2, pp. 541-556, 1999.
- [2] A. A. G. Bruzzone, H. L. Costa, P. M. Lonardo, and D. A. Lucca, "Advances in engineered surfaces for functional performance," *CIRP Annals – Manuf. Tech.*, Vol.57, pp. 750-769, 2008.
- [3] L. De Chiffrel, H. Kunzmann, G. N. Peggs, and D. A. Lucca, "Surfaces in Precision Engineering, Microengineering and Nanotechnology," *CIRP Annals – Manuf. Tech.*, Vol.52, Issue 2, pp. 561-577, 2003.
- [4] R. N. Wenzel, "Resistance of solid surfaces to wetting by water," *Ind. Eng. Chem.*, Vol.28, No.8, pp. 988-994, 1936.
- [5] A. B. D. Cassie and S. Baxter, "Wettability of porous surfaces," *Trans. Farad. Soc.*, Vol.40, pp. 546-551, 1944.
- [6] N. Moronuki, "Surface functions considered from microstructures," *Morikita Publishing*, 2011 (in Japanese).
- [7] M. Shimomura, "New trend of next generation biomimetic material technology learning from biodiversity," *Sci. & Tech. Trends*, Vol.110, pp. 9-28, 2010 (in Japanese).
- [8] T. Darmanin and F. Guittard, "Superhydrophobic and superoleophobic properties in nature," *Materials Today*, Vol.18, Issue 5, pp. 273-285, 2015.
- [9] Q. Xu, W. Zhang, C. Dong, T. Sreeprasad, and Z. Xia, "Biomimetic self-cleaning surfaces: Synthesis, mechanism and applications," *J. R. Soc. Interface*, Vol.13, Issue 122, 2016.
- [10] M. Zhang, S. Feng, L. Wang, and Y. Zheng, "Lotus effect in wetting and self-cleaning," *Biotribology*, Vol.5, pp. 31-43, 2016.
- [11] D. J. T. Kyle, A. Oikonomou, E. Hill, A. Vijayaraghaven, and A. Bayat, "Fabrication and modelling of fractal, biomimetic, micro and nano-topographical surfaces," *Bioinspir. Biomim.*, Vol.11, No.4, 046009, 2016.
- [12] J. Sun, X. Wang, J. Wu, C. Jiang, J. Shen, M. A. Cooper, X. Zheng, Y. Liu, Z. Yang, and D. Wu, "Biomimetic Moth-eye Nanofabrication: Enhanced Antireflection with Superior Self-cleaning Characteristic," *Sci. Rep.*, Vol.8, 5438, 2018.
- [13] M. I. Kayes, A. J. Galante, N. A. Stella, S. Haghanifar, R. M. Q. Shanks, and P. W. Leu, "Stable lotus leaf-inspired hierarchical, fluorinated polypropylene surfaces for reduced bacterial adhesion," *Reactive and Functional Polymers*, Vol.128, pp. 40-46, 2018.
- [14] Y. Zheng, X. Gao, and L. Jiang, "Directional adhesion of superhydrophobic butterfly wings," *Soft Matter*, Vol.3, pp. 178-182, 2007.
- [15] K. Chu, R. Xiao, and E. N. Wang, "Uni-directional liquid spreading on asymmetric nanostructured surfaces," *Nat. Mater.*, Vol.9, pp. 413-417, 2010.
- [16] N. A. Malvadkar, M. J. Hancock, K. Sekeroglu, W. J. Dressick, and M. C. Demirel, "An engineered anisotropic nanofilm with unidirectional wetting properties," *Nat. Mater.*, Vol.9, pp. 1023-1028, 2010.
- [17] C. W. Extrand, "Retention Forces of a Liquid Slug in a Rough Capillary Tube with Symmetric or Asymmetric Features," *Langmuir*, Vol.23, pp. 1867-1871, 2007.
- [18] C. W. Extrand, "Origins of Wetting," *Langmuir*, Vol.32, Issue 31, pp. 7697-7706, 2016.
- [19] K. Asakura and J. Yan, "Water Repellency Control of Oxygen-Free Copper Surface by Diamond-Cut Micro Grooves," *Int. J. Automation Technol.*, Vol.6, No.4, pp. 396-402, 2015.
- [20] J. Kumabe and M. Masuko, "Study on the ultrasonic cutting (1st report)," *Trans. JSME*, Vol.24, Issue 138, pp. 109-114, 1958 (in Japanese).
- [21] E. Shamoto and N. Suzuki, "Ultrasonic vibration diamond cutting and ultrasonic elliptical vibration cutting," *Compr. Mater. Process*, Vol.11, pp. 405-454, 2014.
- [22] S. Xu, K. Shimada, M. Mizutani, and T. Kuriyagawa, "Fabrication of hybrid micro/nano-textured surfaces using rotary ultrasonic machining with one-point diamond tool," *Int. J. Mach. Tools. Manuf.*, Vol.86, pp. 12-17, 2014.
- [23] S. Xu, C. Nishikawa, K. Shimada, M. Mizutani, and T. Kuriyagawa, "Surface Textures Fabrication on Zirconia Ceramics by 3D Ultrasonic Vibration Assisted Slant Feed Grinding," *Adv. Mater. Res.*, Vol.797, pp. 326-331, 2013.
- [24] K. Shimada, T. Hirai, M. Mizutani, and T. Kuriyagawa, "Fabrication of functional surface by ultrasonic-assisted cutting," *J. Jpn. Soc. Abras. Technol.*, Vol.62, No.1 pp. 39-44, 2018 (in Japanese).
- [25] K. Shimada, T. Hirai, M. Mizutani, and T. Kuriyagawa, "Unidirectional Wetting Surfaces Fabricated by Ultrasonic-assisted Cutting," *Int. J. Automation Technol.*, Vol.13, No.2, pp. 191-198, 2019.



Name:
Keita Shimada

Affiliation:
Assistant Professor, Department of Mechanical Systems Engineering, Graduate School of Engineering, Tohoku University

Address:
6-6-01 Aoba, Aramaki, Aoba-ku, Sendai, Miyagi 980-8579, Japan

Brief Biographical History:
2009 Received M.E. degree from Tohoku University
2012 Received Ph.D. from Tohoku University
2012- Assistant Professor, Department of Mechanical Systems and Design, Tohoku University

Main Works:
● Micro/Meso Mechanical Manufacturing (M4 Process), ultrasonic assisted machining, abrasive process

Membership in Academic Societies:
● Japan Society of Mechanical Engineers (JSME)
● Japan Society for Precision Engineering (JSPE)
● Japan Society for Abrasive Technology (JSAT)



Name:
Ziqi Chen

Affiliation:
Graduate School of Engineering, Tohoku University

Address:
6-6-01 Aoba, Aramaki, Aoba-ku, Sendai, Miyagi 980-8579, Japan

Brief Biographical History:
2019 Received M.E. from Tohoku University



Name:
Masayoshi Mizutani

Affiliation:
Associate Professor, Department of Mechanical Systems Engineering, Graduate School of Engineering, Tohoku University

Address:
6-6-01 Aoba, Aramaki, Aoba-ku, Sendai, Miyagi 980-8579, Japan

Brief Biographical History:

2003 Received M.E. from Integrated Design Engineering, Graduate School of Science and Technology, Keio University
2004- Junior Research Associate, Ohmori Materials Fabrication Laboratory, RIKEN
2006 Received Ph.D. from Integrated Design Engineering, Graduate School of Science and Technology, Keio University
2006- Collaboration Researcher, Advanced Development and Supporting Center, RIKEN
2007- Collaboration Researcher, Ohmori Materials Fabrication Laboratory, RIKEN
2009- Special Postdoctoral Researcher, Ohmori Materials Fabrication Laboratory, RIKEN
2011- External Collaborative Researcher, Sophia University
2012- Collaboration Researcher, Ohmori Materials Fabrication Laboratory, RIKEN
2012- Associate Professor, Department of Mechanical Systems and Design, Tohoku University

Main Works:

- Micro/Meso Mechanical Manufacturing (M4 Process), laser process, powder jet deposition (PJD), functional interface, biomaterials, bio-medical applications, biomimetic surface

Membership in Academic Societies:

- Japan Society of Mechanical Engineers (JSME)
 - Japan Society for Precision Engineering (JSPE)
 - Japan Society for Abrasive Technology (JSAT)
-



Name:
Tsunemoto Kuriyagawa

Affiliation:
Professor, Graduate School of Biomedical Engineering, Tohoku University

Address:
6-6-01 Aoba, Aramaki, Aoba-ku, Sendai, Miyagi 980-8579, Japan

Brief Biographical History:

1984-1990 Research Associate, Tohoku University
1990-1992 Assistant Professor, Tohoku University
1991-1992 Visiting Professor, University of Connecticut
1992-2002 Associate Professor, Tohoku University
2003- Professor, Tohoku University

Main Works:

- Nano-precision mechanical manufacturing, Micro/Meso Mechanical Manufacturing (M4 process), powder jet deposition, and creation of functional interface

Membership in Academic Societies:

- Science Council of Japan (SCJ)
 - International Committee for Abrasive Technology (ICAT)
 - International Society for Nanomanufacturing (ISNM)
 - Japan Society of Mechanical Engineers (JSME)
 - Japan Society for Precision Engineering (JSPE)
 - Japan Society for Abrasive Technology (JSAT)
-

Micrometer-scaled hierarchical structures fabricated by ultrasonic-assisted cutting

Keita Shimada^{1, a}, Ziqi Chen¹, Masayoshi Mizutani¹ and Tsunemoto Kuriyagawa²

¹Graduate School of Engineering, Tohoku University, 6-6-01, Aoba, Aramaki, Aoba-Ku, Sendai, Miyagi, 980-8579, Japan

²Graduate School of Biomedical Engineering, Tohoku University, 6-6-01, Aoba, Aramaki, Aoba-Ku, Sendai, Miyagi, 980-8579, Japan

keita.shimada.c6@tohoku.ac.jp *corresponding author

Keywords: surface microstructure, ultrasonic-assisted cutting, wettability.

Abstract. Surface microstructures can confer various functions on materials. Hierarchical, ideally fractal, structures are supposed to be beneficial to obtain functions because such structures can extend the surface area. Therefore, micrometer-scaled combined structures were attempted to fabricate in this study by employing ultrasonic assistance. Ultrasonic-assisted cutting is advantageous to fabricate hierarchical microstructures because the combination of the vibration frequency and simple feed motion leaves microstructures within the macroscopic structures that are shaped if the ultrasonic vibration is not employed. This report focuses on controlling the wettability, a surface function, and various surface structures were fabricated based on locus calculation and the change of wettability was experimentally evaluated.

Introduction

The surface can be defined as the interface where a material interacts with its surrounding environment [1], and most of the significant physical phenomena and chemical actions occur on the surface. Therefore, the surface textures like the asperity, surface area ratio, and spatial frequency affect the surface functionality. Many natural organisms have already acquired surface microstructures on their epidermises to perform more functions; moth eyes, shark skin, gecko feet, and lotus leaves are some of the most prominent examples [2, 3], and biomimetics that is an academic field to acquire functionalities by mimicking natural organisms has currently garnered attention [3, 4]. Focusing on the wettability as an example of the surface functions, the lotus leaf has been giving ideas to fabricate water repellent structures [5–7]: the surface of the lotus leaf consists of micro- and nanostructures and such hierarchical structures can trap air to perform a high hydrophobic state explained by the Cassie–Baxter model [8]. To control the wettability, we have also been attempting to fabricate such hierarchical microstructures with a mechanical machining process, specifically, ultrasonic-assisted cutting [9, 10]. This paper reports the fabrication of micrometer-scaled pyramid and frustum arrays with substructures to confer water repellent property. The feed motion of the machine tool generated the larger structures and ultrasonic vibration concurrently fabricated the finer structures. The wettability of the structured surfaces was then measured with a contact angle meter.

Experimental equipment and conditions

Device for ultrasonic-assisted cutting. The ultrasonic elliptical vibration cutting apparatus employed in this experiment was "Sonic-Impulse EL-50Σ" (Taga Electric Co., Ltd.). It can generate two-axial ultrasonic vibration whose frequency f is 41.4 ± 1.5 kHz in both longitudinal and horizontal directions. Its maximum vibration amplitude is $6.0 \mu\text{m}$ in both directions; while, the recommended value is up to $4.0 \mu\text{m}$ and the value can be set in increments of $0.5 \mu\text{m}$ from the external oscillator. The two vibrations are independent of each other, and elliptical vibration is generated by

synchronizing the phases of the vibrations. A V-shaped single crystal diamond tool with a 0° rake angle and a 14° clearance angle was fixed on the device.

Machine tool. The ultrasonically vibrated tool was mounted on an ultraprecision machine tool "MIC-300" (Nagase Integrex Co., Ltd.) as shown in Fig. 1. It adopts hydrostatic bearings and its positioning resolution is 0.1 nm in the X, Y, and Z axes, and 0.00001° in the C axis.

Workpiece. The machine tool equips a magnetic table, therefore a ferromagnetic stainless steel alloy, SUS420J2, was chosen as the base material of the workpiece, on which electroless nickel-phosphorus (Ni-P) plating (Ni 90%, P 10%) was formed with 60–80 μm in the thickness. The microstructure fabrication was performed on/within the Ni-P layer.

Cutting conditions. The fabrication procedure of micrometer-scaled pyramid and frustum arrays is schematically shown in Fig. 2. Parallel grooves were fabricated unidirectionally at even pitches and the equal depth, and the workpiece was then rotated by 90° and grooved likewise. The cutting depth d was set to 8 μm and the pitch p was 16, 20, 30, 60 μm ; therefore, the individual shape of the array was a pyramid when $p \leq 16 \mu\text{m}$ and a frustum when $p > 16 \mu\text{m}$. The elliptical vibration mode was applied and its amplitude was set to 2.0 μm . The feed speed v was 10 m/min and the pitch of the ultrasonic-vibration-derived microstructures could be estimated between 3.9–4.2 μm by solving $v/f = (10/60 \text{ [m/s]}) / (41.4 \pm 1.5 \text{ [kHz]})$.

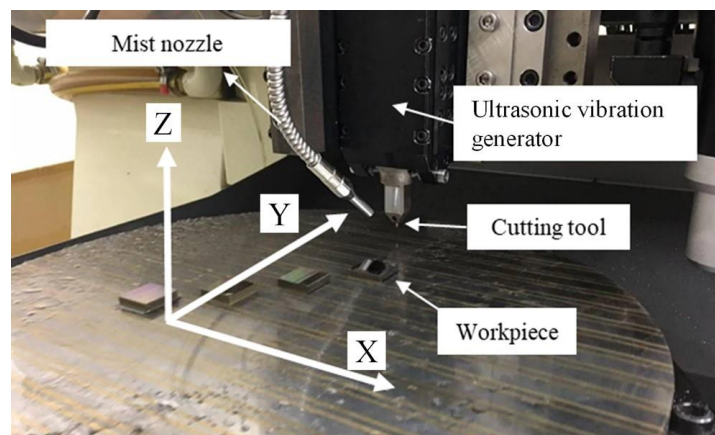


Fig. 1 Experimental setup.

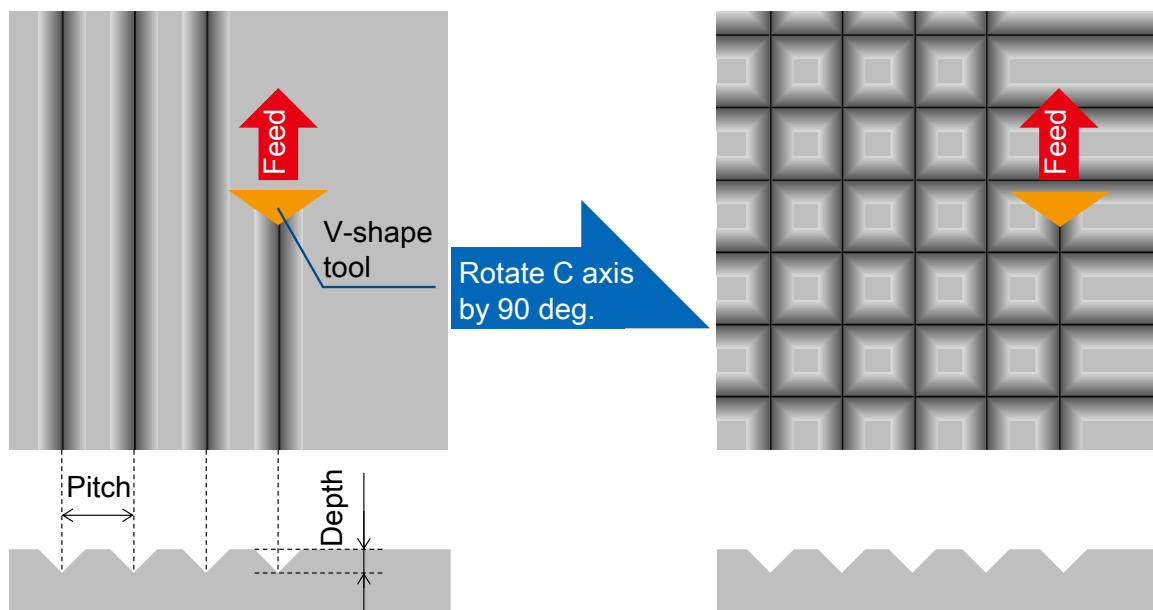


Fig. 2 Fabrication procedure of pyramid and frustum array.

Experimental results

Figure 3 is scanning electron microscopic photographs of the microstructured surfaces and illustrates that the pyramid and frustum arrays with substructures (ripples) derived by ultrasonic vibration were able to be fabricated as designed. The contact angle of the surfaces were then measured with a contact angle meter (DM-501, Kyowa Interface Science Co. Ltd.) to evaluate the wettability quantitatively. Figure 4 concludes the measured values with 0.7 μL refined water droplet and it indicates that the Ni-P surface was originally hydrophilic and transitioned to hydrophobic with the surface textures. Thus, the substructures may capture air and the contact mode may be the Cassie-Baxter mode. Additionally,

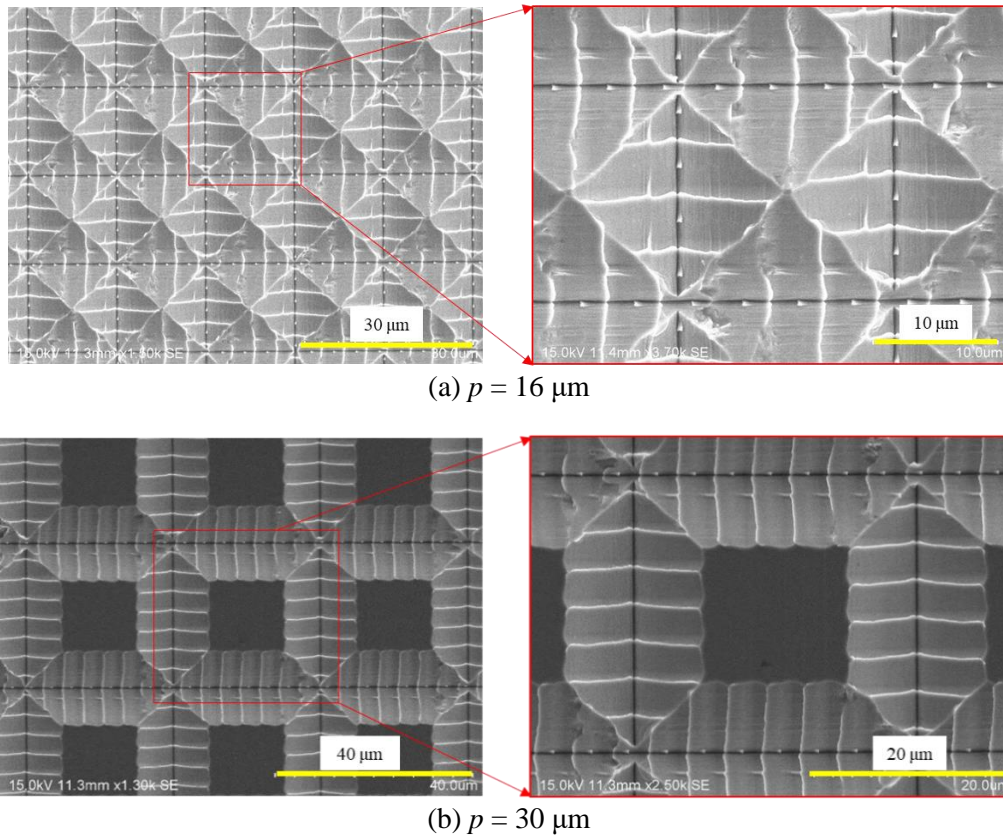


Fig. 3 Fabricated surface textures.

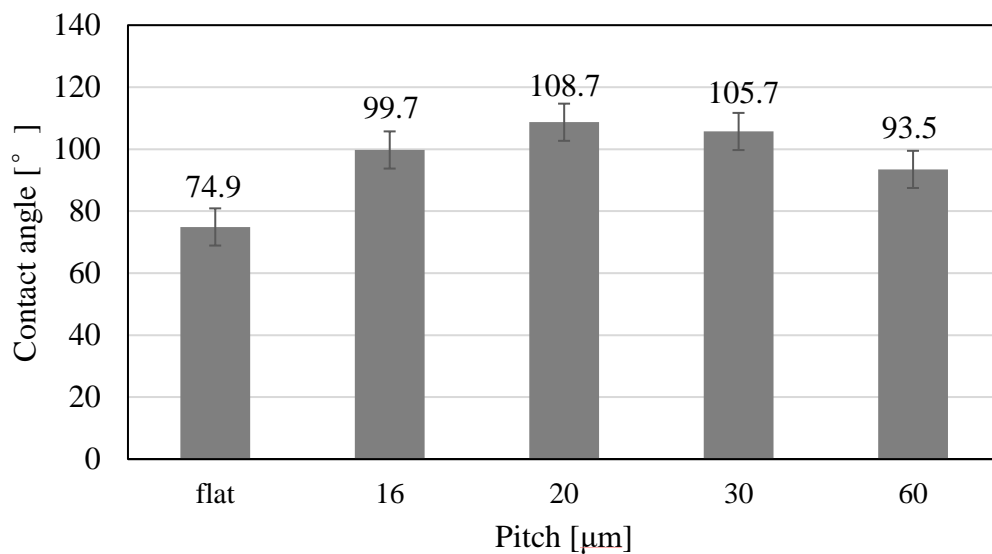


Fig. 4 Water contact angles on the microstructures.

the frustum arrays of $p = 20, 30 \mu\text{m}$ got more hydrophobic than the pyramid array. This result suggests that the small flat zones may give effect to capture air in the microstructures.

Conclusion

This research attempted to fabricate micrometer-scaled hierarchical structures with the assistance of ultrasonic vibration. The pyramid and frustum array microstructures with ripple substructures were successfully fabricated and all of the microstructured surfaces indicated hydrophobicity while the flat surface was hydrophilic. Additionally, the frustum array surfaces with small top zones were more hydrophobic than the pyramid array surface.

Acknowledgment

This research was supported by JSPS KAKENHI Grant Number 18K13666. We would like to express our gratitude for the support.

References

- [1] G.A. Somorjai, Y. Li, Impact of surface chemistry, *Proceedings of the National Academy of Sciences of the United States of America*, 108, 3 (2011) 917–924.
- [2] N. Moronuki, *Surface functions considered from microstructures*, Morikita Publishing (2011) (in Japanese).
- [3] M. Shimomura, New trend of next-generation biomimetic material technology learning from biodiversity, *Sci. & Tech. Trends*, 110, (2010) 9–28, (in Japanese).
- [4] J. Vincent, O. Bogatyreva, N. Bogatyrev, A. Bowyer, A. Pahl, *Biomimetics: Its practice and theory*, *J. Royal Soc. Interface*, 3, 9, (2006) 471–482.
- [5] M. Zhang, S. Feng, L. Wang, Y. Zheng, Lotus effect in wetting and self-cleaning, *Biotribology*, 5, (2016) 31–43.
- [6] R. Nishimura, K. Hyodo, H. Sawaguchi, Y. Yamamoto, Y. Nonomura, H. Mayama, S. Yokojima, S. Nakamura, K. Uchida, Fractal Surfaces of Molecular Crystals Mimicking Lotus Leaf with Phototunable Double Roughness Structures, *J. American Chem. Soc.*, 138, 32 (2016) 10299–10303.
- [7] M. Kayes, A. Galante, N. Stella, S. Haghanifar, R. Shank, P. Leu, Stable lotus leaf-inspired hierarchical, fluorinated polypropylene surfaces for reduced bacterial adhesion, *Reactive and Functional Polymers*, 128 (2018) 40–46.
- [8] A. B. D. Cassie, S. Baxter, Wettability of porous surfaces, *Trans. Farad. Soc.* 40, (1944) 546–551.
- [9] K. Shimada, T. Hirai, M. Mizutani, T. Kuriyagawa, Fabrication of functional surface by ultrasonic-assisted cutting, *J. Jpn Soc. Abras. Technol.*, 62, 1 (2018) 39–44.
- [10] K. Shimada, T. Hirai, M. Mizutani, T. Kuriyagawa, Unidirectional Wetting Surfaces Fabricated by Ultrasonic-assisted Cutting, *Int. J. Automation Technol*, 13, 2 (2019) 191–198.

Design of Pore Morphology in Porous Metal Manufactured via Selective Laser Melting

Shinji Ishibashi^{1,#}, Masataka Chuzenji¹, Takumi Mizoi¹, Masaki Tsukuda¹, Hidakazu Maehana², Keita Shimada¹, Masayoshi Mizutani¹, Tsunemoto Kuriyagawa³

¹ Department of Mechanical Systems Engineering, Tohoku University, Aoba 6-6-01, Aramaki-Aza, Aoba-ku, Sendai, Miyagi 980-8579, Japan

² Komatsu NTC Ltd., 641 Nojiri, Nanto city, Toyama 939-1502, Japan

³ Department of Biomedical Engineering, Tohoku University, Aoba 6-6-01, Aramaki-Aza, Aoba-ku, Sendai, Miyagi 980-8579, Japan

Corresponding Author / Email: shinji.ishibashi.q2@dc.tohoku.ac.jp, TEL: +81-22-795-6949, FAX: +81-22-795-7027

KEYWORDS: Additive manufacturing, Selective laser melting, Porous metal, Ti-6Al-4V, X-ray computed tomography

Porous metal materials have unique features such as low density, adiabaticity, and damping capacity and these features are known to be affected by pore morphology including pore size, shape, and cell structure. To produce a porous metal material with wide range pore type, a variety of porous metal processing has been developed. This research proposes a new manufacturing method of porous metal using selective laser melting (SLM). This method produces porous SLMed objects efficiently by letting naturally arising pores remain in the products; on the other hand, the pore morphology is hardly predictable. To ascertain the relationship between the pore morphology and building conditions, X-ray computed tomography visualized the pore shape and position in the SLMed objects prepared under various building conditions. Additionally, the cross-sectional images were analyzed using an image processing program. The analysis showed that the inclination angle of the pore aligned parallel to the laser scan direction and the porosity increased as the sintered area increased. The above results indicate that the building conditions might control the pore morphologies in SLM products.

1. Introduction

Metal cellular materials exhibit superior functions in terms of lightness, fluid permeability, and thermal conductivity compared to dense metals, and their practical application including lightweight materials, insulation, or filters has been promoted¹. Major fabrication methods of porous metals such as casting process, direct foaming in melt method, spacer method have been developed for many years, and additive manufacturing (AM) technology has also attracted attention in recent years. Most of the porous metals fabricated by AM are open-cell structures whose pores connect each other; while it is generally challenging for the AM to manufacture closed-cell structures. However, Tsukuda et al. proposed a new method to create a closed porous structure using selective laser melting (SLM), which is a representative AM technology³. The feature of their method is to achieve porosity of SLM objects by leaving pores, which had been recognized as defects in the samples. The study clarified the relationship between porosity and manufacturing conditions including the laser scan speed and energy density by evaluating the porosity of the fabricated object, $7 \times 7 \times 7$ mm³ cubes. Additionally, cell structure inside the samples changed from a closed-cell structure to an open cell one as the laser scan speed increased. To extend the application field, it is necessary to control the porosity and pore morphology inside any shape objects.

Thus, this research focused on a sintered area of SLM object and evaluated porosity using X-ray computed tomography (CT) scanning. The pore inclination angle (PIA) and aspect ratio (AR) were also evaluated from the cross-sectional images using an image processing program because these pore parameters are important factors as a mechanical and thermal property of the porous structure⁴.

2. Material and method

2.1 Shaping conditions

ProX100 (3D Systems) with a Gaussian beam fiber laser was used to prepare cubic samples and gas-atomized Ti-6Al-4V powder (OSAKA Titanium technologies Co., Ltd., TILOP64-45) was selected as a shaping material. The powder was layered at a thickness of 45 μ m per layer and sintered with the laser in an argon atmosphere. The scanning speed, scanning width, spot diameter, wavelength, power of the laser were set to 100 mm/s, 70 μ m, 80 μ m, 1070 nm, 50 W, respectively. Under these conditions and the others listed in Table 1, four types of cubic samples with the different sintered areas were shaped. The laser scanning strategy is shown in Fig. 1.

2.2 Analysis conditions of X-ray computed tomography

Two-dimensional images of the cube samples were obtained by X-

ray CT scanning using a ScanXmate-D160TSS105 with a pixel resolution of 7.067 $\mu\text{m}/\text{pixel}$, a voltage of 200 kV, and a current of 200 μA . The analysis domain was $4 \times 4 \times 4 \text{ mm}^3$ at the center of each cube, and it gave the sequential two-dimensional images of the cross-section perpendicular to the building direction. The image binarization and the noise removal were performed by an image processing software ImageJ. Subsequently, its particle analysis program was run to obtain the PIA and AR of each pore. The triangle method and median filter were used as a binarization and noise removal method. The reference radius value of the median filter is 2 pixels, and particles of 9 pixel^2 or less were judged as noise and excluded from particle analyze results.

3. The effect of the sintered area on porosity and pore morphology of SLM objects

Figure 2 shows the relationship between the sintered area and the porosity of the cubic samples and indicates that the porosity increased with increasing of sintered area. Particularly, the porosity got greater approximately three times when the sintered area changes from 49 mm^2 to 95.6 mm^2 . In the samples with the porosity of 10% or more, elongated pores are formed easily because independent pores begin to connect.

The AR of each pore is defined as the ratio of the major and minor axis length, and the larger AR means that the pore is more elongated. The lengths of the major and minor axes were calculated by the ellipse fitting algorithm. The PIA is defined as the angle between the major axis and width axis in Fig. 1. Figure 3 shows the histograms of the PIA to the width direction and the AR in the cube samples. As can be seen in Fig. 3(a), the PIA peaked at $0^\circ\text{--}10^\circ$, $170^\circ\text{--}180^\circ$, and $90^\circ\text{--}100^\circ$ which correspond to the width-axis and length-axis in Fig. 1. This result indicates that the pores tend to be oriented in a direction parallel to the laser scanning strategy. Figure 3(b) shows that all of the cube samples have their modes of AR at the interval of 1.2–1.3. Focusing on Cube 04, the frequency of the mode is decreasing, and it increases at the AR of 1.8 or more. This result indicates that the proportion of elongated pores increases with the increase of the sintered area. From the above results, the sintered area is considered to be one of the important shaping parameters that affect the pore morphology and porosity.

4. Conclusions

The cube samples designed in the different sintered area were shaped by SLM and their porosity and pore morphology were evaluated in detail by X-ray CT scanning. As a result, the porosity showed a positive correlation with the sintered area and showed an increase of more than 4 times at maximum. The analysis of the PIA and AR showed that the pores tended to be oriented in the laser scanning direction, and vertically elongated pores increased as the sintered area increased. Therefore, when fabricating porous metals using SLM, not only energy density or laser scan speed but also the sintered area needs to be considered.

Table 1 The shapes of the samples

	Width [mm]	Length [mm]	Height [mm]	Sintered area [mm^2]
Cube 01	7.00	7.00		49.0
Cube 02	9.78	9.78	7.00	95.6
Cube 03	19.78	19.78		391.2
Cube 04	29.78	29.78		886.8

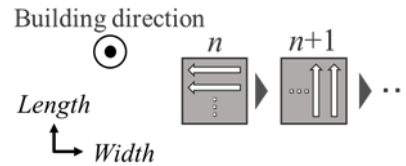


Fig. 1 Schematic of laser strategy

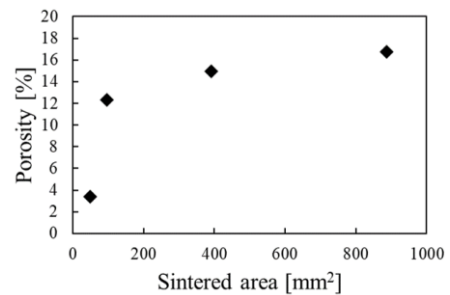


Fig. 2 Sintered area dependence of porosity

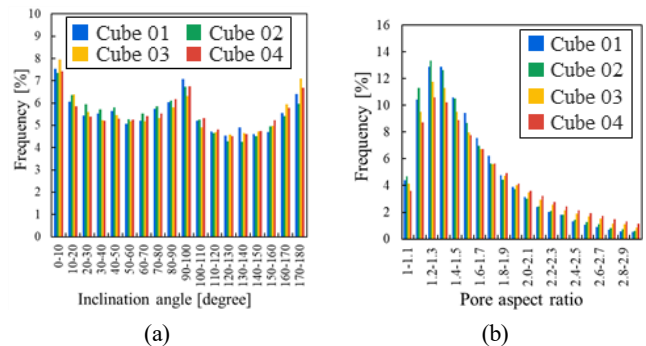


Fig. 3 Histogram of (a) pore inclination angle to the width direction and (b) pore aspect ratio in the cube samples

REFERENCES

- John B., "Manufacture, characterization and application of cellular metals and metal foams," Prog. Mat. Sci., Vol. 46, pp. 559-632, 2001.
- Russell G., Adreas M., "Porous Metals," Phys. Metall., 5th Ed., pp. 2399-2595, 2014
- Masaki T., Shinji I., Takumi M., Hidekazu M., Hiroyasu K., Osamu S., Keita S., Masayoshi M., Tsunemoto K., "Development of high performance porous implants by metal additive manufacturing," Proc. JSPE Sem. Mtg. pp. 415-416, 2018.
- Lorna J. G., Michael F. A., "Cellular solids: structure & properties," Oxford [Oxfordshire]; New York: Pergamon Press, 1988.

A20

Ultrasonic assistance on the generation of hydroxyl radicals in ultrafine bubble suspended water

Keita Shimada^{1,#}, Kazuki Suzuki¹, Masayoshi Mizutani^{1,#} and Tsunemoto Kuriyagawa²

¹ Graduate School of Engineering, Tohoku University, 6-6-01, Aoba, Aramaki, Aoba-Ku, Sendai, Miyagi, 980-8579, Japan

² Graduate School of Biomedical Engineering, Tohoku University, 6-6-01, Aoba, Aramaki, Aoba-Ku, Sendai, Miyagi, 980-8579, Japan

Corresponding Author / Email: keita.shimada.c6@tohoku.ac.jp, TEL: +81-22-795-6949, FAX: +81-22-795-70274

KEYWORDS: Hydroxyl radical, Ultrafine bubbles, Ultrasonic

The ultrafine bubble (UFB) that is defined as a less-than-one-micrometer-diameter bubble has currently caught attention because of its effects. Some of the effects are assumed to attribute to the generation of hydroxyl (OH) radicals due to the implosions of UFBs. The UFBs are, on the other hand, stable in water; therefore, external forces are necessary to implode them, and in this research, ultrasonic vibration was employed to accelerate the generation of OH radicals. Spin trapping agent had been added on both pure and UFB suspended waters and the halves of them were ultrasonically vibrated, and the four solutions were then measured with the spin trapping and electron spin resonance methods. The results quantitatively showed that the UFB suspended water increased the generation of OH radicals.

1. Introduction

Fine bubbles (FBs) generally refer to the bubbles with less-than-100- μm diameters and they are further classified into microbubbles (MBs) and ultrafine bubbles (UFBs): the MBs and UFBs are defined as the bubbles with diameters of 1–100 μm and less than 1 μm , respectively¹⁾. The FBs have been researched and utilized in the industry as ultrasound contrast agents, aerated wastewater treatment, friction reduction in large vessel navigation, etc^{2,3)}. These applications are considered to attribute to the MBs and the effects of the UFBs have not been clarified³⁾. A reason for the difficulty to clarify the mechanism attributes to the difficulty of the measurement: their diameters exceed the diffraction limit of the visible light so their shapes cannot be confirmed with conventional optical methods^{2,3)}; while, the Tyndall phenomenon can be confirmed as well as other colloid suspensions. Therefore, laser-employed measurement methods including dynamic light scattering method and Brownian motion tracking method were developed to detect the UFBs.

Hydroxyl (OH) radicals are highly reactive and are known to arise with ultrasonic cavitation that generates high pressure and high temperature⁴⁾. The MBs and UFBs are also expected to generate OH radicals by their self-collapse effect. Takahashi et al. reported that the OH radicals were detected from the MB-dispersed water without an external stimulus⁵⁾, but Tada et al. pointed out that they could not find

self-collapse phenomenon in MB-UFB water⁶⁾; either way, we considered that the ultrasonic assistance on the UFB-dispersed water (UFB water) could help to generate more OH radicals, which would effectively modify the workpiece surfaces. This report presents the effect of applying ultrasonic vibration to UFB water on generating OH radicals.

2. Detection of ultrafine bubbles and hydroxyl radicals

A static mixer type UFB generator (nanoQuick, NANOX Co., Ltd.) was employed to obtain UFB water. The operation conditions were fixed as follows: the supplied gas was oxygen, the gas supplying pressure was 0.1 MPa, the pump pressure was 1 MPa, the water flow rate was 4.7 L/min, and the operation time was 15 min. The generated UFBs were then measured with a particle analyzer.

2.1 Measurement and count of ultrafine bubbles

The nanoparticle tracking analysis (NTA, NanoSight NS 300, Malvern Panalytical Ltd.), which computes the particle size in liquids with the temporal change of the images of the scattering lights from nanometer-sized particles, was employed to measure and count the UFBs. The bubble size is calculated based on the Brownian motion and the Einstein–Stokes equation.

2.2 Detection of hydroxyl radicals

The OH radicals were detected with electron spin resonance (ESR, JES-FA100, JOEL Ltd.) spectroscopy. Because the OH radicals are as short-lived, whose half-life is 1 ns^7 , a spin trapping agent, 5,5-dimethyl-1-pyrroline N-oxide (DMPO, Labotech Co., Ltd.), was employed to extend the lifetime of the OH radicals to several hours.

3. Experimental results

3.1 Effect of ultrasonic nozzle

First, an ultrasonic nozzle (W-357-1MPD, Honda Electronics Co., Ltd.) was employed to verify if supplying the UFB water with an ultrasonic nozzle was effective. Figure 1 shows the UFB distributions detected with the NTA before and after ultrasonic nozzle jetting, and the total numbers of the UFBs were $(8.15 \pm 0.75) \times 10^8$ and $(8.00 \pm 0.21) \times 10^8$ in before and after ultrasonic nozzle jetting, respectively. These results indicate that there are no significant difference between them. While, as an interesting phenomenon, UFB water was atomized by the ultrasonic nozzle jetting, which phenomenon was not confirmed with purified water.

3.2 Effect of ultrasonic bath

A self-developed ultrasonic bath was employed to confirm the effect on generating the OH radicals. DMPO was mixed with purified water and UFB water and the concentration was adjusted to 0.3 mol/L . The conditions of ultrasonic irradiation was as follows: the frequency was 1.6 MHz , the output power was 30 W , the amount of the samples were $200 \mu\text{L}$, and the irradiation time was 1 min . Figure 2 is the result of the ESR method to measure the amount of OH radicals. It indicates that the UFB water alone did not generate the OH radicals, while the UFBs extended the generation of the OH radicals under the conditions of the ultrasonic irradiation.

4. Conclusions

This report presents the effect of ultrasonic irradiation on UFB water. The ultrasonic nozzle jet did not change the amount of the UFBs, while UFB water was atomized with the nozzle.

The ESR tests indicated that the UFB water provided the effect to extend the generation of the OH radicals in the ultrasonic bath compared to the purified water.

ACKNOWLEDGMENT

This research was supported by JSPS KAKENHI 16H02305, and 19H00734. The authors would like to thank for the financial support.

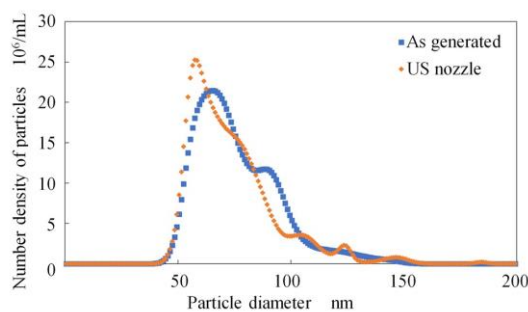


Fig.1 UFB distributions

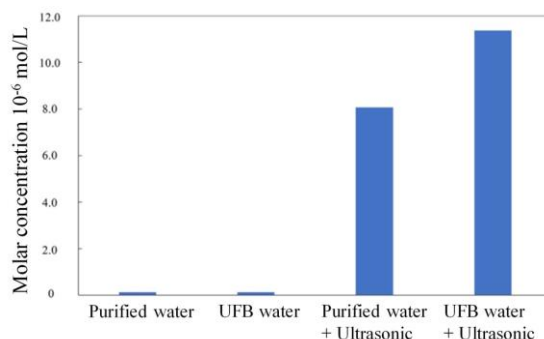


Fig.2 Amount of OH radicals detected by ESR

REFERENCES

1. ISO 20480-1: Fine Bubble Technology –General Principles for Usage and Measurement of Fine Bubbles –Part 1: Terminology (2017).
2. K. Terasaka, Trends and Challenges of Fine Bubble Technology, Chem. Eng. Jpn. 78, 9 (2014) 580–584.
3. K. Yasui, Ultrafine Bubbles, J. Acoust. Soc. Jpn. 73, 7 (2017) 424–431.
4. K. Yasuda, Decomposition of Chemical Compounds by Ultrasound and Development of Sonochemical Reactor, The Chemical Times, 2 (2009) 2–7.
5. M. Takahashi, K. Chiba, P. Li, Free-Radical Generation from Collapsing Microbubbles in the Absence of a Dynamic Stimulus, J. Phys. Chem. B, 111 (2007) 1343–1347.
6. K. Tada, M. Maeda, Y. Nishiuchi, J. Nagahara, T. Hara, Z. Zhouwei, Y. Yoshida, S. Watanabe, M. Ohmori, ESR Measurement of Hydroxyl Radicals in Micro-nanobubble Water, Chem. Lett, 43 (2014) 1907–1908.
7. H. Sies, Strategies of antioxidant defense, Euro. J. Biochem., 215, 2 (1993) 213–219.
8. K. Saito, Certification infrastructure development to support the industrialization of fine bubble technology -Development of test measurement technology for fine bubble certification and cooperation with international standardization-, J. Soc. Instrument and Control Eng., 54, 10 (2015) 752–755.

Bactericidal effect of ultrafine bubble against *Pseudomonas aeruginosa* in grinding fluid

Hiroko YAMADA^{1, a*}, Kensuke KONISHI², Keita SHIMADA^{3, b},
Masayoshi MIZUTANI^{4, c} and Tsunemoto KURIYAGAWA^{5, d}

^{1, 5} Graduate School of Biomedical Engineering, Tohoku University 6-6-01 Aramaki Aoba, Aoba-ku, Sendai 980-8579, Japan

^{2, 3, 4} Graduate School of Engineering, Tohoku University 6-6-01 Aramaki Aoba, Aoba-ku, Sendai 980-8579, Japan

^a hiroko.suzuki.q4@dc.tohoku.ac.jp, ^b keita.shimada.c6@tohoku.ac.jp, ^c masayoshi.mizutani.b6@tohoku.ac.jp,

^d tkuri@tohoku.ac.jp

Keywords: Ultrafine bubbles, Sterilization, Grinding fluid, *Pseudomonas*.

Abstract.

We determined a case of bacterial diversity in an industry-based liquid in-use grinding fluid sample by next-generation sequencing and were mainly dominated by *Pseudomonas* genus. For the bactericidal test, we prepared two types of ultrafine bubbles water (UFB) using air or CO₂. The fresh grinding fluid diluted by each UFB and inoculated 10⁶ CFU/mL of *Pseudomonas aeruginosa* ATCC10145 into each sample. After a two-hour of treatment, no colony detection was shown in CO₂-UFB. We observed specific fluorescently stained bacteria by fluorescence microscope before and after treatment of UFB. After treatment, *P.aeruginosa* was dead by membrane damage. We were able to find that UFB water using CO₂ is effective to control *Pseudomonas* genus in grinding fluid, and elucidate a part of bactericidal mechanisms of UFB.

Introduction

Grinding fluids are generally used in the grinding process, and they have deteriorated with use frequency, and they decay through the action of micro-organisms, mainly bacteria and fungi. They emit unpleasant odors, especially some factories whose temperature is not controlled and/or using the emulsion type fluid. Additionally, the grinding fluid turns into a mist and is spattered to the working space when the grinding fluid is supplied to a grinding wheel under high pressure. Such aerosolized contaminated water or solutions are closely linked to the development of respiratory tract infections. Metalworking fluids used in factories may be implicated in community-acquired pneumonia (CAP) involving previously healthy people in this setting [1]. There are also at risk for infection because grinding fluid is given in an aerosol mist for the workers.

Pseudomonas genus is one of the major bacteria in industry-based liquid in-use water-miscible metalworking fluids including grinding fluids [2]. Especially, *Pseudomonas aeruginosa* is one of the pathogenic bacteria and CAP with *P. aeruginosa* was also reported [1]. The majority of the metalworking fluids are preserved by biocides, but biocides used as preservatives were suspected to create increased dermatitis risks for operators [3]. To solve the problem, non-chemical sterilization is required.

UFB are said to be effective for control of microbe growth [9], but the mechanism is uncertain. In this report, we tried using UFB as a method of controlling the bacterial number in the grinding fluid and preserving grinding fluid from decay.

Material and Methods

Generation of UFB UFB was prepared according to the manual by Nanox Co., Ltd. in the NQ-KP-M1.5 CD-200/60-R3s. The basis of generation is described in Fig. 1.

Grinding fluid sample Both fresh and in-use samples were chemical oil-based, in-use sample collected from systems of grinding operation.

Isolation of bacterial DNA and 16S rDNA metagenome analysis Bacterial genomic DNA (gDNA) was extracted directly from duplicate 750- μ L samples and was stored at -20°C .

Polymerase chain reaction (PCR) amplification of the 16S rDNA fragments prior to 16S rDNA metagenome analysis and data analysis was performed as recommended by Illumina, Inc. in the MiSeq system manual. The principle of the reaction is described in Fig. 2.

Bactericidal test We used *Pseudomonas aeruginosa* ATCC10145. The precultured strain solution (10^8 CFU/ml), fresh grinding fluid, and diluent were aseptically added to sterilized 2-mL cryovials. The initial concentration of the bacteria was checked by the cultivation of the serial dilution method using NAC agar medium (Eiken Kagaku) for 24 hours at 37 degrees Celsius. Other test conditions are described in Table 1. The vials were set in a cool incubator at 23 degrees Celsius. After two hours later, the concentration of the bacteria was analyzed by the cultivation of the serial dilution method using NAC agar medium (Eiken Kagaku) for 24 hours at 37 degrees.

Specific fluorescently staining of bacteria and microscope observation *Pseudomonas aeruginosa* in grinding fluid before and after treatment of UFB were stained by -Bacstain- CFDA (5(6)-carboxyfluorescein diacetate) and Bacstain PI (propidium iodide) solutions (Dojindo Laboratory). The principle of these reagents is described in Fig. 3. Specific fluorescently stained bacteria were observed by a fluorescence microscope (BZ-9000, Keyence).

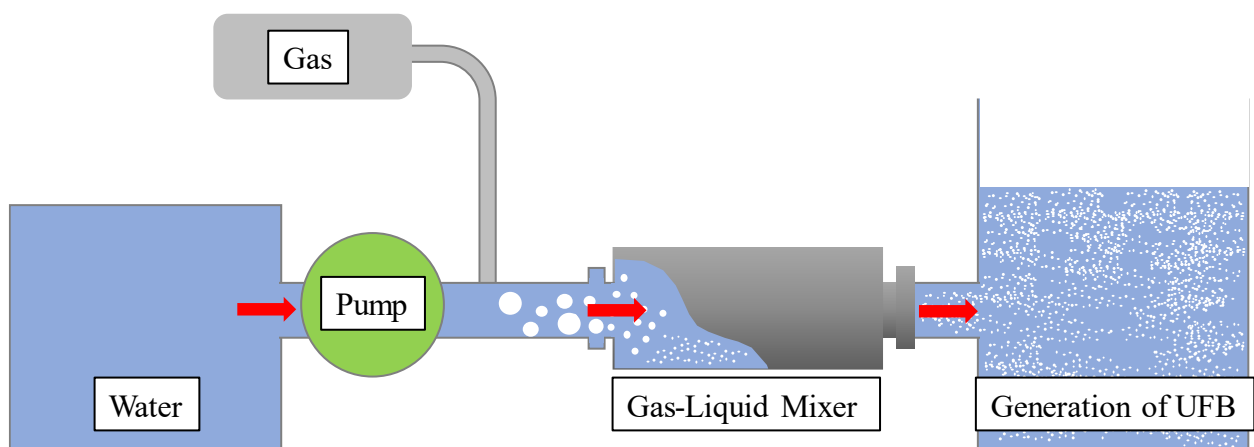
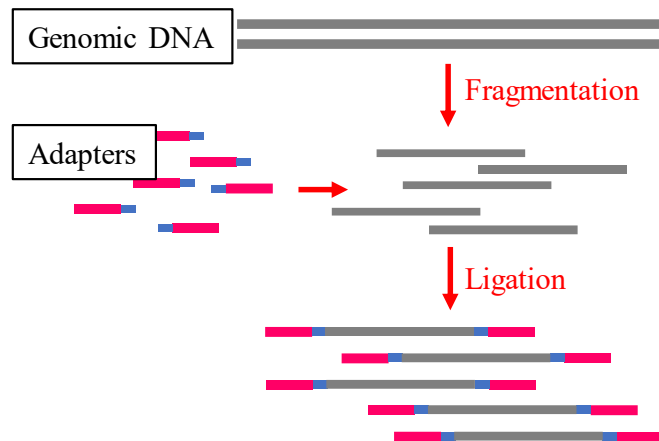
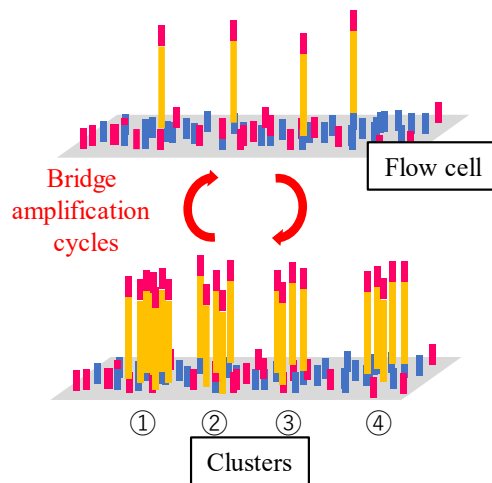


Fig. 1 Extremely-high density UFB generating system [6]

1. Library preparation



2. Cluster amplification



3. Sequencing and Data analysis

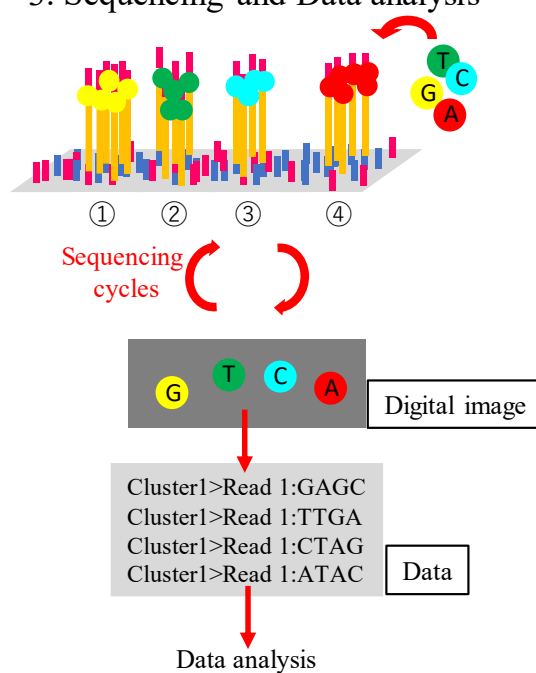


Fig. 2 Next generation sequencing (NGS) [7]

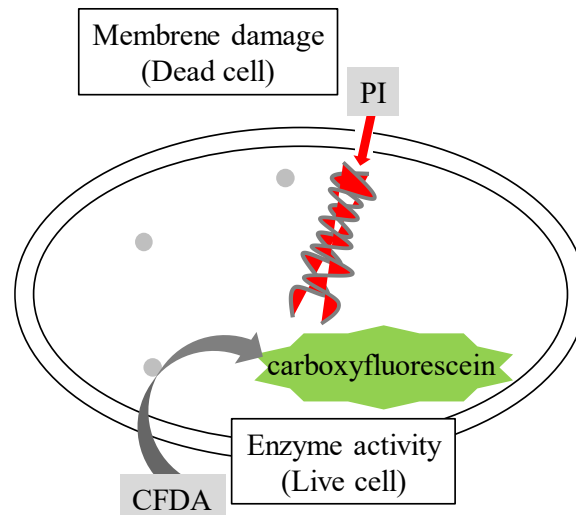


Fig. 3 Microbial cell viability confirmation [8]

Result and Discussion

16S rDNA metagenome analysis (Table 1) We determined a case of bacterial diversity in an industry-based liquid in-use grinding fluid sample by next-generation sequencing and were mainly dominated by *Pseudomonas diminuta* (*Brevundimonas diminuta*) (16.23%). *Pseudomonas* genus is one of the major bacteria in industry-based liquid in-use water-miscible metalworking fluid [2]. The results estimated that this genus existed in the in-use grinding fluid at a great rate (We didn't check the concentration of *Pseudomonas* genus in this sample by cultivation.).

Bactericidal test (Table 2) No colony was detected after a two-hour treatment by CO₂-UFB. The pH of CO₂-UFB water became acid by hydrogen carbonate ions of dissolved carbon dioxide (pH7.0 to pH5.0). We studied the effect of pH on the sterilization of bacteria. The results are shown in Table 2. The condition of pH 5.0 was inhabitable for *Pseudomonas aeruginosa* [4]. The CO₂-UFB had bactericidal activity despite pH 5.0. This result indicated the possibility of bactericidal effect by UFB. The hydroxyl radical was not generated from a dissolving air UFB without a dynamic stimulus [5], we considered the physical impact as a possible cause of sterilization.

Specific fluorescently staining of bacteria and microscope observation (Fig. 4) After CO₂-UFB treatment, *P. aeruginosa* was dead and stained PI. This result showed that bacterial membrane damage caused death. We were not found a noticeable change of forms.

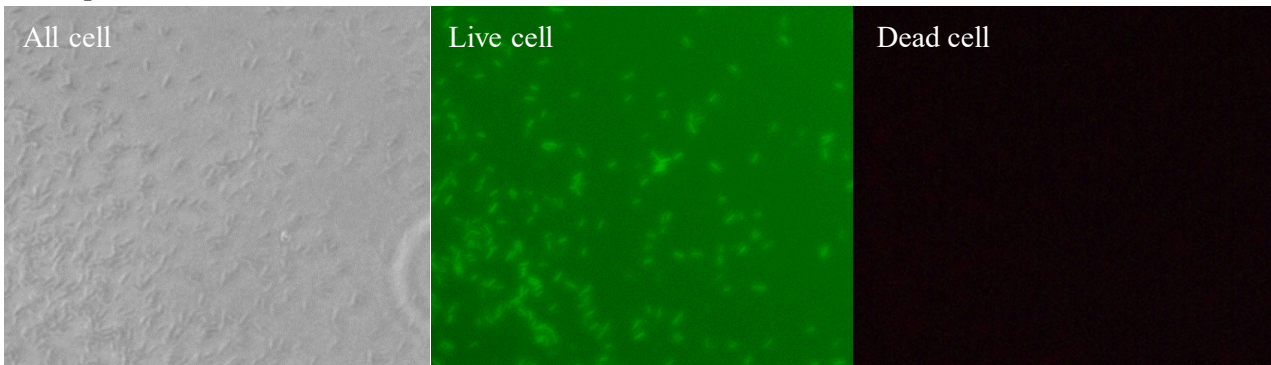
Table 1 Bacterial diversity in in-use grinding fluid sample

Species classification	% Total Reads
<i>Pseudomonas(Brevundimonas) diminuta</i>	16.23
<i>Dyadobacter beijingsis</i>	8.38
<i>Methylobacillus glycogenes</i>	6.05
<i>Thermus thermophilus</i>	4.83
<i>Brevundimonas terrae</i>	3.40
<i>Aminobacter aminovorans</i>	3.16
<i>Comamonas testosteroni</i>	2.68
Unclassified at species level	42.21
Other	13.06

Table 2 Effect of UFB treatment on cell number of *P. aeruginosa*

type of metalworking fluid	additive rate [%]	diluent	gas	pH	initial concentration of <i>P. aeruginosa</i> [CFU/ml]	Number of colonies after treatment [CFU/ml]	sterilization rate [%]
chemical type	2.5	ultrafine bubbles water	Air	7.04	8.0×10^6	$< 8.0 \times 10^6$	0
—	—	ultrafine bubbles water	Air	7.04	8.0×10^6	$< 8.0 \times 10^6$	0
chemical type	2.5	ultrafine bubbles water	CO ₂	5.03	8.0×10^6	0	100
—	—	ultrafine bubbles water	CO ₂	5.03	8.0×10^6	0	100
chemical type	2.5	purified water	—	7.35	8.0×10^6	$< 8.0 \times 10^6$	0
—	—	purified water	—	7.35	8.0×10^6	$< 8.0 \times 10^6$	0
chemical type	2.5	purified water	—	5.01	1.8×10^6	$< 1.8 \times 10^6$	0
—	—	purified water	—	5.01	1.8×10^6	$< 1.8 \times 10^6$	0

After purified water treatment



After CO₂-ultrafine bubbles water treatment



Fig. 4 Effect of UFB treatment on cell membrane damage of *P. aeruginosa*

Summary

The safety control of grinding fluid is the one of important part for machining processing, but biocides used as preservatives were suspected to create increased dermatitis risks for operators [3]. *Pseudomonas* genus was mainly dominated in grinding fluid (Table 1).

In this report, we focused on the UFB generated by different gas and found that CO₂-UFB has bactericidal effect for *Pseudomonas aeruginosa* (Table 2). We tried elucidation of the bactericidal mechanism of the CO₂-UFB using specific fluorescent staining and observed that *P.aeruginosa* was dead by membrane damage addition of UFB (Fig. 4).

Finally, we can conclude that UFB using CO₂ is effective to control *Pseudomonas* genus in grinding fluid without biocides and preserve grinding fluid from decay.

References

- [1] Ferraz de Campos FP, Felipe-Silva A, Lopes ACFMM, Passadore LF, Guida SM, Balabakis AJ, Martines JADS., Community-acquired *Pseudomonas aeruginosa*-pneumonia in a previously healthy man occupationally exposed to metalworking fluids., Autops Case Rep. Sep. 30; 4(3) (2014) 31-37.
- [2] Di Maiuta N, Rüfenacht A, Kuenzi P., Assessment of bacteria and archaea in metalworking fluids using massive parallel 16S rRNA gene tag sequencing., Lett Appl Microbiol., Oct; 65(4) (2017) 266-273.
- [3] Maier, L.E., Lampel, H.P., Bhutani, T. and Jacob, S.E., Hand dermatitis: a focus on allergic contact dermatitis to biocides. , Dermatol Clin 27(2009) 251–264.
- [4] Yasui K, Tuziuti T, Kanematsu W., Mysteries of bulk nanobubbles (ultrafine bubbles); stability and radical formation., Ultrason Sonochem. Nov;48(2018) 259-266.
- [5] Toshikazu Sakazaki, Bacteriology of *Pseudomonas aeruginosa*., Media Circle 10 (1965) 281-289.
- [6] Information on <http://www.nano-x.co.jp/nanoquick>
- [7] Information on <https://jp.illumina.com/>
- [8] Information on <http://www.dojindo.co.jp/products/index.html>
- [9] Asahi Research Center report (RS-1007) Nov;(2016)

Formation of Hydroxyapatite and Zirconia Composite films with Powder Jet Deposition and Their Color Measurement

Keita Shimada^{1, a*}, Takaaki Sunouchi¹, Hiroki Yamamoto¹, Kuniyuki Izumita², Keiichi Sasaki², Masayoshi Mizutani¹ and Tsunemoto Kuriyagawa³

¹Graduate School of Engineering, Tohoku University, 6-6-01, Aoba, Aramaki, Aoba-Ku, Sendai, Miyagi, 980-8579, Japan

²Graduate School of Dentistry, Tohoku University, 4-1, Seiryō-Cho, Aoba-Ku, Sendai, Miyagi, 980-8575, Japan

³Graduate School of Biomedical Engineering, Tohoku University, 6-6-01, Aoba, Aramaki, Aoba-Ku, Sendai, Miyagi, 980-8579, Japan

keita.shimada.c6@tohoku.ac.jp *corresponding author

Keywords: Hydroxyapatite, Zirconium dioxide, Powder jet process, Tooth color.

Abstract. Powder jet deposition (PJD) is a film formation technique that can be employed under atmospheric and room-temperature conditions. PJD has been attempted to apply to dental treatment by utilizing hydroxyapatite (HA) particles. This research focuses on the aesthetic aspect of the PJD dental treatment; specifically, the color tones of the PJD-formed HA films, as well as a zirconia block and a dental shade guide, were measured and evaluated quantitatively in the CIE (Commission Internationale de l'Eclairage) $L^*a^*b^*$ color space. Subsequently, HA and zirconia composite particles were created by a mechanochemical powder fusion device and the particles were employed in PJD to verify whether the formed composite films took on a medium color tone between that of the HA film and the zirconia block.

Introduction

Dental treatment has aspects of functional restoration and aesthetic improvement: generally, the former is paramount, but once the functionality is ensured, the latter is also essential and what people concern about [1, 2]. Repairs of dental cavities, for example, have been filled with alloys, but the composite resins and porcelain that are more aesthetic currently started to be used favorably by patients [3, 4]. Because dental metal allergy is a major issue on metallic fillings [5], choosing metal-free materials is reasonable but aesthetics also affects patients' choices. On the other hand, each material possesses risks of the occurrence of secondary caries and the aged deterioration because they are exposed to the severe environment of human mouths where they experience mechanical and thermal stresses for many decades. Additionally, the composite resin has been pointed out that a more risk of secondary caries [4, 6]. The destructions often initiate at the boundaries of the human teeth and fillings where mechanical and material properties are different. In order to solve these problems, we have been investigating to employ powder jet deposition (PJD) that is a film formation method with high-speed fine particles blasted on substrates under room temperature and atmospheric pressure environment [7]; specifically, fine particles of hydroxyapatite (HA) that is the main component of human teeth are used to collide directly on teeth surfaces and to form films. Akatsuka et al. [8] revealed that HA PJD treatment can form thick films with sufficient bonding strength and hardness on HA substrates. We have also been attempting applying HA PJD treatment on aesthetic dentistry. Because films created with pure HA particles are whitish transparent color, additive components might be needed to hide the substrate color. Izumita et al. [9] reported that titanium dioxide (TiO₂) and HA combined particles can whiten discolored tooth surfaces; on the other hand, the toxicity of TiO₂ nanoparticles have currently been reported [10]. Therefore, zirconium dioxide (ZrO₂) that is a

commonly used material for all-ceramic implants was chosen as the additive materials in this research.

The objective of this report is to evaluate the color tones of the PJD HA films and ZrO₂ quantitatively for expecting the color-modifying ability of ZrO₂. First, the spectral reflectances of HA films and a ZrO₂ disk were measured to obtain the color tones in the CIE (Commission Internationale de l'Eclairage: *French*) $L^*a^*b^*$ color space. Subsequently, HA and ZrO₂ composite particles (hereinafter, simply referred to as 'HA/ZrO₂ particles') were fabricated and employed in PJD to form composite films and the change of the color tones was figured out.

Colors of hydroxyapatite films and zirconia block

Samples for color measurement. A self-developed PJD handpiece was employed and the blasting conditions are listed in Table 1. Microscope slides made of soda-lime glass were chosen as the substrates to form HA films for color measurement because it is a transparent and colorless material that does not disturb the color measurement by reflecting light. Figure 1 shows a microscope slide before and after forming an HA film; on the other hand, the color of ZrO₂ was measured via a commercially available ZrO₂ disk (NANOZR, Panasonic Healthcare: ZrO₂ + HfO₂ 67.9 wt%, CeO₂ 10.6 wt%, Al₂O₃ 21.5 wt%) [11], which was machined in the dimension of 2 mm × 3 mm × t1 mm. All specimens were polished with a waterproof abrasive paper up to 0.01 μm Ra before color measurement to eliminate the effect of the surface topography on the light reflection. Their colors were then measured with a spectrophotometer (CMS-35FS, Murakami Color Research Laboratory) using CIE standard illuminant D65. The light source was a halogen lamp, the irradiation and

Table 1 PJD conditions

Parameters	Values
Blasting Particle	Hydroxyapatite
Particle size	2.2 μm (mean)
Blasting distance	3.0 mm
Supplying pressure	0.5 MPa
Accerelating pressure	0.5 MPa
Blasting duration	30 s
Substrate	Soda-lime glass
Conveying fluid	Air

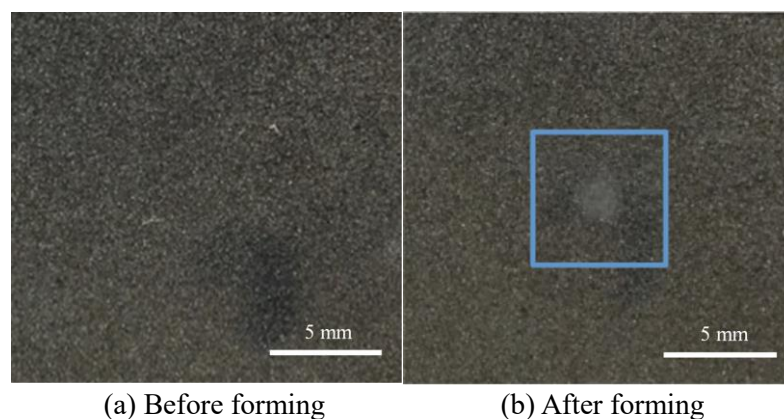


Fig. 1 Formed hydroxyapatite film

measuring diameters were 3.0 and 1.6 mm, respectively, the measurement time was 3.0 s, and the measuring capacity was 390–730 nm. Additionally, the dental shade guide (SG) (Lumin-Vaccum, VITA Zahnfabrik) numbered as A3.5, which is similar to the common Japanese tooth color, was measured as a control. Following the previous research [12], the color measurement of SG was performed in the three areas (the cervical, middle, and incisal areas).

Results of color measurement. Figure 2 illustrates the measured reflectance for each wavelength. The graph indicates that the HA film possessed as uniformly low reflectance as around five percent in the whole measured spectra; therefore, the irradiated white light was almost absorbed or transmitted. The spectra of the three areas of the SG have no significant difference and their reflectances increased linearly from 12% to 20% in the spectral range of 390–600 nm, then became almost constant as around 20%. The ZrO₂ block possessed the largest reflectance in the whole area out of the measured samples. Its reflectance increased largely 37%–62% in 390–500 nm, then increased gradually 62%–65% in 500–730 nm.

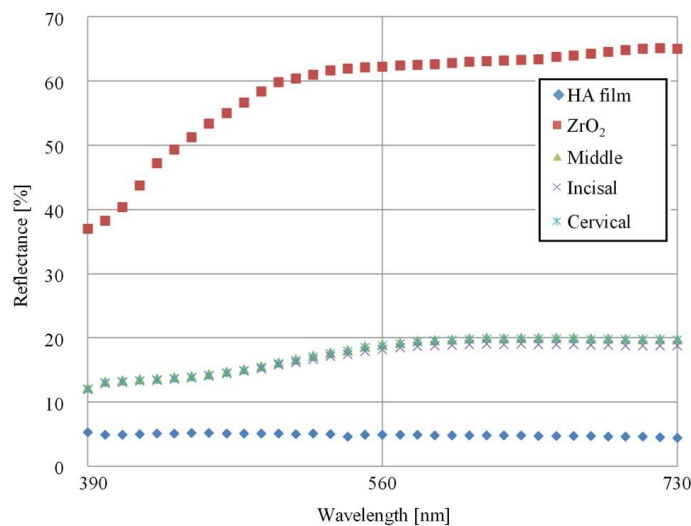


Fig. 2 Spectral distributions of the HA film, zirconia, and shade guide.

These measured spectra were then transformed to the CIE $L^*a^*b^*$ color space to evaluate and compare each color tone quantitatively. The three values (L^* , a^* , b^*) represent for the lightness (black–white: 0–100), green–red (minus–plus), and blue–yellow (minus–plus), respectively [13]. Table 2 lists the calculation results from the values of Fig. 2 and it indicates that both SG and ZrO₂ take yellowish tones.

Table 2 CIE $L^*a^*b^*$ color parameters on SG, HA, and ZrO₂

	L^*	a^*	b^*	
Cervial area	49.86	−0.164	9.346	
Shade guide (A3.5)	Middle area	50.06	−0.176	9.156
	Incisal area	49.19	−0.366	8.398
Hydroxyapatite film on glass	26.47	−0.085	−1.043	
ZrO ₂ block	82.75	−2.845	8.770	

The total color difference ΔE_{ab}^* is defined as the Euclidean metric in the color space, i.e., ΔE_{ab}^* is obtained as

$$\Delta E_{ab}^* = \sqrt{(L^*_2 - L^*_1)^2 + (a^*_2 - a^*_1)^2 + (b^*_2 - b^*_1)^2}. \quad (1)$$

Based on Eq. (1), ΔE_{ab}^* from the middle area of the SG were 25.7 at the HA film and 32.8 at the ZrO₂ block. Because the just noticeable difference in the CIE color space is supposed to be 2.3 [14], these color differences are quite great and they will provide a color change if they are used dental treatment.

Powder jet deposition with composite particles for controlling the color tone

Hybridizing of hydroxyapatite and zirconia particles. The color tone of the SG is approximately in the middle of the HA film and ZrO₂ block in the color space as listed in Table 2; thus, powder hybridizing was performed to clarify if the composite conditions of ZrO₂ and HA particles can control the color tone of PJD films. HA/ZrO₂ particles were created by a mechanochemical powder fusion device (Nanocular, Hosokawa Micron) that possesses a four-bladed impeller in its chamber and particles are hybridized by the stress applied when they pass the gap between the blade and inner wall. Additionally, the device can employ atmospheric plasma to enhance hybridization by cleaning the surfaces of the particles. The hybridizing conditions are listed in Table 3. The operation time was varied to change the degree of hybridization. Subsequently, PJD was performed with the obtained HA/ZrO₂ particles under the conditions listed in Table 1.

Table 3 Conditions of powder hybridization

Parameters	Values
Main particles	Hydroxyapatite, 2.5 μm
Sub-particles	Zirconium dioxide, 10 nm
Blade rotation number	1500 min^{-1}
Operation time	5, 10, 20 min
Hybridizing ratio (ZrO ₂ /HA)	5.0 wt%
Atmospheric plasma generator	100 W, Radio-frequency (13.56 MHz) power
Plasma source gas	Air, 30–50 Pa

Color tones of the films formed by composite particles. The color parameters of the formed HA/ZrO₂ films and the color differences between them and the middle area of the SG are listed in Table 4. These results indicate that the lightness L^* of the composite films became in the middle of the HA film and the ZrO₂ block though their a^* and b^* were outside of the interval. The increase of the hybridizing operation time raises the surface coverage of ZrO₂ sub-particles on the HA main particles; however, the lightness of the formed film reversely decreased with the increase in the operation time.

Table 4 CIE $L^*a^*b^*$ color parameters on HA/ZrO₂

Operation time	L^*	a^*	b^*	ΔE_{ab}^* from SG	
5 min	35.76	0.193	-2.445	18.4	
HA/ZrO ₂ film	10 min	33.28	0.330	-2.448	20.4
	20 min	30.89	0.323	-2.203	22.3
Hydroxyapatite film on glass	26.47	-0.085	-1.043	25.7	
ZrO ₂ block	82.75	-2.845	8.770	32.8	

* The bottom two rows are reappearance from Table 2.

Summary

This research quantitatively evaluated the color tones of the HA film, ZrO₂ block, and HA/ZrO₂ composite films for aesthetic dental treatment of the PJD. The color tone of the PJD formed HA film was dark enough to be recognized, which result indicates that the pure HA film alone cannot change the color tone of the original tooth; on the other hand, the color tone of the ZrO₂ block was strongly bright compared with the SG. Composite particles of HA and ZrO₂ were then created by a mechanochemical powder fusion device, and the PJD films formed with the composite particles took the medium color tones between the HA and ZrO₂.

Acknowledgment

This research was partly supported by the FY2016 New Energy and Industrial Technology Development Organization (NEDO) Strategic Foundation Advanced Technology Support Project (Project consignment type). We would like to express our gratitude for the support.

References

- [1] G. F. Boeira, M. M. S. Salas, D. C. Araújo, A. S. Masotti, M. B. Correa, F. F. Demarco, Factors influencing dental appearance satisfaction in adolescents: a cross-sectional study conducted in Southern Brazil, *Brazilian J. Oral Sci.*, 15, 1 (2016) 8–15.
- [2] M. A. Goulart, A. M. Condessa, J. B. Hilgert, F. N. Hugo, R. K. Celeste, Concerns about dental aesthetics are associated with oral health related quality of life in Southern Brazilian adults, *Ciência & Saúde Coletiva*, 23, 11 (2018) 3957–3964.
- [3] S. Vidnes-Kopperud, A. B. Tveit, T. Gaarden, L. Sandvik, I. Espelid, 'Factors influencing dentists' choice of amalgam and tooth colored restorative materials for Class II preparations in younger patients' *Acta Odontologica Scandinavica* 67, 2 (2009) 74–79.
- [4] M. B. Correa, M. A. Peres, K. G. Peres, B. L. Horta, A. D. Barros, F. F. Demarco, Amalgam or composite resin? Factors influencing the choice of restorative material, *J. Dent.*, 40 (2012) 703–710.
- [5] M. Kitagawa, S. Murakami, Y. Akashi, A. Oka, T. Shintani, I. Ogawa, T. Inoue, H. Kurihara, Current status of dental metal allergy in Japan, *J. Prosthodont. Res.* (2019) (in press).
- [6] V. Moraschini, C. K. Fai, R. M. Alto, G. O. dos Santos, Amalgam and resin composite longevity of posterior restorations: a systematic review and meta-analysis *J. Dent.*, 43 (2015) 1043–1050.

- [7] C. Nishikawa, N. Mizukuchi, A. Tomie, K. Shimada, M. Mizutani, T. Kuriyagawa, Characteristics of Thick Film Deposition in Powder Jet Machining, *Int. J. Automat. Technol.*, 7, 6 (2013) 630–637.
- [8] R. Akatsuka, K. Sasaki, M. S. S. Zahmaty, M. Noji, T. Anada, O. Suzuki, T. Kuriyagawa Characteristics of hydroxyapatite film formed on human enamel with the powder jet deposition technique, *J. Biomed. Mater. Res. B: Applied Biomaterials*, 98B, 2 (2011) 210–216.
- [9] K. Izumita, R. Akatsuka, A. Tomie, C. Kuji, T. Kuriyagawa, K. Sasaki, Development of Powder Jet Deposition Technique and New Treatment for Discolored Teeth, *Interface Oral Health Sci.* 2016 (2016) 257–267.
- [10] M. Z. Rizk, S. A. Ali, M. A. Hamed, N. S. El-Rigal, H. F. Aly, H.H. Salah, Toxicity of titanium dioxide nanoparticles: Effect of dose and time on biochemical disturbance, oxidative stress and genotoxicity in mice, *Biomedicine & Pharmacotherapy*, 90 (2017) 466–472.
- [11] Panasonic: User Manual NANOZR milling blank.
- [12] W. Shiba, M. Uno, H. Ishigami, M. Kurachi, Means for Reproducing Shade Guide Color with Laboratory-cured Prosthetic Composite, *J. Gifu Dent. Soc.* 35, 3 (2009) 149–159 (in Japanese).
- [13] CIE (Commission International de l’Eclairage). Colorimetry, technical report. CIE Pub. No.15, 2nd ed. Vienna: Bureau Central de la CIE; 1986 (corrected reprint 1996).
- [14] G. Sharma, *Digital Color Imaging Handbook*, (1.7.2 ed.) (2003).

Wettability and osteoblast-like cell behavior on zirconia surface irradiated with nanosecond pulsed laser

Tomohiro HARAI^{1, a*}, Keita SHIMADA^{2, b}, Masayoshi MIZUTANI^{2, c}, Satomi OIZUMI^{3, d}, Keisuke NAKAMURA^{3, e}, Masatsugu HIROTA^{4, f}, Tohru HAYAKAWA^{4, g}, Hitoshi OHMORI^{5, h} and Tsunemoto KURIYAGAWA^{1, i}

¹Tohoku University Graduate School of Biomedical Engineering, 6-6-01, Aoba, Aramaki, Aoba-ku, Sendai, Miyagi 980-8579, Japan

²Tohoku University Graduate School of Engineering, 6-6-01, Aoba, Aramaki, Aoba-ku, Sendai, Miyagi 980-8579, Japan

³Tohoku University Graduate School of Density, 4-1, Seiryō, Aoba-ku, Sendai, Miyagi 980-8575, Japan

⁴Tsurumi University School of Dental Medicine, 2-1-3, Tsurumi, Tsurumiku, Yokohama, Kanagawa 230-8501, Japan

⁵Institute of Physical and Chemical Research, 2-1, Hirosawa, Wako, Saitama 351 0198, Japan

^atomohiro.harai.r7@dc.tohoku.ac.jp, ^bkeita.shimada.c6@tohoku.ac.jp,

^cmasayoshi.mizutani.b6@tohoku.ac.jp, ^ds_oizumi@dent.tohoku.ac.jp, ^ekeisuke@m.tohoku.ac.jp, ^fhirota-masatsugu@tsurumi-u.ac.jp, ^ghayakawa-t@tsurumi-u.ac.jp, ^hohmori@mfl.ne.jp, ⁱtsunemoto.kuriyagawa.b3@tohoku.ac.jp

Keywords: Zirconia implant, Nanosecond pulsed laser, Contact angle, Osteoblast-like cell proliferation

Abstract. The purpose of the research described in this paper was to evaluate the physicochemical properties of laser-irradiated zirconia and to verify the detailed effects for biocompatibility. Nanosecond pulsed laser (NPL) was applied to irradiate yttria-stabilized tetragonal zirconia polycrystals (Y-TZP) and ceria-stabilized tetragonal zirconia polycrystals with alumina nanocomposite (Ce-TZP), and they were characterized with point-autofocus-probe 3D measuring, energy dispersive X-ray spectrometry (EDX), and contact angle measurement. Besides, the effects of cell behavior were investigated through the observation of osteoblast-like cells with scanning electron microscopy (SEM) a day after planting, and cell proliferation evaluation three days after planting. The NPL irradiation created two types of surface textures; laser-roughened surface and laser-grooved surface. The contact angle measurement results showed that the irradiated Y-TZP and Ce-TZP obtained more hydrophobic surfaces. The reason was supposed that the contaminant adhesion and roughening during NPL irradiation on the surfaces made the surfaces more hydrophobic. The SEM images show that the cells were extended along with the machine direction on the irradiated samples. However, there was no remarkable difference in the state of cell attachment between two types of materials. The cells on the laser-grooved Y-TZP surfaces encouraged cell growth significantly more than the laser-roughened Y-TZP surfaces. This result suggests the laser-grooved surface had an important role to help cells to grow. On the other hand, the cells on the irradiated Ce-TZP surfaces encouraged cell growth significantly less than the polished Ce-TZP surfaces. This result suggests that the chemical alteration with NPL inhibited the cell growth process, but this result did not relate to the EDX and contact angle results.

Introduction

Zirconia dental implants have garnered attention due to aesthetic whiteness and no risk of metal allergy as an alternative to titanium implants. Yttria-stabilized tetragonal zirconia polycrystals

(Y-TZP) has already been used for clinical application, and ceria-stabilized tetragonal zirconia polycrystals with alumina nanocomposite (Ce-TZP), which has superior toughness and deterioration resistance to Y-TZP [1], has been developed. High biocompatibility is a vital material property for dental implants. Thus, many researchers have examined surface modification of zirconia.

The pulsed laser can perform microfabrication on difficult-to-cut materials by the removal of material caused by local heating. It is also effective to create micro- and nano-scale rough surfaces, which are considered a favorable environment to help cells to grow [2]. Delgado-Ruíz *et al.* reported that the grooved Y-TZP surface with a femtosecond pulsed laser (FPL) had a higher bone-to-implant contact (BIC) when implanted into the edentulous lower jaws of foxhound dogs [3] [4]. However, Hirota *et al.* reported that the grooved surfaces with nanosecond pulsed laser (NPL) increased BIC of Y-TZP, but decreased that of Ce-TZP when inserted into the femur bone defects of Wistar rats [5]. This result supposed that the heat effects with NPL could chemically alter Y-TZP or Ce-TZP surfaces. However, the detailed reason is not clarified.

The purposes of the research described in this paper were to evaluate the physicochemical properties of the NPL-irradiated Y-TZP and Ce-TZP and to verify the detailed effects for biocompatibility. Generally, surface wettability is assumed as an important property on protein adsorption and subsequent cell behavior [6]. Therefore, NPL-irradiated Y-TZP and Ce-TZP were characterized by chemical analysis and contact angle measurement, and the effects of cell behavior were investigated.

Experimental Method

Sample preparation. Two types of zirconia ceramics, 3 mol% yttria-stabilized tetragonal zirconia polycrystals (Y-TZP, YT-3Y-BE, Tosoh) and 10 mol% ceria-stabilized tetragonal zirconia polycrystals with 30 vol% alumina nanocomposite (Ce-TZP, NANOZR, Panasonic Healthcare), were used because additive agents may make differences in their heat effects. The specimens were cut to the size for each evaluation and polished with waterproof abrasive paper (#400, #600, #1000 and #1500).

Surface textures. The zirconia specimens were irradiated using an NPL oscillator (red ENERGY G4 SP-020P-A-EP-Z-F-Y, SPI Lasers) with a Gaussian beam profile in air. Table 1 lists the NPL irradiation conditions and Fig. 1 shows laser scanning passes. Irradiation was performed in two ways, (a) to roughen the surfaces with aggregate debris caused by NPL irradiation and (b) to create grooves (more than 30 μm width and depth); thus, all four combinations of the two treatments (LR: laser-roughening and LG: laser-grooving) and two samples (Y-TZP and Ce-TZP) were obtained, and each sample is abbreviated using the symbols like "LR/Y-TZP" in the following. The surface textures were characterized using a point-autofocus-probe 3D measuring instrument (NH3-T, Mitaka kohki).

Chemical analysis. The laser blackened the Y-TZP and Ce-TZP surfaces. The chemical compositions of the samples were then identified with energy dispersive X-ray spectrometry (EDX, EMAX ENERGY EX-250, Horiba). The samples (ϕ 12 mm \times t 1 mm) were analyzed within the 20 μm \times 80 μm area. As for LG/Y-TZP and LG/Ce-TZP, the analysis was conducted onto the ridge and groove, respectively.

Surface wettability. The contact angle was measured to examine the influence of the textures and the surface energy states on the wettability. The irradiated samples (ϕ 12 mm \times t 1 mm), which were stored in a vacuum desiccator after ultrasonic cleaning (in ethanol for 10 min and in distilled water for 10 min), were determined with a contact angle meter (DM-501, Kyowa Interface Science, Japan) and an analysis software (FAMAS, Kyowa Interface Science, Japan).

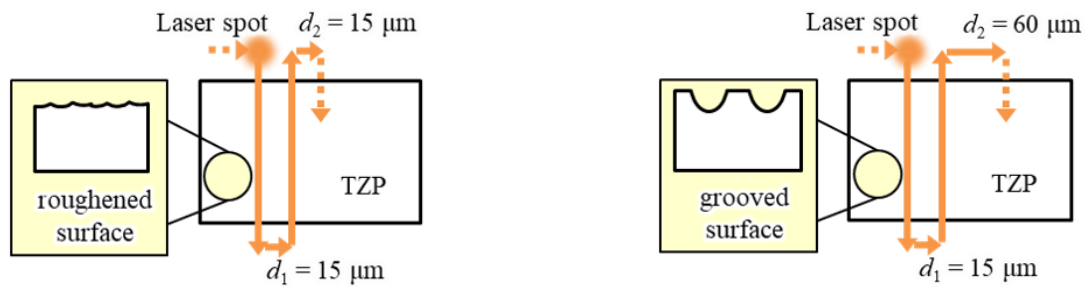
Table 2 shows the conditions, and the droplets were observed as shown in Fig. 2.

Table 1 Irradiation conditions.

Wavelength	Pulse duration	Frequency	Pulse energy	Scanning speed
1064 nm	20 ns	5 kHz	100 μ J	1000 μ m/s

Table 2 Conditions for contact angle measurement.

Measurement	Temperature	Solvent	Droplet size
Tangent method	23°C	Distilled water	5.0 μ L



(a) For the laser-roughened surface.

(b) For the laser-grooved surface.

Fig. 1 Laser scanning passes.

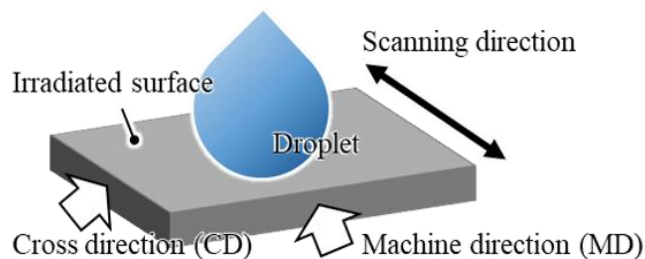


Fig. 2 Observation direction for the droplets.

Cell cultures. Cells were cultured on each irradiated sample. The irradiated samples (5 mm \times 5 mm \times t 1 mm) were sterilized by immersion in 2% glutaraldehyde for 1 h and thrice ultrasonic cleaning (in distilled water for 5 min). For prior culture, MC3T3-E1, an osteoblast precursor cell line derived from mouse calvaria, were grown in α -modified minimum essential medium (α -MEM) containing 10% fetal bovine serum (FBS), 100 units/mL penicillin, and 0.1 mg/mL streptomycin until 80% confluency of a 25 cm² flask. Then, the cells were detached using trypsin and ethylenediaminetetraacetic acid (EDTA), and 50 μ m/L ascorbic acid, 10 mmol/L β -glycerophosphoric acid disodium salt and 0.01 mmol/L dexamethasone were added into the preculture medium. The cells were cultured in 48-well cell culture plates at a density of 30×10^3 cells/cm² on the TZP samples and incubated.

Cell attachment and morphology. Cells on the TZP samples a day after planting were fixed using 4% paraformaldehyde and observed with scanning electron microscopy (SEM, SU1510, HITACHI High-Technologies).

Cell proliferation. Cell proliferation on the TZP samples 3 days after planting was determined by WST-1 based colorimetry (WST-1, Roche Applied Science). Statistical significance of data was followed by Tukey-Kramer honestly significant difference method for multiple comparisons between pairs at $p = 0.05$.

Result and Remarks

Surface texture. Fig. 3 shows the 3D images of irradiated samples and developed interfacial area ratio (*Sdr*, ISO 25178: 1996) of them. The *Sdr* value of the polished Y-TZP was 0.8%, and that of the polished Ce-TZP was 1.3%. These results demonstrate that the NPL irradiation expanded the surface areas, and developed areas of the laser-grooved samples were larger than the laser-roughened samples.

Chemical analysis. Fig. 4 shows the chemical composition of the polished, LR and LG TZP surfaces. It shows the NPL irradiation decreased the oxygen atomic ratio and the atomic ratio of the elements had no significant difference between LR and LG samples. Noda *et al.*[7] reported that a millisecond pulsed laser blackened Y-TZP surfaces due to the reduction of zirconia via Eq. 1.



Thus, the NPL is supposed to reduce the TZP surfaces and resulted in decreasing the atomic ratio of oxygen. Besides, the chemical composition changes might not depend on the ways of laser scanning.

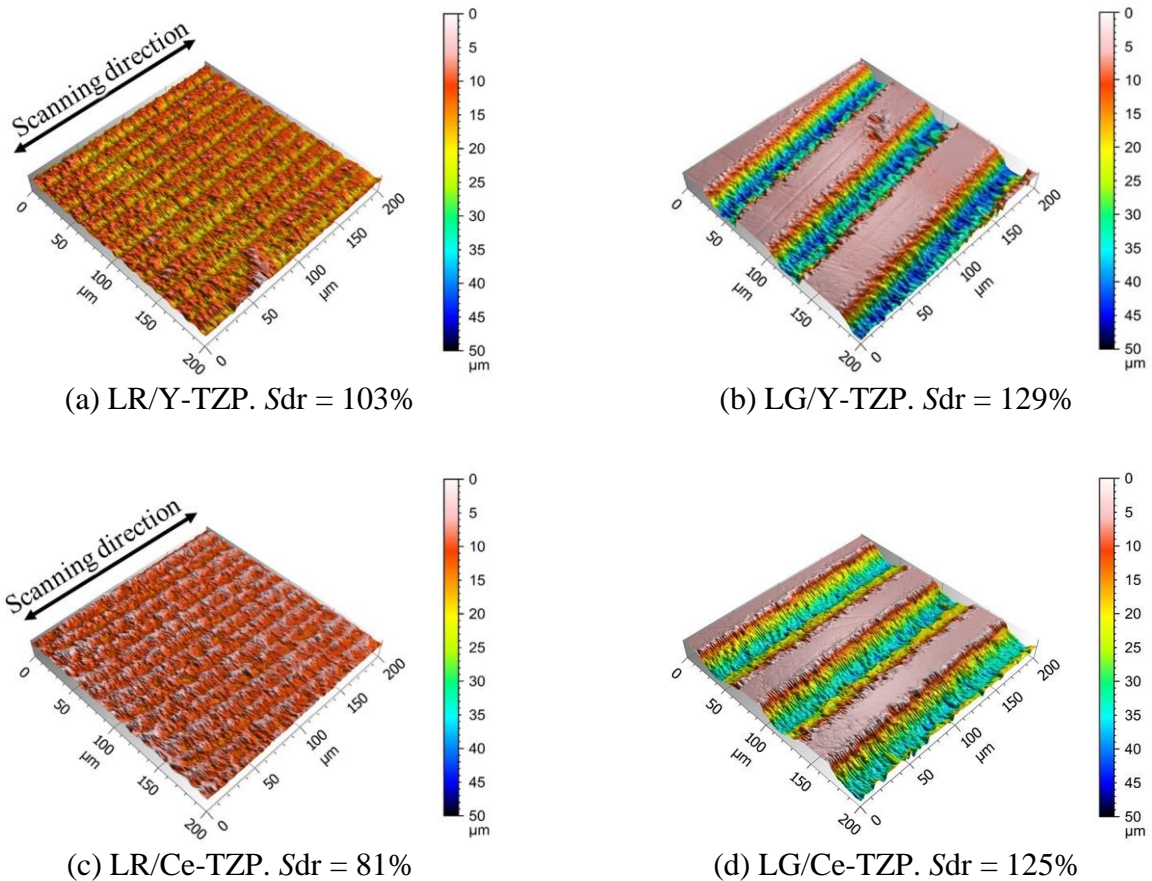


Fig. 3 The surfaces of the irradiated samples and *Sdr* values.

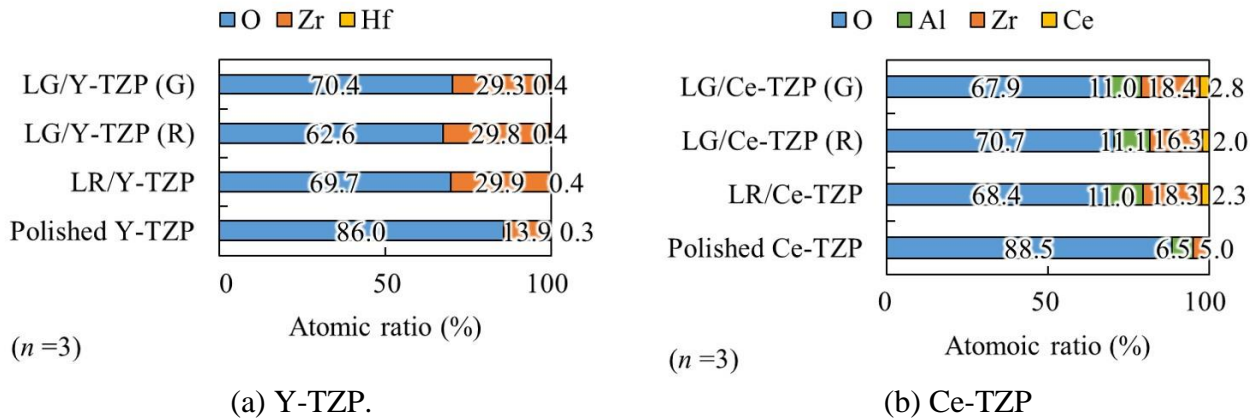


Fig. 4 Chemical composition of the polished and irradiated surfaces. The average values are on the labels ($n = 3$). (G) and (R) indicate the results of the ridge and groove areas, respectively.

Contact angle. Fig. 5 shows the contact angles of the polished and irradiated surfaces, and it demonstrates that the NPL irradiation made Y-TZP and Ce-TZP more hydrophobic. According to Wenzel’s equation [8], the rougher a hydrophobic surface is, the more hydrophobic it gets. Besides, ceramics are generally thought to have hydrophobic surfaces due to the adhesion of contaminants in air. The LR surfaces were supposed to raise the contact angles because the contaminant adhesion and roughening of the surfaces during NPL irradiation made the surfaces more hydrophobic. The droplets on LG/Y-TZP and LG/Ce-TZP had elliptical shapes extended along with machine direction and had no significant difference between them; on the other hand, LR/Ce-TZP had a lower contact angle (almost 110°) than LR/Y-TZP did (almost 140°). On the LG surfaces, droplets were supposed to contact primarily to the areas that were not melted by NPL irradiation. On the LR surfaces, by contrast, droplets contacted the melted and solidified areas. Therefore, it is supposed that the NPL irradiation altered the Ce-TZP surfaces and affected the wettability of Ce-TZP, but notable changes were not confirmed from Fig. 4.

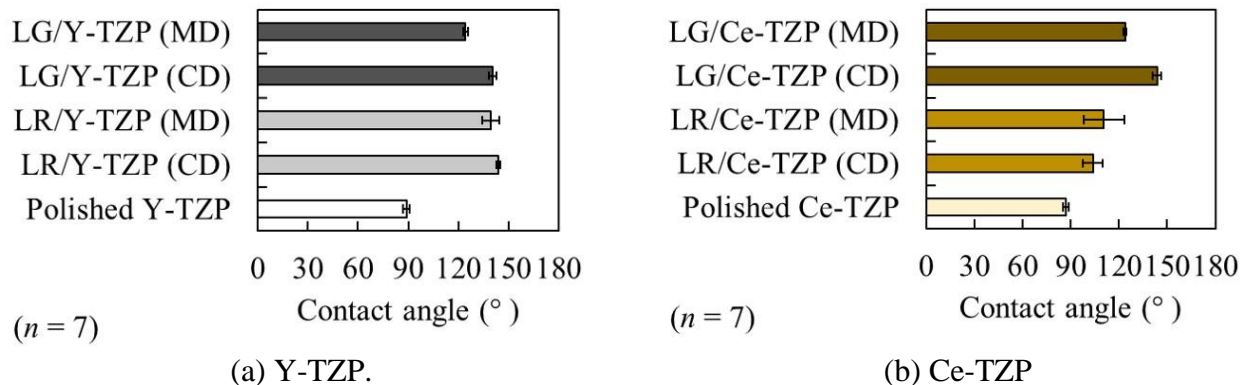


Fig. 5 Contact angle of the polished and irradiated surfaces. MD and CD indicate that the contact angles were observed in the machine direction and cross direction, respectively.

Cell cultures. Fig. 6 shows the SEM images of the cells attaching to the sample surfaces a day after planting. It shows that the cells extended randomly on the polished Y-TZP and Ce-TZP, while along with the machine direction on the irradiated samples. However, there was no remarkable difference in the state of the cell attachment between the two materials. Fig. 7 shows cell proliferation on the polished and irradiated surfaces. The LG/Y-TZP surface encouraged cell growth significantly more than the other Y-TZP surfaces. On the other hand, the LR/Ce-TZP surface encouraged cell growth significantly less than the polished Ce-TZP surface, and cell proliferation on the LG/Ce-TZP surface tended to more increase than the LR/Ce-TZP surface although that was not significant.

These results show the LG surface had an important role to help cells to grow. It was reported that micro- and nano-scale rough surfaces could contribute to cell proliferation [2]. Besides, the cells were

thought to get into the cell-sized grooves on LG/Y-TZP and LG/Ce-TZP and be stimulated from roughened surfaces on the bottoms and the sides. That was supposed to result in increased cell growth. It was confirmed that the NPL-irradiated Ce-TZP surfaces tended to decrease cell growth. This result suggests that the chemical alteration inhibited the cell growth process because there was no remarkable difference in cell attachment and cell morphology between Y-TZP and Ce-TZP.

In the case of titanium surfaces, hydrophilic surfaces are supposed to be better to encourage cell attachment and growth [9]; on the other hand, the above research did not find out the relationship between the cell behavior and the wettability on the zirconia surface. However, the contact angle results also suggest that the Ce-TZP may be specifically altered. Therefore, further chemical analysis with other methods should be conducted to clarify this alteration.

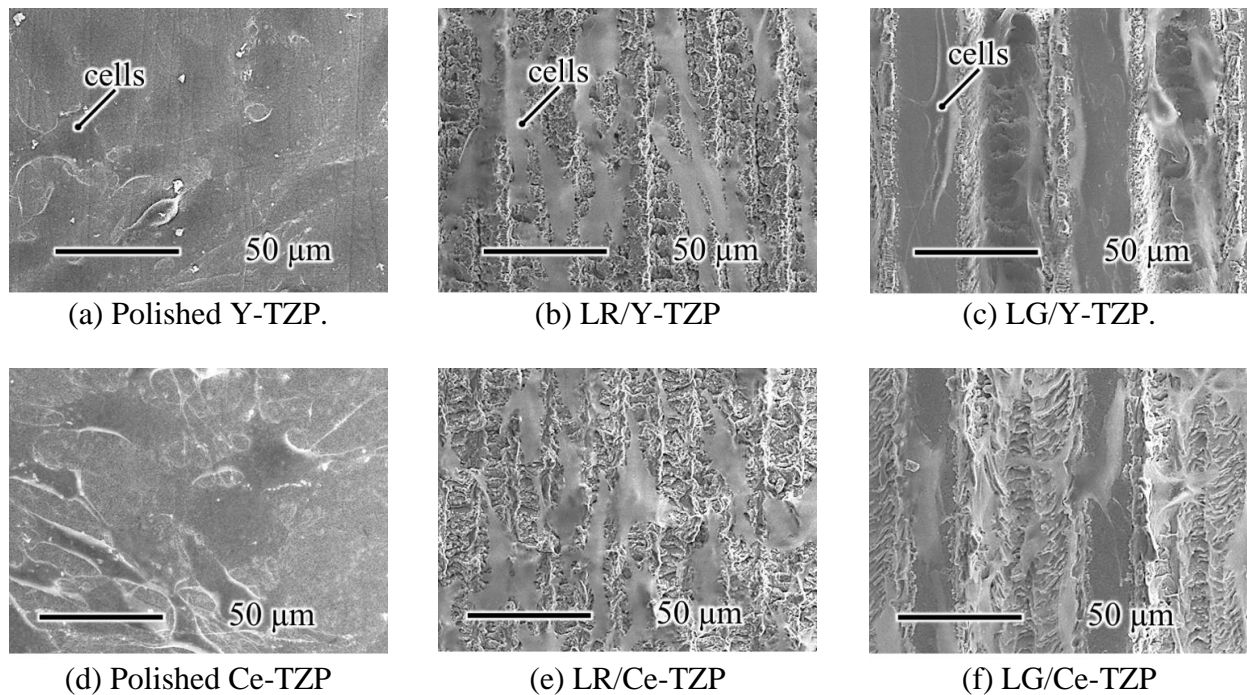


Fig. 6 SEM images of the cells attaching to the polished and irradiated surfaces a day after planting.

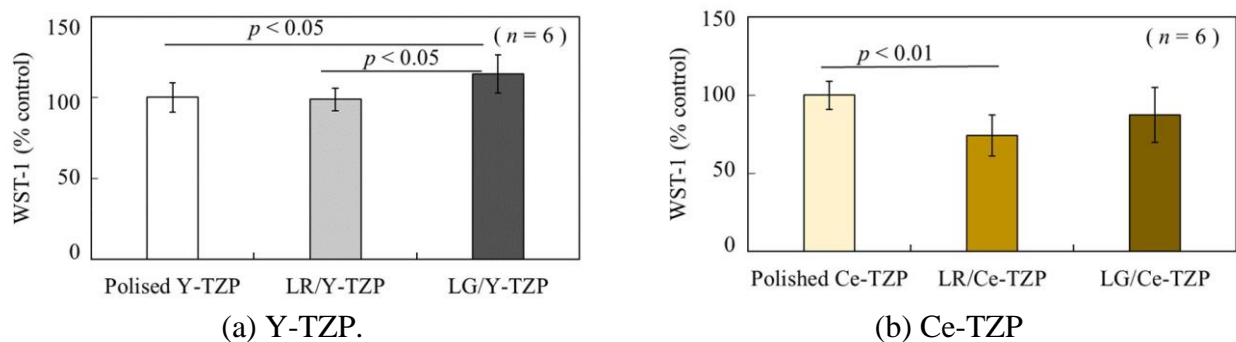


Fig. 7 Cell proliferation on the polished and irradiated surfaces 3 days after planting. The control group was polished Y-TZP in (a), and polished Ce-TZP in (b), respectively.

Summary

To evaluate the physicochemical properties, and to verify the detailed effects for biocompatibility, the NPL-irradiated Y-TZP and Ce-TZP were characterized through chemical analysis and contact angle measurement, and the effects for cell behavior were investigated. From the results and further discussion, the following conclusions were drawn:

1. Micro-grooves created with NPL increased the cell growth on Y-TZP.
2. The cell behavior and the wettability on the zirconia surfaces were not connected in the experiments.
3. Chemical alteration with NPL on Ce-TZP might inhibit the cell growth process.

Acknowledgment

This study was supported in part by JSPS KAKENHI Grant Numbers JP17K06074 and JP17KK0126.

References

- [1] N. Kurizoe, K. Yamada, Y. Suehiro, H. Nakanishi and M. Nawa, High-toughness mechanism of nano-composite ceramic material, Panasonic Electric Works technical report, 59,1 (2013) 71-75.
- [2] T. Hirano, H. Sasaki, S. Honma, Y. Furuya, T. Miura Y. Yajima and M. Yoshinari, Proliferation and osteogenic differentiation of human mesenchymal stem cells on zirconia and titanium with different surface topography, Dental Materials Journal, 34, 6 (2015) 872-880.
- [3] RA. Delgado-Ruíz, JL. Calvo-Guirado, P. Moreno, J. Guardia, G. Gomez-Moreno, JE. Mate-Sánchez, P. Ramirez-Fernández and F.Chiva, Femtosecond laser microstructuring of zirconia dental implants, J Biomed Mater Res B Appl Biomater, 96 (2011) 91-100.
- [4] RA. Delgado-Ruíz, M. Abboud, G. Romanos, A. Aguilar-Salvatierra, G. Gomez-Moreno and JL. Calvo-Guirado, Peri-implant bone organization surrounding zirconia-microgrooved surfaces circularly polarized light and confocal laser scanning microscopy study, Clin Oral Impl Res, 26 (2015) 1328-1337.
- [5] M. Hirota, T. Harai, S. Ishibashi, M. Mizutani and T. Hayakawa, Dent. Mater. J, (2019) in press.
- [6] M. Yoshinari, Y. Oda, T. Inoue and M. Shimono, Dry-process surface modification for titanium dental implants, Metallurgical and Materials Transactions A, 33, 2 (2002) 511-519.
- [7] M. NODA, Y. Okuda, J. Tsuruki, Y. Minesaki, Y. Takenouchi and S. Ban, Surface damages of zirconia by Nd:YAG dental laser irradiation, Dent Mater J, 29, 5 (2010) 536-541.
- [8] R. Wenzel, Resistance of solid surfaces to wetting by water, Ind. Eng. Chem. Res., 28, 8 (1936) 988-994.
- [9] K. Shibata, M. Yoshitani, T. Kanbayashi, R. Kawamura and M. Yoshinari, Influence of Storage in Water after Super-Hydrophilic Treatment of Titanium Surfaces on Osteoblast Behavior Implant, J. Jpn. Soc. Oral, 30, 3 (2017) 200-209.

Topical Review

Manufacturing technologies toward extreme precision

Zhiyu Zhang^{1,2}, Jiwang Yan²  and Tsunemoto Kuriyagawa³

¹ Key Laboratory of Optical System Advanced Manufacturing Technology, Changchun Institute of Optics, Fine Mechanics and Physics, Chinese Academy of Sciences, Changchun 130033, People's Republic of China

² Department of Mechanical Engineering, Keio University, Yokohama 223-8522, Japan

³ Department of Mechanical Systems Engineering, Tohoku University, Sendai 980-8575, Japan

E-mail: yan@mech.keio.ac.jp

Received 5 April 2019, revised 6 May 2019

Accepted for publication 8 May 2019

Published 18 June 2019



Abstract

Precision is one of the most important aspects of manufacturing. High precision creates high quality, high performance, exchangeability, reliability, and added value for industrial products. Over the past decades, remarkable advances have been achieved in the area of high-precision manufacturing technologies, where the form accuracy approaches the nanometer level and surface roughness the atomic level. These extremely high precision manufacturing technologies enable the development of high-performance optical elements, semiconductor substrates, biomedical parts, and so on, thereby enhancing the ability of human beings to explore the macro- and microscopic mysteries and potentialities of the natural world. In this paper, state-of-the-art high-precision material removal manufacturing technologies, especially ultraprecision cutting, grinding, deterministic form correction polishing, and supersmooth polishing, are reviewed and compared with insights into their principles, methodologies, and applications. The key issues in extreme precision manufacturing that should be considered for future R&D are discussed.

Keywords: ultraprecision cutting, grinding, polishing, supersmooth surface, ultraprecision measurement, extreme precision


(Some figures may appear in colour only in the online journal)

1. Introduction

The term 'manufacturing technologies' refers to the processes by which raw materials are transformed into final products. The study of manufacturing technologies has been a part of human activity since ancient times. Three kinds of material processing technologies have been developed in response to manufacturing needs: (1) subtractive manufacturing, (2) additive manufacturing, and (3) material forming.

Subtractive manufacturing is undoubtedly the most widely used process, in which a workpiece is shaped by removing material away from a bulk of material. The process of removing unnecessary material from a workpiece is termed machining. Mechanical machining is further divided into cutting methods, such as turning, milling, drilling, etc, and abrasive machining methods, such as grinding, lapping, and polishing.

Additive manufacturing is a process by which a workpiece is constructed by depositing material in layers such that it becomes a predesigned shape. Three-dimensional (3D) printing is one of the common processes of additive manufacturing. Additive manufacturing is suitable for small-sized components containing enclosed features that cannot be

 Original content from this work may be used under the terms of the [Creative Commons Attribution 3.0 licence](https://creativecommons.org/licenses/by/3.0/). Any further distribution of this work must maintain attribution to the author(s) and the title of the work, journal citation and DOI.

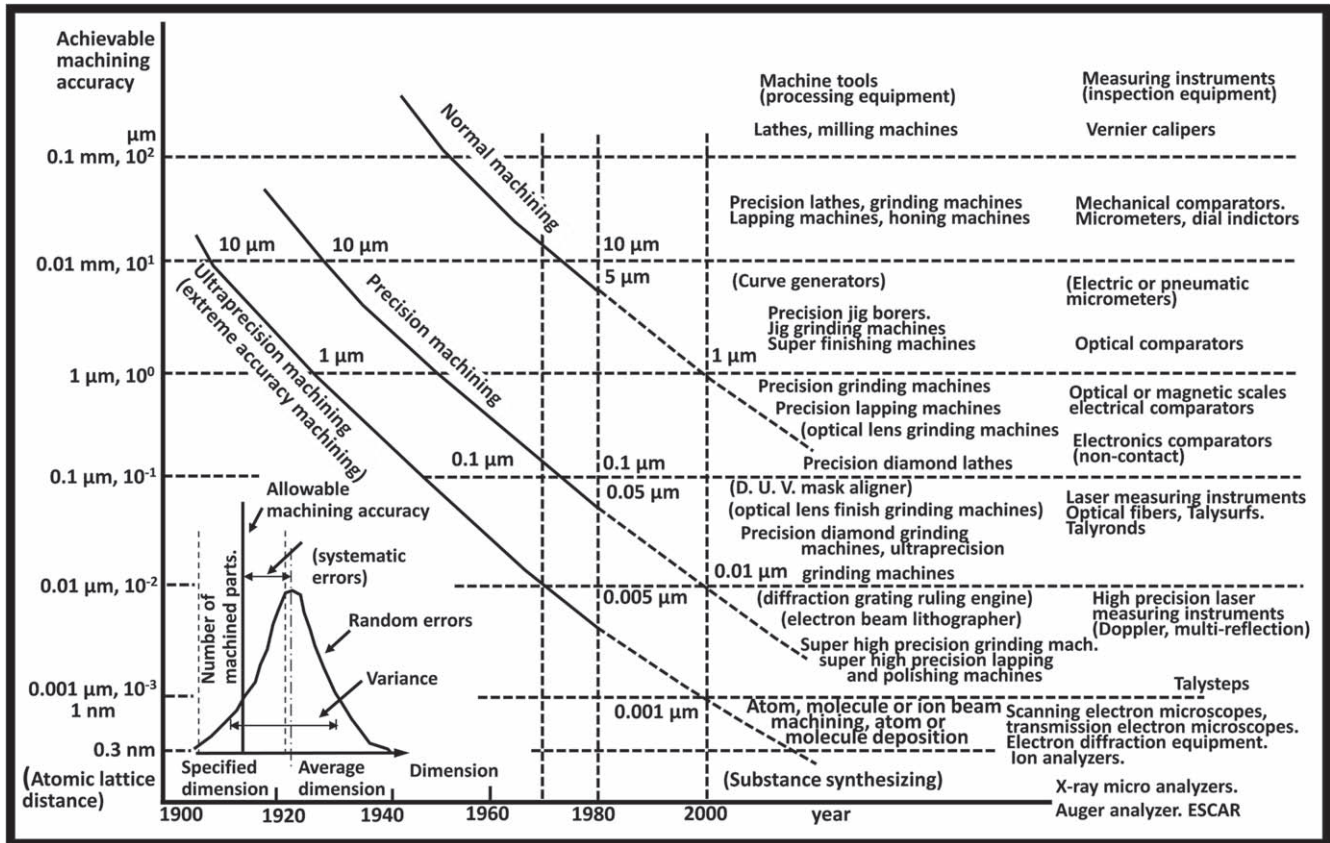


Figure 1. Taniguchi chart to predict the development of machining accuracy.

machined by subtractive manufacturing. Material forming generally refers to methods that change the shape or internal/external structure of the workpiece without changing the material volume. These processes include casting, forging, press/injection molding, stamping, and imprinting. Each of the above-mentioned processes has its own advantages and limitations. Therefore, manufacturing technology encompasses a very vast area and provides the tools that enable fabrication of a broad range of products.

In this paper, we focus on subtractive manufacturing, i.e. machining processes, because a huge number of diverse engineering materials (metals, semiconductors, optical glasses, ceramics, composite materials, and polymers) can be machined; and a large variety of functional surfaces (with optical, mechanical, microfluidic, bionic, or electronic functions) can be achieved. Another reason for the focus on subtractive manufacturing is that this method can achieve extremely high precision which cannot be achieved by other methods.

In recent years, various high-performance optics, optoelectronics, and semiconductor products have emerged which require manufacturing technologies of higher and higher precision. For example, the surface roughness of a substrate used in a ring laser gyroscope is required to reach a roughness average (R_a) of <0.5 nm and a flatness of $N < 30$ nm. The surface roughness of mirrors in deep ultraviolet (DUV) lasers and ultrahigh power laser systems is required to reach an $R_a < 0.2$ nm and a flatness of $N < 60$ nm [1, 2]. In order to

realize extreme ultraviolet (EUV) exposure, the total thickness variation of a 12 inch bare silicon (Si) wafer is required to be less than 200 nm; and the middle spatial frequency roughness is required to be less than 0.1 nm [3]. In addition, inertial confinement fusion (ICF) is a fusion energy research project that attempts to initiate nuclear fusion reactions by heating and compressing a fuel target, typically in the form of a pellet that contains a mixture of deuterium and tritium. To compress and heat the fuel, energy is delivered to the outer layer of the target using high-energy laser beams. Each ICF system requires more than 7000 pieces of high-precision, large optical components [4].

In 1983, Taniguchi proposed a chart to predict the development of achievable machining accuracy over time [5]. The Taniguchi chart is considered to be the Moore's law of the machining field. According to the chart, shown in figure 1, normal machining by the year 2020 comes in at better than 200 nm accuracy. Precision machining comes in currently at about 5 nm capability. It is worth noting that ultraprecision machining (extremely accurate machining) can produce an accuracy of better than 0.3 nm, reaching atomic or molecular scale precision. The way to achieve this precision is either through the subtractive process (atom/molecule removal or ion beam machining) or the additive process (atom/molecule deposition). Taniguchi's predictions are very close to the state-of-the-art (as of the year 2019) process and precision levels, especially for ultraprecision machining accuracy.

Ultraprecision machining is the final processing method for obtaining high form accuracy and low surface roughness. In recent decades, ultraprecision machining has been demonstrated to be a deterministic method for achieving high accuracy and cost-effectiveness for the generation of functional surfaces. At present, through multi-axis machining, optical or near-optical surface finish and micro/nanostructures can be directly created in freeform surfaces. Applications of ultraprecision machining have ranged from optics to illumination, astronomy, automobiles, biomedical products, and so on. Ultraprecision machining technology plays an important role in the construction of a nation's industry and economy.

2. Typical ultraprecision machining processes

At present, ultraprecision machining technologies can be roughly divided into four categories: (1) ultraprecision cutting, (2) ultraprecision grinding, (3) corrective polishing, and (4) supersmooth polishing. This section will provide a brief summary of the fundamentals of these technologies.

2.1. Ultraprecision cutting

Ultraprecision cutting uses ultraprecision lathes and single-crystal diamond tools to machine a workpiece. As the tool-workpiece interface is limited to a very small region approaching a point, ultraprecision cutting is also referred to as single-point diamond turning (SPDT). The diamond tool edge can be sharpened to the nanometer scale, which enables removal of an extremely thin layer of material and finally realizes the generation of high form accuracy and a smooth surface. Ultraprecision cutting is suitable for processing ductile materials, such as nonferrous metals, plastics, and some infrared optical crystal materials. A form accuracy of less than 100 nm and a surface R_a of less than 1 nm can be achieved by ultraprecision cutting [6].

2.2. Ultraprecision grinding

Ultraprecision grinding uses ultraprecision grinders and grinding wheels with fine/ultrafine abrasive grains to obtain a form accuracy of ~ 100 nm and a surface R_a of ~ 10 nm. Ultraprecision grinding is suitable for processing hard and brittle materials, such as fused silica, silicon carbide, ceramics, etc. The grinding wheel usually needs to be precisely dressed to make the abrasive particles keep protruding from the wheel surface. After grinding, the grinding trace left on the ground surface is extremely fine; and the residual surface height is very small [7].

2.3. Corrective polishing

Although ultraprecision cutting and grinding can produce an optical surface which can be directly used for infrared optics and even for visible lights, sometimes after ultraprecision cutting and grinding, the form error of the machined surface cannot meet the high precision requirements, especially for

ultraviolet optics. In such a case, corrective polishing is needed. Polishing has been traditionally used for reducing the surface roughness of a workpiece or changing the dimensional or geometric accuracy of a workpiece by manual control of pad pressure or dwelling time. However, in the field of ultraprecision machining, the polishing pressure and dwelling time can now be precisely controlled on a highly local zone on a workpiece surface, thus corrective polishing is a common method used to achieve nanometric form accuracy.

A variety of corrective polishing techniques were developed to improve the surface form accuracy, such as computer-controlled optical surfacing (CCOS) [8], stressed-lap polishing [9], bonnet polishing [10], and magnetorheological finishing (MRF) [11]. These methods use different polishing tools and abrasive particles to improve the workpiece surface finish by means of mechanical, electromagnetic, chemical, or electrochemical actions. Another nonmechanical method for ultraprecision form correction is ion beam figuring (IBF) [12]. As will be discussed later in this paper, deterministic form correction has been widely used in processing the optical elements with extreme precision, such as a large-aperture telescope and DUV/EUV lithography optics.

2.4. Supersmooth polishing

As for ultraprecision optical elements, not only is high-precision form accuracy required, but a supersmooth surface is indispensable. Some supersmooth polishing techniques have been developed for the purpose of reducing surface roughness, such as bowl-feed polishing [13], float polishing [14], elastic emission machining (EEM) [15], microfluid jet polishing (MFJP) [16], and use of the canon super smooth polisher [17]. Moreover, it should be pointed out that the combination of supersmooth polishing and corrective polishing may be used in the final finishing phase for optical elements with extreme precision where an extremely high level of surface form accuracy and low surface roughness are required at the same time.

To date, there have been a number of review papers in the precision manufacturing field written from different perspectives [18–25]. There have also been several books published recently that review precision manufacturing technologies [26–29]. However, much higher precision has been required in recent years, and advanced optics with more complex surfaces, such as microstructured and freeform surfaces and optics with extremely small/large dimensions have been attracting attention due to their unique optical performance. Continuing improvements and new challenges in the fabrication of large-aperture, extremely accurate, and supersmooth aspheric optical surfaces, such as EUV lithography, require the surface roughness of EUV mirrors to be machined at the subangstrom level [30].

Therefore, a comprehensive review of state-of-the-art manufacturing technologies for achieving extreme precision is necessary. In this paper, we review the latest challenges for manufacturing technologies that have received extensive attention in the high-precision optical fabrication and

optoelectronic engineering fields in recent years and identify some future directions of R&D activities in this area.

3. Advances in manufacturing precision

3.1. Early developments

Ultraprecision machining technology has important applications in the field of optical components fabrication. Because optical elements need to manipulate light waves, the accurate manufacturing of their surfaces should be on the order of optical wavelength. Therefore, the development of ultraprecision machining technology has been driven by the need for ultraprecision optical components.

Ultraprecision cutting technology originated in the 1950s. Ultraprecision cutting, i.e. SPDT technology, was first developed in order to meet the processing requirements of aluminum mirrors [31]. With high processing efficiency and high surface finish, this technology has become the main processing method for optical mirrors, especially for batch processing of aluminum/copper mirrors. With the increasing requirements for processing accuracy during the past decades, ultraprecision cutting has been widely used for processing of nonferrous metals, nonelectrolytic plated nickel, soft and brittle optical crystals, and some optical plastics. The surface roughness can reach the nanometer level, and the surface form accuracy can reach the submicron level [32–34].

Because it is difficult to process hard and brittle materials by ultraprecision cutting, diamond grinding is an alternative used for machining glass and ceramics. In recent years, the development of on-machine dressing technology for grinding wheels has caused ultraprecision grinding to play an important role in the processing of hard and brittle materials.

However, grinding usually generates grinding marks on the surface and internal material defects, i.e. subsurface damage (SSD) inside the workpiece. Thus subsequent polishing is normally needed. For semiconductor wafers, such as silicon, silicon carbide, and gallium nitride, which have plane surfaces, chemo-mechanical polishing (CMP) planarization is generally required to remove the grinding marks and grinding-induced SSD after ultraprecision grinding.

3.2. State-of-the-art precision level

Advances in precision manufacturing have been greatly driven by astronomy. Astronomy is an ancient science, which has a far-reaching and wide-ranging impact on human beings. The development of astronomy urgently requires the construction of advanced experimental equipment. Astronomical telescopes have always been the indispensable research tool to observe distant planets, galaxies, and other astronomical objects. The angular resolution of a telescope optical system is determined by the working wavelength and the system aperture. The relationship can be expressed as [35]:

$$\alpha = \frac{1.22\lambda}{D}, \quad (1)$$

where α is the angular resolution, λ is the working wavelength, and D is the telescope aperture. By increasing the

aperture D , the angular resolution of the system can be effectively improved; and the energy collection ability of the system can be improved at the same time. Thus, more dim objects of the universe can be observed. Therefore, large-aperture aspheric optical elements have been used more and more widely in modern optical telescope systems.

In order to obtain high-resolution images, high form accuracy as well as low surface roughness of less than 1 nm Ra over an aperture range of several meters is required. For example, the primary mirror of a very large telescope is an 8.2 m diameter mirror; and the level of form accuracy achieved is 18–43 nm root mean square (rms) for a surface roughness of 0.8–2 nm over the full aperture [36]. A 14 nm rms form error was achieved for the 8.2 m diameter mirror of the Japanese Subaru Telescope [37]. Moreover, the diameter of the primary reflective mirror in the Hubble Space Telescope (HST) is 2.4 m. The form accuracy achieved in the effective aperture was 8 nm in rms [38–40].

Such rigorous requirements for form accuracy and surface roughness are extremely difficult to achieve and cannot be directly obtained even by ultraprecision turning or ultraprecision grinding methods. Normally, such optical elements need to be manufactured by ultraprecision turning (for ductile materials) or grinding (for hard brittle materials) as the preceding process and ultimately manufactured by a subaperture corrective polishing process with iterative measurements and corrections of local form errors [41]. Sometimes, large-aperture optics have to be decomposed into a number of smaller pieces of segments, and each segment is machined individually. After machining, the segments are then combined together and aligned by numerous high-precision actuators to achieve total form accuracy. In a word, astronomy is undoubtedly one of the main forces driving the development of ultraprecision manufacturing engineering. Astronomers' need for large-aperture telescopes is constantly challenging the extreme-precision manufacturing capabilities of humans.

The aforementioned large-aperture telescopes are mainly used to control visible light with a wavelength band between 350 and 750 nm [42]. If light with a shorter wavelength needs to be controlled, the manufacturing accuracy of optical components will become more stringent. Typical applications of short wavelength optics are objective lenses in lithographic machines, alternatively called steppers, for semiconductor chip fabrication.

In recent decades, there has been rapid progress in the integrated circuit industry with more and more functionality being packed onto a single chip, which is largely being driven by the rapid progress of photolithography [43]. Photolithography is the process of transferring geometric patterns on a mask to the surface of a Si wafer using a stepper. For a lithographic system, the line-width resolution R (minimum feature size) is determined by the Rayleigh formula [44]:

$$R = \frac{k\lambda}{NA}, \quad (2)$$

where λ is the wavelength of light, NA is the numerical aperture (the brightness of the projection lens), and k is a constant process factor.

Table 1. Precision levels and manufacturing methods for typical applications.

Applications	Form accuracy (nm rms)	Surface roughness (nm rms)	Manufacturing methods
Eye glasses	2000	10	Hot press or injection
Illumination optics	300	2	Grinding + polishing
Projector optics	300	1	Precision grinding + polishing
Photo optics, consumer devices	100	1	Ultraprecision grinding + polishing
Space optics	20	0.5	Corrective polishing + supersmooth polishing
DUV projection lithography system	2	0.3	Corrective polishing + supersmooth polishing
EUV projection lithography system	0.1	0.05	Corrective polishing + supersmooth polishing

In order to create finer patterns, a light source providing a shorter wavelength is needed. The state-of-the-art lithography tools use DUV light from argon fluoride (ArF) excimer lasers with wavelengths of 193 nm, which has enabled transistor feature sizes to shrink below 10 nm [45]. A typical projection system consists of 28 fused silica lenses, and 7 of them are aspherical lenses with a maximum diameter of 280 mm [46]. It should be noted that, in the case of lithography optics, the specification for surface roughness measurement is further subdivided into middle spatial frequency range (MSFR), high spatial frequency range (HSFR), and extended HSFR [47, 48]. Carl Zeiss has investigated the influence of errors in different frequency bands on the performance of optical systems [49]. The surface form error causes image distortion and introduces various aberrations. The MSFR error causes small-angle scattering and flares, which will affect the imaging contrast. The HSFR error will cause large-angle scattering and reduce the refractivity of the lenses [50]. Therefore, the errors of every spatial frequency, namely surface form accuracy, waviness, and roughness, should be precisely controlled to the nanometer level.

According to the previous research results, the surface form accuracy of each DUV lens should be 2 nm rms; and the MSFR error should be 0.3 nm rms [51–56]. As the diameter of an atom is 0.1–0.2 nm, the atoms on the surface need to be removed layer by layer if the size fluctuation range of the machined surface is in the subnanometer order, which is the ultimate target processing accuracy, namely, atomic-level accuracy.

Even higher precision is required. Extreme ultraviolet lithography is the latest lithography technology using an EUV wavelength of 13.5 nm [57]. The reflective projection system in an EUV lithographic machine has the highest accuracy of the reflective optical systems. The wavefront error of the all-reflective EUV mirror system is required to be 1 nm, and thus the accuracy of a single mirror element is required to reach the 0.1 nm level. The MSFR, which determines the flare level of the system, is critical in overall EUV lithography. An extremely smooth surface should be polished with MSFR roughness down to 0.05 nm rms [58]. It means that manufacturing technology and metrology should close the loop for form accuracy control on the subatomic level. Therefore, the manufacturing of the EUV mirrors is full of tough challenges, representing the highest level of ultraprecision machining in

the contemporary era [59–64]. Table 1 lists some precision levels and manufacturing methods for typical applications.

In the semiconductor industry, another need for an atomic level surface finish is CMP of bare Si wafers. In general, Si wafers are polished using an elastic polisher and a slurry made from ultrafine silicon dioxide (SiO₂) particles (approximately 10 nm in size) suspended in an alkaline solution of approximately 10 pH. The Si wafers are required to be polished to a high-quality surface with a surface roughness of 0.1 nm *Ra* and a flatness of about 1 μm in the 12 inch range without any resultant defect from the former processes.

Overall, in order to achieve such high flatness and surface finish, the resolution of surface material removal must reach the atomic or subatomic level. The manufacturing process is accompanied by many unprecedented subatomic level phenomena. Therefore, clarifying the new principles and the physical and chemical phenomena of the nanometric- and atomic-level manufacturing processes is the fundamental requirement for the manufacturing of the above-mentioned optical elements.

4. New developments in ultraprecision manufacturing

4.1. Ultraprecision cutting

4.1.1. Materials to cut. Ultraprecision cutting has become one of the most important methods used for the direct machining of ductile materials, such as aluminum, copper, copper alloy, silver, gold, electroless plated nickel, and acrylic plastic, to optical quality without the need for a subsequent polishing process. These materials are very difficult to machine into a mirror surface by abrasive machining processes because they are soft, and the abrasives scratch the finished surface. In addition, this process is unable to produce high levels of flatness at the edges of the machined surface.

On the other hand, some hard and brittle materials, such as Si and germanium (Ge) can also be finished to a surface roughness of a few nm *Ra*. Gerchman and McLain [65] published their results of early work on the machining of Ge in which they diamond-turned Ge to a surface roughness of

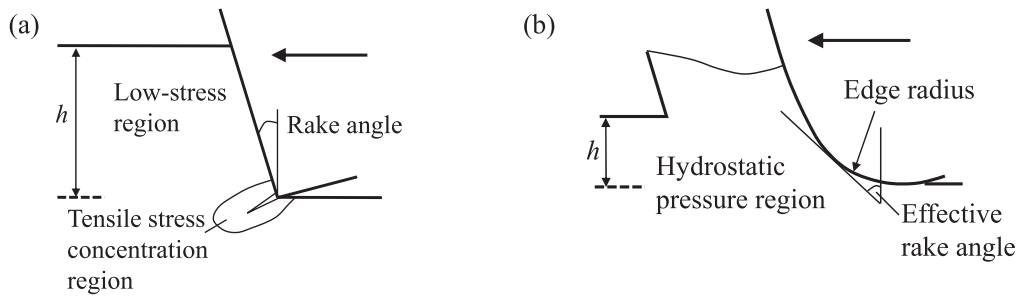


Figure 2. Schematic diagrams for (a) brittle-regime cutting and (b) ductile-regime cutting.

5–6 nm Ra. The machined samples were 50 mm in diameter with spherical surfaces. The material removal rate in diamond turning was given in terms of a tool feed of $2.5 \mu\text{m}$ per revolution of the workpiece together with a $25 \mu\text{m}$ depth of cut. More recently, Shore [66] has reported that material removal rates on the order of $2\text{--}4 \text{ mm}^3$ per minute have been obtained in diamond turning of Ge optics with a 100 mm diameter. The tool life (expressed as the effective cutting distance of the tool) when producing optical surfaces ($<1 \text{ nm Ra}$) at these removal rates was in excess of 12 km. More detail on this subject is provided in the next section.

Every sword has two edges, and diamond cutting is no exception. A diamond tool wears at a very high rate during the cutting process of ferrous materials [67–69]. In general, a diamond tool cannot be used for turning steels, irons, titanium, and pure nickel. This is due primarily to the graphitization of diamond induced by the catalytic reaction with the ferrous materials even at ambient temperatures.

4.1.2. Ductile-regime cutting of brittle materials. In recent decades, research efforts have focused on the ultraprecision diamond turning of hard and brittle materials. It is well known that the surface roughness and SSD caused by diamond turning of a hard and brittle material could be reduced as the undeformed chip thickness t is reduced to the submicron scale or smaller. There exists a critical value for t below which surface damage does not occur. This critical value is known as the critical undeformed chip thickness (t_c). The process of machining hard and brittle materials in such a mode is called ductile-regime machining. When the undeformed chip thickness is larger than t_c , however, cracks are generated, forming fractured cutting chips. These two different machining regimes are schematically shown in figure 2 [70]. The brittle-ductile transition is originated from a tensile to compressive stress state transition in the cutting region due to the effect of edge radius. In order to improve the surface finish in diamond turning of hard and brittle materials, it is desirable to machine them in a ductile-regime way in that continuous cutting chips are formed, thus leaving a crack-free surface.

Ductile-regime cutting can be realized by reducing the undeformed chip thickness to a certain value. The cutting performance is strongly determined by the conditions of the cutting tool edge [69]. If the diamond tool edge wears severely, ductile-regime cutting will change to brittle-regime

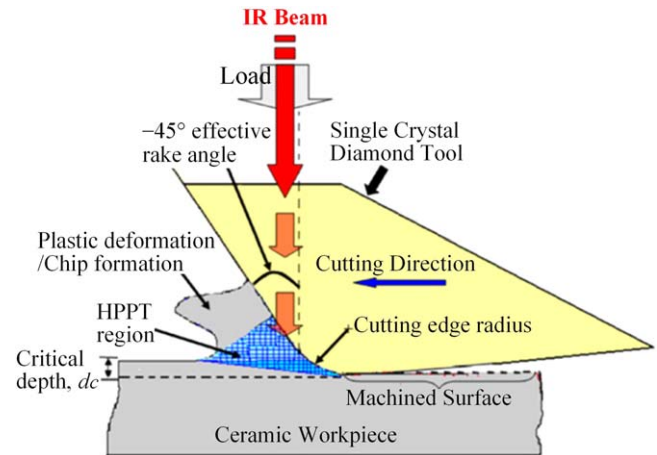


Figure 3. Schematic of laser-assisted cutting by directly heating the cutting zone. Reprinted from [73], Copyright 2015, with permission from The Society of Manufacturing Engineers.

machining even though the undeformed chip thickness is smaller than t_c . Therefore, keeping the cutting tool edge sharp and reducing the tool wear rate plays a significant role in the application of ductile-regime cutting technologies. While tool wear cannot be completely avoided, it can be minimized to some extent if the temperature rise is suppressed and the lubrication of the tool-workpiece interface is improved [71].

Laser-assisted cutting was recently reported to be a potential method for realizing low tool wear ductile cutting of some hard and brittle materials. Traditionally, the heat-assisted cutting techniques were applied in such a way that the heating zone was in front of the cutting tool, softening materials prior to chip formation. In 2005, Patten *et al* [72, 73] proposed micro laser-assisted machining (μ -LAM), as shown in figure 3, where the laser beam passes directly through the cutting tool and heats the cutting zone. After that, Ravindra *et al* [74] investigated the ductile mode material removal and high-pressure phase transformation in silicon during the μ -LAM process. Their results demonstrated that the optimized laser power condition resulted in a greater critical depth of cut and a nearly damage-free or cured diamond structure silicon (Si-I), similar to that of the original workpiece phase.

Using alternative tool materials is another challenge. As diamond tools are prone to graphitization at high temperature, they are not suitable for carbon alloy cutting. Wei *et al* [75]

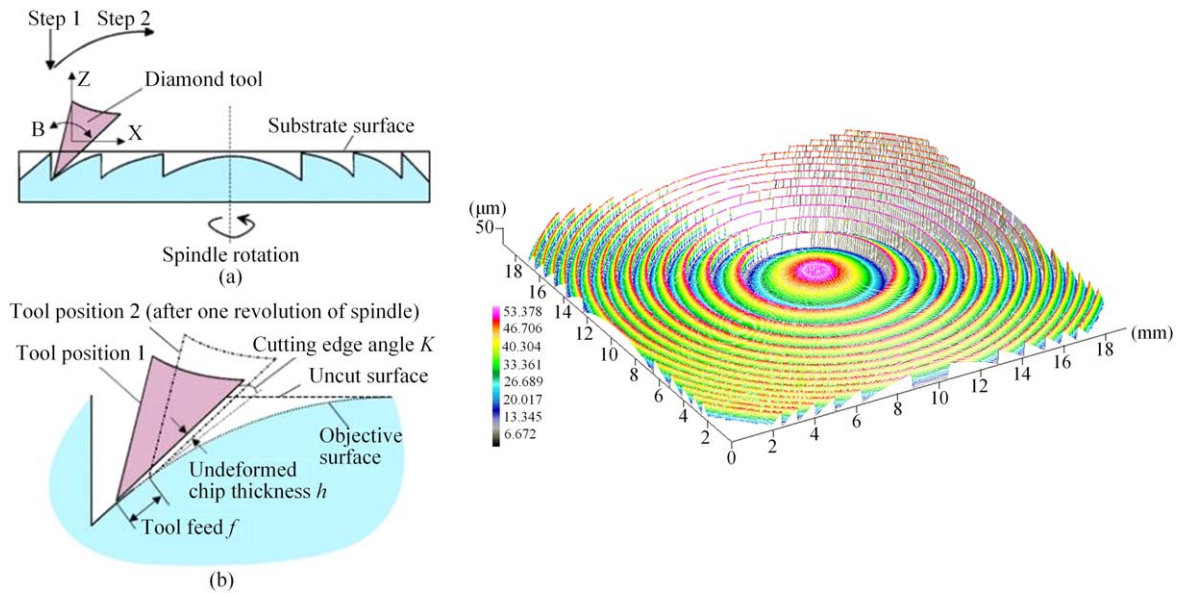


Figure 4. Schematic diagrams for the microgrooving process for fabricating Fresnel lenses on single-crystal Ge and a surface topography of the machined lens. Reproduced from [80]. © IOP Publishing Ltd. All rights reserved.

investigated laser-assisted cutting with a sapphire tool that has high heat resistance.

4.1.3. Microstructure cutting. Microstructures with a high aspect ratio, such as V-grooves, pyramids, and microlens arrays, can enhance the functionality of surfaces in many ways. Such microstructured optics are used in various optical applications for imaging, illumination, or light concentration [76–79]. One example is the Fresnel lens, which can be machined by diamond turning with the tool path matching the contour of the structure. For example, the microgrooving process was performed on single-crystal Ge for fabricating infrared Fresnel lenses [80], where a sharply pointed diamond tool was used to generate the micro-Fresnel structures under three-axis ultraprecision numerical control, as shown in figure 4. By adopting a small angle between the cutting edge and the tangent of the objective surface, this method enabled the uniform thinning of the undeformed chip thickness to the nanometric range and thus provided complete ductile regime machining of brittle materials. A Fresnel lens, which has a form error of $0.5 \mu\text{m}$ and a surface roughness of $20\text{--}50 \text{ nm Ry}$ was successfully fabricated during a single tool pass.

Another example of microstructure cutting on hard and brittle material is the machining for spherical and hexagonal concave microlens arrays on a single-crystal Si wafer by STS diamond turning, as shown in figure 5 [81]. The rapid fabrication of microlens arrays on the surface of single crystal Si was realized by the sectional cutting method where the follow-up error of the tool servo was suppressed. Microlens arrays with a form error of $\sim 300 \text{ nm}$ peak-to-valley (PV) and a surface roughness of $\sim 6 \text{ nm Sa}$ were successfully fabricated.

4.1.4. Ultrasonic-vibration assisted cutting. Hardened steel is a common die material developed for molding plastic and glass optical elements. However, conventional diamond cutting is not applicable to steel materials due to the extremely severe chemical tool wear [82]. In the last few decades, ultrasonic vibration cutting technology has been successfully applied to difficult-to-cut materials [83, 84]. Shamoto *et al* [85] proposed the elliptical vibration cutting (EVC) method, as shown in figure 6. The feasibility of cutting steel with diamond tools was verified by applying EVC. Moreover, the vibration amplitude of the EVC is actively controlled while machining. Thus, the depth of cut can be changed rapidly just like using a fast tool servo (FTS). This technology combines the advantages of EVC and FTS, which enables fabrication of micro/nanostructures on difficult-to-cut materials [86]. The EVC system developed was applied to sculpture arbitrary micro-/nanostructures by vibration amplitude control. Subsequently, a nanometer-scale sculpture was fabricated on a hardened steel surface. Figure 7 shows an example of a machined angle grid surface with a height of $1 \mu\text{m}$ and a wavelength of $150 \mu\text{m}$ on hardened steel [87].

4.1.5. Fly cutting of large crystals. Fly cutting is an intermittent cutting process in which a diamond tool is mounted to the end of a spindle to intermittently cut a workpiece [88–91]. This process has important applications in the production of large flat surfaces. Figure 8 is an example of fly cutting of potassium dihydrogen phosphate (KDP) crystal which has excellent nonlinear optical properties [4]. Potassium dihydrogen phosphate crystal is a typical soft, brittle material which has poor processing properties, such as easy deliquescence and mechanical anisotropy [92]. This makes it one of the most difficult to cut materials. Ultraprecision fly cutting has proven to be an effective processing method to fabricate large-sized KDP crystals. The

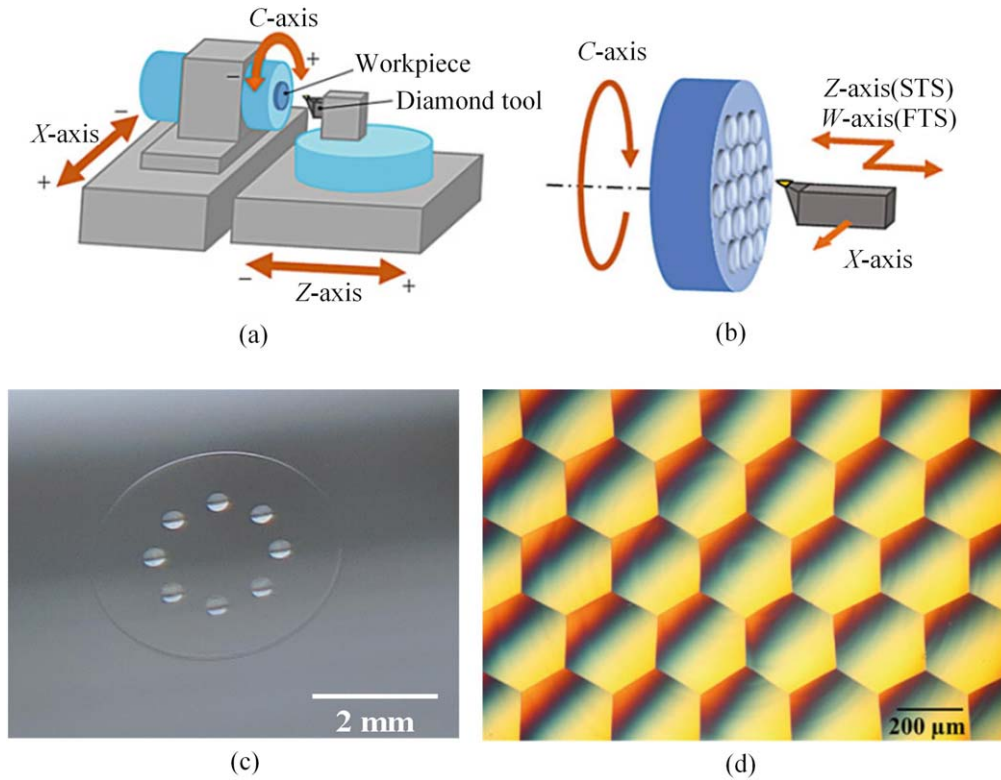


Figure 5. Spherical and hexagonal microlens arrays on a single-crystal Si wafer machined by slow tool servo diamond turning. Reprinted from [81], Copyright 2017, with permission from Elsevier.

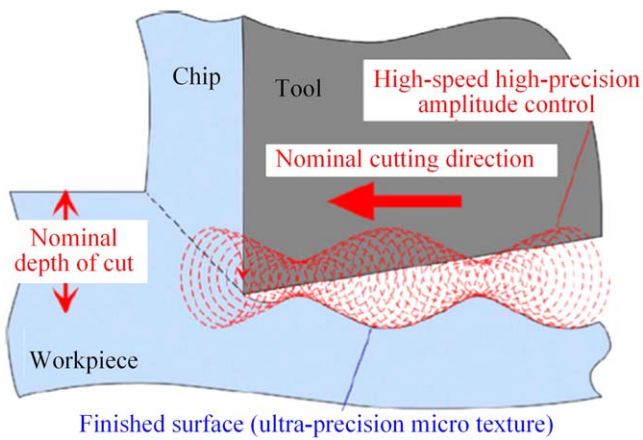


Figure 6. Amplitude control sculpturing method in elliptical vibration cutting. Reprinted from [85], Copyright 1994, with permission from CIRP.

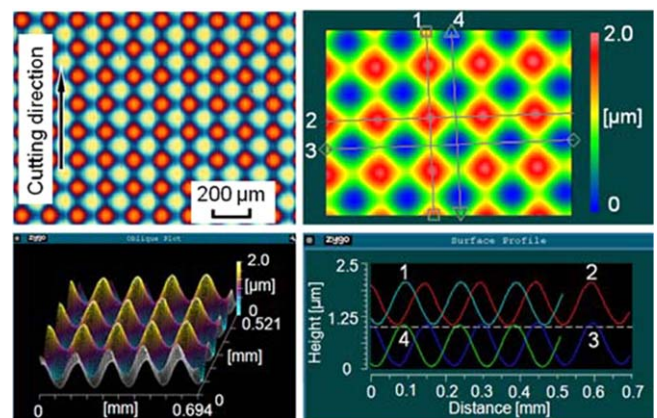


Figure 7. Machined angle grid surface with a height of $1 \mu\text{m}$ and a wavelength of $150 \mu\text{m}$. Reproduced from [87]. CC BY 3.0.

flatness of large KDP crystals was machined within 500 nm , and the surface roughness reached 1 nm Ra [93–95]. Recently, the fly cutting method has also been equipped with a slow FTS to fabricate hybrid structural surfaces on freeform surfaces [96].

4.1.6. Diamond turning of roll-to-roll imprinting molds. Diamond turning of high-precision molds is a vital process for the roll-to-roll resin imprinting process used in fabricating

subwavelength gratings [97–102]. Jones *et al* [103] presented a focused-ion-beam fabricated diamond tool for producing submicron structures through a roll-based mastering method. Burr formation was minimized, and the surface quality of the product was improved by optimizing the tool shape and the microcutting conditions. Liu *et al* [104] suggested that a higher cutting speed was the most critical factor influencing the mold accuracy. The experimental result demonstrated that through the strict control of cutting parameters, diamond turning was an effective approach for ensuring the continual mass production of subwavelength gratings. Moreover, Terabayashi *et al* [105] proposed a method for machining

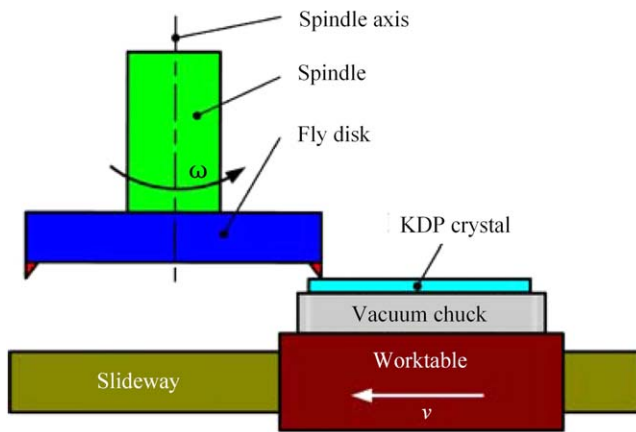


Figure 8. Schematic of the processing of large-aperture KDP crystal by fly cutting. [4] 2016. Reprinted by permission of the publisher (Taylor & Francis Ltd, <http://tandfonline.com>).

two-directional wavy microgrooves by using a slow tool servo (STS) system. As shown in figure 9, microgrooving experiments using a two-axis STS system were conducted on cylindrical oxygen-free copper roller molds to machine various wavy microgrooves. The resulting form accuracy on the roll mold was at the $\sim 1 \mu\text{m}$ level and surface roughness was at the $\sim 10 \text{ nm}$ level. The machined roller mold was used for ultraviolet resin imprinting, and high-precision replication of the two-directional wavy structures was realized. These structures are very useful for reducing fluid drag.

4.2. Ultraprecision grinding

Ultraprecision grinding is primarily used to generate high-quality, functional surfaces made of difficult-to-machine materials, such as hard and brittle materials. Through the multipoint cutting actions of ultrafine abrasive grains, ultraprecision grinding can generate parts with high surface finish, high form accuracy, and high surface integrity at reduced tool wear, compared to diamond cutting.

4.2.1. Ductile mode grinding. The fracture toughness of hard and brittle materials, such as glass, is very small, only 10^{-2} – 10^{-3} of the metal materials [106]. Therefore, cracks appear easily during the grinding of hard and brittle materials. In recent decades, it has been established that the ultraprecision machine enabling an extremely small feed rate can achieve ultraprecision mirror surface grinding, which is similar to the grinding of metal materials. Thus, the transition from brittle-to-ductile material removal is considered to be of great importance for ultraprecision grinding. Until now, intensive research efforts have been focused on the ductile grinding of a variety of hard and brittle materials, such as Si [107], silicon carbide (SiC) [108], and optical glasses [109, 110].

The critical depth of cut (critical chip thickness in a 3D model) for ductile-brittle transition is the most critical parameter to produce a ductile ground surface. Ductile grinding of hard and brittle materials requires a maximum chip thickness not exceeding the critical value for crack

initiation. In most cases, the critical chip thickness in grinding is different from that in cutting due to the significant difference in the edge geometries between a diamond cutting tool and abrasive grains. Several investigations about the critical depth of cut brittle materials have been conducted by indentation and scratching. A simple equation was developed for the calculation of the critical depth of cut in grinding in terms of material properties [111]

$$d_c = 0.15 \left(\frac{E}{H} \right) \left(\frac{K_c}{H} \right)^2, \quad (3)$$

where E is Young's modulus, K_c is fracture toughness, and H is hardness. The critical chip thickness can be estimated from equation (1).

To achieve ductile mode grinding, a diamond wheel having fine/ultrafine grains is critical [112]. Essentially, truing/dressing the wheel surface to make a uniform protrusion of grains is a key point for ductile mode grinding.

4.2.2. Grinding kinematics. In recent years, several grinding kinematics, including cross-grinding, parallel grinding, and wheel-axis adaptive grinding, have been developed for the precision grinding of curved surfaces [113–115]. Cross-grinding is the most common grinding technique for large convex surfaces. As shown in figure 10(a), the rotational direction of the workpiece and the cutting direction of the wheel are perpendicular at the grinding point. The wheel wear is concentrated at the contact point. Therefore, it is difficult to obtain a high form of accuracy when the workpiece is very hard and the size is large. Parallel grinding employs an arc-shaped grinding wheel, where the grinding spindle is tilted with respect to the workpiece axis [113]. As shown in figure 10(b), the grinding point moves along the grinding wheel, thus the wheel wear could be dispersed over a large area, which is helpful for improving form accuracy. However, the form accuracy of the grinding wheel must be high for parallel grinding, which is a critical issue.

Wheel-axis adaptive grinding means the wheel axis always changes to keep the wheel normal to the workpiece surface [116]. As shown in figure 10(c), the grinding point remains constant during grinding as a result of the tool-axis rotation. This grinding mode has a very low requirement of wheel form accuracy. However, wheel wears rapidly at the fixed grinding point, which introduces a gradually increased form error on the ground surface.

4.2.3. In-process dressing technologies. In order to reduce the surface roughness and SSD on ground wafers, grinding wheels with smaller diamond grains are desirable. However, when the size of diamond grains decreases to micron scale with a high concentration, it is very difficult for the wheel to maintain sufficient self-dressing ability [117].

To solve this problem, the electrolytic in-process dressing (ELID) grinding method was proposed. The ELID continuously exposes new sharp abrasive grains by dissolving the bond material (mainly cast iron) around the abrasive grains [118]. As shown in figure 11, the wheel surface had

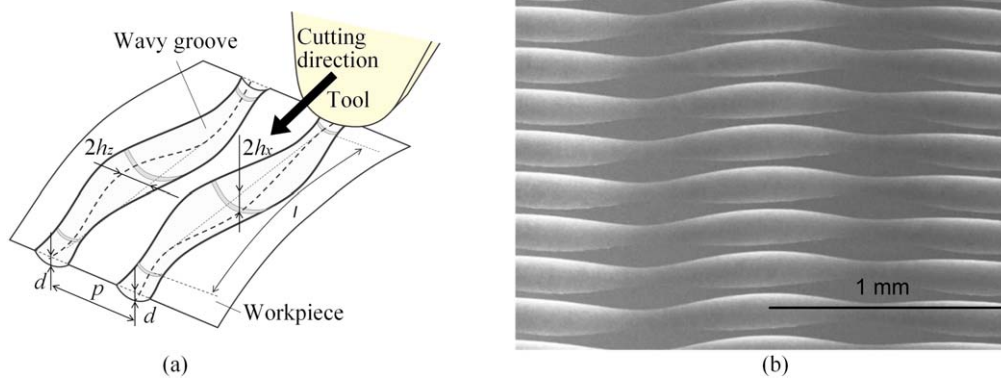


Figure 9. Slow-tool-servo turning for two-directional wavy microgrooves. Reproduced with permission from. Reproduced with permission from [105].

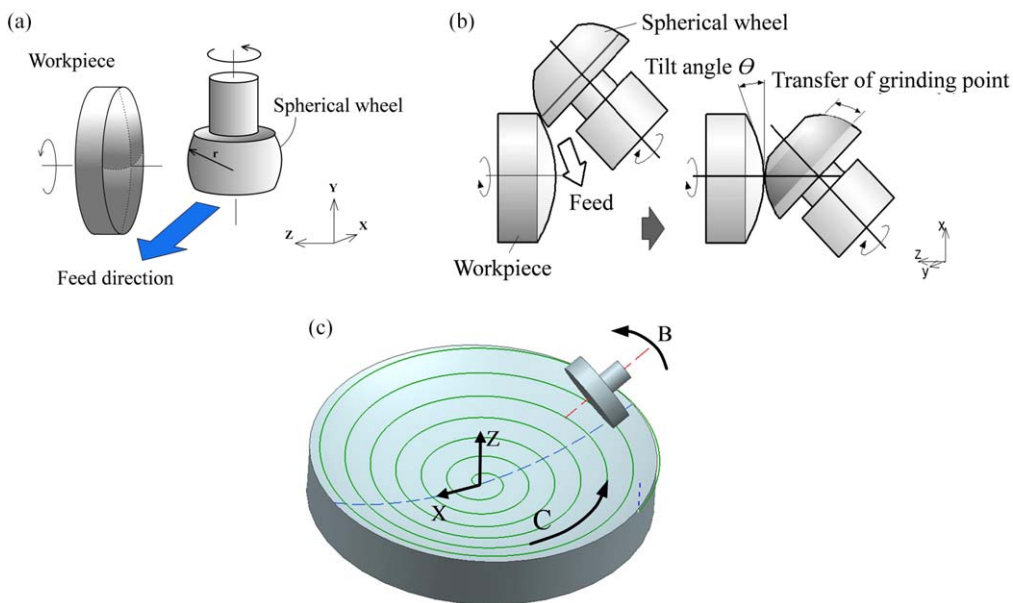


Figure 10. Relative motion between wheel and workpiece: (a) cross-grinding method, (b) parallel grinding method, and (c) wheel-axis adaptive grinding. [116] 2016 © Springer-Verlag London. With permission of Springer.

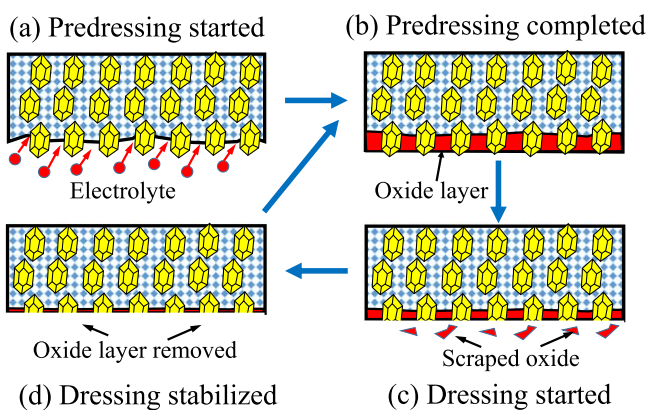


Figure 11. Principle of ELID grinding. Reproduced with permission from [118].

good conductivity at the predressing stage. The conductivity of the wheel surface was reduced with the growth of the oxide layer thickness. However, the oxide layer became worn along with the grinding action. The wear of the oxide layer caused

an increase in conductivity of the wheel surface. Thus, the electrolysis could be restarted and the oxide layer regenerated. By this manner, the protrusion of the grains remains constant during grinding.

In 1985, ELID grinding of ceramics was reported using metal-bond diamond wheels with grain sizes smaller than 30 μm [119]. Afterward, the ELID technique was further improved. In 1995, ELID grinding experiments on silicon wafers were conducted with a 5 nm grain size iron-bonded diamond grinding wheel. A superfine surface with R_a 3.29 \AA was successfully achieved [120]. In recent years, ELID has become an important manufacturing process for hard-to-machine materials, although several technical barriers have been reported for ELID grinding to achieve extreme precision [121]. For example, the material removal rate in ELID grinding of Si wafers is low compared to conventional wafer grinding. As the wheels are dressed during the grinding process, the wheel wear must be precisely compensated for in order to obtain high dimensional accuracy. Thus, it is difficult

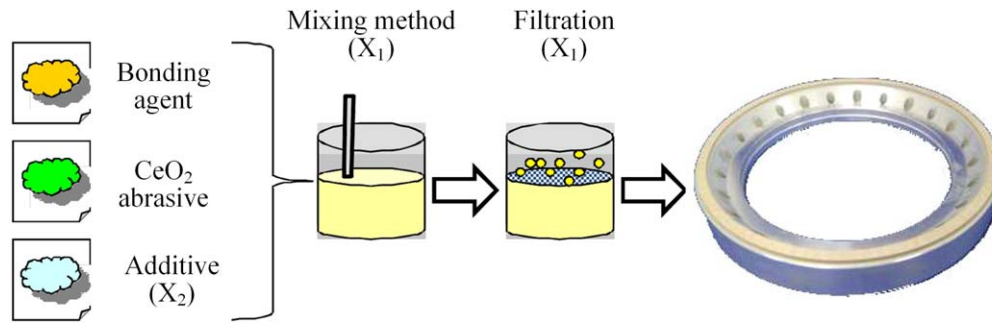


Figure 12. Manufacturing process of the CMG wheel. Reprinted from [130], Copyright 2012, with permission from Elsevier.

for ELID grinding to achieve high wafer flatness. In addition, the oxide layer on the ground surface has been reported to be a problem with ELID grinding [122].

In addition to ELID, there are a variety of other in-process dressing methods, such as electrochemical in-process controlled dressing (ECD) [123], laser dressing [124], laser-assisted dressing [125], water-jet in-process dressing [126], ultrasonic dressing [127], and electrical discharge dressing [128]. These methods all have their advantages and problems and need to be studied further prior to application in ultraprecision grinding.

4.2.4. Chemo-mechanical grinding technology. Diamond grinding induces grinding marks and SSD in the form of crystal defects and amorphous layers [129]. Those defects can be removed in the subsequent CMP process [130]. As an alternative, Zhou *et al* [131] proposed the chemo-mechanical-grinding (CMG) process, which combines the advantages of both grinding and polishing. The CMG is a fixed abrasive process integrating chemical reaction and mechanical grinding into one process and shows advantages against CMP in efficiency, geometric controllability, and waste disposal. Figure 12 shows the manufacturing process of the CMG wheel [132]. The experimental results indicated that the CMG process could achieve supersurface finishing comparable to that obtained from CMP by decreasing the wheel abrasive hardness and introducing chemical reactions with the workpiece surface [133, 134]. The application of CMG in the processing of crystalline materials, such as silicon [135], quartz glass [136], and sapphire [137] have been reported. A major issue in CMG is the relatively low material removal rate.

4.2.5. Microstructure grinding. Microstructures on nonferrous metals can be machined by single-point diamond machining [6]; grinding is preferred for processing hard materials, especially ceramics such as fused quartz glass, SiC, and tungsten carbide (WC). A number of such grinding processes have been developed in recent years. For example, Guo *et al* [138] proposed an ultrasonic-vibration-assisted grinding technique to fabricate microstructured surfaces. The experimental results indicated that the introduction of ultrasonic vibration was able to both improve the surface finish and the edge sharpness of the microstructures. Micro-V-groove arrays and pyramid arrays were successfully

machined on binderless WC as well as SiC. The edge radius of the V-grooves and pyramids was less than $1 \mu\text{m}$ [139].

Figure 13 shows the schematic of grinding microgrooves [140]. The flat diamond grinding wheel is trued into a V-shaped microtip. The wheel moves horizontally along the cutting direction. Yin *et al* [141] developed a V-groove grinding process by applying ELID and microtruing operations. The minimum wheel tip radius of $8.2 \mu\text{m}$ was achieved by microtruing the grinding wheel in a diameter of 305 mm. Finally, a corner radius of V-groove ranging from 15 to $25.8 \mu\text{m}$ could be realized on a Ge surface. The grinding method developed was used in the fabrication of a large Ge immersion grating element for the SUBARU Telescope.

4.2.6. Grinding for large optics. The next generation of ground-based telescopes requires hundreds of meter-scale, off-axis reflective mirrors. To fulfill the fabrication demands, the Cranfield BoX™ grinding machine was developed to provide meter-scale grinding capability for optics at high material removal rates while minimizing levels of SSD [142–145]. The high loop stiffness of the BoX™ machine was demonstrated by the absence of edge roll-off and chipping, as well as the microlevel SSD layer. In the grinding of the European extremely large telescope 1.45 m freeform ZERODUR® segments, an rms form deviation of $<1 \text{ mm}$ for error-compensated grinding with a surface roughness of between 100 and 200 nm Ra was achieved [146].

Zhang *et al* [116] developed an ultrasonic-vibration-assisted, fix-point grinding technology. In-process compensation of surface form error was developed based on the wheel wear prediction and modification of the tool path. Using the grinding strategies developed, a 2 m SiC mirror blank, as shown in figure 14, was ground to a form accuracy of $2 \mu\text{m}$ in rms.

4.3. Corrective polishing

4.3.1. Computer-controlled optical surfacing. The form accuracy of the workpiece finished by cutting and grinding is determined by the high-precision spatial motion trajectory of the ultraprecision machine tools. In theory, the accuracy of a workpiece surface cannot exceed that of the machine tools.

In the 1970s, Rupp proposed the CCOS process [147]. As shown in figure 15, a polishing tool with a smaller

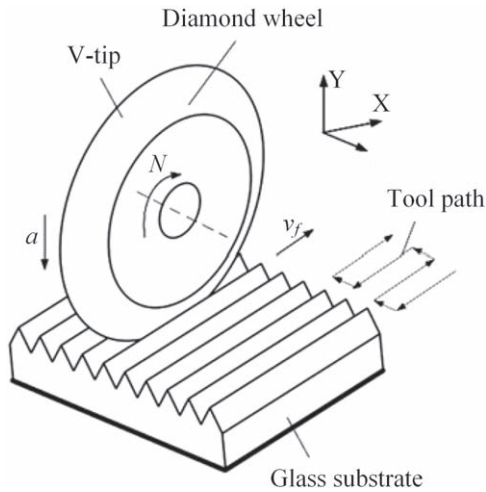


Figure 13. Schematic of microgrinding of microgroove. [140] © Springer Nature Singapore Pte Ltd, 2018. With permission of Springer.

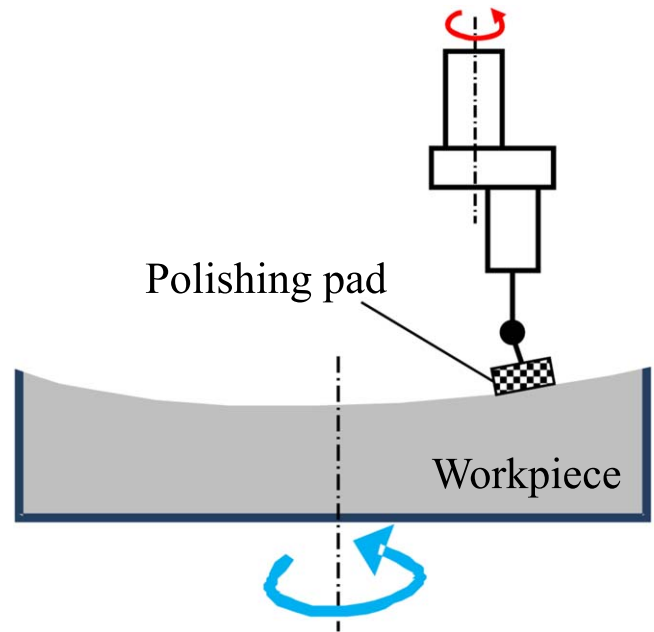


Figure 15. Schematic diagram of the CCOS.

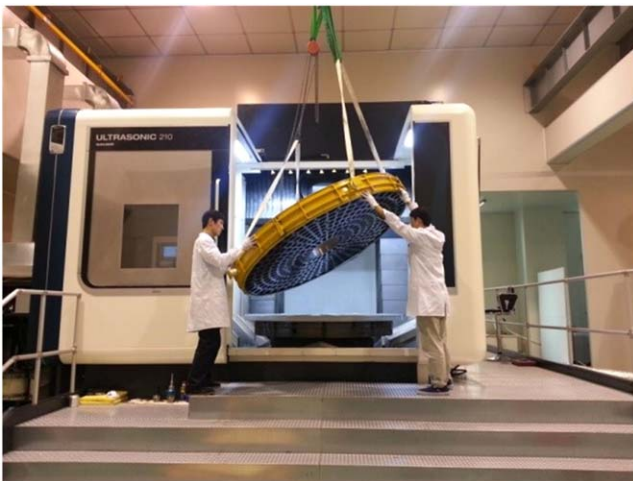


Figure 14. Mounting of a 2 m SiC mirror blank onto a machining center for surface grinding. [116] 2016 © Springer-Verlag London. With permission of Springer.

diameter than the workpiece is controlled to pass through the workpiece surface and polish off a certain amount of material at each individual point.

As shown in figure 16(a), the feed speed along the tool path is purposefully changed to control the dwell time (polishing time) at each point [149]. The polishing tool is controlled to ride on the high regions to cut off the peaks, while skipping the low regions without removing the material there. Therefore, a low frequency surface error can be corrected, as shown in figure 16(a). Theoretically, the amount of material removed is determined by the local dwell time and tool impact function (TIF). The TIF means the spatial removal amount of polishing tool in unit time. The material removed is a convolution of the removal function and the dwell time, given as follows:

$$H(x, y) = R(x, y) ** D(x, y), \quad (4)$$

where $H(x, y)$ is the desired removal function, $R(x, y)$ is the TIF per unit time, and $D(x, y)$ is the dwell time function. As shown in

figure 16(b), the high points in the polishing tool covered area, which suffer greater pressure, were removed first so that the high frequency surface errors were eliminated.

Computer-controlled optical surfacing uses an iterative approach to achieve the desired surface precision. First, the error distribution of the workpiece surface is obtained by accurate measurement. Then, the local dwell time of the polishing tool on the workpiece is calculated. After that, the polishing tool is controlled to correct the local surface errors on the workpiece surface. By sufficient rounds of error correction, extremely high-precision surfaces with a smooth surface could be achieved even using low-precision machine tools [148].

One of the early applications of the CCOS technology is the manufacture of the HST [150], and today CCOS is being widely used in the manufacture of high-precision large aspheric optical surfaces.

In CCOS, the polishing tool makes the physical contact and removes material from the workpiece. Thus, tool development is an especially complex task, especially for aspheric (or freeform) optics manufacturing. Local curvatures of an aspheric surface vary as a function of position on a workpiece; however, the CCOS uses a rigid polishing tool whose shape cannot change during polishing. When polishing a large aspheric surface, a rigid polishing tool cannot follow the curvature changes at different areas of the surface, resulting in the inconsistency of material removal rate and low efficiency of surface error convergence. In order to improve the performance of a rigid polishing tool, several flexible contact polishing methods were proposed to maintain good contact with the workpiece surface. These methods include stressed-lap polishing [151], bonnet polishing [152], and rigid conformal (RC) tool polishing [153], which will be reviewed as follows.

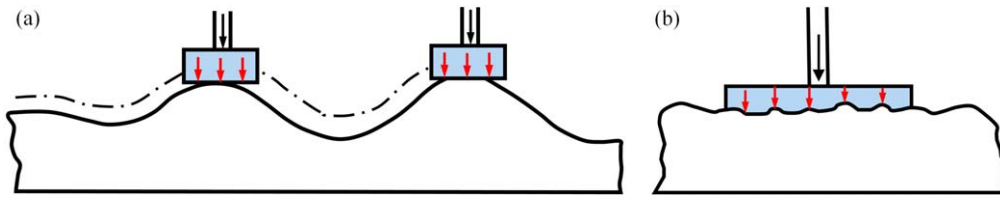


Figure 16. Figuring and smoothing through CCOS. Reprinted from [148], Copyright 1987, with permission from Elsevier.

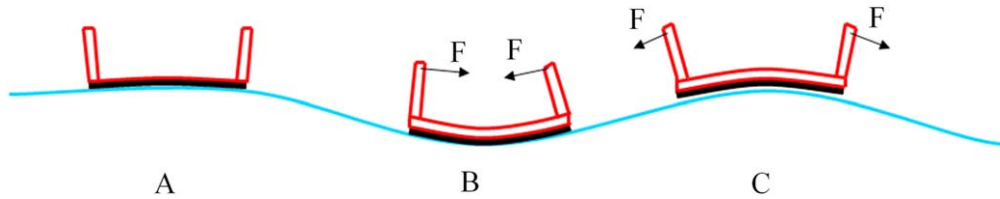


Figure 17. The schematic diagram of stressed-lap polishing technology. Reproduced with permission from [155].

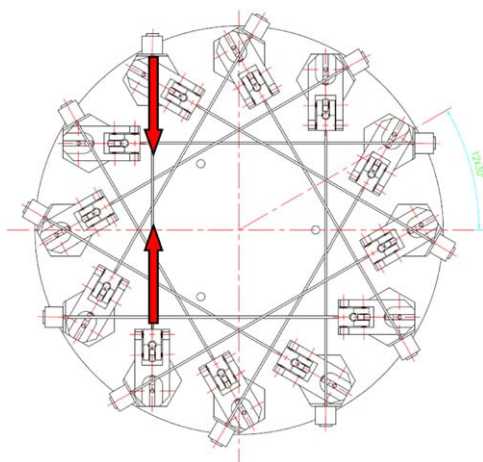


Figure 18. Top view of the stressed lap. Reproduced with permission from [155].

4.3.2. *Stressed-lap polishing.* As early as 1984, Angle *et al* [154] proposed that the polishing tool should be actively deformed in order to reproduce the subaperture shape of the aspheric mirror corresponding to the pad position on the mirror surface, as shown in figure 17 [156]. Based on this concept, several stressed laps were designed to change their shape in-process to coincide with the mirror surface during polishing [157–160]. Figure 18 shows one design of a stressed lap in which the deformation of the pad surface is achieved by drawing steel wire using a servo motor [155]. Stressed-lap polishing has significant advantages in the polishing of superlarge astronomical telescopes. One example is that an 8.4 m diameter primary mirror in the Giant Magellan Telescope (GMT) project was processed by the Steward Observatory Mirror Lab at the University of Arizona [161]. Stressed-lap polishing with a diameter of 1 m was developed. After polishing, full surface roughness and form accuracy reached 20 nm *Ra* and less than 1 μm , respectively [162].

4.3.3. *Bonnet polishing.* As shown in figure 19, the first principle of bonnet polishing is to use a flexible air bonnet as

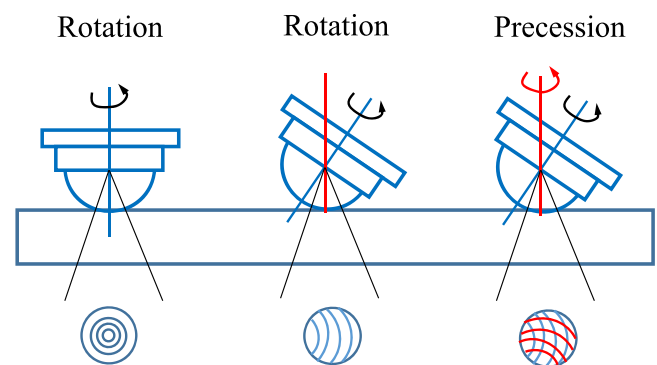


Figure 19. The schematic diagrams of the ‘precession’ motion in bonnet polishing.

the polishing tool [163]. The air pressure in the air bonnet can be adjusted in real time, and the outside of the air bonnet is covered with a layer of polishing cloth. The flexible air bonnet coincides with the workpiece surface.

The second principle of bonnet polishing is to use a kind of motion called ‘precession,’ which is different from the ‘rotation’ and ‘translation’ of a traditional polishing tool [164–166]. The precession motion is divided into two parts: (1) the air bonnet rotates around the normal direction of the tool and (2) the air bonnet rotates around the normal direction of the workpiece at a certain angle, as shown in figure 18. Due to the precession motion, bonnet polishing can homogenize the motion trajectory, thus improving the machined surface roughness.

Bonnet polishing is a kind of flexible polishing, which is characterized by high determinacy of TIF and high convergence efficiency. However, due to the use of a spherical air bonnet, the contact area with the workpiece is small; and the material removal efficiency is low.

4.3.4. *Rigid conformal lap polishing.* In 2009, Kim and Burge proposed a rigid conformal polishing tool that conforms to the aspheric shape yet maintains stability to provide natural smoothing for high spatial-frequency errors on the workpiece [167–169]. The tool uses an elastic rubber paste called

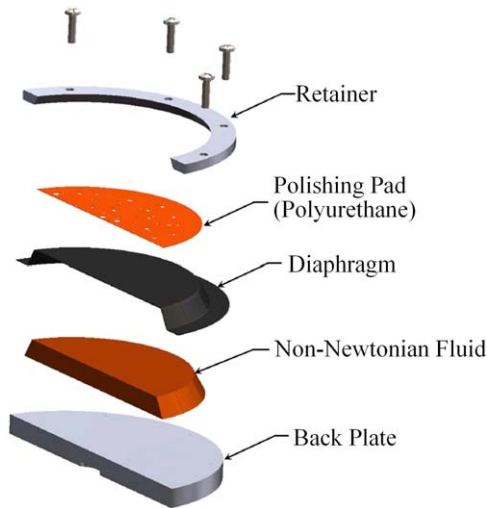


Figure 20. Three-dimensional schematic of rigid conformal lap structure. Reproduced with permission from [153]. © 2010 Optical Society of America.

Silly-Putty® as the deformed layer of the polishing tool, as shown in figure 20. Silly-Putty is an organosilicon polymer and a nonlinear viscoelastic non-Newtonian fluid [170]. The fluid has both flexibility and rigidity for different time scales. Under long-term stress, it shows the fluidity of liquid; under high-frequency stress, it shows the rigidity of solid. Therefore, the rigid conformal polishing tool has not only the ability of a flexible polishing tool for a nonspherical surface but also the smoothing effect of a rigid polishing tool.

Compared with CCOS methods, rigid conformal lap balances the advantages and disadvantages of various processing methods. Therefore, it has various advantages, such as excellent TIF stability, high material removal rate, and good physical smoothing ability. Moreover, rigid conformal lap can provide a supersmooth surface finish with <1 nm rms. This may eliminate the need for the final touch-up step for a supersmooth surface finish. Because of these competitive advantages, the rigid conformal lap polishing is very suitable for processing large aperture aspheric mirrors with high steepness and large deviation. The Steward Observatory Mirror Lab of the University of Arizona successfully applied this technology to the GMT 8.4 m primary mirror fabrication [171].

4.3.5. Magnetorheological finishing. The aforementioned polishing methods made changes to the polishing tool but did not change the polishing fluid or abrasives, thus it was difficult to ensure long-term stability of the TIF because of the poor consistency of particle concentration in polishing regions. In order to solve this problem, MRF was developed.

Magnetorheological finishing was originally proposed by Kordonski *et al* in the former Soviet Union [172]. The working principle of MRF is illustrated in figure 21 [173]. The magnetorheological fluid is composed of base fluid, surfactant, magnetic particles, and polishing particles. Magnetorheological fluid flows out of the nozzle and moves along the polishing wheel to the top area. The viscosity of

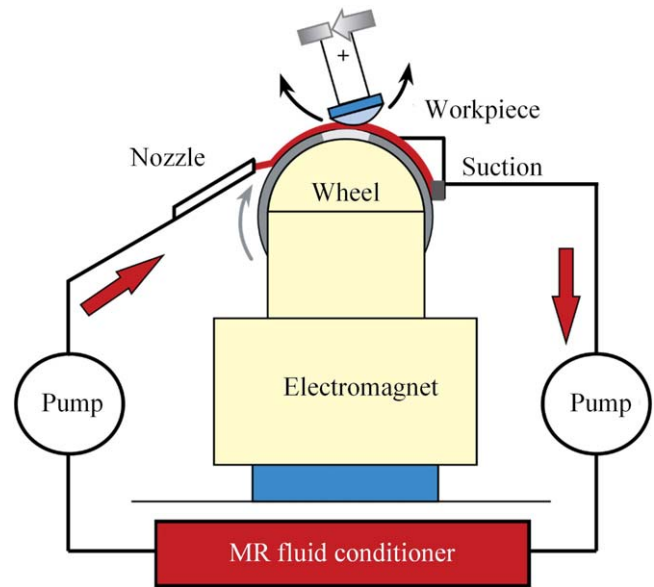


Figure 21. Mechanisms of MRF polishing and its material removal mechanism. Reproduced with permission from [173].

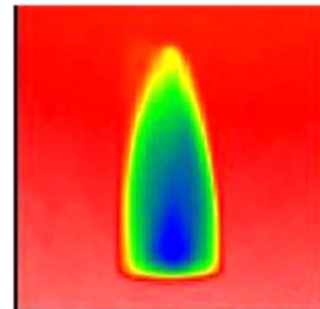


Figure 22. The tool impact function of MRF. Reproduced with permission from [179]. © 2011 Optical Society of America.

magnetorheological fluids increases instantaneously, becoming viscoplastic Bingham medium under the action of a high-intensity gradient magnetic field. When the Bingham medium passes through the narrow gap formed by the workpiece and the polishing wheel, it generates a great shear force at the contact area, thus removing the surface material of the workpiece.

Magnetorheological finishing is a deterministic polishing process because the polishing tool will not dull or wear [174–178]. The shape, the size, and the hardness of the flexible polishing belt can be controlled by adjustment of the magnetic field intensity at the polishing zone. Therefore, the material removal consistency of MRF is greatly improved compared with CCOS.

Figure 22 is the TIF shape of the MRF, which looks like a bullet [179]. Such a TIF has only one peak value and is very helpful for the convergence of surface error. However, the TIF of MRF is very small compared with traditional large polishing tools. Therefore, the material removal rate is low and the processing time of MRF is bound to be very long for large-aperture optical surfaces.

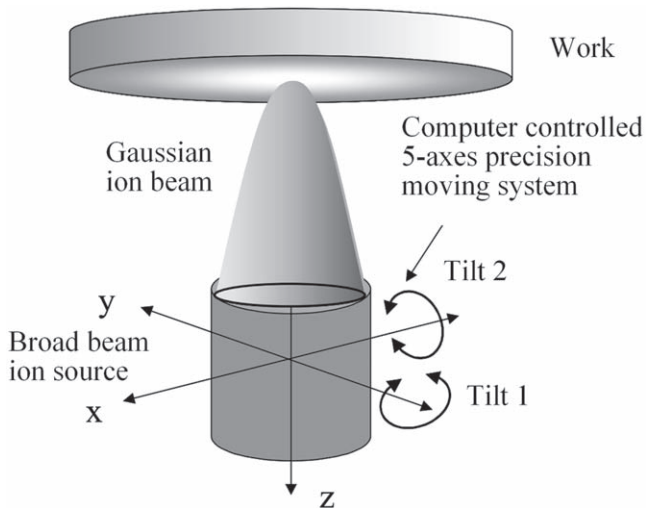


Figure 23. Schematic of the principle of ion beam figuring. [184] 2015 © Springer-Verlag London. With permission of Springer.

4.3.6. Ion beam figuring. The aforementioned polishing methods are all contact processes. The polishing tools exert a certain degree of pressure on the workpiece surface, which leads to print-through of the structure of a light weighted mirror [180]. Moreover, when the polishing tool moves to the mirror edge, the polishing area becomes smaller and the pressure increases, which inevitably leads to the edge roll-off phenomenon [181].

As a noncontact and nonmechanical process, IBF has been successfully applied in the polishing of space mirrors since the 1970s [182, 183]. Figure 23 shows the working principle of IBF [184]. IBF is a method of bombarding high-energy ions (generally argon ions) into the machined surface and removing materials by physical sputtering at the atomic level. One of the main advantages of IBF is the contactless nature of an ion beam as a polishing tool, which eliminates the edge roll-off effects of mechanical tools. Because the energy distribution of an ion beam can be accurately controlled, excellent stability of atomic-level removal can be achieved [185–187].

There are, however, a few trade-offs to these benefits. The deterministic removal of this method depends heavily on the stability of the ion source and the environmental stability of the vacuum chamber. The material removal efficiency of IBF is very low compared to mechanical methods due to atomic-level material removal characteristics.

4.4. Supersmooth polishing

4.4.1. Elastic emission machining. EEM was first proposed as a polishing method by Mori *et al* about 40 years ago [188]. EEM is a noncontact machining method that involves passing a flow of fine powder particles in pure water across the workpiece surface. As shown in figure 24, the particles supplied in a flow of pure water and the topmost atoms of the work surface are chemically removed at the atomic level. Hence, the work surface can be finished without defects. In

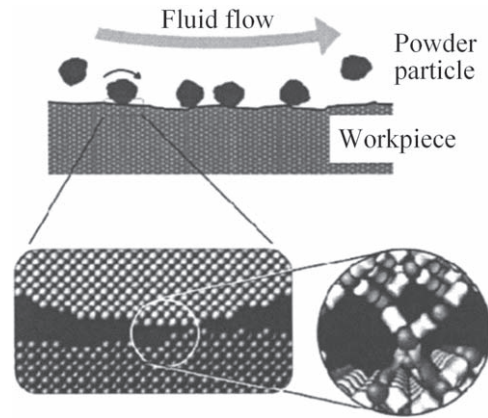


Figure 24. Schematic of atom removal process in EEM. Reproduced with permission from [189]. © American Vacuum Society.

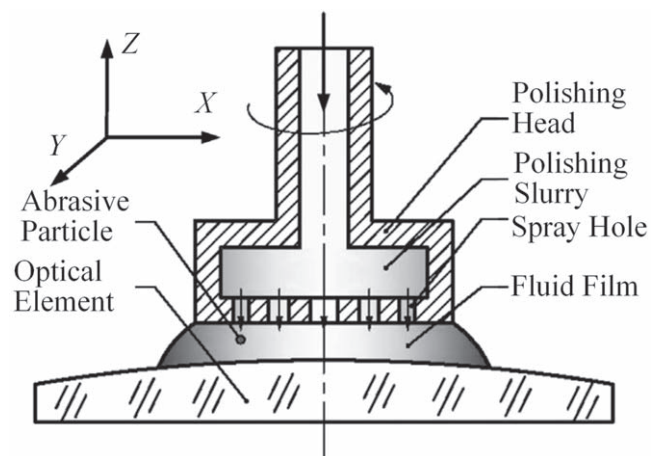


Figure 25. Principle of microfluid jet polishing. Reprinted from [190], Copyright 2013, with permission from Elsevier.

most cases, silica particles with submicron diameters are used as abrasives.

Kanaoka [189] investigated the smoothing performance of rotating-sphere EEM for processing ULE[®] and ZERODUR materials for EUV optics. It was demonstrated that the rms surface roughness converged to a constant value of 0.1 nm after removal of a certain depth of material. The surface roughness can thus be reduced to 0.1 nm rms or better, fulfilling the requirements of the EUV optics.

4.4.2. Microfluid jet polishing. In order to achieve supersmooth lenses for 193 nm projection lithography systems, Ma *et al* [190] proposed a supersmooth polishing method called MFJP, which combined the principles of float polishing, CCOS, and abrasive jet polishing. As shown in figure 25, the polishing slurry outflowed from the spray holes of the polishing head, lifting the polishing tool a certain distance through the dynamic pressure caused by the motion of the polishing slurry. The chemical reaction between the workpiece and the fine powder particles results in the removal of the topmost atoms from the workpiece surface.

A 100 mm diameter (95% effective aperture) fused silica flat optical element was polished using the MFJP method.

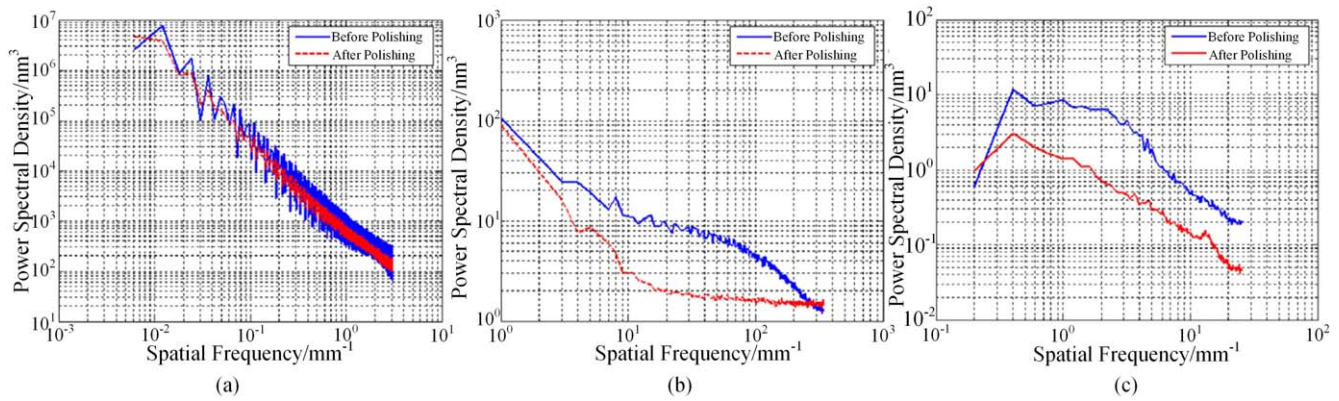


Figure 26. (a) Low, (b) mid-, and (c) high-spatial frequency PSD data. Reprinted from [190], Copyright 2013, with permission from Elsevier.

Testing results showed that the low-spatial form accuracy improved from 3.624 to 3.393 nm in rms, and the midspatial frequency surface roughness improved from 0.477 to 0.309 nm in rms. The high-spatial frequency surface roughness improved from 0.167 to 0.0802 nm in Rq. The power spectral density curve before and after supersmoothing uniform polishing is also shown in figure 26, in which the mid- and high-spatial frequency roughness was significantly improved; but the low-spatial surface form was not obviously changed.

5. On-machine measurement (OMM) and compensation

For the form error correction process, the precise measurement of the machined surface is an essential step. Metrology is the most important supporting technology for ultraprecision manufacturing. Without ultraprecision metrology, there will be no advance in the precision level of manufacturing. Typical surface metrology methods for ultraprecision surfaces include contact/noncontact profilometer, laser interferometer, white light interferometer microscope, and atomic force microscope. However, most of the above-mentioned measurement methods are off-machine methods. Because of the remounting process, off-machine measurements reduce manufacturing efficiency and may cause measurement error due to workpiece remounting and/or environmental changes. In order to solve these problems, on-machine metrology and error compensation based on the measurement result is expected.

There are several methods of realizing OMMs. A touching probe, i.e. the so-called linear variable differential transformer, is always installed on a commercial diamond turning machine. Other methods include laser and chromatic confocal probes, which are noncontact and nondestructive methods for surface measurement. For example, Chen *et al* [191] presented an OMM approach using a sapphire microprobe of 0.5 μm in radius for the grinding of tungsten carbide aspheric molds. The overall form error after grinding was obtained by subtracting the target form from the actual ground form. The aspheric surface had a high form accuracy of 0.177 μm after three compensation cycles. Li *et al* [192]

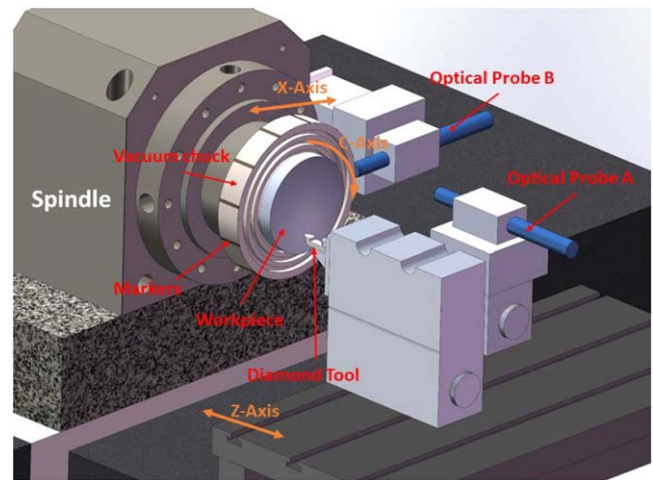


Figure 27. Schematic of the two-probe measurement system mounted on an ultraprecision lathe. Reproduced with permission from [195].

proposed an OMM system based on capacitive displacement sensors for high-precision optical surfaces. A 92% of full aperture measurement of a spherical aluminum mirror with a diameter of 300 mm was carried out, and the complete measurement of the form error required only 5 min. Zou *et al* [193] developed a chromatic confocal sensor to achieve noncontact measurement with nanometer-level accuracy for an ultraprecision turning machine and is capable of reconstructing the 3D surface topography of flat, spherical, and aspheric surfaces. Li *et al* [194] integrated a dispersed reference interferometer on an ultraprecision turning machine. Yan *et al* used a white-light interferometer for nanometer level precision on-machine profiling of curved diamond cutting tools [195]. Both theoretical and experimental investigation was conducted to prove the validity and effectiveness of the proposed calibration methodology. In addition, as shown in figure 27, Yu *et al* [196] proposed an OMM system using two optical probes to rapidly reconstruct the surface form from the radial and axial directions. Thus, a two-step compensation strategy to generate a modified tool path was developed. The results show that the OMM system and compensation strategy

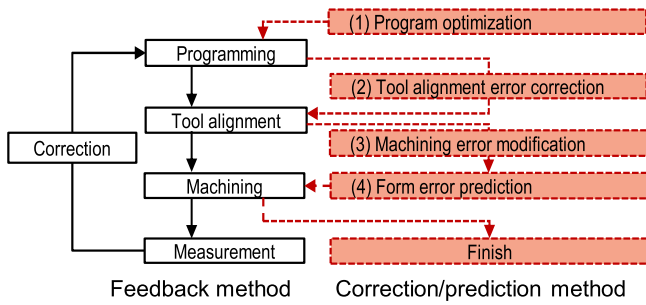
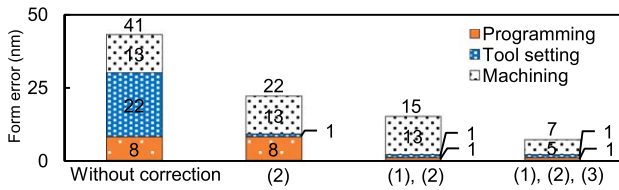
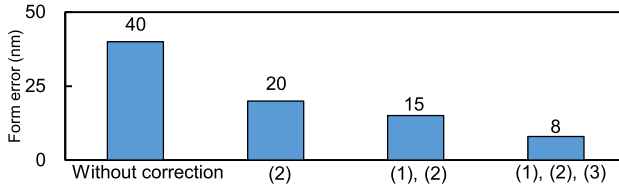


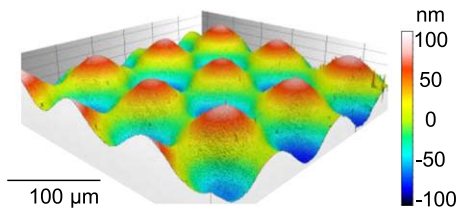
Figure 28. Diagrams of the correction/prediction machining flow. Reproduced from [196]. CC BY 4.0.



(a) Simulation results of form errors.



(b) Cutting results of form errors.



(c) 3D topography of the machined surface.

Figure 29. Results of simulation and experiment of form errors under different conditions of correction/prediction machining. Reproduced from [196]. CC BY 4.0.

were effective for improving the form accuracy while simultaneously enhancing the machining efficiency.

The error compensation strategy is a very important issue. For example, in diamond turning, a typical machining cycle consists of three steps: programming to generate tool paths, tool alignment step for tool-workpiece alignment, and machining for surface generation. A number of factors cause workpiece form errors during each step of the process. In a conventional process flow, the form error is corrected by using feedback correction, thus only a specific error factor is compensated for based on the experimentally measured form error. The machining-measurement cycle must be repeated many times because the form error decreases gradually in each cycle; and it is extremely difficult and time-consuming to reduce the form error completely.

Nagayama *et al* [197] proposed a new process flow which includes error correction and prediction, as shown in figure 28. The flow is composed of four steps: (1) program optimization, (2) tool alignment error correction, (3) machining error modification, and (4) form error prediction. In this flow, all of the main error factors are optimized in Steps (1), (2), and (3) based on error analysis; and the form error of the finished surface is predicted in step (4). All of the error corrections are carried out, and the finished form error is predicted before machining. In this way, a very high form accuracy can be obtained in a single cycle. Figures 29(a) and (b) show the simulation and experiment results of form errors under different conditions. In the simulation, the form error was predicted to be reduced by 80% with correction steps (1), (2), and (3), compared to the case of machining without any corrections. The results of the experiment agree well with the simulated results. Figure 29(c) shows the 3D topography of the surface machined after all of the correction steps. A 10 nm level sinusoidal wave grid was successfully fabricated on a single crystal Si wafer by STS turning, and the form accuracy was 8 nm PV [196].

6. Summary and outlook

Improving form accuracy and surface finish is the permanent pursuit of high-value-added manufacturing technologies. With the demands of the next generation EUV lithography, space optics and laser fusion technology, ultraprecision machining technologies are now stepping from the nanometer scale towards the atomic scale. In the past decades, remarkable advances have been achieved in the area of high-precision manufacturing technologies based on the significant developments in machine building technology, tooling technology, measurement and control technologies. Future R&D issues towards extreme precision manufacturing can be summarized as follows.

(1) Material removal mechanisms at the atomic scale

The theoretical clarification of the basic principles in the material removal process at the atomic level is essential for optimizing existing manufacturing technologies and developing new technologies. In the early 1990s, Japanese scholars used extremely sharpened single-crystal diamond tools to investigate experimentally the minimum chip thickness for metal cutting and demonstrated that a cutting thickness of 1 nm was possible. Cutting experiments in scanning electron microscopes and nanoindentation tests have been also used to clarify the nanoscale phenomena of machining. Such fundamental research will be still important in the future for challenging the ultimate dimensional accuracy of ultraprecision cutting. In recent years, molecular dynamics simulation has been applied to study the nanometric and atomic scale cutting, grinding, and polishing processes, which has made it easier for us to

reveal a material removal mechanism and investigate the machinability of various materials at small scales.

(2) *Surface/subsurface evaluation for extreme-precision machining*

With the development of high-resolution and high-reliability displacement sensors, noncontact OMM technology will have a major breakthrough in the future, which will enable deterministic compensation strategy of surface form errors. On the other hand, SSDs such as potential microcracks, phase transformations, and residual stresses, which cannot be directly measured from the surface, also affects the imaging quality, long-term stability, and laser-induced damage threshold of optical components. Therefore, characterization and control of subsurface properties has become one of the key issues in the optical and semiconductor manufacturing industry. It is necessary to develop integrated evaluation technologies to realize OMM, error compensation, and subsurface evaluation.

(3) *Compatibility of precision and cost-efficiency*

Some ultraprecision machining technologies can achieve high-quality surface finish and surface integrity, but the processing efficiency is very low. It will be a long-term goal of researchers in the field of ultraprecision machining to explore processing methods that can improve both cost-efficiency and accuracy. To achieve this goal, a multidisciplinary approach for manufacturing R&D by interfacing manufacturing with mechanical science, physics, material science and nanotechnology is necessary. There is still a long way to go in this direction towards the industrial application of the extreme-precision machining technologies to mass production of consumer products.

ORCID iDs

Jiwan Yan  <https://orcid.org/0000-0002-5155-3604>

References

- [1] Bordonaro G 2016 DUV Photolithography and materials *Encyclopedia of Nanotechnology* ed B Bhushan (Dordrecht: Springer) (https://doi.org/10.1007/978-94-007-6178-0_370-2)
- [2] Lawson J *et al* 1999 Surface figure and roughness tolerances for NIF optics and the interpretation of the gradient, P-V wavefront, and RMS specifications *Proc. SPIE* **3782** 510–7
- [3] Möller H 2018 Wafer processing *Handbook of Photovoltaic Silicon* ed D Yang (Berlin: Springer-Verlag GmbH)
- [4] Spaeth M *et al* 2016 Description of the NIF laser *Fusion Sci. Technol.* **69** 25–145
- [5] Taniguchi N 1983 Current status in, and future trends of, ultraprecision machining and ultrafine materials processing *CIRP Ann.* **32** 573–82
- [6] Meier A 2015 Diamond turning of diffractive microstructures *Precis. Eng.* **42** 253–60
- [7] Inasaki I 1987 Grinding of hard and brittle materials *CIRP Ann.* **36** 463–71
- [8] Jones R 1986 Computer-controlled optical surfacing with orbital tool motion *Opt. Eng.* **25** 256785
- [9] Anderson D *et al* 1992 Stressed-lap polishing of 3.5-m f/1.5 and 1.8-m f/1.0 mirrors *Proc. SPIE* **1531** 260–9
- [10] Walker D *et al* 2006 Use of the ‘precessions’™ process for prepolishing and correcting 2D & 21/2D form *Opt. Express* **14** 11787–95
- [11] Kordonski V *et al* 1998 Magnetorheological-suspension-based finishing technology *Proc. SPIE* **3326** 527–35
- [12] Allen L 1995 Progress in ion figuring large optics *Proc. SPIE* **2428** 237–47
- [13] Dietz R and Bennett J 1996 Bowl feed technique for producing super smooth optical surfaces *J. Appl. Opt.* **5** 881–2
- [14] Bennett J *et al* 1987 Float polishing of optical materials *J. Appl. Opt.* **26** 696–703
- [15] Mori Y, Yamauchi K and Endo K 1987 Elastic emission machining *J. Precis. Eng.* **9** 123–8
- [16] Beaucamp A 2018 Micro fluid jet polishing *Micro and Nano Fabrication Technology. Micro/Nano Technologies* ed J Yan (Singapore: Springer) (https://doi.org/10.1007/978-981-13-0098-1_10)
- [17] Manabu A *et al* 1995 Super-smooth polishing on aspherical surfaces *J. Nanotechnol.* **6** 111–20
- [18] Shore P *et al* 2010 Precision engineering of astronomy and gravity science *CIRP Ann.* **59** 694–716
- [19] Yuan J, Lyu B, Wei H and Deng Q 2017 Review on the progress of ultra-precision machining technologies *Front. Mech. Eng.* **12** 158–80
- [20] Brinksmeier E, Mutlugunes Y, Klocke F, Aurich J, Shore P and Ohmori H 2010 Ultra-precision grinding *CIRP Ann.—Manuf. Technol.* **59** 652–71
- [21] Esmaeilian B, Behdad S and Wang B 2016 The evolution and future of manufacturing: a review *J. Manuf. Syst.* **39** 79–100
- [22] Komanduri R, Lucca D and Tani Y 1997 Technological advances in fine abrasive processes *CIRP Ann.—Manuf. Technol.* **46** 545–96
- [23] Byrne G, Dornfeld D and Denkena B 2003 Advancing cutting technology *CIRP Ann.—Manuf. Technol.* **52** 483–507
- [24] Fang F, Gu C, Hao R, You K and Huang S 2018 Recent progress in surface integrity research and development *Engineering* **4** 754–8
- [25] Melentjeva R and Fang F 2018 Recent advances and challenges of abrasive jet machining *CIRP J. Manuf. Sci. Technol.* **22** 1–20
- [26] Andrew Y 2015 *Handbook of Manufacturing Engineering and Technology* (London: Springer)
- [27] Li S and Dai Y 2017 *Large and Middle-Scale Aperture Aspherical Surfaces: Lapping, Polishing and Measurement* (China: National Defense Industry Press)
- [28] Yan J 2018 *Micro and Nano Fabrication Technology* (Singapore: Springer) (<https://doi.org/10.1007/978-981-13-0098-1>)
- [29] Trent E and Wright P 2000 *Metal Cutting* 4th edn (Boston, MA: Butterworth-Heinemann) (<https://doi.org/10.1016/B978-075067069-2/50017-6>)
- [30] Rashed M, Hasan M and Luo X 2018 Promising lithography techniques for next-generation logic devices *Nanomanuf. Metrol.* **1** 67–81
- [31] Evans A 1979 Fracture mechanics applied to brittle materials American Society for Testing and Materials *Proc. 11th National Symposium on Fracture Mechanics: Part II*
- [32] Shimada S *et al* 1993 Feasibility study on ultimate accuracy in micro-cutting using molecular dynamics simulations *CIRP Ann.—Manuf. Technol.* **42** 91–4
- [33] Byrne G, Dornfeld D and Denkena B 2003 Advancing cutting technology *CIRP Ann.—Manuf. Technol.* **52** 483–507
- [34] Ohta T, Yan J, Kodera S, Yajima S, Horikawa N, Takahashi Y and Kuriyagawa T 2008 Coolant effects on tool

- wear in machining single-crystal silicon with diamond tools *Key Eng. Mater.* **389–390** 144–50
- [35] Malacara D 1992 *Optical Shop Testing* 2nd edn (New York: Wiley)
- [36] Mueller R, Hoeness H, Espiard J, Paseri J and Dierickx P 1993 The 8.2-m primary mirrors of the VLT *Messenger* **73** 1–8
- [37] Kaifu N 1998 Subaru telescope *Proc. SPIE* **3352** 14–22
- [38] Lallo M 2012 Experience with the Hubble space telescope: 20 years of an archetype *Opt. Eng.* **51** 011011
- [39] Kinney A 1995 Results from the corrected Hubble Space Telescope *Adv. Space Res.* **16** 5–13
- [40] Makidon R B *et al* 2006 The temporal optical behavior of the Hubble Space Telescope: the impact on science observations *Proc. SPIE* **6270** 62701L
- [41] Comley P, Morantz P, Shore P and Tonnellier X 2011 Grinding metre scale mirror segments for the E-ELT ground based telescope *CIRP Ann.—Manuf. Technol.* **60** 379–82
- [42] Wilson R 2002 *Reflecting telescope optics: II. Manufacture, testing, alignment Modern Techniques* (New York, LLC: Springer)
- [43] Helbert J 2001 *Handbook of VLSI Microlithography* (Noyes Park Ridge, NJ: William Andrew)
- [44] Harry J 2011 *Principles of Lithography* 3rd edn (Bellingham, WA: SPIE Press Monograph)
- [45] Lin B 2015 Making lithography work for the 7-nm node and beyond in overlay accuracy, resolution, defect, and cost *Microelectron. Eng.* **143** 91–101
- [46] Ikuta Y, Kikugawa S, Mishihiro T, Shimodaira N and Yoshizawa S 2001 New silica glass (AQF) for 157-nm lithography *Proc. SPIE* **4000** 1510–4
- [47] Sun L *et al* 2013 Review of resist-based flare measurement methods for extreme ultraviolet lithography *J. Micro/Nanolithogr. MEMS MOEMS* **12** 042001
- [48] Dinger U *et al* Fabrication and metrology of diffraction limited soft x-ray optics for the EUV microlithography *Proc. SPIE* **5193** 18–28
- [49] Becker K, Dörband B, Lörcher R and Schmidt M 1999 Aspheric optics at different quality levels and functional need *Proc. SPIE* **3739** 22–33
- [50] Saxer C and Freischlad K 2003 Interference microscope for sub-Angstrom surface roughness measurements *Proc. SPIE* **5144** 37–45
- [51] Ulrich W, Rostalski H and Hudyma R 2002 The development of dioptric projection lenses for DUV lithography *Proc. SPIE* **4832** 158–69
- [52] Cote D *et al* 2000 Advances in 193-nm lithography tools *Proc. SPIE* **4000** 542–50
- [53] Matsuyama T, Ohmura Y and Williamson D The lithographic lens: its history and evolution *Proc. SPIE* **6154** 615403
- [54] Cui Z 2017 *Nanofabrication by photons Nanofabrication* (Basel: Springer) (https://doi.org/10.1007/978-0-387-75577-9_2)
- [55] Bielke A *et al* 2004 Fabrication of aspheric optics: process challenges arising from a wide range of customer demands and diversity of machine technologies *Proc. SPIE* **5252** 1–12
- [56] Kurashima Y, Miyachi S, Miyamoto I, Ando M and Numata S 2008 Evaluation of surface roughness of ULE[®] substrates machined by Ar⁺ ion beam *Microelectron. Eng.* **85** 1193–6
- [57] Wu B and Kumar A 2009 Extreme ultraviolet lithography: towards the next generation of integrated circuits *Opt. Photonics Focus* **7** 1–4
- [58] Migura S 2018 Optics for EUV lithography *EUVL Workshop (Carl Zeiss SMT GmbH)* <https://euvlitho.com/2018/P22.pdf>
- [59] Sugisaki K *et al* 2006 EUVA's challenges toward 0.1 nm accuracy in EUV at-wavelength interferometry *Fringe 2005: The 5th International Workshop on Automatic Processing of Fringe Patterns* pp 252–66
- [60] Kerkhof M 2017 Enabling sub-10-nm node lithography: presenting the NXE:3400B EUV scanner *Proc. SPIE* **10143** 101430D
- [61] Peter S 2005 Extreme ultraviolet lithography: overview and development status *J. Microlith., Microfab., Microsyst.* **4** 011006
- [62] Jiang F, Cheng Y, Isoyan A and Cerrina F 2009 Engineering study of extreme ultraviolet interferometric lithography *J. Micro/Nanolith. MEMS MOEMS* **8** 021203
- [63] Meiling H *et al* 2006 First performance results of the ASML alpha demo tool *Proc. SPIE* **6151** 615108
- [64] Ghosh G, Sidpara A and Bandyopadhyay P 2018 *Fabrication of optical components by ultraprecision finishing processes Micro and Precision Manufacturing, Engineering Materials* ed K Gupta (New York: Springer)
- [65] Gerchman M and McLain B 1988 Investigation of the effects of diamond machining germanium for optical applications *Proc. SPIE* **929** 94–6
- [66] Shore P 1995 *Machining of optical surfaces in brittle materials using an ultraprecision machine tool PhD Thesis* Cranfield University
- [67] Yan J, Syoji K and Tamaki J 2003 Some observations on the wear of diamond tools in ultra-precision cutting of single-crystal silicon *Wear* **255** 1380–7
- [68] Thornton A and Wilks J 1980 The wear of diamond tools turning mild steel *Wear* **65** 67–74
- [69] Oomen J and Eisses J 1992 Wear of monocrystalline diamond tools during ultraprecision machining of nonferrous metals *Precis. Eng.* **14** 206–18
- [70] Yan J, Syoji K, Kuriyagawa T and Suzuki H 2002 Ductile regime turning at large tool feed *J. Mater. Process. Technol.* **121** 363–72
- [71] Yan J, Zhang Z and Kuriyagawa T 2010 Tool wear control in diamond turning of high-strength mold materials by means of tool swinging *CIRP Ann.* **59** 109–12
- [72] Patten J 2015 Micro laser assisted machining *US Patent Specification* 8933366
- [73] Mohammadi H, Ravindra D, Kode S and Patten J 2015 Experimental work on micro laser-assisted diamond turning of silicon (111) *J. Manuf. Process.* **19** 125–8
- [74] Ravindra D, Muralidhar K and Patten J 2012 Ductile mode material removal and high-pressure phase transformation in silicon during micro-laser assisted machining *Precis. Eng.* **36** 364–7
- [75] Wei Y, Park C and Park S 2017 Experimental evaluation of direct laser assisted turning through a sapphire tool *Proc. Manuf.* **10** 546–56
- [76] Brian B, Islam M and Davies I 2018 A review of micro-mechanical cutting *Int. J. Adv. Manuf. Technol.* **94** 789–806
- [77] Chavoshi S and Luo X 2015 Hybrid micro-machining processes: a review *Precis. Eng.* **41** 1–23
- [78] Chang T, Chen Z, Lee Y, Li Y and Wang C 2016 Ultrafast laser ablation of soda-lime glass for fabricating microfluidic pillar array channels *Microelectron. Eng.* **158** 95–101
- [79] Chen H, Zhang P, Zhang L, Liu H, Jiang Y, Zhang D, Han Z and Jiang L 2016 Continuous directional water transport on the peristome surface of *Nepenthes alata* *Nature* **532** 85–9
- [80] Yan J 2005 Micro grooving on single-crystal germanium for infrared Fresnel lenses *J. Micromech. Microeng.* **12** 1925–31
- [81] Mukaida M and Yan J 2017 Ductile machining of single-crystal silicon for microlens arrays by ultraprecision diamond turning using a slow tool servo *Int. J. Mach. Tools Manuf.* **115** 2–14
- [82] Paul E, Evans C, Mangamelli A, McGlauffin M and Polvani R 1996 Chemical aspects of tool wear in single point diamond turning *Precis. Eng.* **18** 4–19

- [83] Brinksmeier E, Gläbe R and Osmer J 2006 Ultra-precision diamond cutting of steel molds *CIRP Ann.—Manuf. Technol.* **55** 551–4
- [84] Song Y, Nezu K, Park C and Moriwaki T 2009 Tool wear control in single-crystal diamond cutting of steel by using the ultra-intermittent cutting method *Int. J. Mach. Tools Manuf.* **49** 339–43
- [85] Shamoto E and Moriwaki T 1994 Study on elliptical vibration cutting *CIRP Ann.—Manuf. Technol.* **43** 35–8
- [86] Zhou J, Li L, Naples N, Sun T and Yi A 2013 Fabrication of continuous diffractive optical elements using a fast tool servo diamond turning process *J. Micro-Mech. Microeng.* **23** 075010
- [87] Zhang J, Suzuki N and Shamoto E 2013 Investigation on machining performance of amplitude control sculpturing method in elliptical vibration cutting *Proc. CIRP* **8** 328–33
- [88] Zhang S, To S, Zhu Z and Zhang G 2016 A review of fly cutting applied to surface generation in ultra-precision machining *Int. J. Mach. Tools Manuf.* **103** 13–27
- [89] Fang F and Liu Y 2004 On minimum exit-burr in micro cutting *J. Micromech. Microeng.* **14** 984–8
- [90] Chen W, Liang Y, Luo X, Sun Y and Wang H 2014 Multi-scale surface simulation of the KDP crystal fly cutting mechanism *Int. J. Adv. Manuf. Technol.* **73** 289–97
- [91] Zhang F, Wang S, An C, Wang J and Xu Q 2017 Full-band error control and crack-free surface fabrication techniques for ultra-precision fly cutting of large-aperture KDP crystals *Front. Mech. Eng.* **12** 193–202
- [92] Campbell J *et al* 2004 NIF optical materials and fabrication technologies: an overview *Proc. SPIE* **5341** 84–101
- [93] Fang T and Lambropoulos J 2002 Microhardness and indentation fracture of potassium dihydrogen phosphate (KDP) *J. Am. Ceram. Soc.* **85** 174–8
- [94] Zhao Q *et al* 2009 Investigation of anisotropic mechanisms in ultra-precision diamond machining of KDP crystal *J. Mater. Process. Technol.* **209** 4169–77
- [95] Zong W *et al* 2013 Finite element simulation of diamond tool geometries affecting the 3D surface topography in fly cutting of KDP crystals *Int. J. Adv. Manuf. Technol.* **68** 1927–36
- [96] Wang S, An C, Zhang F, Wang J, Lei X and Zhang J 2016 An experimental and theoretical investigation on the brittle ductile transition and cutting force anisotropy in cutting KDP crystal *Int. J. Mach. Tools Manuf.* **106** 98–108
- [97] Kong L B, Cheung C F and Lee W B 2016 A theoretical and experimental investigation of orthogonal slow tool servo machining of wavy microstructured patterns on precision rollers *Precis. Eng.* **43** 315–27
- [98] Yu D P, Hong G and Wong Y 2012 Profile error compensation in fast tool servo diamond turning of micro-structured surfaces *Int. J. Mach. Tools Manuf.* **52** 13–23
- [99] Tan H, Gilbertson A and Chou S 1998 Roller nanoimprint lithography *J. Vac. Sci. Technol. B* **16** 3926–8
- [100] Mäkelä T *et al* 2007 Continuous roll to roll nanoimprinting of inherently conducting polyaniline *Microelectron. Eng.* **84** 877–9
- [101] Mäkelä T *et al* 2005 Utilizing roll-to-roll techniques for manufacturing source-drain electrodes for all-polymer field-effect transistors *Synth. Met.* **153** 285–8
- [102] Pastorelli F *et al* 2016 The organic power transistor: roll-to-roll manufacture, thermal behavior, and power handling when driving printed electronics *Adv. Eng. Mater.* **18** 51–5
- [103] Jones V *et al* 2009 Roll to roll manufacturing of subwavelength optics *Proc. SPIE* **7205** 720501
- [104] Liu C, Yan J and Lin S 2016 Diamond turning of high-precision roll-to-roll imprinting molds for fabricating subwavelength gratings *Opt. Eng.* **55** 064105
- [105] Terabayashi T and Yan J 2017 Ultraprecision machining of wavy microstructures on roller surfaces by using a slow tool servo *Proc. 13th CHINA-JAPAN Int. Conf. on Ultra-Precision Machining Process (CJUMP2017)*
- [106] Sehgal J and Ito S 1999 Brittleness of glass *J. Non-Cryst. Solids* **253** 126–32
- [107] Liu J, Pei Z and Fisher G 2007 Grinding wheels for manufacturing of silicon wafers: a literature review *Int. J. Mach. Tools Manuf.* **47** 1–13
- [108] Yin L, Vancoille E, Lee L, Huang H, Ramesh K and Liu X 2004 High-quality grinding of polycrystalline silicon carbide spherical surfaces *Wear* **256** 197–207
- [109] Heinzel C and Rickens K 2009 Engineered wheels for grinding of optical glass *CIRP Ann.* **58** 315–8
- [110] Hwang Y, Kuriyagawa T and Lee S 2006 Wheel curve generation error of aspheric microgrinding in parallel grinding method *Int. J. Mach. Tools Manuf.* **46** 1929–33
- [111] Bifano T, Dow T and Scattergood R 1991 Ductile-regime grinding—a new technology for machining brittle materials *J. Eng. Ind.-Trans. ASME* **113** 184–9
- [112] Grimme D, Rickens K, Zhao Q and Heinzel C 2006 Dressing of coarse-grained diamond wheels for ductile machining of brittle materials *Towards Synthesis of Micro/Nano-Systems (London)* pp 305–7
- [113] Saeki M, Kuriyagawa T, Lee J and Syoji K 2001 Machining of aspherical opto-device utilizing parallel grinding method *Proc. 16th Annual Meeting of the ASPE* pp 433–6
- [114] Tohme Y 2007 Grinding aspheric and freeform micro-optical molds *Proc. SPIE* **6462** 64620K
- [115] Kuriyagawa T, Zahmaty M and Syoji K 1996 A new grinding method for aspheric ceramic mirrors *J. Mater. Process. Technol.* **62** 387–92
- [116] Zhang Z, Yang X, Zheng L and Xue D 2016 High-performance grinding of a 2-m scale silicon carbide mirror blank for the space-based telescope *Int. J. Adv. Manuf. Technol.* **89** 463–73
- [117] Carlisle K and Stocker M 1997 Cost-effective machining of brittle materials (glasses and ceramics) eliminating/minimizing the polishing process *Proc. Int. Soc. Opt. Eng.* **3099** 46–58
- [118] Ohmori H 1992 Electrolytic in-process dressing (ELID) grinding technique for ultraprecision mirror surface machining *Int. J. Japan Soc. Prec. Eng.* **26** 273–8
- [119] Murata R, Okano K and Tsutsumi C 1985 Grinding of structural ceramics (some applications of electrolytic in-process dressing to abrasive cut-off operation) *Grinding Symp. PED* vol 16 ed M C Shaw pp 261–72
- [120] Ohmori H and Nakagawa T 1995 Analysis of mirror surface generation of hard and brittle materials by ELID (electrolytic in-process dressing) grinding with superfine grain metallic bond wheels *CIRP Ann.—Manuf. Technol.* **44** 287–90
- [121] Liu J, Pei Z and Fisher G 2007 ELID grinding of silicon wafers: a literature review *Int. J. Mach. Tools Manuf.* **47** 529–36
- [122] Fathima K, Kumar A, Rahman M and Lim H 2003 A study on wear mechanism and wear reduction strategies in grinding wheels used for ELID grinding *Wear* **254** 1247–55
- [123] Kramer D, Rehsteiner F and Schumacher B 1999 ECD (electrochemical inprocess controlled dressing), a new method for grinding of modern high-performance cutting materials to highest quality *CIRP Ann.—Manuf. Technol.* **48** 265–8
- [124] Matsuura H, Hane K, Kunieda Y, Yoshihara N, Yan J and Kuriyagawa T 2007 Development of laser dresser for resin bonded diamond wheel *Key Eng. Mater.* **329** 169–74
- [125] Zhang C and Shin Y 2002 A novel laser-assisted truing and dressing technique for vitrified CBN wheels *Int. J. Mach. Tools Manuf.* **42** 825–35
- [126] Yao P *et al* 2014 High efficiency abrasive waterjet dressing of diamond grinding wheel *Adv. Mater. Res.* **1017** 243–8

- [127] Kitizig H, Tawakoli T and Azarhoushang B 2016 A novel ultrasonic-assisted dressing method of electroplated grinding wheels via stationary diamond dresser *Int. J. Adv. Manuf. Technol.* **86** 487–94
- [128] Yan J and Tan T H 2015 Sintered diamond as a hybrid EDM and grinding tool for the micromachining of single-crystal SiC *CIRP Ann.* **64** 221–4
- [129] Kang R, Tian Y, Guo D and Jin Z 2003 Present status of research and application in ultra-precision grinding technology of large-scale silicon wafer *Diam. Abrasives Eng.* **136** 13–8
- [130] Aida H *et al* 2012 Ultraprecision CMP for sapphire, GaN, and SiC for advanced optoelectronics materials *Curr. Appl. Phys.* **12** S41–6
- [131] Zhou L, Kawai S, Honda M, Shimizu J, Eda H and Yakita A 2002 Research on chemomechanical-grinding (CMG) of Si wafer (1st report) *J. Japan. Soc. Precis. Eng.* **68** 1559–63
- [132] Zhou L, Eda H, Shimizu J, Kamiya S, Iwase H and Kimura S 2006 Defect-free fabrication for single crystal silicon substrate by chemo-mechanical grinding *CIRP Ann.* **55** 313–6
- [133] Tian Y, Zhou L, Shimizu J, Tashiro Y and Kang R 2009 Elimination of surface scratch/texture on the surface of single crystal Si substrate in chemo-mechanical grinding (CMG) process *Appl. Surf. Sci.* **255** 4205–11
- [134] Huang H, Wang B, Wang Y, Zou J and Zhou L 2008 Characteristics of silicon substrates fabricated using nanogrinding and chemo-mechanical-grinding *Mater. Sci. Eng. A* **479** 373–9
- [135] Eda H *et al* 2001 Development of single step grinding system for large scale Φ 300 Si wafer *CIRP Ann.—Manuf. Technol.* **50** 225–8
- [136] Zhou L, Shiina T, Qiu Z, Shimizu J, Yamamoto T and Tashiro T 2009 Research on chemo-mechanical grinding of large size quartz glass substrate *Precis. Eng.* **33** 499–504
- [137] Wu K, Zhou L, Onuki T, Shimizu J, Yamamoto T and Yuan J 2018 Study on the finishing capability and abrasives-sapphire interaction in dry chemo-mechanical-grinding (CMG) process *Precis. Eng.* **52** 451–7
- [138] Zhao Q and Guo B 2015 Ultra-precision grinding of optical glasses using mono-layer nickel electroplated coarse-grained diamond wheels: II. Investigation of profile and surface grinding *Precis. Eng.* **39** 67–78
- [139] Guo B and Zhao Q 2017 Ultrasonic vibration assisted grinding of hard and brittle linear micro-structured surfaces *Precis. Eng.* **48** 98–106
- [140] Xie J 2018 Precision Grinding for functional microThe next generation of ground-based telescopes requires structured surface *Micro and Nano Fabrication Technology, Micro/ Nano Technologies* ed J Yan (Singapore: Springer) (https://doi.org/10.1007/978-981-13-0098-1_9)
- [141] Yin S, Ohmori H, Uehara Y, Shimizu T and Lin W 2004 Micro V-groove grinding technique of large germanium immersion grating element for mid-infrared spectrograph *JSME Int. J. C* **47** 59–65
- [142] Tonnellier X, Morantz P, Shore P, Baldwin A, Evans R and Walker D 2007 Subsurface damage in precision ground ULE and Zerodur surfaces *Opt. Express* **15** 12197–205
- [143] Tonnellier X 2009 Precision grinding for rapid manufacturing of large optics *PhD Thesis* England: Cranfield University
- [144] Tonnellier X, Morantz P, Shore P and Comley P 2010 Precision grinding for rapid fabrication of segments for extremely large telescopes using the Cranfield BoX *Proc. SPIE* **7739** 773905
- [145] Shore P *et al* 2005 Grinding mode of the ‘BOX’ ultra precision free-form grinder *Proc. 20th Annual ASPE Meeting ASPE*
- [146] Comley P, Morantz P, Shore P and Tonnellier X 2011 Grinding metre scale mirror segments for the E-ELT ground based telescope *CIRP Ann.—Manuf. Technol.* **60** 379–82
- [147] Rupp W 1972 Loose-abrasive grinding of optical surfaces *Appl. Opt.* **11** 2797–810
- [148] Jones R and Plante R 1987 Rapid fabrication of large aspheric optics *Precis. Eng.* **9** 65–70
- [149] Wang C, Yang W, Wang Z, Yang X, Hu C, Zhong B, Guo Y and Xu Q 2014 Dwell-time algorithm for polishing large optics *Appl. Opt.* **53** 4752–60
- [150] Endelman L 1993 Hubble space telescope: mission, design, problems, and solutions *Proc. SPIE* **2513** 1204–17
- [151] West S *et al* 1994 Practical design and performance of the stressed-lap polishing tool *Appl. Opt.* **33** 8094–100
- [152] Zeng S and Blunt L 2014 Experimental investigation and analytical modelling of the effects of process parameters on material removal rate for bonnet polishing of cobalt chrome alloy *Precis. Eng.* **38** 348–55
- [153] Kim D and Burge J 2010 Rigid conformal polishing tool using nonlinear visco-elastic effect *Opt. Express* **18** 2242–57
- [154] Angel J 1985 Glass mirrors for space telescopes *Proc. SPIE* **0542** 32–4
- [155] Luo X, Zheng L and Zhang X 2010 Fabrication of large off-axis asymmetry aspherics using stressed lap with orbital tool motion *Proc. SPIE* **7654** 765408
- [156] Martin H, Anderson D, Angel J, Nagel R, West S and Youn R 1990 Progress in the stressed-lap polishing of a 1.8-m/1 mirror *Proc. SPIE* **1236** 682–90
- [157] Zhao H *et al* 2015 Deformation verification and surface improvement of active stressed lap for 4 m-class primary mirror fabrication *Appl. Opt.* **54** 2658–64
- [158] Haitao L *et al* 2013 Study on active lap tool influence function in grinding 1.8 m primary mirror *Appl. Opt.* **52** 7504–11
- [159] Angel J, Davison W, Hill J, Mannery E and Martin H 1990 Progress toward making lightweight 8 m mirrors of short focal length *Proc. SPIE* **1236** 636–40
- [160] Burge J 2014 Large optics fabrication and testing at the college of optical Sciences *Proc. SPIE* **9186** 918608
- [161] Martin H *et al* 2003 Fabrication of mirrors for the Magellan telescopes and large binocular telescope *Proc. SPIE* **4837** 609–18
- [162] Zhao H, Li X, Fan B and Zeng Z 2016 Experimental dynamic deformation analysis of active stressed lap *Appl. Opt.* **55** 1190–7
- [163] Walker D *et al* 2002 The precessions process for efficient production of aspheric optics for large telescopes and their instrumentation *Proc. SPIE* **4842** 73–84
- [164] Wang C *et al* 2014 Highly efficient deterministic polishing using a semirigid bonnet *Opt. Eng.* **53** 095102
- [165] Kim D W, Martin H and Burge J H 2012 Control of mid-spatial-frequency errors for large steep aspheric surfaces *Optics InfoBase Conf. Papers, Optical Fabrication and Testing* (<https://doi.org/10.1364/OFT.2012.OM4D.1>)
- [166] Kim D W, Martin H M and Burge J H 2013 Optical surfacing process optimization using parametric smoothing model for mid-to-high spatial frequency error control *Proc. SPIE* **8884** 88840B
- [167] Shu Y, Nie X, Shi F and Li S 2014 Compare study between smoothing efficiencies of epicyclic motion and orbital motion *Optik* **125** 4441–5
- [168] Shu Y, Kim D W, Martin H M and Burge J H 2013 Correlation-based smoothing model for optical polishing *Opt. Express* **21** 28771–82
- [169] Song C *et al* 2017 Improving smoothing efficiency of rigid conformal polishing tool using time-dependent smoothing evaluation model *Photonic Sens.* **7** 171–81

- [170] Fischer-Cripps A C 2004 Multiple-frequency dynamic nanoindentation testing *J. Mater. Res.* **19** 2981–8
- [171] Johns M 2008 The Giant Magellan telescope (GMT) *Proc. SPIE* **6986** 1–12
- [172] Harris D C 2011 History of magnetorheological finishing *Proc. SPIE* **8016** 80160N
- [173] Jacobs S, Arrasmith S and Kozhinova I 1999 An overview of magnetorheological finishing (MRF) for precision optics manufacturing *Ceram. Trans.* **102** 185–99
- [174] Kordonski W I and Golini D 2001 Fundamentals of magnetorheological fluid utilization in high precision finishing *Intell. Mater. Syst. Struct.* **10** 683–9
- [175] Jacobs S D *et al* 1994 Magnetorheological finishing: a deterministic process for optics manufacturing *Proc. SPIE* **2576** 372–82
- [176] Jacobs S D *et al* 1999 Magnetorheological finishing of IR materials *Proc. SPIE* **3134** 258–69
- [177] Kozhinova I A, Arrasmith S R, Lambropoulos J C and Jacobs S D 2001 Exploring anisotropy in removal rate for single crystal sapphire using MRF *Proc. SPIE* **4451** 277–85
- [178] Shorey A B 2000 Mechanisms of the material removal in magnetorheological finishing (MRF) of glass *PhD Dissertation* University of Rochester
- [179] William K and Sergei G 2011 Material removal in magnetorheological finishing of optics *Appl. Opt.* **50** 1984–94
- [180] Patterson K and Pellegrino S 2013 Ultralightweight deformable mirrors *Appl. Opt.* **52** 5327–41
- [181] Satake U, Enomoto T, Obayashi Y and Sugihara T 2018 Reducing edge roll-off during polishing of substrates *Precis. Eng.* **51** 97–102
- [182] Wilson S and Mcneil J 1987 Neutral ion beam figuring of large optical surface *Proc. SPIE* **818** 320–4
- [183] Allen L and Romig H 1990 Demonstration of an ion-figuring process *Proc. SPIE* **1333** 164–70
- [184] Xie X and Li S 2013 Ion beam figuring technology *Handbook of Manufacturing Engineering and Technology* ed A Nee (London: Springer) (https://doi.org/10.1007/978-1-4471-4976-7_65-1)
- [185] Drueding T *et al* 1995 Ion beam figuring of small optical components *Opt. Eng.* **34** 3565–71
- [186] Xie X, Yu H, Zhou L, Dai Y and Li S 2012 High thermal expansion optical component machined by ion beam figuring *Opt. Eng.* **51** 013401
- [187] Yin X, Deng W, Tang W, Zhang B, Xue D, Zhang F and Zhang X 2016 Ion beam figuring approach for thermally sensitive space optics *Appl. Opt.* **55** 8049–55
- [188] Mori Y, Yamauchi K and Endo K 1987 Elastic emission machining *Precis. Eng.* **9** 123–8
- [189] Kanaoka M, Liu C, Nomura K, Ando M, Takino H and Fukuda Y 2007 Figuring and smoothing capabilities of elastic emission machining for low-thermal-expansion glass optics *J. Vac. Sci. Technol. B* **25** 2110
- [190] Ma Z, Peng L and Wang J 2013 Ultra-smooth polishing of high-precision optical surface *Optik* **124** 6586–9
- [191] Chen F, Yin S, Huang H, Ohmori H, Wang Y, Fan Y and Zhu Y 2010 Profile error compensation in ultra-precision grinding of aspheric surfaces with on-machine measurement *Int. J. Mach. Tools Manuf.* **50** 480–6
- [192] Li X, Zhang Z, Hu H, Li Y, Xiong L, Zhang X and Yan J 2018 Noncontact on-machine measurement system based on capacitive displacement sensors for single-point diamond turning *Opt. Eng.* **57** 044105
- [193] Zou X, Zhao X, Li G, Li Z and Sun T 2017 Non-contact on-machine measurement using a chromatic confocal probe for an ultra-precision turning machine *Int. J. Adv. Manuf. Technol.* **90** 2163–72
- [194] Li D, Tong Z, Jiang X, Blunt L and Gao F 2018 Calibration of an interferometric on-machine probing system on an ultraprecision turning machine *Measurement* **118** 96–104
- [195] Yan J, Baba H, Kunieda Y, Yoshihara N and Kuriyagawa T 2007 Nano precision on-machine profiling of curved diamond cutting tools using a white-light interferometer *Int. J. Surf. Sci. Eng.* **1** 441–55
- [196] Yu J, Shen Z, Wang X, Sheng P and Wang Z 2018 *In situ* noncontact measurement system and two-step compensation strategy for ultraprecision diamond machining *Opt. Express* **26** 30724
- [197] Nagayama K and Yan J 2018 A comprehensive error correction/prediction system for tool-servo driven diamond turning of freeform surfaces *Proc. Euspen's 18th Int. Conf. & Exhibition (Venice, Italy)* pp 51–2

究極の形状創成と機能創成が拓く 高付加価値製造技術*

To the New Frontiers of Pico-Precision & Function-Generation Machining for High Value Manufacturing

厨川常元**

Tsunemoto KURIYAGAWA

Key words

form generation, function generation, functional interface, nano- & pico-precision machining, nano/micro/macro hybrid structure, hybrid machining

1. はじめに

あらゆる機械やその部品は工作機械から作り出されている。この工作機械業界の売上高状況を知ることは、日本のものづくり分野の活性度を知る上で重要である。売上高はリーマンショックで一時的に落ち込んだものの、現在ではそれ以前の水準に戻り、さらなる上昇を続けている。平成27~28年の統計では4兆3910億円となっている。これからも日本の“ものづくり”が世界をリードしていくためには、海外の技術では到達できない、より高い精度と付加価値をもった製品開発を強力に推進していかなければならない。

従来のものづくりでは、加工された製品の形状精度（ここでは、理論的に正確な寸法によって定められた幾何学的に正しい断面曲線からのずれの大きさをいう）と表面粗さの二つが評価基準であり、それらが設計どおりにできていれば十分であった。しかし、加工精度を極限まで追求しようとする場合、加工面に残留するナノオーダーのうねり模様が問題となり、均一な加工面を得ることが難しい。このうねり模様を除去し、加工面の均一性を得る加工法が必要不可欠となる。本報では、最初に非球面研削加工を例にとり、究極の加工精度を得るために検討してきた種々の研削法について紹介する。しかし、これからはこのような単純な“形状創成”のみでは不十分と考えられる。そこで次に、製品により高い付加価値を発現させるための“機能創成”を加味した新しいものづくりについて紹介する。そして本報では、“形状創成+機能創成=機能創成加工”によって実現される高付加価値加工について考察する。

2. 究極の形状創成を目指して

2.1 パラレル研削法

現在行われている軸対称非球面の代表的な研削法を図1

(a)に示す。図に示すように砥石軸と工作物軸とが直交する縦型構成で、 xy 軸の2軸同時制御によって加工が行われる¹⁾。この方式では、研削点において工作物の回転方向と砥石の周速ベクトルが直交（クロス）するのが特徴で、図2(a)に示すように工作物半径方向の研削条痕が形成される。そこで、この研削方式をクロス研削と名付ける。

多くの場合、クロス研削では作業面をV字形に成形したそろばん玉状砥石のエッジが使用される。研削方向に垂直な砥石断面上の一点で研削が行われるため、砥石の摩耗や砥粒の目つぶれが一カ所に集中するという欠点があり、工作物がセラミックスのように高硬度である場合や、大口径である場合には効率的に研削することは事実上不可能となる。そこで図1(b)に示すように、工作物の回転方向

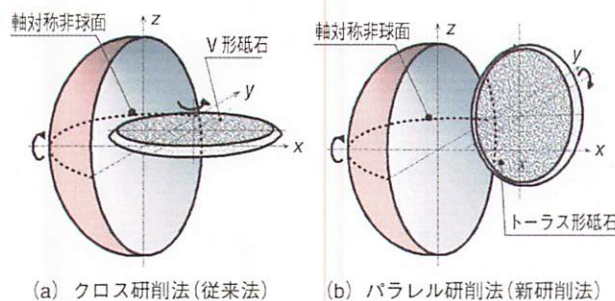


図1 非球面研削法の比較

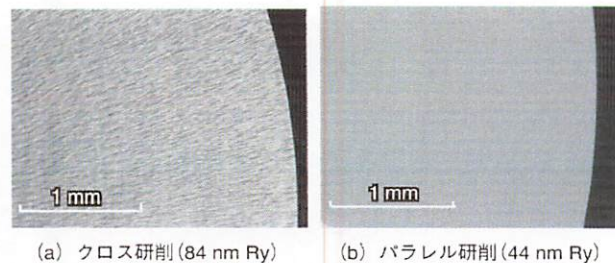


図2 研削表面のノマルスキー顕微鏡写真

*原稿受付 平成31年2月4日

**正会員 東北大学大学院医工学研究科 (仙台市青葉区荒巻字青葉6-6-01)

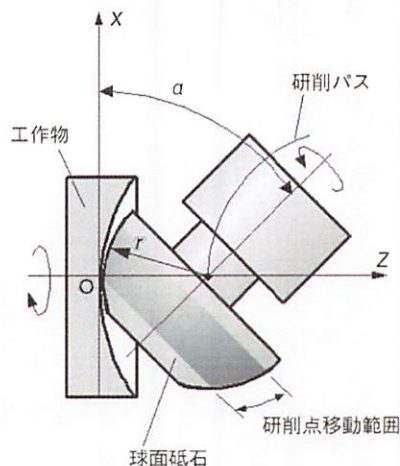


図3 円弧包絡研削法

と砥石の周速ベクトルが平行になるような研削法を考え、平行研削と名付ける。クロス研削法と平行研削法との違いは、工作物の移動方向と砥粒切れ刃の切削方向との違いだけである。もし球状の砥石を使用した場合でも、幾何学的にはまったく同一である。しかし、研削理論²⁾を用いて仕上面粗さを理論的に計算すると、これらはまったく異なった結果となる。すなわち、クロス研削より平行研削のほうが有効切れ刃数が増加するため、すべての研削条件において平行研削のほうが仕上面粗さは小さくなることが明らかになった³⁾。実際に超硬金型を研削した表面のノマルスキー顕微鏡写真を比較したものを図2に示す。クロス研削の場合と比較すると明らかのように、まったく同じ砥石、研削条件であるにもかかわらず、平行研削による仕上面粗さのほうが約1/2と小さいことが分かる。このように仕上面粗さを良くする研削法が平行研削である。

2.2 円弧包絡研削法

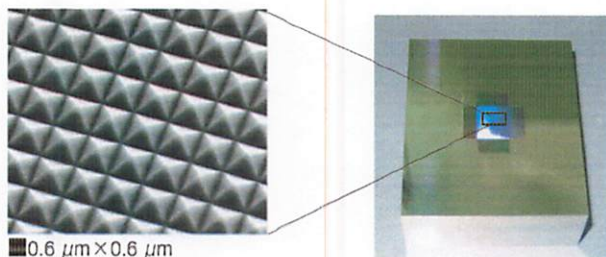
前述したように、従来の研削方法（クロス研削）では砥石断面上の研削点に変化せず、その一点でのみ研削が行われるため、そこに摩耗が集中することを指摘した。そのためドレッシング間寿命が短くなり、大きな工作物の場合には能率良く研削することは事実上不可能となる。さらに最も致命的な点は、非球面の形状精度の劣化を引き起こすことである。この問題点を解決するには、一点に固定されていた研削点を砥石幅方向に移動させればよい。そのためには図3に示すように円弧断面を有する砥石を使用し、その円弧断面の包絡により非球面形状を創成研削すればよい⁴⁾。この場合、図に示すように有効研削幅が増大し砥石摩耗が分散する。その結果、円弧包絡研削法では砥石摩耗の大幅な低減が可能となり、非球面研削における形状精度の大幅な改善が達成される。

2.3 超安定研削法

非球面研削加工の難しさは、ナノオーダの仕上面粗さと高精度の輪郭形状が同時に要求される点である。これらの



(a) 装置外観



(b) 加工部詳細と加工した微細構造体

図4 1 Å分解能の5軸加工機

問題に対しては、上述の平行研削法と円弧包絡研削法の併用により大きな効果が上がることを示した。その結果、形状精度50~100 nm、表面粗さ10~30 nm Ryが達成されている。しかし、より鮮明で精細な光学像を得るために、非球面レンズに要求される精度は年々高くなってきている。そして現在では、形状精度1 nm以下、表面粗さ数Åが要求されるようになってきた。これを実現するためには、現在の非球面研削加工での残された問題点である、レンズ加工表面に発生するうねりの3次元形状（形状誤差パターン）を除去する必要がある。そのためには加工表面の形状誤差パターンが均一になるように、加工結果に影響を与えるすべてのパラメータを所定の値に完全に制御して、一切変動がない、ばらつきがない、揺らがない加工、すなわち超安定加工（fluctuation-free machining）を

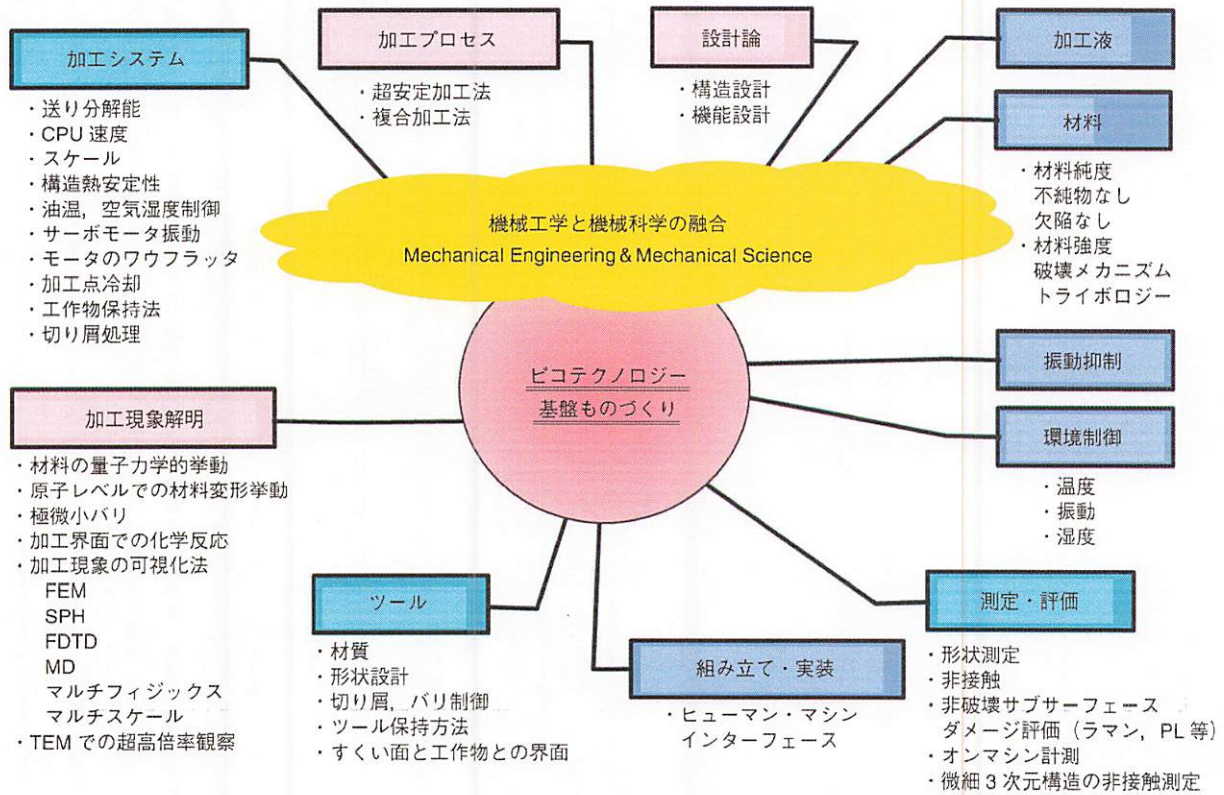


図5 ピコ精度加工の基盤技術

実現する必要がある。この問題に関しては、本特集記事の“超安定加工法に関する理論的解析”を参照されたい。

3. ピコ精度加工技術

現在、1 nm 以下の精度を要求される超高精度部品のニーズも高まってきている。この傾向が、今後、ますます高まってくるのは必至である。このような超高精度加工を達成するためには、前述したような加工法の開発のみならず、ハードウェアである工作機械の超高分解能化が重要である。例えば、近年の工作機械の分解能はすでに 1 nm を切っており、100 pm (1 Å) 分解能の加工機も開発されている。すなわちナノ精度加工からピコ精度加工への挑戦である。図4はxyz軸分解能が1 Åを実現した5軸加工機の外観と加工物である。今後、同様のピコ精度加工機が複数の企業から発売されるであろう。

しかし、このようにピコ精度加工を実現しようとした場合、加工機の超高分解能化だけでは不十分である。そのほかにピコ精度領域での加工プロセス、設計論、加工現象説明、工具開発、組み立て実装、測定評価等、周辺技術の開発研究が必要不可欠である。また同時に、これまでの機械工学を支えてきた構造力学、破壊力学等に加え、分子動力学や量子力学等を加味したいわゆる機械科学的なアプローチも必要不可欠となろう。図5にピコ精度加工を研究開発する上で重要となる基盤技術を示す。

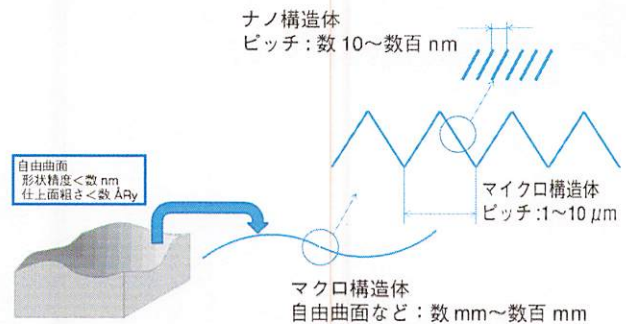


図6 ナノ・マイクロ・マクロ複合構造体

4. 機能創成加工による高付加価値創成を目指して

前述したように、超精密加工表面上に微細構造体を創成したり、あるいは加工表面近傍の結晶構造を制御したりすることにより、新たな機能を発現させるための加工法が提唱されている。すなわち、“形状創成+機能創成”により高付加価値を創成する機能創成加工である。

ニーズが高い表面機能として、無反射性、撥水性、防汚性等が挙げられる。これらの機能を発現するための構造の一つに、マイクロ~サブミクロンオーダーの複合構造体が挙げられる。そして、このような微細構造体を従来のマクロ構造体の上に創成するための技術が求められている。すなわち、図6に示すような、nm オーダーの平滑面を有す

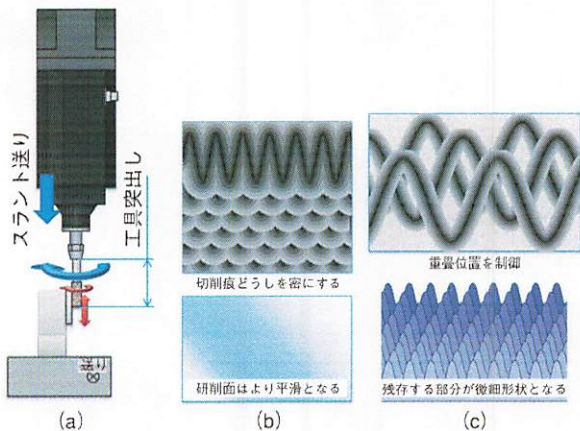


図7 複合振動援用加工による微細形状創成原理

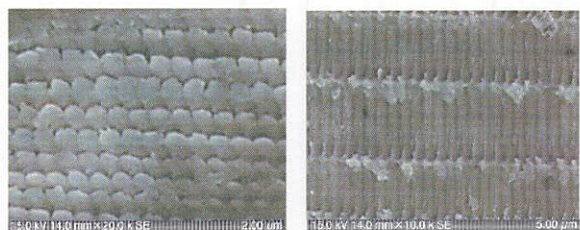


図8 ハイブリッド振動研削で作製した500 nm ピッチの周期構造体

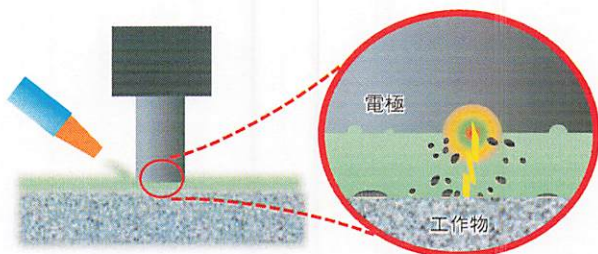


図9 プラズマショット法の概略

るマクロサイズの自由曲面（あるいは平面）上に、マイクロサイズの機能性微細構造が形成され、さらにその表面上にナノサイズの微細構造が重畳して形成されたナノ・マイクロ・マクロ複合構造体である。このようなナノ・マイクロ・マクロ複合構造体は、従来の機能に光学的あるいは電気的、熱的、機械的に特異な機能を加味することが期待されている。

4.1 ハイブリッド振動加工法

この加工法は、軸方向とそれに直交するたわみ方向2軸の合計3軸方向に工具を超音波加振し、それによって得られる運動軌跡を工作物に転写することで、微細パターンを創成するものである⁵⁾。3D 超音波援用スピンドルの先端にマイクロ砥石やダイヤモンド工具を取り付けて加工を行う。図7 (a) に3D 超音波スピンドルを示す。図7 (b), (c) は砥粒切れ刃、あるいはダイヤモンド工具の切削軌跡

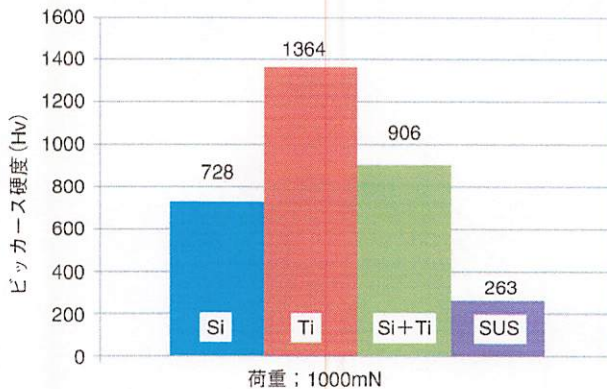


図10 プラズマショット法による加工表面硬化

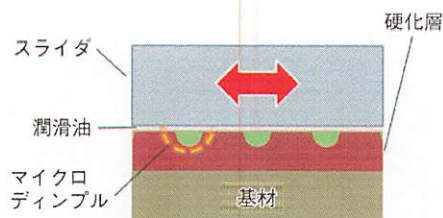


図11 プラズマショット法と研削加工によって創成されるプラトリー構造

を示したものであるが、それらが重畳する位置を制御することにより、鏡面になったり、微細形状を有する加工面になったりする。図8に本手法で創成した500 nm ピッチの微細周期構造を示す。

4.2 プラズマショットプロセス

プラズマショット (PS) 法は、放電加工を応用した表面処理手法である。PS 法は、図9に示すように電極-工作物間に連続的なパルス放電を発生させることにより電極を溶融させ、工作物上に移行させることで改質層を形成する。本手法では、微細なパルス状の放電が局所的に繰り返されるため、被処理材表面には微細なディンプル（マイクロディンプル）が形成される。また、それと同時に電極材料が溶融した状態で工作物側に移行し、一部基材と混合溶融させることで密着性の高い改質層を形成できる。これらの特徴を活かすことで、低摩擦かつ低摩耗を有する表面の創成が期待できる。例えば、Tiを含有した電極材料を使用した場合、Tiは放電現象とともに電極から放電油中に飛び出し、放電油中の炭素と結合しTiCとなって、工作物表面に打ち込まれる。その結果、工作物表面の硬度は増加する。このように、PS法では狙った部分を硬化させることができる。その結果を図10に示す。SUS材の場合、硬度は5倍以上になっている⁶⁾。

さらにプラズマショットした部分を研削加工することにより、高い潤滑性をもつとされる図11に示すような「プラトリー構造」を創成することができる。

5. おわりに

本報では、ものづくり技術者にとっては普遍的な目標である究極の加工精度を目指した種々の加工法と、超精密加工表面上に微細構造体を創成したり、加工表面近傍の結晶構造を制御したりすることにより、新たな機能を発現させるための機能創成加工を紹介した。今後、さまざまな複合加工法が開発されていくと考えられるが、最終的な目標を見据えた、バックキャスト的発想で開発研究すべきである。今後のピコ精度加工研究の進展が、非常に楽しみである。

参考文献

- 1) 鈴木浩文, 小寺直, 前川茂樹, 森田訓子, 桜木英一, 田中克敏, 前田弘, 厨川常元, 庄司克雄: マイクロ非球面の超精密研削に関する研究 (斜軸研削法によるマイクロ非球面の鏡面研削の可能性検証), 精密工学会誌, **64**, 4 (1998) 619.
- 2) S. Matsui and K. Syoji: On the Maximum Height Roughness of Ground Surface, Technology Reports, Tohoku Univ., **38**, 2 (1973)

615.

- 3) 佐伯優, 厨川常元, 庄司克雄: パラレル研削法による非球面金型加工に関する研究, 精密工学会誌, **68**, 8 (2002) 1067.
- 4) 厨川常元, 立花亨, 庄司克雄, 森由喜男: 円弧包絡研削法による非軸対称非球面セラミックスミラーの加工, 日本機械学会論文集 (C編), **63**, 611 (1997) 2532.
- 5) S. Xu, K. Shimada, M. Mizutani and T. Kuriyagawa: Fabrication of hybrid micro/nano-textured surfaces using rotary ultrasonic machining with one-point diamond tool, International Journal of Machine Tools & Manufacture, **86** (2014) 12.
- 6) 京泉朋希, 江川諒仁, 柴田頼人, 加藤千拓, 鷲見信行, 嶋田慶太, 水谷正義, 厨川常元: プラズマショット法と研削加工による低摩擦・低摩耗の創成, 砥粒加工学会誌, **62**, 7 (2018) 371.



厨川常元

1984年東北大学大学院工学研究科精密工学専攻博士課程単位取得退学, 工学博士。1984年東北大学工学部助手, 1990年同講師, 1992年同助教授, 2003年より工学研究科教授。現在は医工学研究科・研究科長・教授, 精密工学会フェロー, 砥粒加工学会会長, 日本学術会議会員。

機能性発現のための超音波援用切削による 微細テクスチャリング

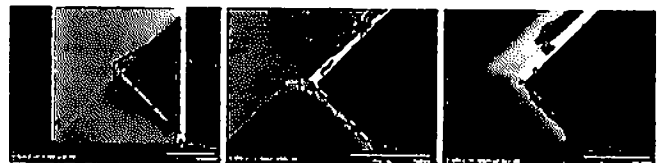
＝濡れ異方性および単方向濡れ発現の試み＝

東北大学 嶋田 慶太・水谷 正義・厨川 常元

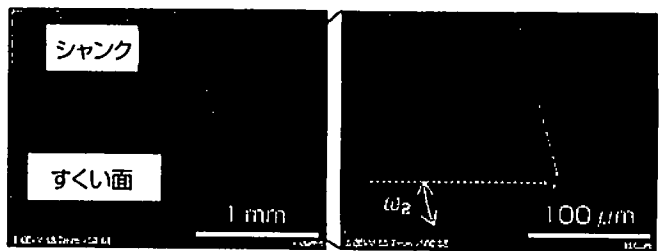
1. はじめに

加工の要求精度の高度化と、それに伴う工作機械の高精度化の繰り返しのより、近年では機械加工の分野においても表面粗さや指令最小単位などにおいて、「ナノ」はおろか「ピコ」という言葉すら聞かれるようになった⁽¹⁾⁽²⁾。そうした中で、ものづくりには形状創成に加え、撥水・親水性などの濡れ性、無反射や再起反射などの光学特性を含む機能創成も同時に行えることが求められると予想される⁽²⁾。このような機能性は自然界にすでに備えられており、材料的・化学的な性質のほかに、表面の微細構造が機能性発現のカギを握っていることが知られている⁽³⁾。そこで、機械加工で模倣することができれば、機能性表面を得られると期待される。そこで我々は超精密加工と比較して安価な超音波援用切削がテクスチャリングに有効な手段として考え、研究を行っている⁽⁴⁾。超音波援用切削で得られる振動由来の特徴的なツールマークを工具・工作物の並進、回転、超音波周波数と組合せマイクロン～サブマイクロンレベルの微細構造を比較的容易かつ高速に創成することができる⁽⁵⁾。本稿では、とくに濡れ性に焦点を絞り、濡れ異方性と単方向濡れについて紹介する⁽⁶⁾⁽⁷⁾。

変化させた。その工具を超音波振動装置 (Ultrasonic generator SC-450 SP-H24、多賀電気株) に把持させ、それらを新世代加工システム(株)製デスクトップ4軸加工機TRIDER-X (NX-DF-ELD22) 上に配置した。本スピンドルは軸方向と円周方向に超音波振動を独立して付与できる特徴を有しており、一台で多様なパターンの加工に対応可能である。また被削材としては、被削性が良好で超精密切削に通じてさまざまな精密機器部品に利用されるタフピッチ銅C1100Pを使用し、水溶性加工液を噴射しながら加工を行った。



(a) 濡れ異方性用



(b) 単方向濡れ用

第1図 ダイヤモンドバイトのSEM像

2. 超音波テクスチャリングによる特徴的な濡れ性の発現

2-1 共通装置・工具

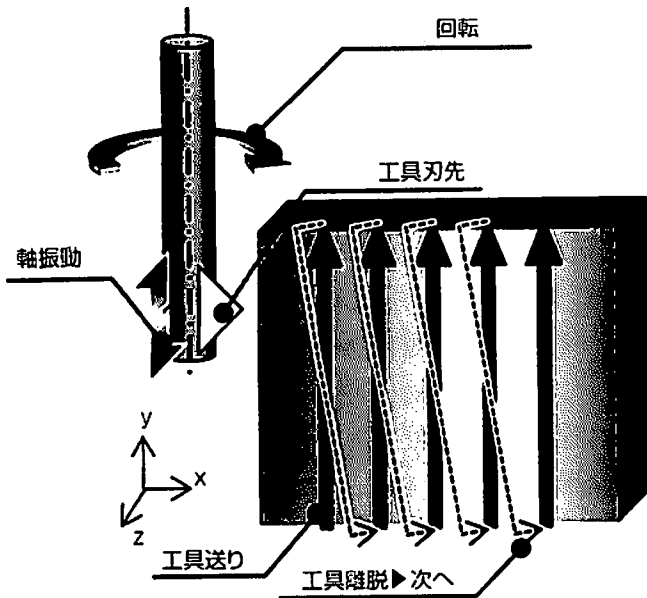
本節ではまず用いた実験装置および工具についてまとめる。

工具材質には微細形状創成を要することから微細な先端形状を有する単結晶ダイヤモンド工具を用い、創成したい形状に応じて第1図のように工具形状も

2-2 濡れ異方性加工⁽⁸⁾

濡れ異方性は方向によって濡れ性が異なる性質であり、液滴の流れる方向の制御を可能とする。本研究では第2図に示すような送り、工具回転、および超音波振動を組み合わせることで複合的微細構造を

創成し、濡れ性に与える影響を検証した。工具には正弦波状に工具が運動した際に左右方向に対してすくい面を持つよう第1図(a)のような構造とした。加工条件の詳細は第1表に示すとおりである。表のうち a_2 および b_2 は微細構造の寸法であり、それぞれ送りと工具回転によるマークおよび工具回転と超音波振動によるマークに対応し $a_2 = v/n$ および $b_2 = 60\pi nd/f$ として求められる。

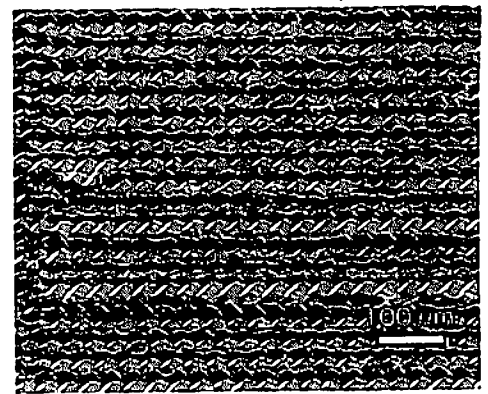


第2図 超音波テクスチャリングの概要

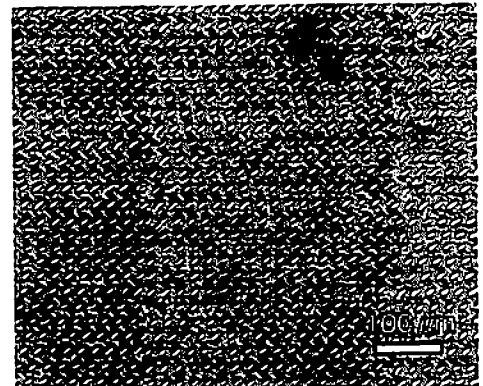
第1表 実験条件

工具回転速度 n min^{-1}	1500	3000	3000
送り速度 v mm/min	15	60	60
振動周波数 f kHz	25		
振動振幅 A μm	1.5	3	3
微細凸構造 a_2, b_2 μm	10	20	20
送りピッチ a_1 μm	400	400	200
切り込み深さ d μm	15		

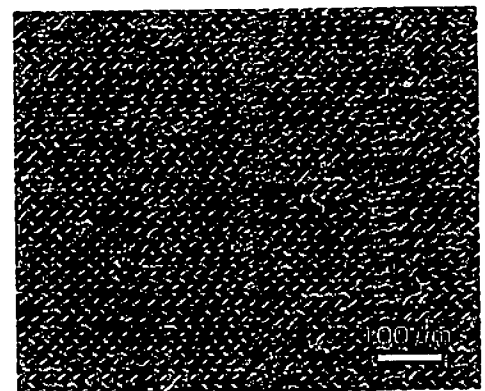
第3図が創成した複合微細構造である。バリや材料の盛り上がりの確認ができるものの、超音波振動による正弦波状の切削軌跡により設計寸法通りの微細構造が形成されていることが確認できる。本構造に対して濡れ性の検証として接触角試験を行った結果を第4図にまとめる。液滴種は純水で液量は $5\mu\text{L}$ であり、 $\alpha = 0^\circ, 90^\circ$ はそれぞれ工具の送り運動に平行、垂直な方向に見た場合の液滴の接触角を示してい



(a) $a_1 = 400 \mu\text{m}, a_2 = 10 \mu\text{m}$

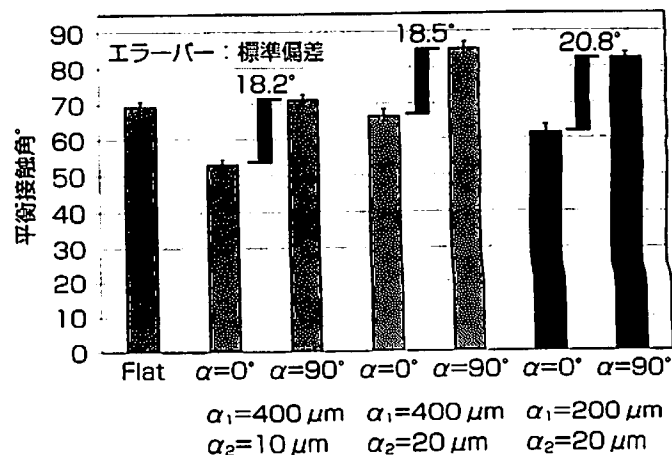


(b) $a_1 = 400 \mu\text{m}, a_2 = 20 \mu\text{m}$

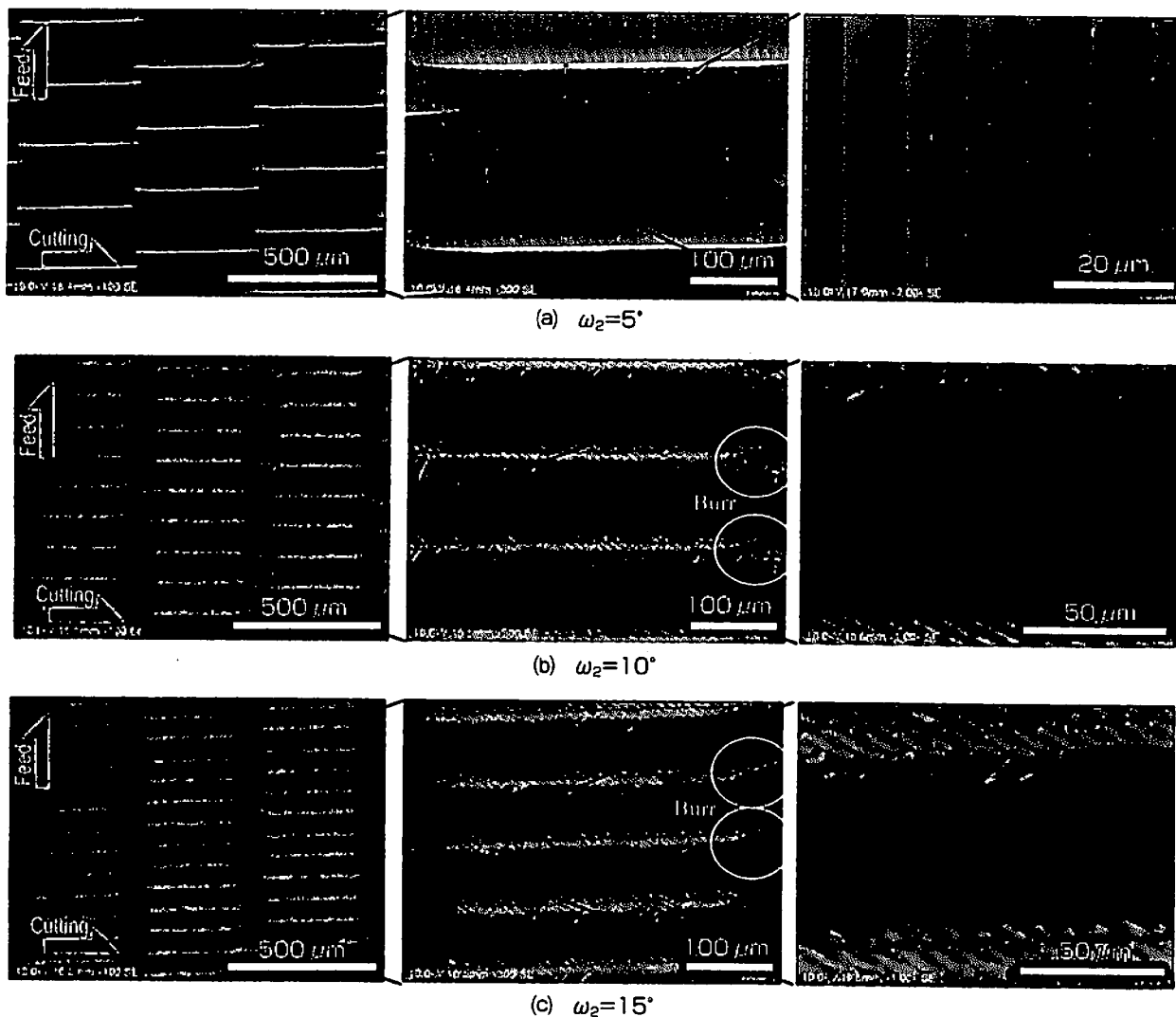


(c) $a_1 = 200 \mu\text{m}, a_2 = 20 \mu\text{m}$

第3図 超音波テクスチャによる複合微細構造のSEM像



第4図 複合微細構造による接触角の変化



第5図 超音波テクスチャによる複合微細構造のSEM像

る。同図が示すように濡れ性の異方性が発現されており、また鏡面（図中、“Flat”）の場合と比較して方位によって親水側と撥水側を跨ぐように変化した場合も確認できる。

2-3 単方向濡れ加工⁽⁷⁾

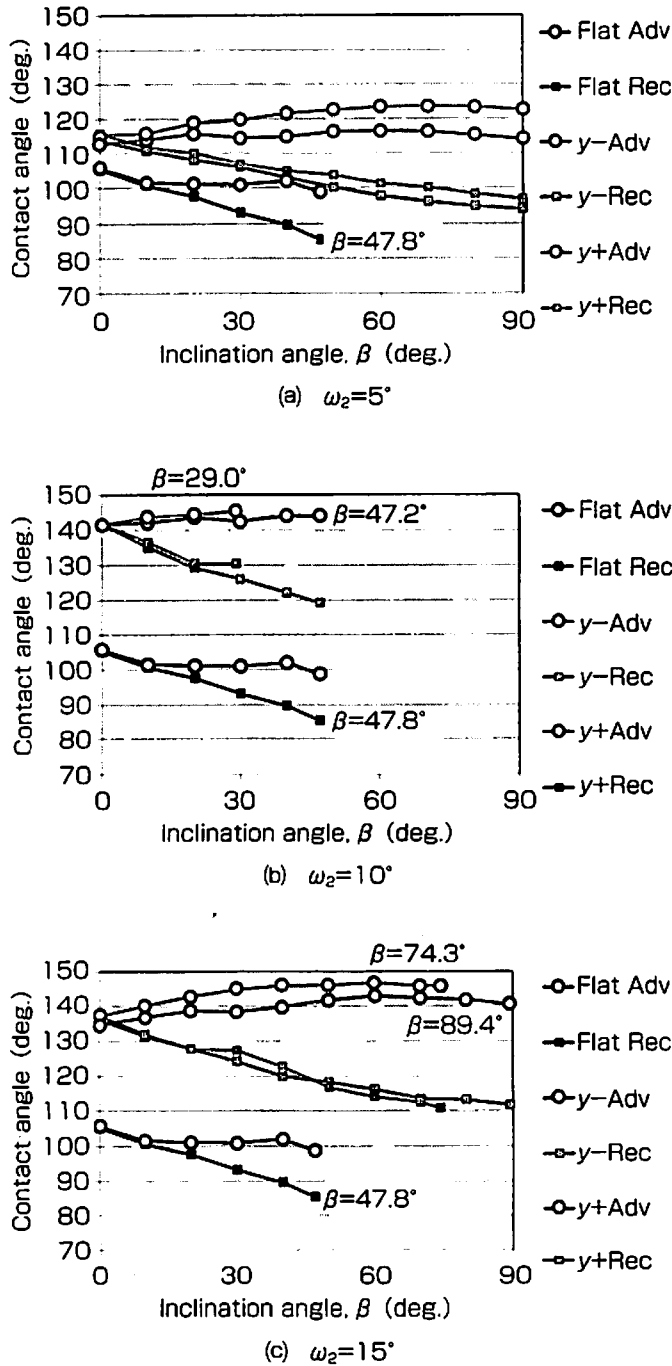
単方向濡れに関してはモルフォチョウの翅の表面構造⁽⁸⁾を参考とした傾斜的な構造を創成した。加工の概要は前節と同様に第2図のように運動させ、超音波振動のみ軸方向に対してたわみ振動を2軸組み合わせることで楕円振動を発生させて微細構造を創成した。また第1図(b)のような90°のV形状の工具を用い、傾斜角 ω_2 が5°、10°、15°の3種を用いた。加工条件の詳細は第2表のとおりである。

第5図が作成した構造であり、90°の溝内部に材料を積み重ねた微細構造が創成されていることが確認できる。また創成した表面での液滴の滑落試験の

第2表 実験条件

傾斜角、 ω_2 , deg.	5	10	15
工具回転速度 n min ⁻¹	1000		
送り速度 v mm/min	200	100	70
構造高さ、 μm	17.4	17.6	18.8
振動振幅（楕円型）、 A_c , μm	15		
送りピッチ、 a_1 , μm	400		
切り込み深さ d μm	20		

結果を第6図に示す。横軸が基板の傾き角であり、90°までにプロットが途絶えている場合には滑落したことを示しており、 β が平均値を示している。またyのプラスとマイナスの記号は傾ける方向をAdvが前進角、Recが後退角を示している。微細構造を有する場合にはいずれも平滑面と比べて滑落角が増大している。これは構造によるピン止め効果が影響



第6図 複合微細構造による滑落角の変化

したと考えられる。また $\omega_2=5^\circ$ の場合には滑落しなかったが、 10° および 15° の場合には滑落角が方向によって異なっており、単方向濡れを効果が認められる。

3. おわりに：まとめ

本稿では、超音波加工により創成した微細構造により濡れ異方性および単方向濡れに関する研究について紹介した。これらの機能性については実際に作製して実験的に検証するだけでなく、解析的な手

法による解明も不可欠であり、我々も熱力学的接触角解析を用いてシミュレーションを試みている⁽⁶¹⁷⁾。まだ実験・解析の両面とも狙った機能性を発現させる、もしくは定量的に効果を予想するという域には達していないが、機能創成加工として工学的・工業的に貢献できるよう研究を進めていく所存である。

<参考文献>

- (1) 青山藤調郎ら：座談会「精密工学」の向かうべき方向、精密工学会誌、Vol.84、No.1、pp.1-6 (2018)
- (2) 厨川常元：医工連携による精密工学の新展開－機能創成加工が拓く新しいものづくり－、精密工学会誌、Vol.84、No.1、pp.42-45 (2018)
- (3) 編著 諸貫信行：微細構造から考える表面機能 第2章自然界に見る表面機能、森北出版、pp.12-30 (2011)
- (4) 徐少林・嶋田慶太・水谷正義・厨川常元：超音波テクスチャリングによる微細構造創成、超音波テクノ、Vol.28、No.6、pp.51-54 (2016)
- (5) Shaolin Xu, Keita Shimada, Masayoshi Mizutani, Tsunemoto Kuriyagawa: Fabrication of hybrid micro/nano-textured surface using rotary ultrasonic machining with one-point diamond tool, International Journal of Machine Tools & Manufacture, 86, 12-17 (2014)
- (6) 嶋田慶太・平井拓弥・水谷正義・厨川常元：超音波援用切削による機能性テクスチャリングの創成、砥粒加工学会誌、Vol.62、No.1、pp.39-44 (2018)
- (7) Keita Shimada, Takuya Hirai, Masayoshi Mizutani, Tsunemoto Kuriyagawa: Unidirectional Wetting Surfaces Fabricated by Ultrasonic-Assisted Cutting, International Journal of Automation Technology, Vol.13, No.2, pp.191-198 (2019)
- (8) Y.Zheng, X.Gao, L.Jiang: Directional adhesion of superhydrophobic butterfly wings, Soft Matter, Vol.3, pp.178-182 (2007)

【筆者紹介】

嶋田 慶太

東北大学 大学院 工学研究科 機械機能創成専攻
知的デザイン学講座 助教

水谷 正義

東北大学 大学院 工学研究科 機械機能創成専攻
准教授

厨川 常元

東北大学 大学院 医工学研究科 教授

機能性インターフェース創成を可能とする超音波振動援用プラズマ放電研削加工システムの開発

=電気加工における超音波振動援用効果の紹介=

ミクロン精密(株) 小林 敏・立花 亨
 東北大学 嶋田 慶太・水谷 正義・厨川 常元

1. はじめに

電解研削では砥石を負極、工作物を陽極にし、その間を電解液で満たし通電しつつ工作物表面を溶かしながら除去する。工作物の硬度に影響されずに低い研削抵抗で加工することができるため、軸付き砥石を用いる小径深穴内周面研削には大きなアドバンテージがある加工法となる。

しかし、実際に具現化するには、様々な課題があるものの、超音波振動の援用がそれらを解決に導いた。

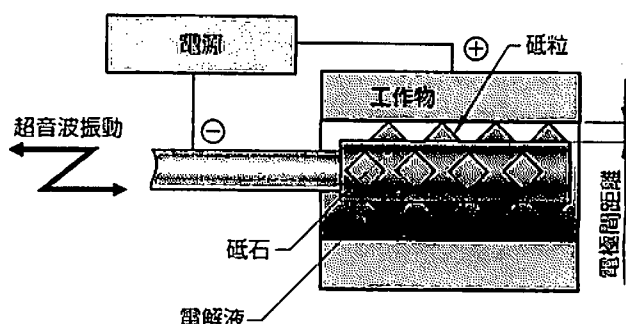
電解研削において超音波がどのような作用をしているか、そして放電研削への発展、さらに同加工法がもたらした機能性インターフェース創成という先進技術の概要を紹介したい。

2. 超音波振動援用電解研削

「電解加工」プラス「超音波振動研削」が超音波振動援用電解研削 (Ultrasonic Assisted Electrolytic grinding、以下UAE研削と呼ぶ) である⁽¹⁾⁽²⁾。

第1図に内周面のUAE研削の原理を模式図で示す。ここでは砥石に含まれる砥粒は工作物表面を除去する作用に加えて電極間スペーサの役割を担う。砥石は、導電性ボンド砥石とし、研削液には電解液を用いる。両極間に数Aの電流を印可し、電解反応により陽極の金属を溶解させて砥粒でそれを除去しながら新生面を露出させて加工を持続させる。

しかし、小径深穴内周面の電解研削には、主に以下に述べる3つの課題があるため安定した加工の持続を困難にしていた。そこで、砥石に伝搬させた超音波振動がもたらす効果を適切に活用するにより、



第1図 UAE研削の模式図

それら課題を解消することができた。なお、適用した超音波振動は軸方向振動40 kHz、砥石先端の振幅は約10 μm である。

2-1 超音波振動の消泡効果

工作物小径内周面と砥石間に電解液を供給しながら電圧を印加すると、第2図(a)で示すように水の電気分解で気体が発生し工作物内は気泡が充満し、安定した電解研削が困難であった。そこで、砥石に超音波振動を伝搬させると、第2図(b)に示すように大きな気泡が消失した。これにより電極間に電解液を安定して供給可能になったと考えている。

2-2 超音波振動の短絡抑制効果

電極間距離が0.02 mm以下になると電極間の電位差が低下しはじめ、電極が接触する前に電位差がなくなる⁽³⁾⁽⁴⁾、つまり短絡する。このことは電極間のスペーサとなっている砥粒サイズが限定されることを意味し、鏡面研削のような微細砥粒を用いた加工は困難となる。第3図(a)は回転中(図中、矢印方向に回転)の砥石外周にFe材を約10 Nで押し付けた状態で電圧を印加した様子を示しているが、同図よりわずかに電解反応を示す気泡が確認できる。そこで

砥石に超音波振動を伝搬させると第3図(b)に示すように電解反応が促進されていることが確認できる。

2-3 超音波振動の洗浄効果

電解反応により砥石の母材表面が酸化被膜で覆われ、導電性が失われ、安定した電解研削を持続できない場合の復活に向けて酸化被膜の除去、洗浄効果を確認するため砥石とFe材の配置を第3図と同様にし、砥石回転を停止した状態で観察した。

第4図(a)に示す状態から通電(第4図(b))し、電解停止(第4図(c))になったところで砥石に超音波振動を伝搬させると、第4図(d)に示すように砥石の母材表面が活性化し電解反応を継続させることが可能になった。

第5図(a)に粒度#2000の電着砥石を用いたUAE研削による加工面を示す。第5図(b)では超音波振動援用研削特有の波形状の切削軌跡が確認できる⁽⁵⁾⁽⁶⁾。「電解加工」プラス「超音波振動研削」で生まれたUAE

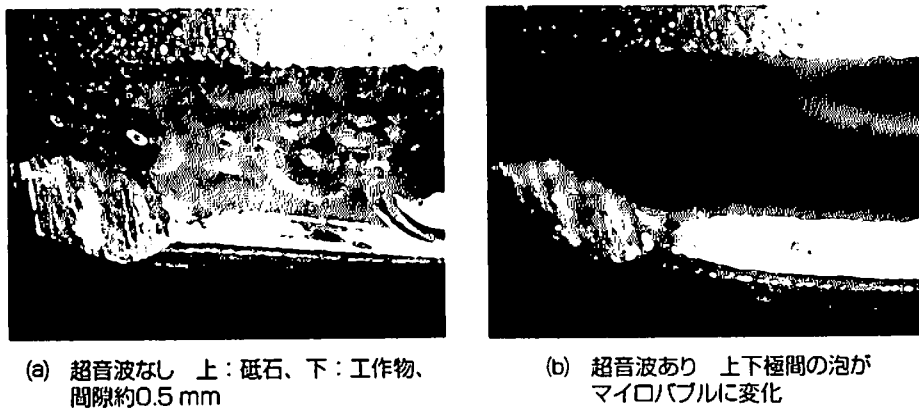
研削であるが、単なる加工方法の組み合わせのプラスではなく、工具と加工面の間では多くの相乗効果を確認できた。

3. 超音波振動援用プラズマ放電研削

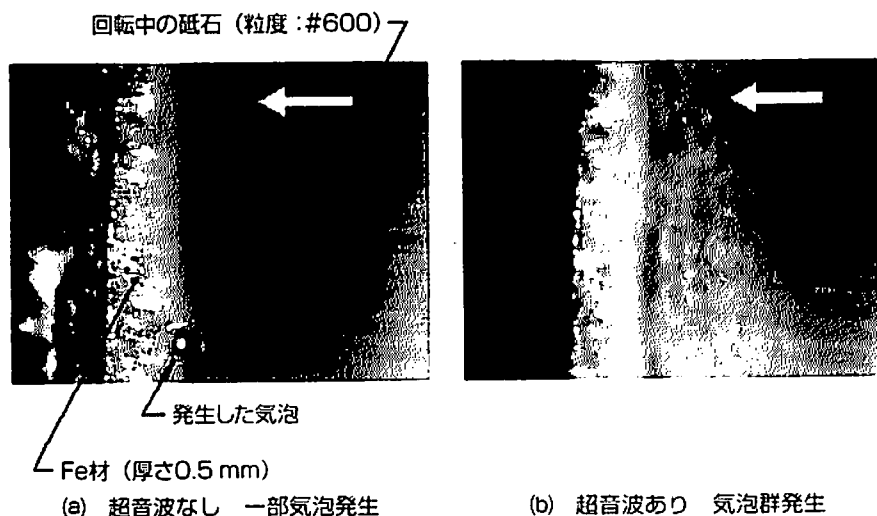
「UAE研削」マイナス「加工液中電解質」が超音波振動援用プラズマ放電研削(Ultrasonic assisted Plasma Discharge grinding、以下UPD研削と呼ぶ)である。第6図で示す実験装置でUAE研削の実験中に、加工液タンク内の電解液を純水に交換して加工したところ、加工面は光沢面から梨地面に変化し、加工量はUAE研削より大きく増加した。そして、その加工面はこれまでの光沢面とは異なる性質をもたらすことが判った。

3-1 超音波振動による流動抵抗の変化

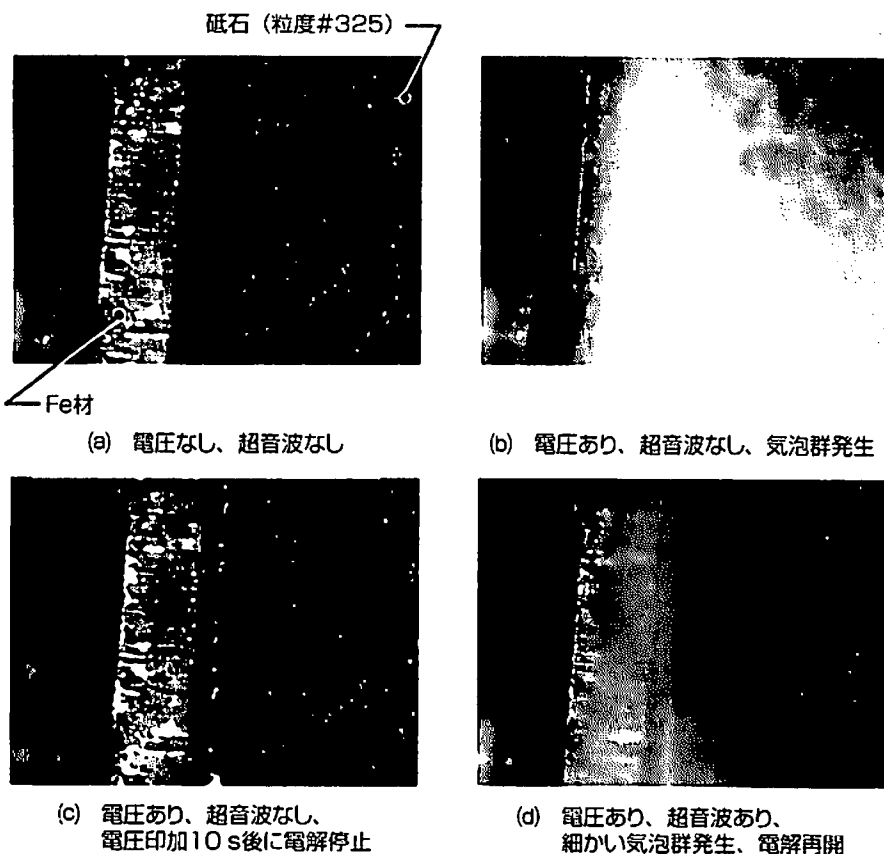
止まり孔の小径内面研削ではセンターホールを有する砥石を用いるケースが多い。小径のセンターホ



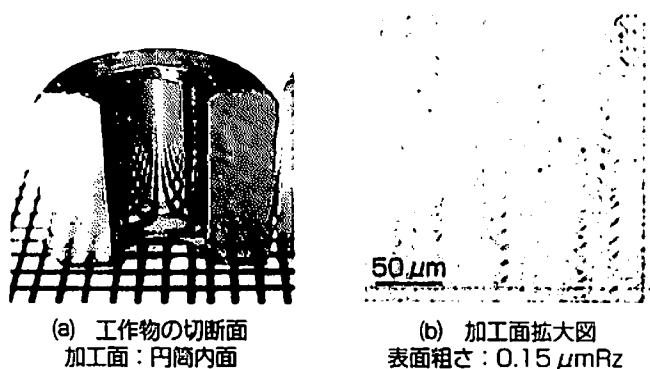
第2図 超音波振動の消泡効果



第3図 超音波振動の短絡抑制効果



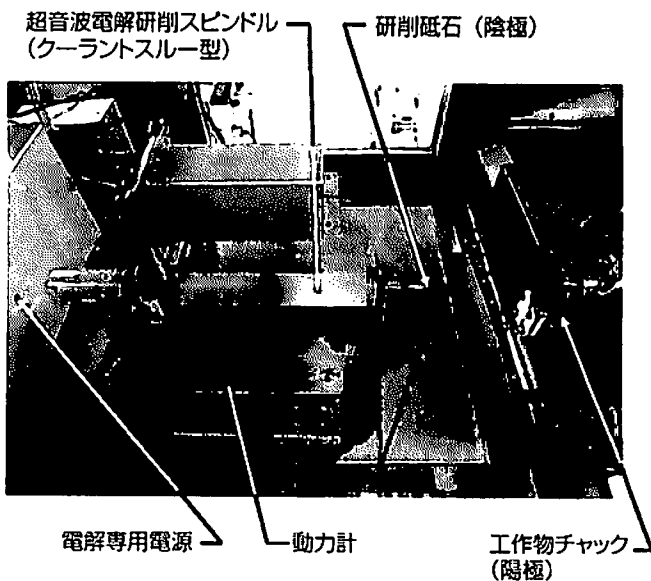
第4図 超音波振動の洗浄効果



第5図 UAE内面研削加工面

ールから水を安定して噴出させるためには、通常、高圧ポンプが必要になる。超音波振動は、そのセンターホールを通過する水の流動抵抗を軽減する。

第7図(a)に示すのは内径0.4 mmのセンターホールを有する外径3 mmの軸付き砥石である。そこに一定の圧力で水を送り先端から水を滴下させる。そこで砥石に超音波振動を伝搬したところ、第7図(b)に示すように滴下していた水は勢いよく先端から流出した。特にセンターホール内に空気が混入すると、滴下が停止する程度のポンプ圧であったが、超音波振動を伝搬させるとスムーズに水が流出するの



第6図 実験装置
ベースマシン：内面研削盤MIG-101WS型 (ミクロン精密製)

を確認している。

3-2 「UPD研削」プラス「マイクロバブル」

超音波振動により、液中で発生させたマイクロバブルを利用して安定した微細なプラズマ放電の発生を追究した。放電は液相より気相で発生しやすく、またマイクロバブル界面には電荷が帯びているとい

われている。従ってマイクロバブルリッチな加工液を研削液としてUPD研削を行うことで、砥石と工作物の間には安定したプラズマ環境が得られるものと考察した。

第8図に鋳鉄平板をUPD研削している様子を示す。使用した砥石は鋳鉄を母材とし、粒度#2000で電極間距離を5 μ m程度に設定した。砥石回転4000 rpmで、砥石に伝搬させた超音波振動は軸方向振動50 kHz、砥石先端の振幅は6 μ mである。

第9図(a)に加工液に純水を使用したUPD研削の加工面を示すが、ほとんど放電痕が生成されていない。

第9図(b)にはマイクロバブラーを通した純水を用いた際の加工面を示す。放電痕が均一に生じている。このことは、超音波振動で発生するマイクロバブルだけでは不十分で、外部からマイクロバブルを取り入れ、その濃度を高めることがUPD研削では重要であることを示唆している。

3-3 「UPD研削」 プラス「パルス電流」

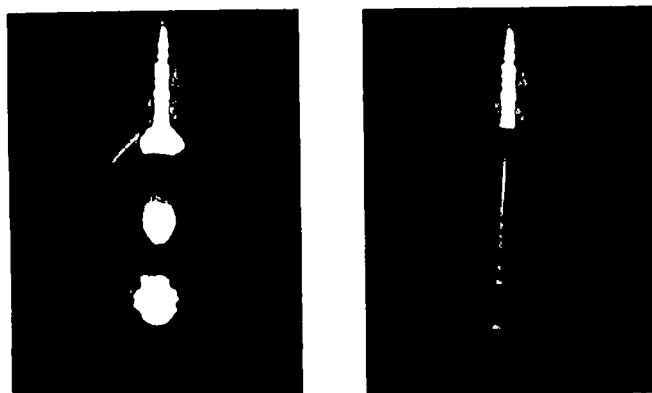
UPD研削において電極に印加する電流は重要な

条件である。その中で最も重要なのは直流電流をパルスで送ることであった。電流のON/OFFは超音波振動と同様にUPD研削では重要な役割を果たす。第10図(a)、第10図(b)では、従来の直流電流を用いた場合の加工とUPD研削専用開発したパルス電源装置を用いた場合の加工の様子を示す。画面左が回転砥石、右が工作物である。パルス電流を用いることで砥石と工作物間に安定した微細放電が発生することを確認できる。

3-4 機能的インターフェース創成

近年、製品の高機能化ニーズが高まり、軽量、高強度、高耐熱性、耐摩耗性を有する素材を用いた部品加工が増加している。そこで、従来加工技術では対応しにくい難削材において、UPD研削により加工面の機械的特性変化による難削材の快削化、さらに低強度材においては、高強度化加工を可能とし、それらのニーズを量産化対応も含めて解決を図る。

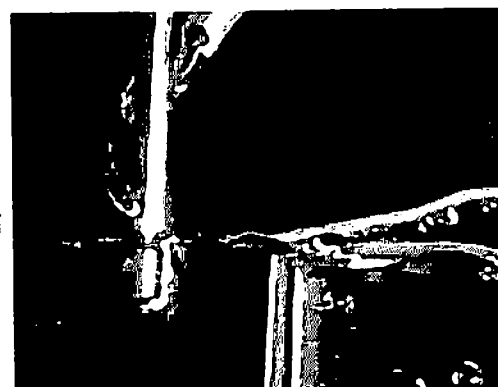
すなわち、加工面に特定の元素をドーピングすることにより、加工面近傍において化学組成や構造を変化(改質)させ、高い表面機能を有する界面、いわゆる“機能的インターフェース”を創成する⁽⁷⁾こ



(a) 超音波なし
圧送された水が滴下する

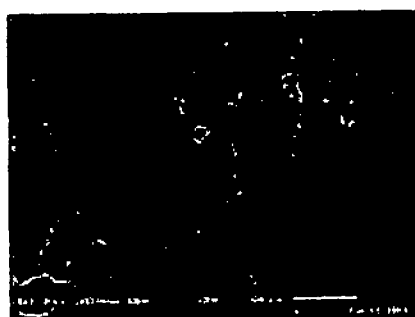
(b) 超音波あり
滴下していた水が流出する

第7図 センターホール砥石における超音波援用による通水性能の向上効果

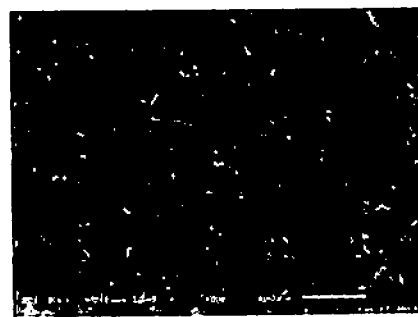


砥石

第8図 鋳鉄平板のUPD研削の様子

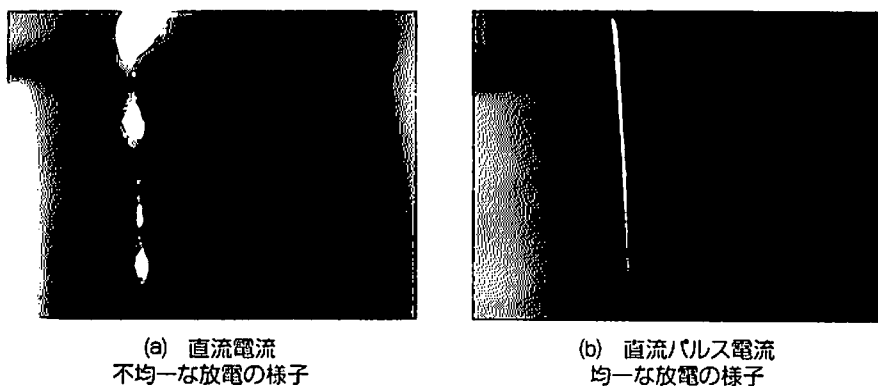


(a) 加工液：純水

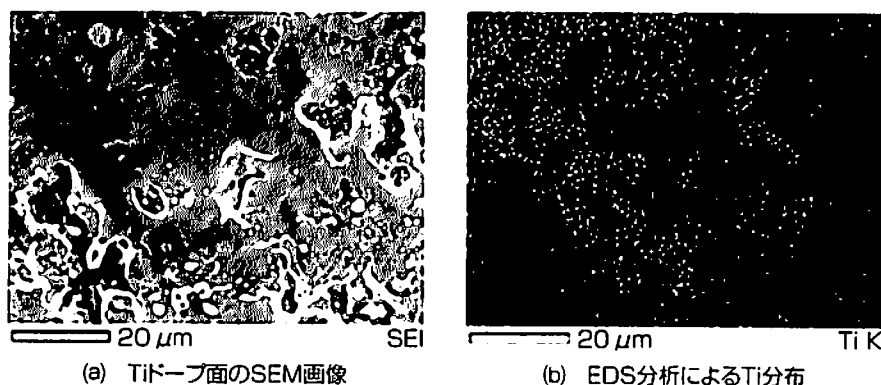


(b) 加工液：マイクロバブル水

第9図 マイクロバブル水を用いたUPD研削加工



第10図 パルス電流の効果



第11図 UPD研削後のTiドーブ面とTi分布

とを目指している。

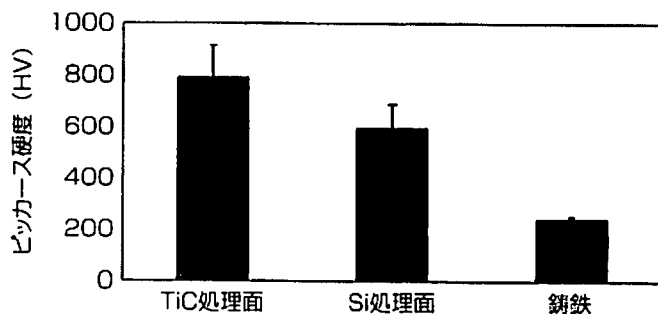
まず、焼結チタンを母材とした砥石を試作した。その狙いはUPD研削加工面へのチタンドーブである。放電の場合、負極から陽極へ電子が飛ぶ。同様に負極である砥石母材の元素は、陽極の工作物へ、いわゆる“打ち込む”ほどの高いエネルギーを有して移動し注入されることが判っている。

チタンボンド砥石を用いて鋳鉄をUPD研削した表面について第11図(a)にSEM画像、第11図(b)にEDS分析によるチタン分布を示す。

また、その表面の硬度をTiC処理面、およびシリコンドーブしたSi処理面との比較で第12図に示す。素材の鋳鉄表面よりも硬度が増していることを示している。

さらに、UPD研削した鋳鉄表面は摩擦係数が低減する。表面硬度が増大し、放電痕が形成される表面形状がその効果を創成していると考えられる。研削加工で平面精度を得て、放電痕が油だまりの役割を有し、高硬度で高寿命な摺動面を創成する。

すなわちUPD研削により工作物の表面形状を形



第12図 UPD研削後の表面硬度の比較

成しながらそこに機能性を付与する新たな技術となる可能性を見出している。放電痕のサイズを制御して、ドーブする元素を選択し、さらにはマイクロバブルに取り込まれる気体成分の選択で、今後、様々な機能性インターフェース創成が可能になると考える。

4. おわりに

UAE研削で、硬い材料を軟らかくして加工した。UPD研削では、軟らかい材料を加工して硬くした。これらの外部エネルギーを活用した研削加工におい

ては、砥粒の突き出し量に相当する、工具と加工材料の間隙が重要なポイントとなった。

特に「超音波振動」プラス「パルス電流」は、その微小な間隙から多くの新しい現象が生まれてくるように思われる。

謝辞

本研究開発は平成25～27年度戦略的基盤技術高度化支援事業の一環としてなされたものである。共同研究をさせていただいた(大)東北大学、(大)秋田県立大学、山形県工業技術センター、(株)カナック各位、ならびに、アドバイザーとしてご支援をいただいた富士ダイス(株)、多賀電気(株)各位ほか、(国研)理化学研究所、日本工業大学、(株)マイスター、ジャスト(株)、(株)IJR各位のご指導、ご協力を御礼申し上げます。

さらに本研究開発の機会を与えていただいた東北経済産業局関係各位に深甚なる謝意を表します。

<参考文献>

- (1) Satoshi Kobayashi, Keita Shimada, Chikashi Murakoshi, Kazunori Koike, Masayuki Takahashi, Toru Tachibana and Tsunemoto Kuriyagawa : International Journal of Automation Technology Vol.7, No.6, pp.654-662, November 2013
- (2) 小林敏・高橋征幸・立花亨・厨川常元・嶋田慶太：マイクロ超音波・電解ハイブリッド内面加工装置の開発、精密工学会誌、Vol.80、No.2、p146、2014
- (3) 佐藤健児：特集5 電解研削の理論と応用、機械工作、Vol.12、No.83、p.31、1965.5
- (4) 河村末久・矢野章成・樋口誠宏・杉田忠彰：研削加工と砥粒加工、共立出版、p.136 (1984)
- (5) Keita SHIMADA, Tianfeng ZHOU, Jiwang YAN and Tsunemoto KURIYAGAWA : Statistical approach for calculating ground surface roughness of ultrasonic-assisted grinding, Journal of the Japan Society for Abrasive Technology, Vol.56, No.11, pp.752-757 (2012)

- (6) Keita SHIMADA, Pay Jun LIEW, Tianfeng ZHOU, Jiwang YAN and Tsunemoto KURIYAGAWA : Statistical Approach Optimizing Slant Feed Grinding, Journal of Advanced Mechanical Design, Systems, and Manufacturing, Vol.6, No.6, pp.898-907 (2012)
- (7) Satoshi KOBAYASHI, Toru TACHIBANA, Chikashi MURAKOSHI, Kazunori KOIKE, Tsunemoto KURIYAGAWA and Masayoshi MIZUTANI : Development of ultrasonic vibration assisted plasma discharge grinding processing system enabling functional interface creation, Journal of the Japan Society for Abrasive Technology, Vol.62, No.2, pp.63-66 (2018)

【筆者紹介】

小林 敏

ミクロン精密(株) 技術部 技術開発課 参与

立花 亨

ミクロン精密(株) 技術部 技術開発課 参与

嶋田 慶太

東北大学 大学院工学研究科 機械機能創成専攻 助教

水谷 正驥

東北大学 大学院工学研究科 機械機能創成専攻 准教授

厨川 常元

東北大学 大学院医工学研究科 教授

● 優良技術図書案内

GMP準拠 細胞処理施設の基本

境 弘夫 編 A5判232頁 2,800円+税

お問合せは日本工業出版(株) フリーコール 0120-974-250 <https://www.nikko-pb.co.jp/>

機能創成加工から「未来の医療」へ 開発中に生まれるシーズを次々生かす

「医工連携は自然発生しにくい」「互いに行き来して実験・研究できる環境が必要」

取材で耳にするこうした言葉が気になっていった。そこで08年、大学院に逸早く「医工学研究科」を開設した東北大学を訪ね、17年度から第4代研究科長を務める厨川常元氏に、医工連携の経験と方法、同科の人材育成の仕組みを聞いた。

厨川氏は、生体機能創成学研究分野（医工学研究科）と、ナノ精密度加工分野（工学研究科）の教授でもある。研究の根幹に「超精密加工」という汎用性の高い技術があり、研究開発の過程で新たな

シーズを複数得て、次の研究につなげてきた。

例えば、ある加工技術を開発しようとするれば、目的とする技術だけでなく、その評価に必要な計測法や機械・装置も開発する。目的とは異なる現象が見出されることもある。それらが新たなシーズにつながるというわけだ。

「医工学研究科」では医工連携研究が中心かと思いきや、厨川氏は「医学・医療は、シーズの応用分野のひとつに過ぎない」と言い切る。その一方で、「これからの超高齢社会を考えると、高機能インターフェイス創成などの工学的アプローチが、予防医療や治療に貢献できる可能性は高い」と語る。

高付加価値化で「一番手」に

厨川氏のキャリアはジェットエンジン用の耐熱合金を「バリバリ

削る」ことから始まった。その歩みは、過去40年に起きた日本の「ものづくり」の変化と重なる。

①高エネルギーをめざした80年代
東北大学工学部と大学院で精密工学を学んだ70～80年代は大量生産・大量消費型の「ものづくり」全盛期。米国の大学に留学したときに航空機エンジンメーカーでタービンなどの機械加工研究を目の当たりにし、帰国後は「いかに速く削るか」を研究して難削材の高エネルギー加工をめざした。

砥石で、材料の不要部分をわずかず削り、材料の不要部分を除去して、所要の形状、寸法、表面状態にすることを「研削」という。当時、ダイヤモンドや、それに次ぐ硬度を持つCBN（立方晶ホウ化窒素）を用いた研削用砥石が普及しつつあったが、切れ味をよくする方法はまだなかった。そこで「目立て」の技術を開発し、機

械メーカーで広く使われるようになった。

②表面の形状づくりに取り組んだ90～00年代

90年代のバブル崩壊後の景気低迷で、工学研究者やものづくり企業は、ナノ精度の超精密加工技術を用いた製品に軸足を移した。その結果、光学素子や半導体デバイスの開発・製造技術が進化、日本の産業基盤を支えるまでになった。

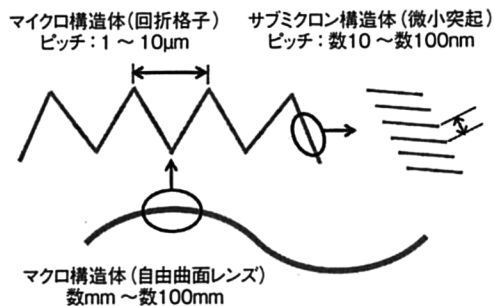
この時期、厨川氏は研削のターゲットをレンズや光学系部品の金型に定め、光学機械メーカーとの共同研究を多く行なった。研究の焦点は、「表面を磨く」あるいは「形状を創り出す」ことにあった。00年代半ば頃までに確立された非球面レンズ加工などの技術は、現在もカメラ、スマートフォンなど身近な道具や、内視鏡などに生かされている。

③機能の付加に活路を求める現在
ところが、00年代以降、人件費の安いアジア諸国の台頭や、メーカーの海外展開により現地調達が進んだことで、製造業における日本の国際競争力が低下した。



医工学研究科を率いる厨川教授

図1 ナノ・マイクロ・マクロ複合構造体による機能性インターフェイス創成(例)



そこで厨川氏は、次の一手として「形状創成+機能創成による機能創成加工」を提案している。そのためにはナノ精度、さらにはピコ精度で形状創成するだけでなく、その加工表面上に微細構造体をつくったり、加工表面近傍の結晶構造を制御したりすることで、新たな機能を持たせ、さらに高い付加価値を生み出す必要がある。

例えば、自由画面レンズ上にミクロンオーダーの回折格子、さらにその上に数百ナノミクロンピッチの微小突起を形成した「ナノ・マイクロ・マクロ複合構造体」は、「モスアイ(蛾の目)構造」と呼ば

④今後は予防への応用も視野に、これまでの研究を医療に生かす有望な分野の一例として歯科がある。厨川氏の研究室では、直径1ミクロン以下から数十ミクロンの粒子を高速かつ高密度に噴射して付着を行う「パウダージェットデポジション(PJD)技術」の応用を推進している。

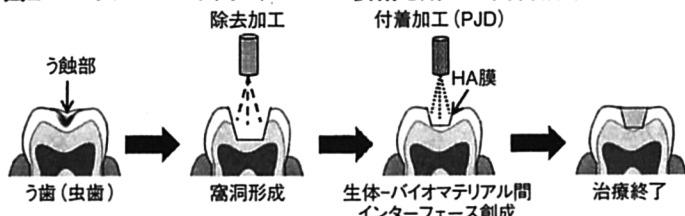
エナメル質の成分であるハイドロキシアパタイト(HA)の微粒子を噴射、人歯のエナメル質表面にHA膜を成膜することに世界で初めて成功した。

れる無反射機能を持つ光学素子となり得る。

強い日射しでスマホの画面が光って文字が読みとれなくなるのは、太陽光の反射が画面内から発する光を上回るからだ。「無反射機能を使った日なたでも見やすいスマホがあれば、多少価格が高くても欲しい人がいるでしょう」(厨川氏)。

このほかにも、使用する材料や微細構造を変化させることによつて、防曇、防汚、超撥水、親水など、さまざまな機能の発現が可能だという。

図2 パウダージェットデポジション技術を用いた歯科治療



この方法は、痛みが少なく、自然に近い歯質を得られる点で、従来の治療法とは一線を画す。現在、知覚過敏の新しい治療法として期待されている。また、エナメル質表面の微細な傷を埋め、より白く透明感のある歯を維持する「審美歯科」や、歯茎部に抗菌性HA微粒子で成膜して歯周病を防ぐ「予防歯科」も夢ではない。

さらに、「生体に優しいバイオインターフェース創成」も、医療分野に近い研究だ。例えば、人工股関節などのチタン系材料にレーザー照射し、生体活性機能を付与することにも成功した。埋め込んだ際に、生体由来のHA

(骨や歯の主成分)が自然に析出しやすい表面構造ができたのである。この方法を利用すれば、手術を受ける人の骨との固着性に優れた人工骨頭や、歯科インプラントの作成が可能である。

◇ ◇ ◇

以上は研究内容のほんの一部だが、手にしたシーズの応用先を考えるにあたっては、「一番手になることが重要だ」(厨川氏)。研究開発から社会実装までは時間と費用がかかるため、手術支援ロボットのように、他国が最初に開発した製品は、国内需要(売上高や利益の見込み)との兼ね合い次第で「海外メーカーから買うほうがよい」という判断になりがちだからだ。

これからの「ものづくり」では、将来何が求められるか、何が売れるかを十分予想し、必要な技術や解決すべき課題を明らかにする「バックキャスト的発想」が求められる、というのが厨川氏の持論だ。

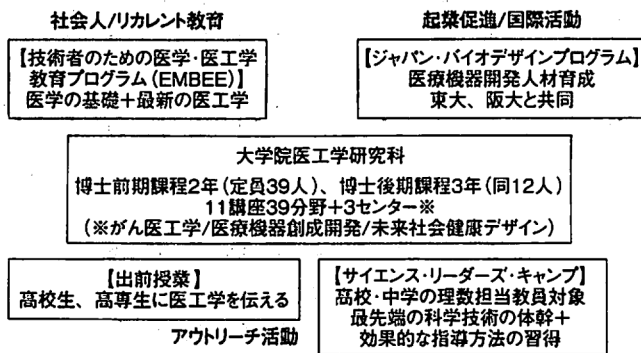
世界に類を見ない速度で高齢化が進む日本では、その経験を逆手にとって発想の材料にできるかもしれない。

表 東北大学大学院医工学研究科の構成 (2019年7月現在) 筆者作成

講座	分野
計測・診断医工学	●生体超音波医工学●バイオセンシング医工学 ●分子構造解析医工学●医工放射線情報学
治療医工学	●生体電磁エネルギー医工学●超音波ナノ医工学 ●★腫瘍医工学☆先進歯科医工学●医用材料プロセス工学 ●生体機能材料プロセス工学
生体機械システム医工学	●生体流体力学●医用ナノシステム学 ★病態ナノシステム医工学●ウェットデバイス工学
生体再生医工学	★感覚再建医工学★神経外科先端治療開発学 ★消化管再建医工学☆骨再生医工学★分子病態医工学
社会医工学	★リハビリテーション工学★健康維持増進医工学 ●医療福祉工学●神経電子医工学●ライフサポート工学
医療機器創成医工学	★医用イメージング●医用光学●生体機能創成学 ●ナノデバイス工学○近未来生命情報工学
生体流動システム医工学	●融合シミュレーション医工学●医用流動光学
人工臓器医工学	★人工臓器医工学
生体材料学	●医用金属構造形態制御学●医用金属材料学
生体システム制御医工学	●サイバー医療システム●知能システム医工学 ●ニューロロボティクス
生体情報システム学	●生物規範ロボティクス●マイクロ磁気デバイス医工学 ○ナノバイオ医工学

講座責任者の専門分野 ●工学(25) ★医学(9) ●★工学・医学(1) ☆歯学(2) ○農学(1) ○理学(1)

図3 東北大学における医工学人材育成 (2019年7月現在)



10講座31研究分野で発足した医学研究科は、現在11講座34研究分野になり、学生数も増加傾向にある。

保健・生物・農学・農学系及び理工学系の学部卒業者は、博士前期課程で「医学基礎科目」を学ぶ。次いで応用科目を学ぶコースが3つあり、医工学の知識・技術を用いて医学・生物学の基礎学理を解明する「基礎医工学コース」、

革新的診断・治療技術の開発を目的とする「応用医学コース」、医療機器に特化した実用研究をめざす「医療機器創生コース」から選択できる。その後、博士後期課程で開講されている。

学部での専攻は工学系が多く、08～17年に修士課程を修了した290人中医学系は9%弱、博士課程では60人中17%弱だった。社会

人院生も多く、厨川氏の研究室の場合は10人中8人を占める。

また、「リカレント教育」にも力を入れている。メーカー勤務でキャリアを重ねても、医療機器事業に参入するとなると、「医学の言葉」を理解し、医師と話す必要に迫られる。そうした社会人に対して、大

アップデートした「EMBEE」(Education of Medicine and Biomedical Engineering for Engineer)を開講した。臨床医学の各領域とその理解に必要な基礎医学をひとつの講義にまとめるとともに、機械、電気、マテリアルといった工学の各分野の最新情報も紹介していくプログラム構成となっている。

そのほかに、医療機器イノベーションをけん引する人材育成プログラム「ジャパンバイオデザイン」も好評である。開発の初期段階から事業化を目標に、医療現場のニーズを実現する製品開発を試みるのが特徴である。

その一方で、医工学人材の裾野を広げるために、中高生や理数担当教員を対象とするアウトリーチ活動も行っている。

これらは医学を日本の今後の成長戦略の鍵となる分野と捉え、一大学の問題にとどまらず、将来を担う人材の育成を行わねばならないという使命感が根底にあつての仕組みと言える。

学院以外にも1年単位で講義を受け、実験・実習を行うプログラム「REDEEM」(医療工学技術者創成のための再教育システム)が用意されている。これまでの受講者は2000人以上となった。

19年4月からは、さらに

【技術者のための医学・医工学教育プログラム(EMBEE)】
医学の基礎+最新の医工学

【サイエンス・リーダーズ・キャンプ】
高校・中学の理数担当教員対象
最先端の科学技術の体幹+効果的な指導方法の習得

【出前授業】
高校生、高専生に医学を伝える

アウトレチ活動

【ジャパン・バイオデザインプログラム】
医療機器開発人材育成
東大、阪大と共同

大学院医工学研究科
博士前期課程2年(定員39人)、博士後期課程3年(同12人)
11講座39分野+3センター※
(※がん医工学/医療機器創成開発/未来社会健康デザイン)

社会人/リカレント教育

起業促進/国際活動

筆者作成

医学・医療ライター本島玲子

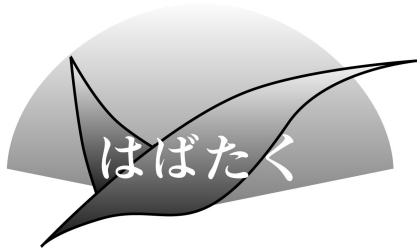


図1 公益財団法人いわて産業振興センター。

地元貢献を目指して

公益財団法人いわて産業振興センター
ものづくり振興部産学連携室；研究支援員、
東北大学大学院工学研究科 博士課程後期課程1年
久慈千栄子

1. はじめに

私は、2016年3月に東北大学大学院工学研究科機械システムデザイン専攻 博士課程前期2年の課程(修士課程)を修了し、2016年4月より、富士フイルム株式会社 R&D 統括本部生産技術センターにて子会社工場の工程改善に務めておりました。2018年9月より、現職である公益財団法人いわて産業振興センターにUターン転職し、2019年4月より東北大学大学院工学研究科機械機能創成専攻 博士課程後期3年の課程(博士課程)に社会人ドクターとして進学。現在は博士号取得を目指しながら、研究支援員として地元貢献のための研究に取り組んでおります。私の研究生活の中で金属材料に携わっている機会は少なく非常に恐縮ではございますが、この度縁がありまして「はばたく」執筆の貴重な機会をいただきましたので、これまでの経験を振り返り、現在の研究活動について述べさせていただきます。

2. 研究生活と企業経験

まずは、学生時代から現在までご指導をいただいている、厨川常元教授の研究室をご紹介させていただきます。研究室では、切削加工や旋削加工、レーザー加工やプレス加工など、幅広い加工分野においてナノ精度の機械加工を行い、加工表面に任意の機能を発現する微細3D構造を創成するなど、新たなものづくり技術の可能性を探求しております。その中で私は、学部4年生から修士課程2年生までの3年間、パウダージェット加工を用いた新たな歯科治療法に関する研究に取り組んでおりました。本研究では、ヒト歯と同様の成分を持ち、生体親和性の高いハイドロキシアパタイト $\text{Ca}_{10}(\text{PO}_4)_6(\text{OH})_2$ というセラミクス材の微粒子を歯に直接衝突させることにより、虫歯の除去や新たな歯質の創生を目指しています。先行研究により、この除去加工と付着加工を左右するメインファクターの特定と、最適加工条件選定の検討が行われておりましたが、材料の破壊や付着のメカニズム解明の検討は行われておりませんでした。そこで私は、延性の小さいセラミクス材の変形を再現するため、平滑化粒子法(SPH法)を用いて粒子の衝突時の応力分布や破壊挙動を解析し、分子動力学解析を併用することで原子結合により付着する領域の特定を行いました⁽¹⁾。しかし、研究活動は上手くいくことだけではなく、従来付着するとされていた加工条件であっても粒子が付着せず、試行錯誤する日々が続きました。先生方と議論し、先輩と試行錯誤を行う中、東北大学金属研究所 今野豊彦教授のもと、TEMによる粒子の観察を行う事で、衝突させる粒子の十分な結晶成長が必要であることを明らかにしました⁽²⁾。研究活動はスムーズに進むことだけではありませんでしたが、材料加工の原理原則を掴むためには、根気よく様々な視点から材料自体の理解を深めること

が重要であることを学び、材料研究へ対する興味もより強くなっていきました。

修士課程の修了後は企業に就職し、生産技術センターに所属しました。企業時代は主に子会社工場の工程改善を担当し、ものづくりの現場に密着した業務を行いました。製造能力強化の任務を遂行する中で、日々の製造やトラブル対応と並行してQCD(Quality(品質)・Cost(コスト)・Delivery(納期))を担保するものづくり体制を確立していくには、製造部や設計部門など、様々な関係者との協力が必要不可欠となります。それぞれの専門が異なる集団で意思疎通を行う難しさや、何よりも研究室で行う研究とリアルなものづくり現場のギャップを肌で感じ、自分の経験不足・知識不足を痛感しました。しかし、様々な立場の人間が意見を出し合うことで自分一人では思いつかない考えやアプローチが生まれる面白さも体感し、製造現場の方々の生の声を聞いていく中で、研究員としてもっと現場に寄り添ったものづくり技術の開発を試みたい、という気持ちが生まれていきました。そのためには、自分の専門分野の間口を広げ、より多くの企業の方々と接していくべきだと感じ、転職を決意しました。

3. 研究支援活動について

現在は、地元岩手県の公益財団法人いわて産業振興センター(図1)に所属しております。弊センターは、県内の産業振興を推進するため、県内中小企業に対し経営相談や販路開拓、金融支援、研究開発における産学官連携のためのマネジメント等の総合支援を行う県の中核的支援機関です。今年度から、新たな試みとして「若手専門人材確保支援事業」を創設、2名の研究員をセンター内に直接配置し、県内大学や企業の研究活動のサポートを行っております。私はこの研究員として機械加工分野を担当しています。また、新たな技術を県内企業に移転するための研究テーマを模索し、自身の担当する分野では、「難加工材料であるアモルファス金属の加工に関する研究」、「各金属材料に対する高効率放熱表面創生の研究」の2つの基礎研究を推進しています。金属材料に対する加工については経験が少なく、暗中模索の日々ですが、企業の方々にご助力いただきながら研究活動を行える環境にやりがいを感じております。岩手県は自社に研究開発部門を置く企業はまだ多いとは言えませんが、開発した技術を企業へ移転する事で微力ながら地元の技術力向上に貢献できるよう邁進して参ります。

最後になりますが、この場をお借りしまして日頃研究をご指導いただいております東北大学の先生方、地方独立行政法人岩手県工業技術センターの職員様、ご助力頂いております企業の皆様へ深く御礼申し上げます。

文 献

- (1) 水谷正義, 久慈千栄子, 大久洋幸, 西村俊亮, 水谷公一, 赤塚 亮, 佐々木啓一, 徐少林, 嶋田慶太, 厨川常元: 砥粒加工学会誌, **61**(2017), 28-33.
- (2) 富江瑛彦, 久慈千栄子, 大久洋幸, 嶋田慶太, 水谷正義, 佐々木啓一, 厨川常元: 日本機械学会論文集, **81**(2015). (2019年10月30日受理)[doi:10.2320/materia.59.161] (連絡先: 〒020-0857 盛岡市北飯岡 2-4-26)

選択的レーザー溶融法による根状多孔質構造体の創成

東北大・院 ○中善寺優昂, 石橋信治, 溝井琢巳, コマツ NTC 前花英一,
東北大・工 嶋田慶太, 水谷正義, 東北大・医工 厨川常元

1 緒言

多孔質金属材料は緻密材にはない特異な性質を有しており、軽量構造材料、断熱材、衝撃吸収材などとして多くの分野での活用が期待されている¹⁾。特に医療分野では、インプラントを多孔質化することにより、応力遮蔽現象の緩和²⁾や、孔内骨成長による強固な骨結合の獲得³⁾などが期待できる。現在では選択的レーザー溶融法 (SLM: Selective Laser Melting) をはじめとした金属積層造形法 (MAM: Metal Additive Manufacturing) の発展により、多孔質構造体を高い形状設計自由度で作製することが可能となっている。しかし、多孔質構造体の設計には専用の設計ソフトを用いることに加え、形状再現が可能な限界寸法を制約として加味する必要がある。したがって、設計領域の大きさに左右されず、かつ簡便な多孔質金属材料の作製手法が望まれる。

著者らは、SLM を利用し、造形条件の制御により一般的に欠陥とされる SLM 造形物内部の空孔を積極的に活用する新たな多孔質金属材料の作製手法を提案している⁴⁾。得られる構造体を根状多孔質構造体 (RPS: Rhizoid Porous Structure) と称している。この名称は図 1 に示すような本構造の数十〜数百マイクロンオーダーの特徴的な連結孔に由来する。先行研究では、造形条件のエネルギー密度および走査速度の変更により空孔率を任意に操作できることを明らかにした⁴⁾。最終的には、力学的あるいは機能的な事前設計から適切な造形条件を導出し、複数の機能性を相乗的に備えた高機能性インプラントをニアネットシェイプで作製することを目指す。

本報では、SLM による空孔制御における空孔率の制御可能範囲を把握するため、RPS における空孔率の上限値を検討した。また、造形した RPS 試験片を用いて圧縮試験を実施し、その機械特性を評価した。

2 造形条件と内部空孔の関係

2.1 実験手法

金属積層造形装置 ProX100 (3D Systems) を用いて Ti-6Al-4V 合金 (以下 64Ti) 製の SLM 試料 (7mm 角立方体) をアルゴン雰囲気中で造形した。固定した造形条件はレーザースポット径 80 μm, レーザ走査幅 $d = 70 \mu\text{m}$, 積層厚 $t = 45 \mu\text{m}$ であり、レーザー走査経路は層ごとに 90°ずつ回転させた。変更した条件はレーザー出力 W とレーザー走査速度 s であり、各パラメータから式(1)によって求められるエネルギー密度 E_d を表 1 にまとめる。なお後述するが、下線付き数値は造形不可であった条件をあらかじめ示している。また、試料の空孔率は X 線 CT スキャンにより算出した。

$$E_d = \frac{W}{t \cdot ds} \quad (1)$$

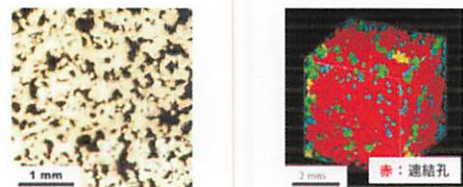


図 1 RPS の内部空孔

表 1 造形条件とエネルギー密度の関係

エネルギー密度 J/mm ³	走査速度 mm/s		
	430	500	550
出力	25	18.5	15.8
W	30	22.1	19.0
	35	25.8	22.2
	40	29.5	25.4
	45	33.2	28.6

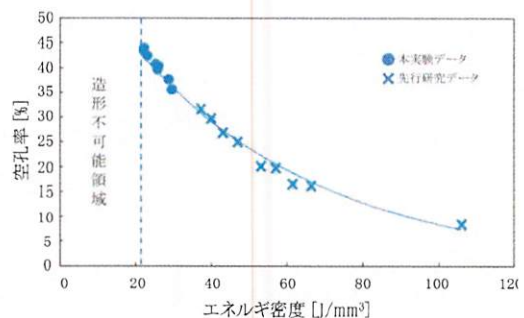


図 2 空孔率とエネルギー密度の関係

2.2 結果および考察

各試験片のエネルギー密度と空孔率の関係を図 2 に示す。一部の空孔率は先行研究を引用した。同図より、エネルギー密度の増加に伴って空孔率は指数関数的に減少していることが分かる。これは、熱投入量の増加が粉末の溶融を促進し、安定したメルトプールの形成を誘起したためであると考えられる。なお $E_d = 14.4\text{--}20.2 \text{ J/mm}^3$ の 6 条件では試験片がその形状を保持できず、実質的に造形が不可能であった。したがって、本実験系での RPS の造形可能なエネルギー密度下限値 $E_{d\text{min}}$ は 22 J/mm^3 程度であった。SLM において造形が成功するためには、粉末層の溶融と同時に、既に凝固が完了しているため下層との接合が必須となる。すなわち、 $E_d \leq E_{d\text{min}}$ では良好な層間接合が得られず、粉末供給時に付与される外力によって容易に形状が崩壊したと考えられる。この $E_{d\text{min}}$ は粉末の粒度分布や粉末層の積層厚によって概ね決定されると考えられる。以上より、本実験環境によって得られる空孔率の上限値は 45%程度であることが明らかとなった。

3 RPSの圧縮強度特性

3.1 実験手法

試験片は直径 5 mm、高さ 10 mm の円柱とし、表 2 に示す 6 条件で造形を行った。なお、表中に示されていない条件は前節と同様である。各条件によって得られる空孔率は走査速度の小さいほうから、それぞれ 8.56、16.3、20.2、25.2、29.7、31.9% である。圧縮試験機の試験速度は 1 mm/min とし、得られた応力-ひずみ線図から弾性率と最大圧縮応力を算出した。また、試験片の破断面を走査型電子顕微鏡 (SEM) で観察した。

3.2 結果および考察

本試験により得られた応力-ひずみ線図を図 3 に、空孔率と最大圧縮応力および弾性率との関係を図 4 と図 5 にそれぞれ示す。両値は空孔率の増加に伴って線形的に減少した。この傾向は、空孔率の増加に伴った 64Ti 基底領域の減少によって空孔近傍での応力集中が増長されたことに起因すると考えられる。また、本実験によって得られた弾性率は最大でも 20.1 GPa であり、64Ti パルク材の弾性率 110 GPa 程度³⁾と比べて 1/5 以下である。これだけ低い弾性率は、例えば、金属製インプラントと生体骨 (弾性率 20~30%程度⁴⁾) との弾性率の乖離に起因して生じる応力遮蔽問題の解決に一定の効果をもたらすと考えられる。また、破断面の SEM 画像の一部を図 6 に示す。同図 (a), (b) より、空孔率が低い試験片の破断面ではディンプルパターンが主体的に存在し、延性的な破壊形態であることが示唆された。一方、同図 (c), (d) ではディンプルパターンはほとんど確認されず、すべりを伴った脆性的な破断面が認められた。これらの結果は、空孔形態の違いが構造の局所的な変形プロセスに影響を与えることを示唆している。

4 結言

本研究により得られた結果を以下に示す。

- 1) 実験環境において、RPS を有する造形物を良好に造形するために必要なエネルギー密度の下限値はおおよそ 22 J/mm³ である。
- 2) 現手法で得られる RPS の最大空孔率は約 45% である。
- 3) RPS 試験片の最大圧縮応力と弾性率は空孔率の増加に伴って単調に減少した。
- 4) RPS 試験片の弾性率は従来パルク材と比べて 1/5 と非常に小さい値を示した。

参考文献

- 1) 小橋真, ポーラスメタルの現状と展望, 軽金属, 55, 7 (2005) 327-332
- 2) Sajad Arabnejad et al, Fully Porous 3D Printed Titanium Femoral Stem to Reduce Stress-Shielding Following Total Hip Arthroplasty, J Orthop Res, 35, 8 (2017) 1774-1783.
- 3) 丹羽健ら, Ti-Zr 合金多孔体インプラント内への骨組織侵入と骨結合力, 日口腔インプラント誌, 19, 4 (2015) 29-35.
- 4) 佃将希ら, 金属積層造形法による高機能多孔質インプラントの開発, 精密工学会春季大会学術講演会講演論文集, (2018)
- 5) 岸雄雄, チタンテクニカルガイド-基礎から実務まで-, 内田老鶴園, (1993) 202.
- 6) 中野貴由, 付加製造技術 (3D プリンター) による金属系生体機能性材料の開発, スマートプロセス学会誌, 3,3 (2014) 167-174.

表 2 造形条件

レーザー出力 W	50
走査速度 mm/s	150, 240, 300, 340, 400, 430

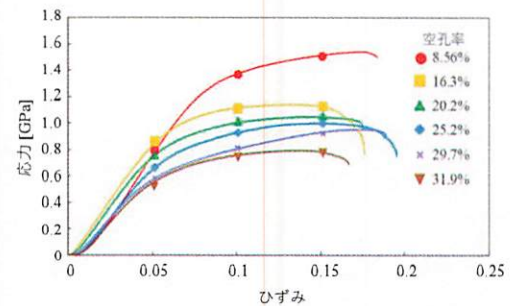


図 3 応力-ひずみ線図

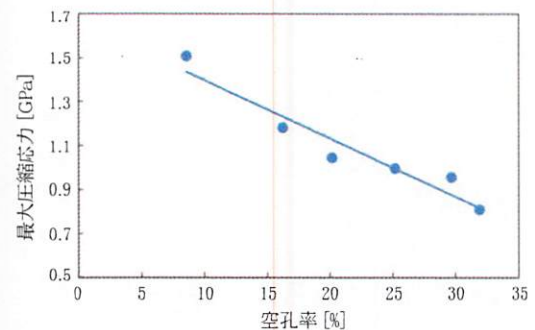


図 4 最大圧縮応力と空孔率の関係

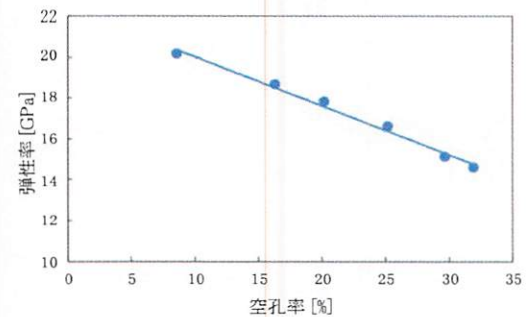


図 5 弾性率と空孔率の関係

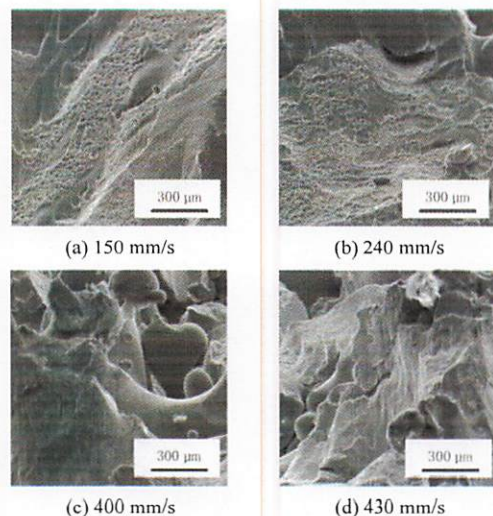


図 6 破断面 SEM 画像

パウダージェットデポジションの審美歯科治療への応用

本郷那美*1, 山本浩己*1, 富江瑛彦*3, 泉田一賢*2, 佐々木啓一*2, 嶋田慶太*1, 水谷正義*1, 厨川常元*3

Nami HONGO, Hiroki YAMAMOTO, Akihiko TOMIE, Kuniyuki IZUMITA, Keiichi SASAKI,

Keita SHIMADA, Masayoshi MIZUTANI and Tsunemoto KURIYAGAWA

Key words: hydroxyapatite, zirconium dioxide, abrasive blast, composite particles

1. 緒言

近年、歯科医療分野では生体機能の回復・改善に加え、歯の色調を美しく保つ審美歯科治療の需要が高まっているが、現時点では、安全で確実な技術は確立されていない。この課題を解決すべく、常温大気圧下で粒子を高速で衝突させ成膜するパウダージェットデポジション(以下 PJD)法の審美歯科治療への応用を試みる。人歯の主成分であるハイドロキシアパタイト(以下 HA)粒子を用いた PJD 法による補綴および予防歯科的な有用性は既実証されており、現在臨床試験が行われている。一方、純粋な HA 薄膜では隠蔽性に乏しいことから、インプラント材として利用が拡大している ZrO₂の粒子を HA と複合することで審美治療に適用することを検討している。本報では、まず ZrO₂粒子単体の PJD 実験により、成膜性および審美性を検証した。またその結果より、ZrO₂粒子は成膜性に劣ることが判明したので、同粒子と HA を複合した HA/ZrO₂複合粒子および比較のために粒径の異なる 2 種の HA 粒子を複合した HA/HA 複合粒子を作成し、その成膜性を検証した。

2. ZrO₂粒子による成膜と色調評価

2.1 ZrO₂粒子の成膜実験

図 1 に歯科治療用に開発されたチューブ搬送式 PJD 装置の外観を示す。この装置は、圧縮供給ガスが粒子を充填したタンク内に流入し、粒子がチューブ内を通りハンドピース部へと搬送される仕組みである。粒子はハンドピース噴射口付近で加速ガスと合流して加速された後噴射され、対象物へ衝突して成膜に至る。同装置の粒子タンクに粒径 2.7 μ m の ZrO₂粒子を充填し、表 1 の条件のもと成膜実験を行った。図 2 が形成した膜の非接触 3 次元形状測定機で測定結果であり、膜厚約 2.0 μ m の薄膜形成を確認できる。ZrO₂粒子でも PJD 法により成膜可能であることがわかった。

2.2 ZrO₂粒子膜の色調評価

色調評価には、分光測色方式に属した高速分光光度計を用いた。図 3 に示す分光分布の測定結果より、全体的に ZrO₂膜は HA 基板よりわずかに反射率が高かった。また、どちらも波長が大きくなるにつれて反射率が単調に減少しているが、ZrO₂膜は減少傾向が比較的小さく、より色の偏りが少ない白



図 1 PJD 装置

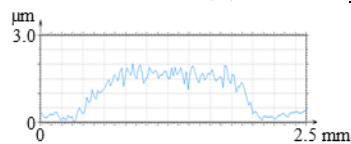


図 2 ZrO₂膜断面プロファイル

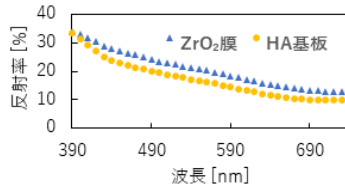


図 3 ZrO₂膜と HA 基板の分光分布

基板材料	HA
搬送流体	空気
加速圧力	0.2MPa
供給圧力	0.5MPa
噴射時間	30s
噴射距離	5.0mm

表 2 L*a*b*値

	ZrO ₂ 膜	HA 基板
L*	52.19	47.43
a*	-1.575	-1.618
b*	-11.55	-12.82

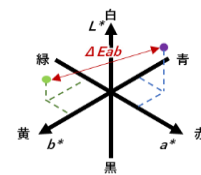


図 4 色空間の模式図

色に近い。次に図 3 の結果を CIE L*a*b*表色系に変換し、色差を求めた結果を表 2 に示す。L*, a*, b*値はそれぞれ、明暗、赤緑、青黄の度合いを表し、図 4 の色空間における座標、つまり色を決定する値である。色差 ΔE_{ab} は同図における 2 点間の距離として以下の式で求められる。

$$\Delta E_{ab} = \sqrt{(\Delta L^*)^2 + (\Delta a^*)^2 + (\Delta b^*)^2} \quad (1)$$

ここで ΔL^* , Δa^* , Δb^* は色空間内での明度と色度の差である。一般的に $\Delta E_{ab} = 2.3$ を丁度可視差異として扱うことが多い³⁾。計算の結果、ZrO₂膜と HA 基板との色差は 4.93 と 2.3 を上回るため、有効な色差といえる。さらに表 2 から、求めた色差は ΔL^* が支配的で、ZrO₂膜の形成により L*値が増加したことを考慮すると、人が十分に識別できる程度に明度が高くなったと判断できる。したがって本実験において、色の偏りが少なく HA 基板より高い明度を有する白色の ZrO₂膜の成膜に成功したといえ、PJD 法を用いた ZrO₂粒子によるホワイトニング効果を確認した。

3. 粒子の複合化による成膜性変化

3.1 複合粒子の作成

HA 粒子単体では PJD 法により数十 μ m 以上の成膜を実現している¹⁾。そこで第 2 章で示した ZrO₂粒子の成膜性を改善すべく、HA 粒子と複合した HA/ZrO₂複合粒子を作成し、その成膜性について検証した。図 5 に示す複合化装置に投入

*1 東北大学 大学院工学研究科:〒980-8579 仙台市青葉区荒巻字青葉 6-6-01 Graduate School of Engineering, Tohoku University
*2 東北大学 大学院歯学研究科:〒980-8575 宮城県仙台市青葉区星陵町 4-1 Graduate School of Dentistry, Tohoku University
*3 東北大学 大学院医工学研究科:〒980-8579 仙台市青葉区荒巻字青葉 6-6-12 Graduate School of Biomedical Engineering, Tohoku University

された粒子は、高速回転する攪拌翼と容器内壁の間を通過する際に受けるせん断力によりメカノケミカル反応を生じさせる。この反応により子粒子を母粒子に対して高強度に固定でき、粒子噴射時の破碎・分離等を防ぐことができる。本装置を用い、表 3 の条件下で HA/ZrO₂ 複合粒子および比較用の HA/HA 複合粒子を作成した。同表で粒径はメディアン径を、複合比率は生成時の母粒子に対する子粒子の重量比率を意味する。図 6 は以上の粒子の走査型電子顕微鏡 (SEM) 像であり、母粒子表面上に使用した子粒子の大きさ相当の微粒子の付着が確認できることから、HA/ZrO₂ および HA/HA 複合粒子が作成できたと判断した。

3.2 複合粒子の成膜実験

前節で作成した HA/ZrO₂ 複合粒子、HA/HA 複合粒子、およびその未処理の HA 母粒子を用いて、前章と同様に表 1 の条件下で成膜し、それら 3 つの膜を非接触 3 次元形状測定器により測定した。図 7 が各膜の断面プロファイルであり、同図(a)より、前章の ZrO₂ 粒子に比べ、HA/ZrO₂ 粒子による厚膜化が可能であることがわかる。一方、同図(b)のとおり、成膜性は未処理 HA 粒子が最も高く、以下、HA/HA 複合粒子、HA/ZrO₂ 複合粒子の順番であった。これらの結果は被加工物衝突と粒子の最表層、複合粒子であれば子粒子の物性が影響を及ぼしたと推定できる。HA は水酸基、カルボキシル基などの官能基に高い吸着性を有し、自身もまた水酸基を持つことから、HA 粒子は HA 基板に付着しやすいと考えられる⁴⁾。また同材料の基板と粒子間で物性値の差異が無く、互いに親和的であることも成膜性の高さに影響していると考えられる。一方、ZrO₂ には化学的吸着性は確認されておらず、また HA 基板と異なる物性値を有するため、HA/ZrO₂ 複合粒子の成膜性は低下したと考察できる。

さらに、粒子形状の変化が成膜性に及ぼす影響を考える。西川は平滑粒子法により、球状粒子の衝突界面における最大圧力は立方体粒子の約 1/5 であることを求め、その圧力下で形成された球状粒子膜は多面体形粒子膜と比べて基板との結合強度が小さく、剥離しやすいことを示している⁹⁾。そこで HA/HA 複合粒子と未処理 HA 粒子の各 10 枚の SEM 画像から円形度 φ の平均値を算出し、複合化処理による粒子形状の変化を評価した。円形度とは、真円を 1 とした場合の形状の複雑さを表す特徴量で、次式で定義される。

$$\phi = \frac{4\pi S}{L^2} \quad (2)$$

ここで、L は周長さ、S は面積を表す。図 8 の計算結果から、複合化処理により粒子の円形度が 1 に近づくことがわかる。また円形度の平均値は HA 複合粒子で 0.857、HA 未処理粒子で 0.612 であった。これは、複合化処理の過程で、翼や円筒内壁、他粒子間での衝突およびせん断力により、粒子の角が削られたことによると推定できる。以上より、複合化処理により粒子の円形度が増大し、成膜性の低下に繋がることを実験的に確認した。

4. 結言

本研究では、PJD 法を審美歯科治療にも応用するための基礎的検討として、HA 粒子と ZrO₂ 粒子を用いた成膜実験およ

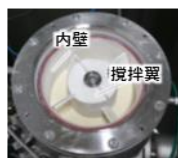
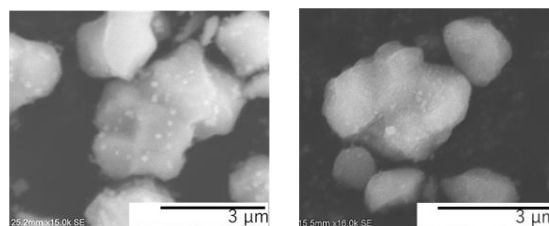
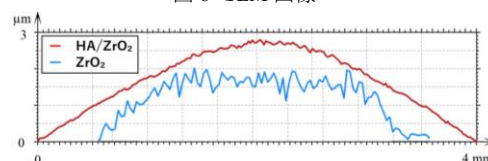


図 5 複合化装置

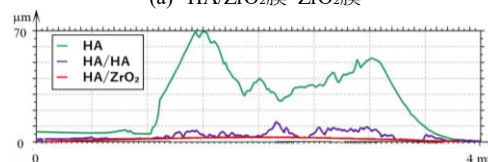
母粒子	HA 2.5μm
子粒子	ZrO ₂ 10nm
	HA 10 nm
回転数	1500rpm
複合時間	5min
複合比率	5%



(a) HA/ZrO₂ 複合粒子 (b) HA/HA 複合粒子
図 6 SEM 画像



(a) HA/ZrO₂ 膜・ZrO₂ 膜



(b) HA 膜・HA/HA 膜・HA/ZrO₂ 膜

図 7 各膜の断面プロファイル

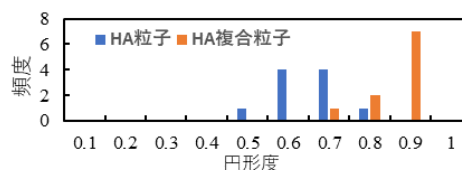


図 8 円形度ヒストグラム

び色調評価を行った。以下に得られた結論を示す。

- (1) 厚さ約 2.0μm の ZrO₂ 膜を HA 基板上に形成できた。
- (2) 成膜した ZrO₂ 膜は十分な明度を有し、かつ色の偏りの少ない白色膜であった。
- (3) 高い成膜性を有する HA 粒子を ZrO₂ 粒子と複合することで、成膜性が向上可能であることを示した。
- (4) 複合粒子の成膜性低下は、子粒子の物性と複合化処理による円形度の変化に起因することを明らかにした。

5. 謝辞

本研究は平成 28 年度新エネルギー・産業技術総合開発機構 戦略的基盤技術高度化支援事業(プロジェクト委託型)の助成を受けたものである。

6. 参考文献

- 1) R. Akatsuka, K. Sasaki, M. S. Sepasy Zahmaty, M. Noji, T. Anada, O. Suzuki, T. Kuriyagawa: Characteristics of hydroxyapatite film formed on human enamel with the powder jet deposition technique, J. Biomedical Material Research, Part B, (2011)
- 2) 簾内崇彰, 東北大学工学研究科, 2018 年度修士学位論文, パウダージェットデポジションによる複合粒子に関する研究
- 3) Sharma, Gaurav (2003). Digital Color Imaging Handbook (1.7.2 ed.)
- 4) 青木秀希, 矢嶋龍彦, 小山利幸: 驚異の生体物質アパタイトと表面技術, 表面技術, 一般社団法人表面技術協会 (2007)
- 5) 西川智弘, 東北大学工学研究科 2013 年度博士学位論文, パウダージェットデポジションに関する研究

プラズマ援用パウダージェットデポジションに関する研究

森田隆輝^{*1}, 本郷那美^{*1}, 山本浩己^{*1}, 嶋田慶太^{*1}, 水谷正義^{*1}, 厨川常元^{*2}

Study on atmospheric-pressure plasma assisted powder jet deposition

Ryuki Morita, Nami Hongo, Hiroki Yamamoto, Keita Shimada, Masayoshi Mizutani, Tsunemoto Kuriyagawa

Key words: atmospheric-pressure plasma, powder jet deposition, hydroxyapatite, dental treatment

1. 緒言

近年、歯科医療分野では生体機能の回復・改善に加え、歯の色調を美しく保つ審美歯科治療の需要が高まっている。著者らは、常温大気圧下で高速に粒子を衝突させて成膜するパウダージェットデポジション(以下、PJD)法を用いて、人歯の主成分であるハイドロキシアパタイト(以下HA)粒子と白色で審美的な歯科セラミック材料のジルコニア(以下ZrO₂)粒子を複合したHA/ZrO₂を、ヒト歯に直接成膜する手法を提案している^{1), 2)}。HA粒子PJD法では数十μmの成膜を実現しており、その有用性は臨床試験により既に実証されている¹⁾。ZrO₂に関しては、ヒト歯との弾性率の差異や化学的親和性などから成膜性の低下が懸念されており、篠内³⁾らはHA/ZrO₂複合粒子の成膜率は数μm程度と報告している。したがって、複合粒子を用いたPJD法の審美歯科治療への応用には低成膜性が問題である。

そこで本報では、大気圧プラズマ(以下、AP)をPJD法に採用することによるHA/ZrO₂複合粒子の成膜性向上を検証する。APは、人体に対する侵襲性は少なく、照射面の殺菌効果を狙った歯周病治療への応用がなされるなど、PJD歯科治療との親和性の高い手法であると考えられる。本報では、グライディングアーク放電³⁾による窒素流入型低温APをHA基板表面に照射することでプラズマ処理を施し、その後定点PJD噴射によりHA粒子の成膜性の変化を検証した。

2. プラズマ援用 PJD 装置と実験条件

図1は歯科治療用PJD装置の外観である。まず供給ガスを粒子タンクより負圧とし粒子を吸引する。その粒子がタンク、ハンドピース部まで搬送され、ノズル付近で加速ガスと合流して所定の速度まで加速された後噴射され、対象物へ衝突して成膜に至る。図2にAP発生装置、図3にAP発生装置ハンドピース構造を示す。ペン型のハンドピースからトーチ内部の電極間でアーク放電を生成し、そこに窒素ガスを流し込むことで、APをHA基板まで照射する。本実験では、図4に示す通り、

このペン型ハンドピースをPJD装置ハンドピースと基板の間に固定してAP照射を行った。実験の条件は表1に示す。



図1 PJD 装置



図2 AP 発生装置

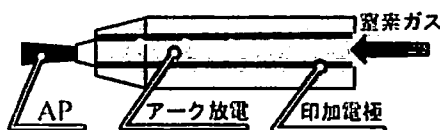


図3 AP 発生装置ハンドピース内部構造



図4 AP 援用 PJD 実験時の様子

表1 実験条件

HA 噴射条件	
基板材料	HA
搬送流体	空気
加速圧力	0.2 MPa
供給圧力	0.5 MPa
噴射時間	30 s
噴射距離	5.0 mm
プラズマ処理条件	
搬送流体	N ₂
供給圧力	0.1 MPa
AP 照射時間	5, 15, 30 s
待機時間	0, 5s, 40 s

*1 東北大学大学院工学研究科:〒980-8579 宮城県仙台市青葉区荒巻字青葉6-6-01

Graduate School of Engineering, Tohoku University

*2 東北大学大学院医工学研究科

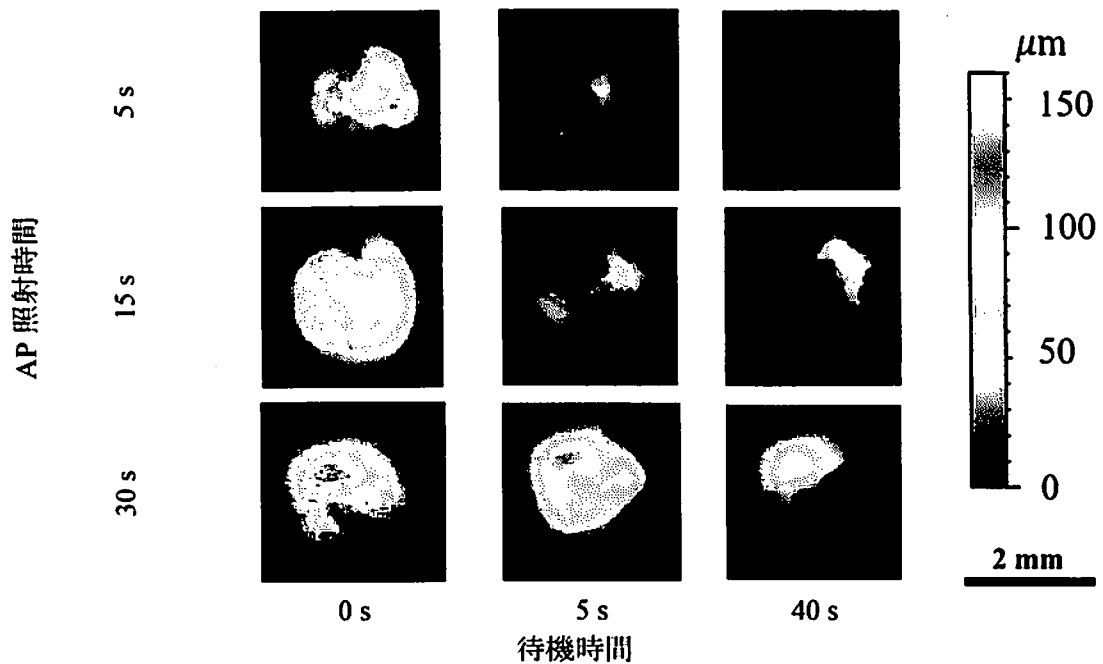


図6 各プラズマ処理での成膜結果

3. AP 援用 PJD による成膜性の変化

最も成膜性の高いプラズマ処理条件を選定するために表1の条件下で定点PJD噴射を9回行った。表1のAP照射時間、待機時間、噴射時間に関する実験経過を図5に示す。各条件におけるHA粒子膜の3次元形状を図6、膜厚と待機時間の関係を図7に示す。この結果より、最適プラズマ処理条件はAP照射時間30 s、待機時間0 sであることが分かった。

APをHA基板表面に照射することで基板表面に搬送気体として使用した窒素ガスが電離し衝突することで励起され、基板表面がHA粒子と結合しやすい官能状態となり、PJD法の第一層の積層が効率よく行われ、成膜性が向上したと考えられる。また、基板表面は酸素や有機物が付着しているが、プラズマ処理により表面が洗浄されたことも要因だと考えられる。

4. 結言

本研究では、PJD法を審美歯科治療に応用するにあたって課題となる、HA/ZrO₂複合粒子の低成膜性を改善させるための基礎検討として、AP援用PJD法によりHA粒子の成膜実験を行った。以下に得られた結論を示す。

- (1) HA基板へのAP照射時間が長く、待機時間が短い条件が最適プラズマ処理であることを明らかにした。
- (2) 本実験における最適プラズマ処理条件下でのHA粒子膜厚は、プラズマ未処理より約2倍大きかった。
- (3) AP援用PJD法により、HA/ZrO₂複合粒子の成膜性を向上させる可能性を示唆した。

5. 謝辞

本研究は平成28年度新エネルギー・産業技術総合開発機構戦略的基盤技術高度化支援事業(プロジェクト委託型)および科研費(JP18K13666)の助成を受けたものである。



図5 AP 援用 PJD 噴射実験経過

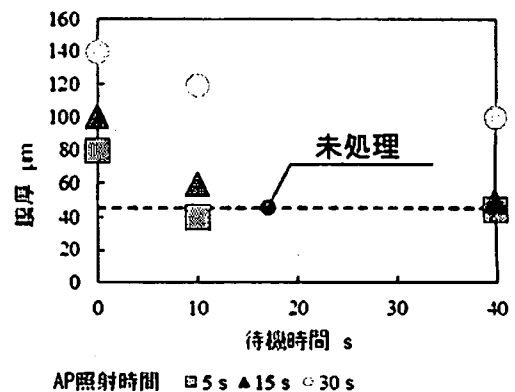


図7 HA 粒子成膜と待機時間の関係

6. 参考文献

- 1) R. Akatsuka et al., Characteristics of hydroxyapatite film formed on human enamel with the powder jet deposition technique, J Biomed Mater Res, 98B 2 (2011) 210-216.
- 2) 藤内崇彰, パウダージェットデポジションによる複合粒子に関する研究, 東北大学工学研究科, 2018年度修士学位论文
- 3) 北川貴之ら, グライディングアーク放電の流量依存性と非平衡状態への遷移, 応用物理学会, 2012

Study of Tape CMP Grinding of Gallium Nitride Wafer

Kota ORINO

Abstract

Power semiconductors are used in various kinds of electronic devices in modern society, and the improvement of power semiconductors is essential for miniaturization, weight reduction and power saving of electronic devices. However, the physical properties of silicon (Si) that is mainly used in power semiconductor substrates are reaching the theoretical limit. Therefore, such materials as gallium nitride (GaN) and silicon carbide (SiC) have been attracting attention as new semiconductor substrate materials. These materials possess better physical properties including a wide band gap, high breakdown strength and thermal conductivity than Si. SiC is suitable for devices that control high voltage and current, GaN is suitable for compact and high-frequency devices. Therefore, they are certainly expected to bring significant performance improvement in power semiconductors. On the other hand, their material properties like chemical stability, hardness, and brittleness, cause problems in the manufacturing phase; specifically in chemical mechanical planarization (CMP), considerable time is required to remove completely the residual damaged layer in rough-machining. Therefore, this thesis introduced tape CMP polishing that is ultraviolet (UV) and nanodiamond (ND) assisted tape polishing as a new method of CMP. UV etches the GaN surface and promotes generating gallium oxide (Ga_2O_3) that is half as hard as GaN. NDs can pull out Ga atoms in the GaN substrate if a sufficient pressure and relative velocity are applied between them. The advantages of tape polishing are a constant supply of new abrasives and an increase in effective abrasives. These advantages cause fine surface roughness with little damage. The purpose of this thesis is that achieving more efficient CMP than conventional CMP by tape CMP polishing.

Chapter 1 introduces the background and objectives of this thesis.

In Chapter 2, the basic material removal ability of the ND was evaluated through a ball-on-disk friction test on GaN substrates. Two types of ND dispersions, pure water dispersing negatively and positively charged NDs (hereinafter, referred to as ND-N and ND-P, respectively) and pure water alone as the control were utilized in the tests and the concentration of the dispersions was tested within 0.0001–0.1 wt%. The test load was set to 50, 100, and 200 g. The quantity of material removal and the residual damaged layer were then assessed from the processed workpieces via white light interferometric photographs and photoluminescence (PL), respectively. The ND-N dispersion provided the largest material removal amount under the same load condition. The material removal amount was increased with the concentration of NDs but the increase was saturated at around 0.001 wt% in both suspensions. The friction marks with the ND-N suspension raised a greater PL signal than those with ND-P; thus, the ND-N might contribute to minimizing residual damaged layer compared to ND-P. To sum up these results, the ND-N suspension with a concentration of 0.001 wt% or more was optimal for tape CMP polishing.

In Chapter 3, in order to optimize the conditions for tape CMP polishing, UV assisted tape polishing was conducted using #10000 and #20000 mesh-sized diamond (D) and alumina (WA) abrasive films and the polishing

efficiency and surface integrity including the roughness and thickness of the residual damaged layer were assessed. The D10000 film marked the highest polishing rate and the WA10000 film improved the surface roughness the most. On the other hand, some scratches were observed after polishing by the D20000 and WA20000 films. There were no significant differences in the PL signals between before and after polishing except for D10000. WA10000 was optimal for tape CMP polishing because the surface roughness is more important than the polishing efficiency.

In Chapter 4, surface roughness, amount of polishing and the residual damaged layer were assessed after UV assisted tape polishing and tape CMP polishing using WA10000. In addition to the PL measurement, a transmission electron microscope (TEM) was used to assess the residual damaged layer, and its observation clarified that the depth of the residual damaged layer before polishing was about 480 nm, which was beyond the range of the PL measurement. The depths of the residual damaged layers after UV assisted WA10000 tape polishing and after tape CMP polishing were around 390 nm and 330 nm, respectively. Therefore, assisting ND was more effective in removing the residual damaged layer. Finally, the PL signals after tape CMP polishing were larger than after UV assisted tape polishing. For all of these reasons, the increase in the removal amount is possible without an increase of residual damaged layer by assisting ND.

In Chapter 5, the general conclusions of this study are summarized.

Study on high functionality of cutting tool by Plasma-Shot Treatment

Yorihito Shibata

Abstract

High-efficiency cutting has increasingly been demanded high-mix low-volume production; however, the tool life is a bottleneck for realizing more efficient manufacturing because the cutting tools are exposed in a severe environment of high temperature and high pressure in high cutting speed, which can extensively raise the wear rate. To protect the tools from wear, surface treatment technology is applied on the surface to form wear-proof layers. Conventional surface treatment technologies include chemical vapor deposition and physical vapor deposition. The disadvantages of the conventional surface treatment are low adhesion for coating and the thickness nonuniformity in applying to the complex surfaces. The surface treatment technologies for solving these disadvantages are plasma shot (PS) treatment. In this process, arc discharges occur between the workpiece and the electrode, and the electrode partially melts and transfers to the workpiece surface during the discharge. The PS treatment can give various surface characteristics by using an appropriate electrode material; e.g. a previous study reports that a modified layer with a high hardness was successfully formed on iron-based materials by using TiC electrode; however, the PS treatment has the disadvantage of occurring shape deterioration called "sagging" when this treatment is applied to the cutting edge of tools. Thus, this thesis introduces a new PS treatment that solves the shape deterioration in the cutting edge by adjusting the position of the electrode, which is named position-adjusted PS (PA-PS) treatment. Moreover, this thesis introduces another PS treatment named "structured-electrode PS (SE-PS) treatment" in which dimples are arrayed in stripes. The fabricated microtextures on the tool are expected to reduce the expansion of the adhesion range and trap wear debris. Cutting experiments were then carried out for evaluating the effectiveness of the microstructure on the high-speed steel (HSS) tools in the cutting process. This thesis consists of five chapters.

Chapter 1 is the introduction of this study. The mechanism and feature of PS treatment were explained. Moreover, two new PS treatments, PA-PS and SE-PS, were proposed. The details of HSS that is a common material for cutting tools were explained. Finally, the objectives of this thesis and the organization of this thesis were described.

In Chapter 2, the PS treatment was applied to HSS surfaces using a TiC electrode to confirm the effect of the discharge current (I_p) on forming a single dimple and evaluate the modified layer. The diameter of a single dimple increased by the increase of I_p but its growth became saturated after $I_p = 10$ A. The roughness of single dimple also was increased as I_p increased.

The roughness of the modified layer increased when I_p increased. Energy-dispersive X-ray spectrometry (EDX) shows Ti atom and the atom density increased when I_p and the electrode consumption volume (V_e) increased. The friction test confirms that the friction of the modified surface was reduced by discharge dimples under low load conditions. The Vickers hardness test confirms that the hardness of the modified surface was about 300 to 600 HV larger than that of an untreated HSS surface. The hardness also increased with increasing I_p . The size of the deterioration of the edge of the modified layer increased when I_p increased. Therefore, the characteristics of the

modified layer were confirmed when I_p and V_e were changed.

In Chapter 3, the modified layers were formed by PA-PS and SE-PS. The PA-PS is a treatment adjusting the end of the electrode in several tens of micrometers from the edge of the workpiece to avoid deteriorating the edge form. The SE-PS is a PS treatment with a structured electrode to control the treated and untreated zones; the structures on the electrode are fabricated by wire electric discharge machining.

As a result, the PA-PS achieved to form a modified layer without deteriorating the edge shape of the workpiece under $I_p = 21$ A. The SE-PS formed modified layer that dimples were controlled the treated and untreated zones. The width of the unmodified part on the machined area decreased when I_p and the electrode machined width (w) increased. The machined area showed arc discharge obliquely occurred from the edge of the TiC electrode to the workpiece. The distance of the arc discharge increased with increasing I_p . The friction test confirms that the friction of the SE-PS treated surface under $I_p = 3$ A was not significantly different from that of the normal PS treatment. However, the friction of this treatment was slightly smaller than normal PS treatment under low load conditions. Therefore, the characteristics and appropriate treatment conditions of new two PS treatments are cleared.

Chapter 4, cutting experiments were carried out using the tool with microstructure prepared in Chapter 2, and Chapter 3. The prepared HSS tools were (a) unmachined tool, (b) tool treated by normal PS treatment under $I_p = 3$ A, (c) tool treated by "PS treatment using textured electrode" under $I_p = 3$ A, (d) tool treated by normal PS treatment under $I_p = 21$ A, (e) tool treated by "Changed machining position treatment" under $I_p = 21$ A. Cutting experiments were carried out under wet conditions and dry conditions.

As a result, black adhesion on cutting face and burning on the flank was confirmed under wet conditions by a Digital microscope. The range of burning on the flank increased when cutting distance increased. In (a), the adhesion area was expanded to a maximum area when the cutting distance was 50 m and this area was kept. The adhesions accumulated in the same adhesion area when the cutting distances were 150 and 300 m. In others, the adhesion range gradually increased as the cutting distance increased. In (c), the adhesion area was specially expanded in the groove on the microstructure surfaces. The white light interferometric figures show that the adhesion area under (d) was the smallest in all conditions. Moreover, this area was 50 % smaller than that of (a).

The dynamometer shows that the cutting forces under (b) and (c) were lower than those of others. The cutting force under (d) became the largest in all conditions. The cutting force under (e) was lower than that of (d) because "Changed machining position treatment" reduces cutting force. The expansion of the adhesion area under (b) and (c) under dry conditions more accelerated than those of wet conditions when cutting distance increased. Therefore, the adhesion range was small at $I_p = 21$ A, and the cutting force was small at $I_p = 3$ A.

Chapter5 presents the general conclusion obtained in this study

Study on creation of fine periodic structure on V-shaped groove with short-pulsed laser

Ryohei TAKASE

Abstract

In recent years, there have been increasing demands for high functionality, adding high values and saving energy of industrial products. Functional surface creation technology is attracting attention because it dramatically improves the properties of material and adds new functions with creating microstructures on the order of micro- nanometers on the material surface. These microstructures require suitable shapes and dimensions for the required functionality. Many studies have been conducted on a single processing method to create microstructures that can add some functionalities on material surface; while, there are few reports on composite structures created by combining single processing method, and the behavior of composite structure has not been clarified. However, “functional composite microstructures” created with combining some functional surfaces expected to have potential that can combine some functionality or exhibit unknown functionality. Therefore, in this study, functional composite microstructures were attempted to fabricate with combining the cutting process that has various advantages as a functional surface creating method, and the LIPSS (laser-induced periodic surface structures) created by short-pulsed laser (SPL), which is expected to further expand demand and industrial application in the future; in particular, create nanometers scale LIPSS into micrometers scale structure created with cutting process. The currently supported principle of LIPSS generation assumes only plane surface, however for practical use of SPL, it is important to clarify the behavior of LIPSS generation on non-planar surface.

The purpose of this thesis is to create LIPSS with SPL on the slope of V-shaped microgrooves (hereinafter, simply referred to as “V-grooves”) created by ultraprecision cutting, investigate the effect of the surface shape on LIPSS creation, and clarify the principle of LIPSS generation on the slope. In addition, wettability was evaluated because it is expected to be applied to various products as a functional evaluation, and investigate the effect of the composite microstructures made with V-grooves and LIPSS on the wettability.

This thesis is composed of five chapters.

Chapter 1 states the background and the objectives of this thesis.

In Chapter 2, 90° V-grooves were fabricated by ultraprecision cutting as an example of non-planar surface, and the SPL was irradiated on them to create the LIPSS on their slope areas. The LIPSS was successfully fabricated on the slope area of the V-grooves by laser irradiation; however, under specific conditions, the LIPSS were created in a different direction and had a pitch width from those fabricated on the plane. As

opposed to the LIPSS created on the plane surface, on the slope of the V-groove that is parallel to the V-groove regardless of the polarization direction and has narrower pitch than laser wavelength as UNPL (unidirectional narrow pitched LIPSS). Then, in order to verify the cause of why the LIPSS were differently fabricated, similar irradiation experiments were performed on 120° V-grooves, having a wider apex angle than 90°, and a one-sided slope that extracted one side of V-grooves.

The experimental result suggested that the interferences between the incident laser and the reflection on the slope of the V-grooves and between the incident laser and diffracted light generated at the edge of the V-grooves affected to the fabrication of different LIPSS.

In Chapter 3, the principles of the LIPSS generation on the slope of the V-grooves obtained in the previous chapter were examined with image analysis and electromagnetic field analysis by finite-difference time-domain (FDTD) method. The results of pitch width measurement and electromagnetic field analysis showed that the generation of the UNPL at the 90° V-groove slope was caused by the effect of interference between incident laser and reflected laser at the V-groove slope. On the other hand, it was clarified that the creation principle of UNPL created at the 120° V-groove slope is based the other theory described in Chapter 2. The experimental results about irradiation number dependence of LIPSS generation showed that the principle of LIPSS generation on the slope of V-grooves varied with irradiation number and the energy density.

In Chapter 4, V-grooves and LIPSS composite microstructures (hereinafter, simply referred to as "V-L structures"), LIPSS on the slope of the V-grooves, were fabricated by the ultraprecision cutting and the SPL and the contact angle (CA) was determined by dropping water droplets on the surface of the composite microstructures. The CA increased on the 90° V-L structured surfaces compared to on the 90° V-groove alone surfaces; contrastingly, it decreased on the 120° V-L structured surfaces. These differences might be brought that the LIPSS changed the behavior of water droplets that were attract to or repelled from the inside of the V-grooves. On the other hand, LIPSS orientation provided no significant change in the CA; therefore, LIPSS orientation might not possess enough effects to inhibit the extension of water droplets.

In Chapter 5, the general conclusions of this study are summarized.

修了年度	2019 年度	課程	博士課程前期 2 年の課程
英文 Abstract			
Title:	Study on creating functional biointerfaces by laser irradiation		
Author:	Chiaki TAKITA		
Supervisor:	Tsunemoto KURIYAGAWA		
<p>Dental health is closely related to quality of life (QOL) improvement, and implant therapy is effective in prosthesis for missing teeth and recovery of QOL. Currently, however, inflammation caused by bacterial infection is a problem in implant therapy. The purpose of this study is to create ideal functional biointerfaces that have both biocompatibility and anti-bacterial adhesion properties, e.g. hydrophobicity and photocatalytic activity by the simultaneous process of microfabrication and chemical property changes on the material surface with nanosecond pulsed laser.</p> <p>This thesis is composed of five chapters. Chapter 1 states the background and the objectives of this thesis.</p> <p>In Chapter 2, laser processing was applied to Ti-6Al-4V alloy surfaces to create grooves and micro-irregularities on the surfaces. The surfaces became hydrophobic due to topographical changes and chemical stabilization, and the oxygen vacancies introduction into the oxide layer was suggested, which is thought to contribute to the improvement of photocatalytic activity.</p> <p>In Chapter 3, the bacteria tests using E. coli and S. aureus were performed and the results suggested that grooves rather than hydrophobicity contributed to antibacterial adhesion property.</p> <p>In Chapter 4, the cell proliferation and differentiation using osteoblast-like cells were performed on Samples A and B, on which bacterial adhesion increased and decreased respectively in the test of the previous chapter. The result showed that Sample A inhibited cell growth, and Sample B did not affect it. In conclusion, functional biointerfaces for dental implants may be realized by forming grooves suppressing bacterial adhesion and suitable micro-irregularities promoting cell growth. In Chapter 5, the general conclusions of this study are summarized.</p>			
和文アブストラクト			
論文題目:	レーザ照射による機能性バイオインタフェース創成に関する研究		
提出者氏名:	瀧田 千秋		
指導教員:	厨川 常元		
<p>歯の健康は生活の質 (QOL) 向上に密接な関係があり、インプラント治療は欠損歯を補綴し QOL 回復に有効である。インプラントでは現在、細菌感染による炎症が問題であることから、本研究ではナノ秒パルスレーザ加工により材料表面の微細加工と化学的性質変化を同時に行い生体適合性と、細菌付着抑制の性質—疎水性、光触媒能などを両立したインプラントにとって理想的な機能性表面の創成を目指す。</p> <p>本論文は 5 章構成である。第 1 章では、上記の研究背景と研究目的を詳述する。</p> <p>第 2 章では、Ti-6Al-4V 合金表面にレーザ加工を施し、表面に溝形状や微細凹凸構造を形成した。表面は形状変化と化学的安定化により疎水化し、酸化皮膜へは光触媒能向上に寄与すると考えられる酸素欠陥導入が示唆された。</p> <p>第 3 章では、大腸菌と黄色ブドウ球菌を用いた細菌試験を行った。その結果、細菌付着抑制には表面の疎水化ではなく、溝形状が寄与することが示唆された。</p> <p>第 4 章では、研磨試料 (コントロール)、細菌付着が増大した試料 (試料 A) と、付着低減が示唆された試料 (試料 B) に対して骨芽細胞様細胞を用いた増殖・分化試験を行った。その結果、試料 A は細胞の成長を抑制し、試料 B は細胞の成長に影響を及ぼさなかった。以上より、細菌付着抑制効果の可能性がある溝形状と、細胞の成長促進のための適度な微細凹凸を併せ持つ表面が機能性表面実現には必要であることが示唆された。第 5 章は本論文の結論である。</p>			

Development of Dental Handpiece of Powder Jet Deposition

Hiroki YAMAMOTO

Abstract

The human teeth, which are hard tissues in the human oral cavity, are important structures related to mastication, pronunciation, respiration, and facial features. The occlusal abnormalities have been pointed out that they can have adverse effects on the body and mind, so maintaining healthy teeth is extremely important for improving quality of life. In the current caries treatment method, the prepared cavities where the decayed part is removed are filled by a dental restoration made of metal, resin, etc., using medical adhesive. However, these dental restorations have problems of mismatching in mechanical characteristics, biocompatibility, and aesthetics; consequently, the use of the original materials of the human teeth is ideal for restorative treatment. To realize the ideal, a new dental treatment method has been proposed by using powder jet deposition (PJD) technique to make coatings on human teeth. With this technology, a powerful coating can be formed by colliding particles at high speed under room temperature and atmospheric pressure. By using particles of hydroxyapatite (HAp), a major component of human hard tissue, films with properties similar to human enamel can be formed directly on human teeth. Clinical experiments of PJD treatment were performed using the developed equipment called tube-conveying type for particle ejection. However, the HAp particles are hygroscopic and become easily viscous, thus they can cause a choke of the flow path and sudden spray of particles. To solve these problems, a prototype device called a compacted powder-loaded type handpiece has been developed; particles are supplied by cutting a compacted powder. In this study, the blasting characteristics and optimum cutting conditions of this device are investigated. In addition, we verify the optimal flow path shape and particle dispersibility for HAp deposition.

Chapter 1 is the introduction of this thesis. The background of the present research, the achievements and remaining problems of the previous study and the objectives of the present study are described.

In Chapter 2, standard PJD tests were performed using the compacted powder-loaded type device to assess the blasting characteristics and cutting conditions. The temporal changes of particle spraying amount were assessed on the current model and the prototype. The results showed that the prototype could spray particles stably; while, the spraying amount fluctuated greatly in the current type. Next, the compressed particles were cut by different cutting speeds and rotation speeds, then the particle size distribution and the film shape were observed. Those results showed that a larger feed rate contributed to a better particle dispersibility and the processing mode shifted to the deposition more than the removal.

In Chapter 3, in order to improve the problems in the blasting by the compacted powder-loaded type device, the shape of the nozzle flow path was optimized. The conventional nozzle had a part where the cross-sectional area decreased rapidly in the flow path, which caused a pressure loss. Consequently, the particle velocity at the moment of the collision was lower than that of the tube-conveying type, and the deposition efficiency was poor.

In addition, the surface of the formed film became rough in both types. To solve these problems, the diameter of the nozzle outlet was reduced to accelerate particles and increase collision density. The results of computational fluid dynamics (CFD) using the flow path model of diameter reduction nozzles indicated that the reduction of nozzle outlet diameter could increase the particle velocity and density at the moment of the collision. Then, a thick smooth film with a maximum height of 30 μm and a volume of 6.43 million cubic micrometers was successfully formed under the conditions of 0.2 MPa supplying pressure and 0.8 mm outlet diameter. In addition, the particle size distribution showed that the smaller the diameter of the outlet through which the particles pass, the better the particle dispersibility. This tendency is due to the rapid acceleration of the particles and the increase of the internal static pressure. Based on these results, the interaction between the particle dispersibility and film surface roughness was investigated. Comparison of particle dispersibility and film surface roughness showed that powders with primary particles of 16.5% or more by volume produced a film with a smooth surface. Furthermore, particles with an equivalent circular diameter smaller than 4 μm were defined as primary particles. Finally, a mapping of the smoothness of the film surface was created based on the particle dispersibility and particle velocity.

In Chapter 4, five types of metal nozzles were fabricated to verify the effect of the nozzle shape on the particle dispersibility. The nozzles were classified into straight-, stepped-, and bend-type flow paths. Firstly, every nozzle was designed with the CAD and the particle velocities at the collisional moment were calculated with the CFD under the supplying pressure of 0.1–0.5 MPa. From those data, the graphs and approximate expressions showing the relationship between the supply pressure and the particle collisional velocity were created about each nozzle. The collisional speed 163.7 m/s was set as the reference speed and the supply pressures of each nozzle at which the collision velocity becomes the reference speed was calculated using the approximate formula. The results of the blasting experiments and the particle size distribution at those pressures showed that acceleration at the step and collision with the wall at the bend disperse the particles, and rectification of the air through the long pipe causes the particles to aggregate. Additionally, a film by L24 nozzle had a volume of 25.9 million cubic micrometers. A comparison of the particle size distribution and the film surface suggested that the large agglomerated particles caused the roughening of the film surface. Film formation experiments using a powder mixture of conventional particles and large particles supported this. The relationship between the size of agglomerated particles causing surface roughness and collision velocity agrees with the relationship between the particles median diameter and collision velocity calculated in the previous research: $V_c = 450.99d - 0.38$. This fact indicates that large aggregated particles behave like large particles and that the target value of dispersibility can be calculated from the collision velocity.

In Chapter 5, the general conclusions of this research are summarized.

【令和元年度卒業生】

	氏名	研究テーマ	所属先・勤務先
学 部 生	伊藤 優汰	金属積層造形法を用いた 3 次元窒素拡散チタン構造体創成に関する研究	進学（工学研究科）
	中村 隼太	ナノ精度研削砥石のための均一分散分級技術の開発	進学（工学研究科）
	皆川 敦暉	アモルファス合金の新しいプレス加工法の提案	進学（工学研究科）
	森田 隆輝	プラズマ援用パウダージェットデポジションに関する研究	進学（工学研究科）
大 学 院 博 士 課 程 前 期	折野 光汰	窒化ガリウムウエハのテープ CMP 研磨法に関する研究	旭化成株式会社
	柴田 頼人	プラズマショット法に関する研究	丸紅株式会社
	高瀬 稜平	短パルスレーザー照射による V 溝への微細構造創成に関する研究	サントリー株式会社
	瀧田 千秋	レーザー照射による機能性バイオインターフェース創成に関する研究	株式会社村田製作所
	山本 浩己	歯科用パウダージェットデポジションハンドピースの開発	JFE エンジニアリング株式会社
博 士 課 程 後 期	鷹巣 良史	窒化ガリウムウエハの紫外線援用高効率・低ダメージ加工に関する研究	パナソニック株式会社 (社会人ドクターとして所属)
	前花 英一	微細ラティスコーティングに関する研究	コマツ NTC 株式会社 (社会人ドクターとしての所属)

【研究室だより】

昨年度末から本年度の現在までは新型コロナウイルスの影響により波乱続きの状況でございます。研究室への入室制限やテレワーク推奨など、例年とはまったくことなる状況となっており、4、5月は研究推進が困難な状況ではございました。今後どのような状況になるともわかりませんが、今は少しずつ状況が改善されてはおりますので、このまま徐々に研究を推進していきたいと存じますので、引き続き皆様のお力添えをいただければ幸いです。

令和2年6月
助教 嶋田 慶太